A COMPREHENSIVE STUDY OF NOVA PERSEI 2018: A GAMMA-RAY BRIGHT NOVA FROM A KNOWN DWARF NOVA

by

FIONA JO MURPHY-GLAYSHER

A thesis submitted in partial fulfilment of the requirements of

Liverpool John Moores University for the degree of

DOCTOR OF PHILOSOPHY

February 2023

Abstract

The eruption of a classical nova (CN) is an extremely energetic transient event that produces a rapid optical brightening of 10-15 magnitudes, followed by a slower decline in luminosity. A CN is a binary system consisting of a white dwarf (WD) primary that accretes stellar material from the less-evolved donor star. In the majority of systems, mass transfer onto the WD takes place via an accretion disk. A thermonuclear runaway is triggered when sufficient mass has accumulated on the WD, and the energy thus injected into the WD envelope causes the high velocity expulsion of the envelope in the nova eruption. Due to the rapid ejection of this shell of material, the WD photosphere expands and then contracts, which is observable as the brightening and subsequent fading of the nova light curve.

A dwarf nova (DN) outburst is less luminous than a CN eruption, and occurs when material in the accretion disk is suddenly deposited onto the WD due to thermal or tidal instabilities within the disk. The corresponding release of gravitational potential energy powers the increase in luminosity.

V392 Persei is a known DN that underwent a CN eruption on April 29 2018, with γ-ray emission detected from the system the following day. V392 Per provided the first opportunity to study the γ-ray emission processes in a previously studied nova system. Here we report ground-based optical, *Swift* UV and X-ray, and *Fermi*-LAT γ-ray observations following the eruption for almost three years.

The optical light curve reveals that V392 Per is one of the fastest evolving novae yet observed, with a t_2 decline time of 2 days. Early spectra present evidence for multiple and interacting mass ejections, with the associated shocks driving both the γ-ray and early optical luminosity. V392 Per entered Sun-constraint within days of eruption. Upon exit, the nova had evolved to the nebular phase, and we saw the tail of the super-soft X-ray phase. Subsequent optical emission captured the fading ejecta alongside a persistent narrow line emission spectrum from the accretion disk.

Ongoing hard X-ray emission is characteristic of a standing accretion shock in

an intermediate polar. Analysis of the optical data reveals an orbital period of 3.230 ± 0.003 days, but we see no evidence for a WD spin period. The optical and X-ray data suggest a high mass WD, the pre-nova spectral energy distribution (SED) indicates an evolved donor, and the post-nova SED points to a high mass accretion rate.

Following eruption, the system has remained in a nova-like high mass transfer state, rather than returning to the pre-nova DN low mass transfer configuration. We suggest that this high state is driven by irradiation of the donor by the nova eruption. In many ways, V392 Per shows similarity to the well-studied nova and DN GK Persei.

A preliminary photoionization analysis of the early nebular spectra was performed in an attempt to constrain the ionization conditions within the nova shell. Three key emission line flux ratios were measured from the spectra. The plasma simulation and spectral synthesis code CLOUDY was used to produce an array of models that varied the effective temperature of the WD (the ionizing source), and the electron density and metallicity of the nova shell. The measured line ratios were compared with the predicted ratios for the models. Although the results were inconclusive, they indicated some constraints on the ionization conditions that were consistent with what we might expect for a nova shell.

Finally, some suggested developments of the work discussed in this thesis are presented. The first extension considered is a more complete analysis of the photoionization conditions within the shell of V392 Per, accompanied by morpho-kinematic modelling to constrain the geometry of the nova shell. Another avenue to progress this work is to conduct a further monitoring campaign on V392 Per and ascertain the ongoing mass transfer state of the system. Polarimetric observations may reveal signals of the WD magnetic field, or of a degree of dust production within the expanding shell. Perhaps the most exciting possibility would be to apply the same analytical techniques to observations of a system similar to V392 Per, but which does not experience Sun constraint at such an early stage of its evolution.

Declaration

The work presented in this thesis was carried out at the Astrophysics Research Institute, Liverpool John Moores University. It is the original work of the author in its entirety, unless otherwise stated.

No portion of the work referred to in the thesis has been submitted in support of an application for another degree or qualification of this or any other university or other institute of learning.

Fiona Jo Murphy-Glaysher
Astrophysics Research Institute
Liverpool John Moores University
IC2, Liverpool Science Park
146 Brownlow Hill
Liverpool
L3 5RF
UK

22nd February 2023

Dedication

This thesis is dedicated to my wonderful Mum, Josephine Murphy. Your love, support and encouragement were unwavering, and I benefitted greatly from your belief in the value of education, and in me. I know you would be very proud of me.

Acknowledgements

"*For my part, I know nothing with any certainty*

but the sight of the stars makes me dream..."

Vincent Van Gogh, 1888

I would like to begin by expressing my gratitude to Matt Darnley. Your support and encouragement have been amazing throughout the time I have worked with you, from working on the MSc project, through applying for PhDs, and most of all - during the last four years. Your knowledge of novae is encyclopaedic - I can only hope that one day I will know half as much about them as you do! Scientifically, you have taught me so much, and your seemingly endless enthusiasm and patience have been invaluable, particularly during the lockdowns due to COVID, and while working on the paper.

Next, I would like to extend my thanks to my other supervisors, Andy Newsam and Éamonn Harvey. You have both been hugely helpful over the course of the PhD. Andy, your passion for outreach and art have been inspiring. You have also helped me to clarify my explanations of my work, and make me very glad that I had so many X-ray photons to work with (even though I would have liked more)! Éamonn, when I think of you, I can't help but get a mental replay of you talking about the geometry of a nova shell, with liberal references to polar cones and how everything depends on whether you are looking down the barrel of a gun or from a different viewing angle.

The next person I would like to thank is Kim Page. Your help and advice about all things *Swift* related has been incredibly useful, and I appreciate your enthusiasm and your tireless updates through the *Swift* nova CV mailing list.

To Phil James and Marie Martig, my PhD mentors, thank you for all of your help and support over the last four years. You are both part of the beating heart of the ARI, and I know I'm not the only person who thinks so.

Within the ARI, there are too many people to thank individually. I have immensely enjoyed being a part of the department. I count myself privileged to have had the opportunity to work with so many lovely, friendly people, who are also dedicated and professional. Not only that, but I have found the department to be inclusive, and striving to become even more so. I would like to thank Anna Hodgkinson, Caroline Ramsay, Danielle Coogan and Dan Harman for everything you do for the department. I have had innumerable fascinating discussions with people about so many different topics, scientific and otherwise. To everyone who I have spoken to in journal clubs (particularly all of the past and present members of the Time Domain group), at the pub, at the bowling alley, at Thursday coffee, or just when bumping into each other in the corridors or the kitchen, thank you for enhancing my experience of conducting research for my PhD.

In particular, I would like to thank all of the other PhD students I have overlapped with for contributing to the atmosphere I have so enjoyed over my time at the ARI, not to mention some great trips to the pub, and company at conferences. There are far too many amazing people to name, so I will limit myself to the people who started at the same time as me, Allister, Conor, Danny, Sam and Shaun. And a special mention has to go to Conor (again!) and Mike, my PhD brothers.

Funding for my studies was provided jointly by UKRI/STFC under grant number ST/S505559/1 and by the Faculty of Engineering and Technology, Liverpool John Moores University. I would like to thank the administration team at FET for everything they do to keep so many things running smoothly.

I would also like to thank my examiners, Stewart Eyres and Chris Copperwheat, for an interesting and thought-provoking discussion of my research. Your suggested corrections have certainly improved this thesis.

And last, but certainly not least, thank you to my family. I couldn't have completed this PhD, or my OU degree and MSc, without the love and support of my husband, Paul Glaysher. You have cheered me up during tough times, and we have

enjoyed so many laughs together. To my sons, Xander and Dante, you enrich my life so much and it has been amazing seeing how much you have changed over the time I have been doing my PhD. I would also like to thank Blair Murphy, my Dad, for so much, not least of which was introducing me to science fiction films and TV such as Star Wars and Star Trek, which inspired my love of physics and astrophysics.

Contents

List of Figures

List of Tables

Chapter 1

Introduction

1.1 History of Novae

The word nova comes from the Latin "stella nova", meaning new star. This name arose due to the sudden brightening of a star such that it became visible to the naked eye, originally thought to be the birth of the star. These sudden appearances have been observed since ancient times, with the earliest known observation of a nova eruption recorded by Chinese astronomers in the 14th Century BCE (Li, 1988).

A catalogue of novae and supernovae predating 1604, observed before the invention of telescopes, was published by Bode & Evans (2008). There was no distinction between the two classes prior to the 20th Century. The fast declining Nova Scorpii 1437, erupting on 11 March 1437, was one of the best located classical novae detected in the pre-telescopic era. It has been claimed the 'Star of Bethlehem' was also a possible nova observation, coinciding with the Chinese and Korean records from around 5 BCE (Clark et al., 1977), although this was refuted by Schaefer (2013). Another interesting pre-telescopic nova observation was that of CK Vul (Shara et al.,

1985), which was observed during 1670. However, recent observations suggest this was not a nova eruption (Evans et al., 2016), but could instead have been a merger between a white dwarf-brown dwarf binary (Eyres et al., 2018).

At the end of the 19th Century, astronomers began to monitor the sky more systematically, using photographic plates to record the observations (Bode & Evans, 2008). This marked a surge in the detection of novae, beginning with T Aur in 1892 (Campbell, 1893), which was the first nova system to be observed spectroscopically. Only when eclipses were discovered in the light curve of DQ Her was it realised that novae were binary objects (Walker 1954; Kraft 1964). So far, over 500 Galactic novae and more than 1000 extragalactic novae have been detected.

1.2 Classical Novae

Classical nova (CN) eruptions are highly energetic explosive transients, with only supernovae (SNe) and gamma-ray bursts (GRBs) exceeding their energy output. CNe are binary systems in which a white dwarf (WD) accretes hydrogen-rich material from a donor star via an accretion disk (Warner, 1995, see Section 1.4). Accretion proceeds via Roche-lobe overflow for the majority of CNe; those with main sequence or sub-giant donors. For CNe with giant donors, material is accreted from the giant's wind (Darnley et al., 2012; Darnley, 2021). The accreted envelope builds in temperature and pressure until a thermonuclear runaway occurs (Starrfield et al., 1976, 2016; Starrfield, 1989), blasting material from the WD's surface, leaving the WD and donor relatively unscathed (as discussed in Section 1.5). The CN is observed as a rapid increase in optical luminosity of 10–15 magnitudes, followed by a slower decline.

Within a given volume, the annual rate of CN eruptions is much higher than the rate of SN explosions or GRB events, and many CNe have erupted within the Milky Way and nearby galaxies. Therefore CNe can more readily be studied in greater detail due to their proximity and frequency. This makes them prime sources to inform our understanding of accretion processes, dust production, nuclosynthesis and particle acceleration in shocks.

CNe are one of the key sources of ^{7}Li (Izzo et al. 2015; Tajitsu et al. 2015), ^{13}C, ^{15}N and ^{17}O in the ISM (Gehrz et al. 1998; Jose 2016), rendering them crucial laboratories to help understand the chemical composition of stars and galaxies. Significantly, as will be discussed in section 1.8, recurrent novae (RNe) are one of the main single degenerate candidate progenitors for Type Ia Supernovae (SNeIa). The remarkable recurrent nova M31N 2008-12a is the leading candidate SN Ia progenitor due to its growing, already near-Chandresekhar mass WD (Darnley et al., 2017).

1.3 Cataclysmic Variables

CNe are a sub-type of cataclysmic variable (CV); a class that includes dwarf novae (DNe) and nova-like (NL) variables. DN outbursts are less luminous than CN eruptions and are powered by the release of gravitational potential energy, which can occur when hydrogen-rich material in the accretion disk is suddenly deposited onto the WD. The mass transfer rate through the disk of a DN is typically lower than that of a CN or NL. DN outbursts occur in systems where the accretion rate ($\dot{M}$) is lower than the critical rate (Smak, 1983, see their Equation 2), due to thermal or tidal instabilities within the disk (Osaki, 1996). The instabilities are responsible for 'dumping' large amounts of stellar material onto the surface of the WD, releasing substantial gravitational potential energy – visible as the DN outburst. For a given

disk radius, CVs with high $\dot{M}$ produce hot, stable disks – the NL systems, that do not show DN outbursts (Osaki, 1996; Warner & Woudt, 2003).

There are three sub-types of DN (Osaki, 1996). U-Geminorum, or SS Cyg, type DNe experience fairly regular quasi-periodic outbursts. Z-Camelopardis type DNe experience frequent outbursts, punctuated by standstills where the DN maintains a brightness intermediate between its quiescent and outburst magnitudes. The SU Ursa Majoris type DN exhibits two types of outburst. The normal short outburst typically lasts a few days, whereas the superoutburst has a duration of around 14 days.

1.4 Accretion

For all CVs, if the companion is a main sequence or sub-giant star, the system will be a close binary with orbital separation of a few $\times R_{\odot}$, with a Roche lobe-filling donor. As the donor's radius grows due to normal evolutionary processes, or as gravitational radiation very slowly drives down the orbital separation (in the case of novae with very short orbital period), some Solar composition material in the outer envelope of the donor experiences a stronger gravitational potential from the WD than from its own core. In this way, material can be stripped from the star and spill through the inner Lagrangian point into the WD's Roche lobe (see Figure 1.1). This is referred to as Roche-lobe overflow.

Alternatively, if the star is a red giant, the binary system will have a larger orbital separation, so the secondary will not necessarily fill its Roche lobe. However, due to its extended size and relatively low surface gravity, the giant will experience a strong stellar wind. A large amount of hydrogen-rich material, typically $10^{-6}\,\mathrm{M}_{\odot} \lesssim \dot{\mathrm{M}} \lesssim$

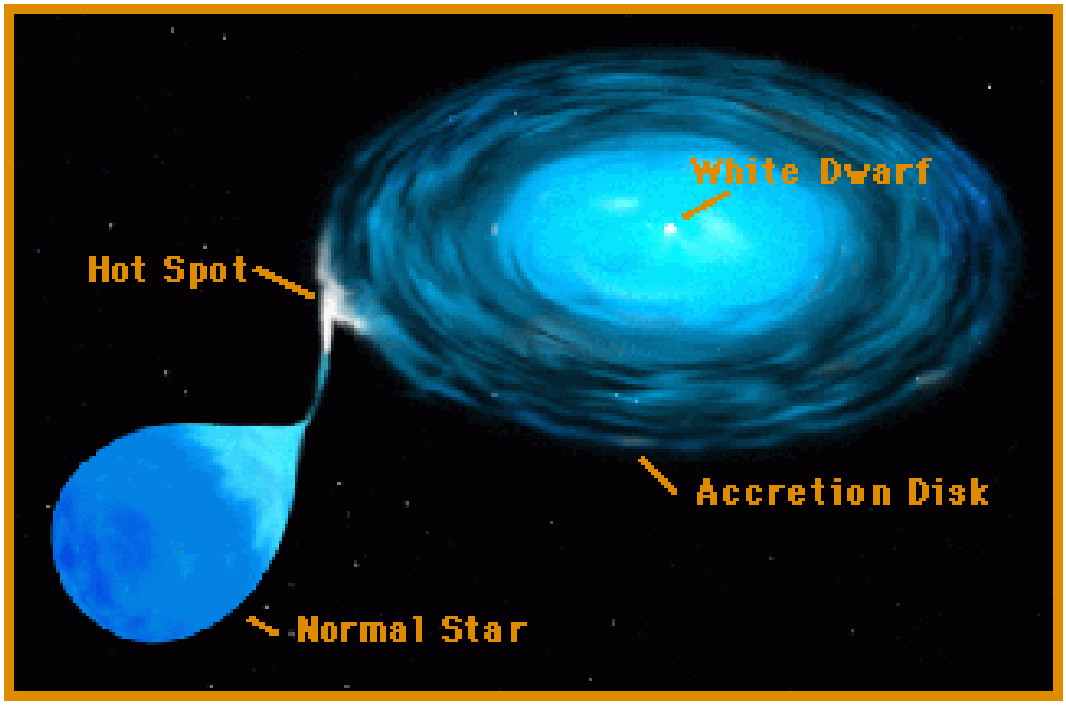

Figure 1.1: Accretion from a donor star onto a non-magnetic WD via an accretion disk, showing the hot spot. Figure available via Wikimedia commons `https://commons.wikimedia.org/wiki/File\protect\protect\leavevmode@ifvmode\kern+.2222em\relaxDiagram_of_a_Cataclysmic_Variable.png`

$10^{-4}\,M_\odot$ (van Loon et al., 2006), will stream out of the Roche lobe of the secondary, some of which will pass through the inner Lagrangian point and into the lobe of the WD, and some of the rest will enter the circumbinary regime, orbiting the binary system without being bound to either star individually.

The stellar material entering the WD's lobe has a high angular momentum due to the short orbital period of the binary, particularly in the case of a main sequence secondary, with orbital periods in the range $1.4 \lesssim P_{orb} \lesssim 8$ hours. Sub-giant companions have typical orbital periods of hours to days, whereas symbiotic novae with red giant companions have orbital periods of hundreds of days (Bode, 2010). As such, due to conservation of angular momentum, an accretion disc will form around the WD (Warner, 1995). The hydrogen-rich material in the accretion disk will move closer to the disk centre due to viscous and turbulent processes, with a typical accretion rate of $\dot{M}_{acc} \approx 10^{-9}\,M_\odot\,yr^{-1}$ (Bode, 2010; Warner, 2008). Eventually, it

will fall onto the WD's surface and heat up due to the conversion of gravitational potential energy into thermal energy.

1.4.1 Stable vs unstable accretion

The disk instability model (DIM) for DNe was first suggested by Osaki (1974), and applied to U Gem DN systems. It proposed that mass transfer from the secondary star proceeds at a constant rate, with mass being stored in the accretion disk until a critical mass is reached. At this point, a disk instability occurs, allowing mass transfer to the WD to take place at a rate exceeding the mass transfer from the secondary, releasing much of the gravitational potential energy that was stored within the disk. The accretion stream from the donor star onto the disk forms a hot spot. During the quiescent phase between DN outbursts, the hot spot and the accretion disk dominate the luminosity of the system.

Meyer & Meyer-Hofmeister (1981) suggested that the thermal limit cycle instability is responsible for triggering the liberation of mass from the accretion disk in DIM. In Figure 1.2, the thermal limit cycle for accretion disks is illustrated. In panel (a), there are two stable regions, indicated by the solid lines. The lower stable region, increasing in surface density to $\Sigma_{\rm max}$, is cold and convective with a low mass accretion rate and viscosity. The upper stable region, increasing in surface density from $\Sigma_{\rm min}$, is hot and radiative, with a high mass accretion rate and viscosity. The intermediate (unstable) region is indicated by the dashed line, and decreases in accretion rate as surface density increases. Within this region, accretion alternates between short, radiative periods of high mass accretion and long, convective periods of low mass accretion (Meyer & Meyer-Hofmeister, 1981). When accretion through the disk is stable, there will not be a DN outburst.

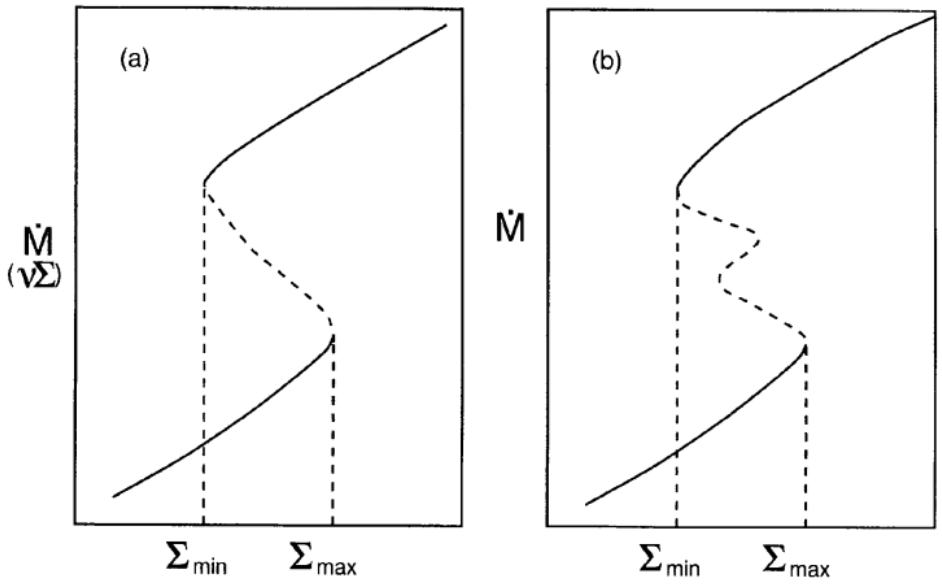

Figure 1.2: Panel (a): The thermal equilibrium S-shaped curve in the $\Sigma - \dot{M}$ phase-space of an accretion disk. Panel (b) illustrates a more complicated form of the thermal limit cycle, resembling the letter ξ. Figure appeared as Figure 4 in Osaki (1996), ['Dwarf-nova Outbursts', Osaki, PASP, 108, 39, 1996 DOI `http://doi.org/10.1086/133689` ©The Astronomical Society of the Pacific. Reproduced by permission of IOP Publishing. All rights reserved.]

For long orbital period systems, the regions of stability and instability within an accretion disk are shown in Figure 1.3 by the thermal equilibrium S-curves on the surface density-effective temperature phase-space ($\Sigma - T_{\rm eff}$) for disks of various radii from 10^9 to 10^{12} cm (Bollimpalli et al., 2018). For each radius, there are two stable regions, with similar gradient in the phase-space. In the cool region, the gas in the disk is in neutral atomic or molecular form. In the hot region, the hydrogen in the accretion disk is fully ionized. The intermediate region, forming the middle part of the "S", experiences both thermal and viscous instabilities. If the disk occupies this region of phase space, the CV will exhibit DN outbursts. The stable regions for a given disk radius are represented by different values of the viscosity parameter α. For the cold branch, the viscosity parameter is given by $\alpha_c \approx 0.02 - 0.04$, whereas $\alpha_h \approx 0.1 - 0.2$ for the hot branch.

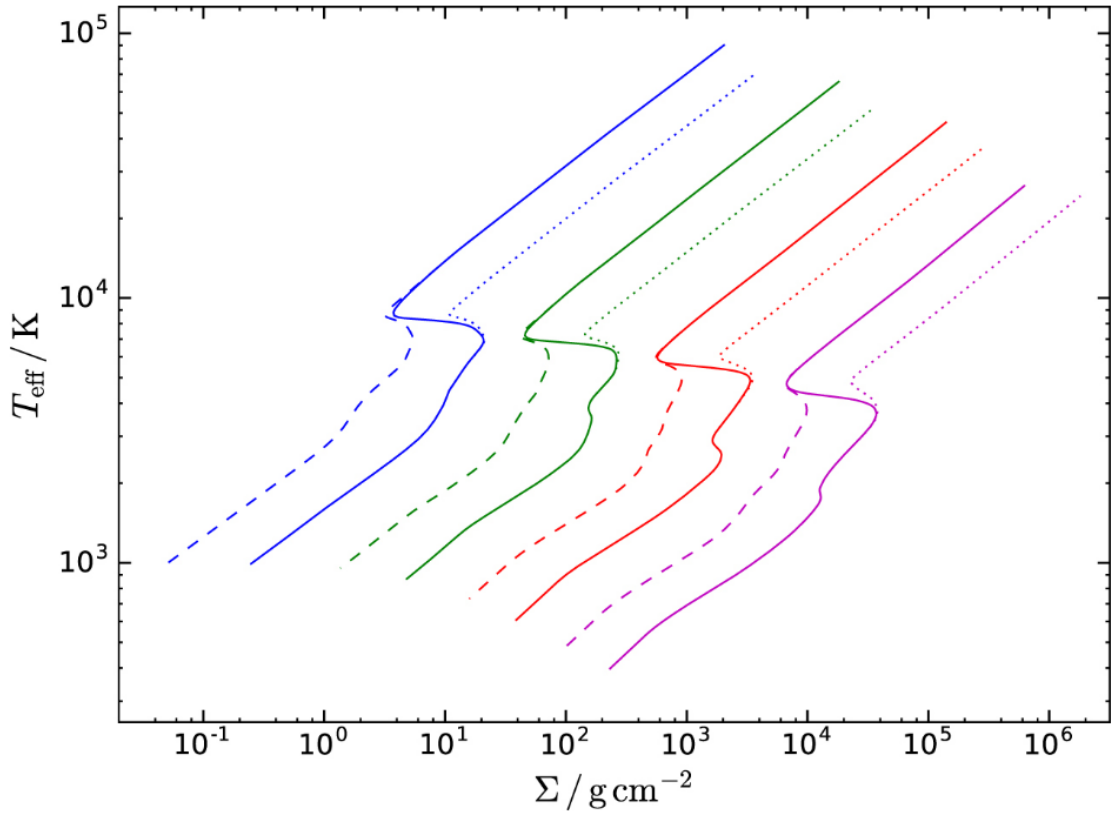

Figure 1.3: Stability of accretion within disk, shown by S curves of $\Sigma - T_{\rm eff}$ for a 1.35 $M_\odot$ WD. The blue, green, red and purple lines indicate disk radii of 10^9, 10^{10}, 10^{11} and 10^{12} cm, respectively. Dashed lines represent $\alpha = 0.1$, dotted lines represent $\alpha = 0.01$. The solid lines show the path that would be traced by real disks of a given radius. The disks exhibit high viscosity at high effective temperatures, and low viscosity at low effective temperatures. The shape of the S-curve is similar to that shown in Figure 1.2, except here the vertical axis shows $T_{\rm eff}$ instead of $\dot{M}$. Figure taken from Bollimpalli et al. (2018) ['Disc instabilities and nova eruptions in symbiotic systems: RS Ophiuchi and Z Andromedae', Bollimpalli et al., Mon. Not. R. Astron. Soc., 481, 5422, 2018 DOI `https://doi.org/10.1093/mnras/sty2555`].

1.4.2 Accretion in Magnetic CVs

The mode of accretion described above is typical for a CN. However, there are (observationally) rare instances when accretion follows a slightly different path. In the case of intermediate polars, such as DQ Herculis and GK Persei, the inner part of the accretion disk is disrupted by the WD's magnetic field of intermediate strength $10^6 \lesssim \mathrm{B} \lesssim 10^7 \mathrm{G}$ (Bode & Evans, 2008; Bode, 2010; Woudt & Ribeiro, 2014). When accreted material reaches the truncated inner part of the accretion disk, it streams along the magnetic field lines of the WD, forming "accretion curtains" of luminous material (Warner, 1995). Material in the disk moves through the curtains and then falls onto the surface of the WD at one (or occasionally both) of its magnetic poles.

In polars, such as Nova Cygni 1975 (V1500 Cyg) and Nova Sagittarii 1998 (V4633 Sgr) (Lipkin & Leibowitz, 2008), the WD has a very strong magnetic field of $\mathrm{B} > 10^7\,\mathrm{G}$ that funnels the accreted material directly onto the WD surface, with no accretion disk (Bode, 2010).

1.5 Nuclear Burning and the Thernonuclear Runaway

As the donor material builds up on the degenerate surface of the WD, the base of that envelope increases in temperature and pressure until hydrogen burning begins, initially via the proton-proton chain, but as the temperature rapidly increases to $T > 4 \times 10^6\,\mathrm{K}$ nuclear fusion proceeds via the CNO cycle (Bode & Evans, 2008). Finally, when the temperature exceeds $T > 10^8\,\mathrm{K}$, the hot CNO cycle begins to dominate.

The ignition mass, or critical mass, is given by:

$$M_{crit} = 4\pi R_{WD}^4 P_{crit}/GM_{WD} \tag{1.1}$$

where $P_{crit} \sim 10^{19}$ Pa. Figure 1.4 shows that the ignition mass decreases as the WD mass increases.

As the material at the WD's surface is degenerate, pressure and temperature are decoupled, and the accreted material on the surface does not expand as the temperature soars. As a result, there is a thermonuclear runaway (TNR) (Bode et al., 2009; Bode, 2010; Starrfield et al., 2016). During TNR, convection can dredge up some material from the WD interior, such as carbon, oxygen, neon or magnesium. The TNR generates sufficient energy to increase the temperature beyond the Fermi temperature, thereby breaking the degeneracy and recoupling temperature and pressure.

As the pressure rises, the accreted envelope expands, and does so with a velocity higher than the WD's escape velocity. Hydrogen, helium and other products of the recent nuclear burning, possibly mixed with WD core material, are ejected from the WD in the nova eruption. Typical masses and velocities of the ejecta respectively are in the range $10^{-5} \leq M_{ej} \leq$ few $\times\, 10^{-4}\, M_\odot$ and few $\times\, 10^2 \leq v_{ej} \leq$ few $\times\, 10^3\, km\, s^{-1}$ (Bode, 2010).

1.6 The nova ejecta and panchromatic emission

The material thrown off the surface of the WD form the nova ejecta and consists of hot, optically thick gas. This gas forms a shell of increasing radius spreading out from the WD, emitting blackbody-like continuum radiation. As the ejecta

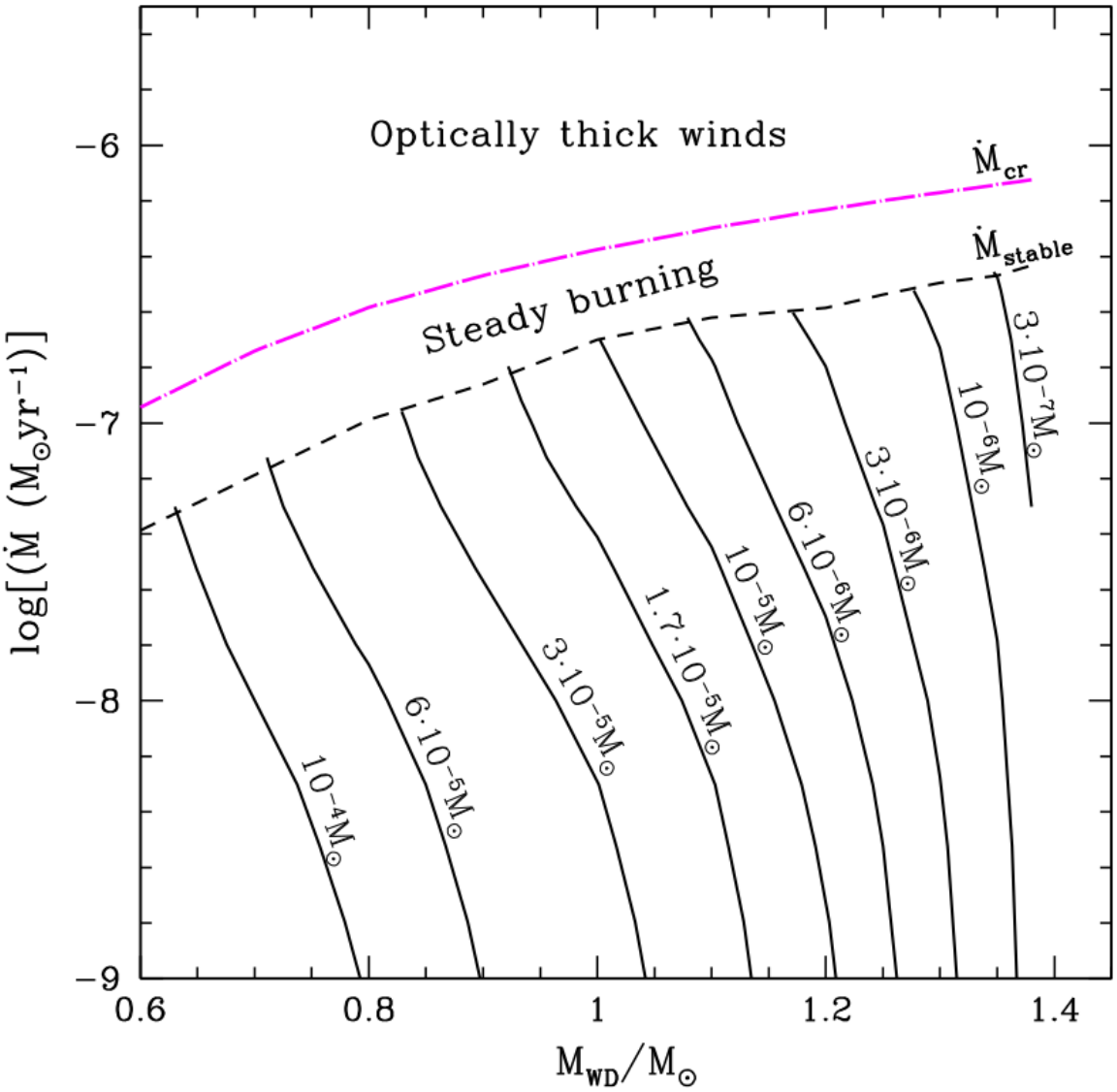

Figure 1.4: Plot showing the ignition mass for novae in the plane of log (accretion rate) vs WD mass. Figure appears as Figure 3 in (Kato et al., 2014) ['Shortest Recurrence Periods of Novae', Kato et al., Astrophys. J., 793, 136, 2014 DOI `https://doi.org/10.1088/0004-637X/793/2/136` ©AAS. Reproduced with permission.]

expand, the nova's optical luminosity increases rapidly with the expansion of the pseudophotosphere (the final optical depth of the optically thick ejecta), which is the source of the continuum emission. During this period of rapid expansion, the WD will reach a state of quasi-hydrostatic equilibrium, regulating the hydrogen burning. This hydrogen shell burning will proceed at a nearly constant rate until the nuclear fuel is exhausted (Hachisu & Kato, 2006).

The ejecta density and temperature fall with the increase of the shell's radius, until the expanding ejecta become optically thin. At this stage, the pseudophotosphere begins to recede towards the WD's surface, causing a decline in the optical light curve (Warner, 2008). There is a corresponding increase in luminosity in bluer wavebands. This occurs because the photosphere becomes ever closer to the surface of the WD, hence the increase in photospheric temperature and the shift in continuum emission from optical towards UV wavelengths (Bode, 2010).

As the hydrogen burning phase proceeds, the mass loss rate decreases and flux is redistributed to higher frequencies. As the UV emission declines, supersoft x-ray emission begins (Hachisu & Kato, 2006).

1.7 The maximum magnitude-rate of decline (MMRD) relationship

During early observations of novae in M31, Hubble noted that the brighter a nova was at its peak, the faster it faded (Hubble, 1929). Observations of novae in the Milky Way then confirmed that the same relationship also applied to Galactic novae (Mclaughlin, 1945). As further observations were carried out (de Vaucouleurs, 1978; Cohen, 1985; della Valle & Livio, 1995; Downes & Duerbeck, 2000), it became

accepted that the rate of decline of a nova was linked to its maximum brightness, which became known as the maximum magnitude vs rate of decline, or MMRD, relationship. It appeared to apply in different environments, suggesting that novae could be useful distance indicators.

However, even as the number of observations and the quality of the calibration increased, the scatter of ~ 0.5 mag in the relationship remained. In addition, the MMRD relationship did not provide a good fit for all novae, particularly the recurrent novae (Schaefer, 2010), which are discussed more in Section 1.8. As such, the MMRD has some issues in its use to determine the distance to Galactic novae, and CNe are not the best choice of distance indicator.

The general premise of the MMRD has been called into question by recent studies. In 2011, Kasliwal et al. (2011) reported the discovery of a previously unseen population of "faint-fast" novae based on a deep, high cadence optical survey of extragalactic novae, primarily focussing on M31. These faint-fast novae are less luminous and decline faster than expected according to the MMRD relationship. Indeed, they occupy the same phase-space as the Galactic recurrent novae, as discussed by Kasliwal et al. (2011).

A survey of novae in M87 also revealed the presence of a population of faint-fast novae (Shara et al., 2016). The presence of a significant population in both M31 and M87 suggests that faint and fast novae are ubiquitous, and present a strong challenge to the MMRD, as stated by (Shara et al., 2017b). Furthermore, following the release of Gaia DR2 (Gaia Collaboration, 2018) parallaxes and distance estimates, Schaefer (2018) compared previous distance estimates to novae from various methods, including applying MMRD relations, and found that the MMRD was a poor method to determine distances to Galactic novae, in agreement with Shara et al. (2017b). In contrast, Selvelli & Gilmozzi (2019) used a virtually identical sample of Galactic

novae (only differing by one or two systems), and found that Gaia DR2 distance estimates were in good agreement with those found using the MMRD.

Theoretical models of the nova phase-space suggest that the standard MMRD relationship is populated by systems with high WD mass and low mass accretion rate for the bright and fast end, and low WD mass and high mass accretion rate for the faint and slow novae (Yaron et al., 2005). Systems with a high WD mass and high mass accretion rate would be expected to behave observationally like the faint-fast novae. Indeed, the photospheric radius of a faint and fast nova at optical maximum will be smaller than that of a standard CN, with a correspondingly high effective temperature. Therefore, UV emission will dominate the energy output at the time of the optical peak (Darnley et al., 2016).

By contrast, if a nova were bright and slow, it would belong in the currently unoccupied phase-space of the MMRD diagram. It would be expected to have a low WD mass and low mass accretion rate. Such a system would accrete a high-mass envelope before ignition occurred, and the large mass of its ejecta would lead to a slow evolution, with the peak of its energy output in the infra-red (Darnley & Henze, 2020). The *Spitzer Space Telescope* survey of extragalactic IR transients (Kasliwal et al., 2017) found 14 systems which were "eSpecially Red Intermediate-luminosity Transient Events", or SPRITES, which inhabit the IR luminosity gap between CNe and SNe. The SPRITES had no optical counterparts (to a deep limit), and some evolved on very slow timescales ($< 0.1\,\mathrm{mag\,yr^{-1}}$). Perhaps some of the SPRITES are bright, slow novae (Darnley & Henze, 2020). Some luminous red variables, sometimes called luminous red novae, could be very slowly evolving novae, as suggested by Shara et al. (2010), and supported by their grid of nova models with low mass, cold WDs and low mass accretion rates.

An updated MMRD relationship, based on novae in M31 and the Large Magellanic

Cloud (LMC), and calibrated for the Milky Way by Della Valle & Izzo (2020), is shown in Figure 1.5. Also shown is their plot showing the relationship between Gaia and MMRD distances. Della Valle & Izzo (2020) found that the novae in M31 and the LMC were best fitted with a reverse-S-shaped relation. They applied the same shape to Galactic novae, but still showed the best-fit linear relation.

1.8 Recurrent Novae

Recurrent novae (RNe) have been observed in eruption more than once. This is a purely observational definition, subject to strong selection effects, including the time since accurate records of observations were kept, and the time since more systematic surveys began using telescopes with large fields of view. The upper limit on the recurrence period for a recurrent nova, i.e. the time between subsequent classical nova eruptions, is just under 100 years (Anupama 2008; Darnley et al. 2012). Observations are more frequent and cover more of the sky as time increases.

All novae are inherently recurrent as a CN eruption leaves both the WD and its companion intact, so eventually accretion will resume. The range of recurrence periods $P_{\rm rec}$ is large, with recurrence times of up to a few $\times 10^6$ years theorised, so only those systems with relatively short recurrence periods meet the criteria to be classified as recurrent novae.

Galactic recurrent novae include the long orbital period systems RS Ophiuchi, T Coronae Borealis, V3890 Sagittarii and V745 Scorpii, and the short period systems U Scorpii, V394 Coronae Austrinae, CI Aquilae, IM Normae, and T Pyxidis (Anupama, 2008), as well as the more recently identified V2487 Ophiuchi (Pagnotta & Schaefer, 2014). Many extragalactic recurrent novae have also been discovered, primarily in

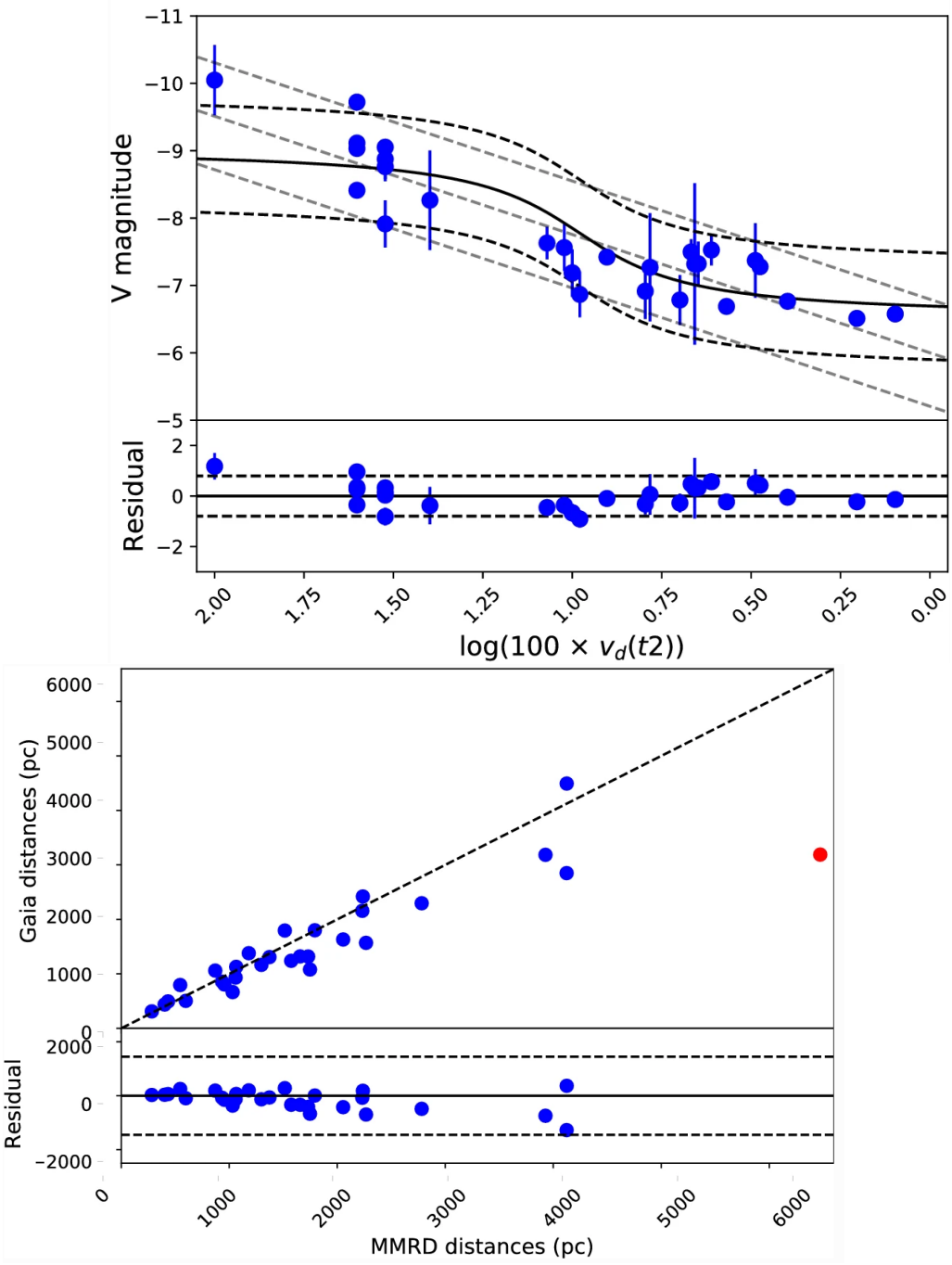

Figure 1.5: Upper panel: the MMRD relationship for the Milky Way. The black, curved lines represent the S-shape reverse relation, with the solid line showing the best fit. The grey dashed-lines show the linear best fit. The dashed lines around the S-shape and linear best fits indicate their respective $\pm 3\sigma$ strip. Lower panel: The relationship between Gaia DR2 and MMRD distances. The smaller the distance, the better the agreement between the two. The red dot represents the outlier, CI Aquilae. Plots appeared as Figures 35 and 36 in Della Valle & Izzo (2020). ['Observations of galactic and extragalactic novae', Astron. Astrophys. Rev., 28, 3 DOI `https://doi.org/10.1007/s00159-020-0124-6` Reproduced with permission from Springer Nature; permission conveyed through Copyright Clearance Center, Inc.]

M31, but also in the Small Magellanic Clouds.

RS Oph is the most-studied long period RN. The suspected missing eruption of RS Oph in 1945, which occurred primarily during the seasonal observing gap, was confirmed by Adamakis et al. (2011) by examination of the long term light curve. The system contains a red giant donor star (hence the long orbital period), and γ-rays were detected during the early stages of its 2021 eruption by Fermi-LAT (Page et al., 2022). For the first time, Very High Energy (VHE) γ-emission (with energy in the range 60 GeV to 250 GeV) was detected from a nova by the Major Atmospheric Gamma Imaging Cherenkov (MAGIC) Telescopes (Acciari et al., 2022) and the High Energy Stereoscopic System (HESS) (H. E. S. S. Collaboration et al., 2022), which both use Cherenkov radiation to detect particle showers released by γ-rays.

The remarkable nova M31N 2008-12a has a very short recurrence period of only a year (Darnley et al., 2016), making it the most rapidly recurring nova known to date. Recurrent novae with a recurrence period of $P_{rec} \leq 10$ years are known as rapid recurrent novae, or RRNe (Darnley & Henze, 2020). Models have even suggested RNe could have a recurrence period as low as 2 months (Kato et al., 2014; Hillman et al., 2016). Examples of RRNe, listed in Darnley & Henze (2020), include the Galactic nova U Scorpii, with its recurrence period of 10 years, a single nova in the Large Magellanic Cloud, LMCN 1968-12a, and eight novae in the Andromeda Galaxy, M 31. The M 31 RRNe are M31N 1963-09c, M31N 1984-07a, M31N 1990-10a, M31N 1997-11k, M31N 2006-11c, M31N 2007-11f (and of course, the prototypical M31N 2008-12a).

The mass of the WD and its mass accretion rate are the key factors which determine P_{rec} for a nova. The higher M_{WD} and $\dot{M}_{acc}$, the shorter the recurrence period. The rapid recurrent novae have WD masses close to the Chandrasekhar limit in addition to high mass accretion rates. The prototypical rapid recurrent nova is

M31N 2008-12a, which has erupted every year since its discovery in 2008. With its near-Chandrasekhar mass of $M_{WD} \sim 1.38 M_{\odot}$ (Kato et al., 2015) and an accretion rate of $\dot{M} \sim 10^{-6}\,M_{\odot}\,yr^{-1}$ (Darnley et al., 2017), M31N 2008-12a is growing its WD mass. It is the most promising pre-explosion SNIa candidate: with its predicted mass accumulation efficiency of $\eta \sim 0.63$ (Kato et al., 2015), it would grow to the Chandrasekhar mass within $20,000$ years (Darnley et al., 2017). At this point, its fate would depend on the WD composition. If it's a CO WD, it would undergo a SNIa eruption; an ONe WD would undergo accretion induced collapse.

1.8.1 Type Ia Supernovae

Recurrent novae are one of the best candidate progenitors for Type Ia Supernovae (SNeIa; Pagnotta & Schaefer 2014) due to their high $\dot{M}$ and M_{WD}. There are thought to be two routes towards SNeIas (Hillebrandt & Niemeyer, 2000), via the single degenerate channel (Whelan & Iben, 1973) or the double degenerate channel (i.e. the binary systems comprising either one or two bodies consisting of degenerate material, such as a WD). The double degenerate channel requires the merger of two degenerate objects (Webbink, 1984), whereas the single degenerate channel involves the mass growth of the degenerate object until it reaches the Chandrasekhar mass. Since rapid RNe involve a WD growing in mass (Hillman et al., 2016), they are a prime candidate for SNeIa progenitors.

A promising candidate for the the double degenerate progenitor route to SNIa production are the AM Canum Venaticorum (AM CVn) systems, which are ultra-compact binaries consisting of a WD accreting hydrogen-deficient material from a companion, which is itself at least somewhat degenerate. Photometric analysis of ES Ceti, the AM CVn with the shortest-known orbital period, revealed a low mass donor star that is nearly fully degenerate, suggesting this will evolve to a double degenerate

system (Copperwheat et al., 2011). Therefore gravitational radiation could reduce the angular momentum of ES Cet until the components merge, potentially initiating a SNIa eruption in the future.

Population studies of RNe could yield invaluable insights into the contribution of RNe to the population of SNeIa. This is important as SNeIa are widely used distance indicators throughout astrophysics, being of particular use in Cosmology due to their high luminosity enabling their detection at high redshift. However, recent studies indicate a diversity in the shape of SNeIa light curves, suggesting they may not be the easily standardisable, homogeneous sample once assumed. This suggests that at least two different populations of SNeIa may arise from different progenitors, with different metallicity and redshift (Dominguez et al., 2001; Brandt et al., 2010). Therefore it is important to calculate the rate of SNe attributed to each channel. Similarly, it is important to determine the maximum rate of SNeIa produced by RNe. In this way, the potential contribution of RNe to the single degenerate and the overall SNeIa rate could be evaluated. However, we should bear in mind that in order for recurrent novae with high $\dot{M}$ and M_{WD} to evolve into SNeIa, they would need to have a net mass gain over the course of their ongoing eruptions. Furthermore, the composition of the WD is important, as ONe WDs undergo accretion induced collapse rather than a thermonuclear explosion (Pagnotta & Schaefer, 2014).

1.9 X-ray and UV emission from novae

1.9.1 X-ray flash

In the very early stages of the nova eruption, the energy released during the onset of the thermonuclear runaway reaches the surface of the WD, and the effective

temperature rises rapidly to in excess of 10^6 K. The WD emits thermal radiation, emitting a strong X-ray signal with a soft spectrum. This emission had long been theorised (Bode & Evans, 2008, see chapter by Krautter), but was detected for the first time in 2020 (König et al., 2022). When the nova shell is ejected and expands, cooling adiabatically in the process, the shell rapidly becomes optically thick to X-rays. This means that the X-ray flux outside the pseudo-photosphere decreases very quickly, and X-rays would only be detectable for a few hours - hence the use of the term "X-ray flash".

The eRosita all-sky survey detected a short, soft X-ray flash from the nova YZ Reticuli in July 2020 (König et al., 2022). The survey took observations of the field around YZ Ret every four hours, and no X-ray signal was detected in the observations preceding or following the X-ray flash detection, putting an upper limit of 8 hours on the duration of the flash. ASAS-SN detected the optical rise of the nova 11 hours after the X-ray flash (Sokolovsky et al., 2022).

1.9.2 Super-soft source phase

Days to months after the eruption onset, on a time-scale dependent on the ejecta mass and velocity (which are themselves driven by the WD mass and $\dot{M}$), the ejecta will expand until the plasma density is reduced sufficiently to allow the pseudo-photosphere to recede back to the surface of the WD. Once this happens, the ejecta become optically thin to X-rays again. If the nuclear burning on the WD surface has not yet exhausted the accreted hydrogen fuel, then the ongoing hydrogen burning will emit soft X-rays that can be detected externally to the system (Bode & Evans, 2008, see chapter by Krautter). The nuclear burning will continue with approximately constant luminosity, $L \sim L_{\mathrm{Edd}}$, where L_{Edd} is the Eddington luminosity. As the burning proceeds, the photosphere, which expands to the size of a red giant during

the fireball phase (Starrfield, 1989), will shrink, so the surface temperature of the WD photosphere will increase. When the fuel is exhausted, the WD will cool at constant radius. X-rays from a nova outburst were first detected from GQ Muscae (around 460 days after the eruption began) by the Channel Multiplier Array detector on board the European X-ray Observatory Satellite, EXOSAT, in 1984 (Ögelman et al., 1984).

The super-soft source (SSS) phase is the name given to the period when these soft X-rays are detected. The start of the soft X-ray detection is referred to as the turn-on time, $t_{\rm SSS,on}$, and the end of the detection as the turn-off time, $t_{\rm SSS,off}$. The turn-on time is purely observational as the nuclear burning is thought to continue from the start of the TNR, but only becomes visible when the ejecta become optically thin. In contrast, the turn-off time corresponds to the end of the nuclear burning. However, the WD will continue to emit soft thermal X-rays during the initial cooling stages, so observationally $t_{\rm SSS,off}$ only measures the time when the soft X-ray luminosity drops below the detection limit of the X-ray observatory. Therefore, an extragalactic nova will be observed to have a later $t_{\rm SSS,on}$ and an earlier $t_{\rm SSS,off}$ than would the same nova located in the Galaxy.

The duration of the SSS phase depends on the WD mass, with higher mass WDs having shorter SSS phases and reaching higher black-body temperatures. This was shown by Henze et al. (2011, 2014) in their studies of M31 novae. Given the distance to M31, the difference between distances to individual systems within the galaxy is negligible, so all nova systems can be considered to be at the same distance. This assumption eliminates the impact of the sometimes significant distance uncertainties for Galactic novae. Figure 1.6 shows that the turn-off time increases with the turn-on time, but decreases with blackbody temperature. The turn-on time increases with the R-band t_2 decline time, and decreases with faster ejecta velocities. Higher mass WDs need to accrete less hydrogen to trigger the TNR, as indicated by the ignition

mass contours in Figure 1.4. The ejected mass is lower than for a less massive WD, and the ejecta velocity is faster, so the ejecta become optically thin to X-rays at an earlier stage. There is less fuel available for nuclear burning, and it burns faster.

It is also possible for the SSS phase to be extended if accretion resumes while nuclear burning is ongoing as this would replenish the hydrogen available. This was suggested as a possible explanation for the long super-soft source phase of V723 Cas (Ness et al., 2008), as well as the longer than expected SSS phase of V407 Lup (Aydi et al., 2018b). In contrast, the peculiar 2016 eruption of the RRN M31N 2008-12a had a shorter than usual SSS phase, thought to be due to the slower reformation of its accretion disk, that could not effectively refuel the nuclear burning (Henze et al., 2018). This was suggested to be caused by a lower than usual quiescent accretion rate, which contributed to the formation of a less massive accretion disk, which was more easily disrupted by the nova eruption. Consequently, there was not sufficient accretion onto the WD to prolong the SSS phase as much as typically observed.

1.9.3 Hard X-ray emission

During the nova eruption, hard X-rays can be produced by shocks within the gas, generating a thermal bremsstrahlung spectrum. These shocks can occur internally within the nova ejecta, or between the nova ejecta and a pre-existing circumstellar material, either from a red-giant wind in a symbiotic system, or perhaps from a previous nova eruption. An alternative source of hard X-rays is accretion, taking place via a disk or magnetic accretion directly onto the WD (Bode & Evans, 2008, see chapter by Krautter).

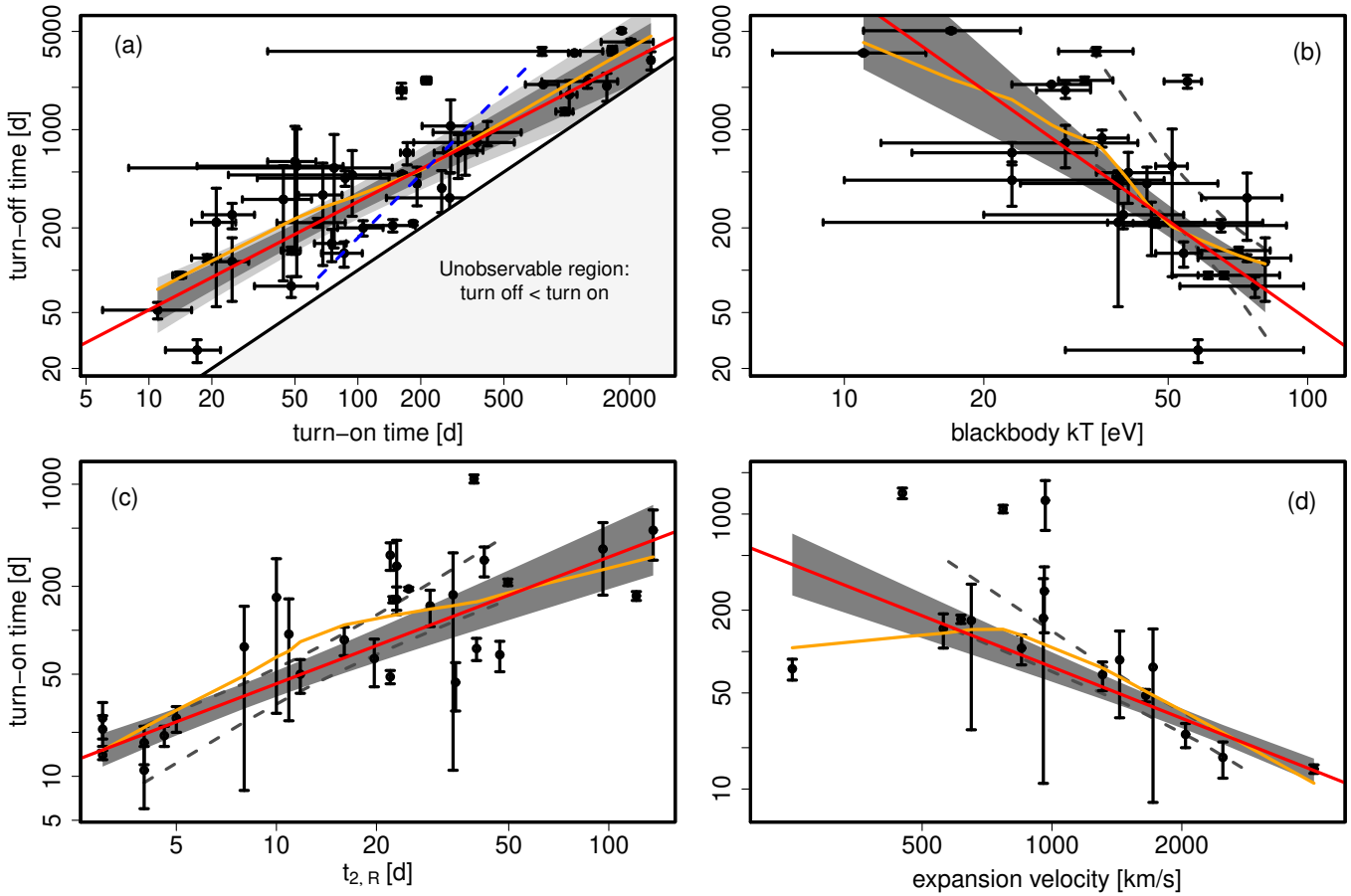

Figure 1.6: Super-soft source turn-on time and turn-off time relations for novae in M31. Each panel shows a smooth fit to the data points in orange and a power-law fit in red. The 95% confidence regions around the power-law fit are shaded in dark grey. Different correlations are shown in the panels: (a) turn-on time against turn-off time, (b) blackbody temperature against turn-off time, (c) R-band t_2 time vs turn-on time, and (d) expansion velocity vs turn-on time. Figure taken from Henze et al. (2014) ['X-ray monitoring of classical novae in the central region of M 31 III. Autumn and winter 2009/10, 2010/11, and 2011/12', DOI `https://doi.org/10.1051/0004-6361/201322426` Credit: Henze M., et al., A&A, 563, A2, 2014, reproduced with permission ©ESO.]

V2487 Ophiuchi was the first nova where hard X-ray emission covering the energy range 0.3 to 8.0 keV was detected in 2001, 2.7 years after the eruption, signalling the resumption of accretion (Bode & Evans, 2008, see chapter by Krautter). The X-ray detection was positionally coincident with a detection 8 years before the eruption of V2487 Oph. The spectrum was similar to that of a typical CV. Since then, evidence of accretion resuming in the period shortly after the nova eruption has been detected in multiple systems (Osborne, 2015), such as in U Sco within 35 days of the eruption (Ness et al., 2012), in HV Ceti 65 days after outburst (Beardmore et al., 2012), and in the γ-ray detected V959 Mon within 150 days of eruption. As discussed by (Ness et al., 2013), the nova outburst might heat the secondary sufficiently to elevate the Roche-lobe overflow, allowing the accretion disk to reform sooner.

In a nova system, the primary source of luminosity other than nuclear burning is accretion, with a significant proportion of the energy emitted in X-rays (Mukai, 2017) and UV. In a polar CV, X-rays are produced in shocks within the accretion column onto the WD, as discussed in (Beardmore et al., 2012).

1.9.4 UV emission

As discussed in Section 1.6, while nuclear burning proceeds on the WD surface, the bolometric luminosity of the nova is expected to be constant. When the optical luminosity decreases during the very early stages of the eruption, the UV luminosity experiences a corresponding increase (Warner, 2008, and references therein). The UV luminosity was found to persist for months in early satellite UV observations of FH Serpentis (Gallagher & Code, 1974, as discussed by Chomiuk et al. (2021a)). This effect is the result of a shift in the peak of the spectral energy distribution of the nova emission towards bluer wavelengths as the ejecta expand. The optical depth of the ejecta falls as the density decreases, and the pseudo-photosphere shrinks towards

the size of the WD, experiencing higher effective temperatures in the process.

However, *Swift* observations of novae with the X-ray Telescope (XRT) paint a conflicting picture of the theorized constant bolometric phase (Page et al., 2020). Observations of V2491 Cygni found an absence of evidence for this constant bolometric luminosity phase (Page et al., 2010). In the case of V745 Scorpii, assuming a constant bolometric luminosity would require the photosphere to shrink by a factor of 30 in 2 days (Page et al., 2015). In contrast, Nova SMC 2016 and V407 Lup appear to exhibit nearly constant bolometric luminosity for over 100 days (Aydi et al., 2018a,b), and RS Oph for around 15 days (Page et al., 2020, and references therein).

Both V2491 Cyg and V745 Sco appear to show no correlation between the X-ray and UV luminosity, and the UV emission of V5668 Sgr exhibited a dust dip while the X-ray emission was unaffected during this epoch. This suggests the X-rays and the UV emission arises in different locations in these nova systems (Page et al., 2020). UV, optical and X-ray emission from HV Cet are in phase and vary with a timescale of 1.77 days. This modulation is proposed to arise due to occultation of the bright inner part of the accretion disk by its disk rim in time with the orbital period, whereby X-rays emitted by the WD are scattered and reprocessed into UV and optical emission (Beardmore et al., 2012).

Shock-heated gas behind shock fronts within the ejecta of novae cools rapidly by the emission of UV photons (Chomiuk et al., 2021a). Most of the luminosity of the WD is emitted in the ultraviolet energy range (Chomiuk et al., 2021a), and UV emission is observed from the accretion disk (Godon et al., 2017).

Table 1.1: The key isotopes involved in the production of gamma-rays due to radioactive decay. This table appears as Table 1 in Hernanz (2014).

Isotope	Lifetime	Type of emission	Main disintegration process	Nova type
^{13}N	862 s	511 keV line & continuum	β^+- decay	CO & ONe
^{18}F	158 min	511 keV line & continuum	β^+- decay	CO & ONe
^{7}Be	77 days	478 keV line	e^- capture	CO
^{22}Na	3.75 years	1275 keV & 511 keV lines	β^+- decay	ONe
^{26}Al	10^6 years	1809 keV & 511 keV lines	β^+- decay	ONe

1.10 Gamma-ray emission from novae

1.10.1 Radioactive emission

Nearly fifty years ago, it was realized that classical novae could be sources of γ-rays (Clayton & Hoyle, 1974; Clayton, 1981). Radioactive nuclei produced in nova eruptions emit γ-rays when they decay (Bode & Evans, 2008, see chapter by Hernanz). Table 1.1 shows the principal isotopes expected to decay and produce γ-rays. The γ-ray emission, predicted to be in the MeV energy range, would act as a direct tracer for the nucleosynthesis occurring on the surface of the WD during the TNR (Hernanz, 2014).

The isotopes ^{13}N and ^{18}F are synthesised during the TNR via the CNO cycle and hot-CNO cycle respectively. Both isotopes have short lifetimes, and are produced by both CO and ONe WDs, whereas the other isotopes in Table 1.1 are produced primarily on one or the other. Positrons produced in the β^+-decay of ^{13}N and ^{18}F annihilate with electrons in the WD envelope or expanding ejecta, producing γ-rays: an emission line at 511 keV, and a continuum arising from the Compton down-scattering of the annihilation photons.

When ^{7}Be captures an electron, it transforms to an excited state of ^{7}Li, which

emits a γ-ray photon of 478 keV when it subsequently de-excites. Production of ^{7}Li was thought to occur primarily during nova eruptions on CO WDs, whereas ^{22}Na and ^{26}Al are primarily synthesised on ONe WDs. However, recent observations of V6595 Sagittarii suggest that ^{7}Li can be produced in ONe WDs at similar levels to CO WDs (Molaro et al., 2022).

The synthesis of ^{22}Na from ^{20}Ne proceeds via two proton captures and β^{+}-decay. Then ^{22}Na undergoes a further β^{+}-decay to reach an excited state of ^{22}Ne, which moves to a lower energy state of ^{22}Ne by emitting a γ-ray photon of energy 1.274 MeV. The positron emission contributes to the 511 keV annihilation line.

When the isotope ^{25}Mg captures a proton, it forms spin isomers of ^{26}Al, denoted by $^{26}\mathrm{Al}^{g}$ for the ground state and $^{26}\mathrm{Al}^{m}$ for the isomeric state. The ground state $^{26}\mathrm{Al}^{g}$ undergoes either β^{+}-decay or electron capture to transform to an excited state of ^{26}Mg, which subsequently de-excites by emitting a 1.809 MeV γ-ray photon. The isomeric state $^{26}\mathrm{Al}^{m}$ undergoes β^{-}-decay directly to the ground state of ^{26}Mg, without the emission of a 1.809 MeV γ-ray photon.

Annihilation radiation would only be emitted at high levels for a day, around a week before the peak optical peak, and would be dominated by positron emission from the short-lived isotopes ^{13}N and ^{18}F. Positron emission from ^{22}Na can contribute to the annihilation emission line at a lower level, but only for around the first week of the eruption, as after this time the expanding envelope no longer has sufficient optical depth to stop the ^{22}Na from escaping (Hernanz, 2014).

Line emission at 478 keV and 1.274 MeV, from ^{7}Be and ^{22}Na respectively, is long-lasting due to the corresponding isotope lifetimes of 77 days and 3.75 years. The 478 keV emission reaches its maximum around 5 to 13 days after eruption, whereas the 1.274 MeV emission takes around 10 to 20 days to rise to its peak, then slowly

declines. In contrast, the lifetime of ^{26}Al is so long (10^6 years - longer than the typical recurrence period of a classical nova) that emission at energy 1.809 MeV, will not be detected from an individual event. However, diffuse emission from ^{7}Be, ^{22}Na and ^{26}Al, built up from isotopes ejected from CN eruptions on multiple systems, could in principle be detected (Bode & Evans, 2008, see chapter by Hernanz).

Over the years, theoretical developments in nucleosynthetic yields, nuclear rates of reaction and radiation transport have changed the maximum flux and light curve shape expected at each energy, and hence the distance at which the γ-rays are expected to be observable (see e.g., discussion in Siegert et al. (2018)). To date, prompt γ-ray emission from nucleosysnthesis has still not been detected, either from observations of individual classical novae , or in diffuse form from many CN eruptions (Siegert et al., 2021, see their analysis of INTEGRAL data). Indeed, a recent analysis of an array of models of nova eruptions on CO or ONe WDs found that the expected flux in the 511 keV emission line from nova eruptions had been vastly overestimated in earlier models, as the envelope remains opaque to soft γ-rays for longer than previously theorised (Leung & Siegert, 2022).

1.10.2 Shock emission

The predicted soft γ-ray emission from radioactive nuclei has not been detected, but an unexpected source of more energetic γ-rays from CNe was discovered in 2010. Abdo et al. (2010) first reported detection of γ-ray emission from a nova; the ejecta of the symbiotic nova V407 Cygni shocked its surrounding circumstellar wind, accelerating charged particles to relativistic velocities and emitting γ-ray photons of energy > 100 MeV (see Section 1.10.3 for further information on the hadronic and leptonic emission processes). Since that initial discovery, γ-ray signatures have been exhibited in increasing numbers of classical novae (see Aydi et al., 2020b; Chomiuk

et al., 2021a, for recent reviews). Several γ-ray detected novae occurred in systems with red giant donors: V407 Cyg, V1535 Sco (Franckowiak et al., 2018), and the recurrent novae V745 Sco (Cheung et al., 2014; Banerjee et al., 2014), V3890 Sgr (Buson, Jean & Cheung, 2019) and RS Oph (Cheung, Ciprini & Johnson, 2021). In these systems, the shocks generating the γ-rays are likely to originate in collisions between the nova ejecta and the dense red-giant winds and circumbinary material.

In contrast, the other γ-ray emitting novae have main sequence companions and are unlikely to be surrounded by dense winds. Such systems include V959 Mon, V1324 Sco, V339 Del (Ackermann et al., 2014), V407 Lup, V5856 Sgr (Li et al., 2017), V1369 Cen, V5668 Sgr (Cheung et al. (2016); Franckowiak et al. (2018)), V906 Car (Stanek et al., 2018), V357 Mus (Li et al., 2018a), V5855 Sgr (Nelson et al., 2019), YZ Ret (Li et al., 2020b) - the system where the first X-ray flash was detected (König et al., 2022), V549 Vel (Li et al., 2020a), and V1674 Herculis (Li, 2021).

As mentioned in Section 1.8, in recent observations of RS Oph, Very High Energy (VHE) γ-emission (with energy in the range 60 GeV to 250 GeV) was detected from a nova for the first time by the Major Atmospheric Gamma Imaging Cherenkov (MAGIC) Telescopes (Acciari et al., 2022) and the High Energy Stereoscopic System (HESS) (H. E. S. S. Collaboration et al., 2022), which both use Cherenkov radiation to detect particle showers released by γ-rays.

In γ-ray emitting systems, the shocks are proposed to be due to interaction between multiple ejection components (Aydi et al., 2020b). The initial ejection contains the bulk of the ejected mass, with subsequent ejection events containing shells of lower and lower mass, hence travelling with higher and higher velocities. When the faster shells catch up and collide with the earlier shells, forward and reverse internal shocks are produced, which in turn interact with the other shells. These shocks will accelerate charged particles, electrons or protons, to relativistic velocities,

hence the emission of gamma-rays.

In Figure 1.7, which appears as Figure 13 in Chomiuk et al. (2021a), we see a schematic diagram of intra-ejecta, or internal, shocks. We view the binary system side-on, with the orbital plane projecting vertically into and out of the page. The WD and donor star are shown as white and red circles respectively. The shell from the initial ejection event is shown in blue, travelling at the slow velocity v_s equatorially (at a small solid angle around the orbital plane). The shell from the next ejection event, shown in red, is travelling spherically at the fast velocity v_f. When the fast ejection component collides with the slow ejection component, forward and reverse shocks propagate through the ejected shells, heating the gas behind the shock fronts to 10^6 to 10^7 K. Ions and electrons in the gas can reach relativistic velocities by undergoing diffusive shock acceleration (DSA). This is the process whereby charged particles are highly accelerated by means of repeated reflection by magnetic field inhomogeneities at shock fronts in the plasma, gaining energy with each reflection.

The shock-heated gas behind the shock fronts rapidly cools by emitting UV and X-rays in a cooling layer, and forms a cool, thin central shell where thin-shell instabilities lead to corrugation on a length scale similar to the thickness of the shell. Since the central shell is cooler than the ionization temperature of hydrogen, it is neutral. The central shell and the partially neutral, slow ejected shell are both able to absorb the UV and X-ray emission, which is reprocessed into UV, optical and infra-red emission. The orange circles in Figure 1.7 represent the relativistic ions and electrons, which move by advection into the central shell, and emit gamma rays as they cool. As the delay between the optical and gamma-ray emission is minimal, the respective light curves are correlated.

Figure 1.7: Schematic diagram of intra-ejecta, or internal, shocks between nova shells leading to emission of γ-rays. The initial, slower (equatorial) ejection of matter, shown in blue, is caught up to and shocked by the later, faster (spherical) ejection of matter, shown in red. As a result of the collision, forward and reverse shocks propagate through the shells, heating the gas behind the shocks. The ions and electrons, accelerated by diffusive shock acceleration to relativistic velocities and shown as orange circles, move by advection into the cool central shell, emitting γ-rays as they cool. By emitting UV and X-rays, the gas rapidly cools, and the cooler, neutral gas in the cool central shell and the partially neutral shell absorbs the UV and X-ray emission, re-processing it into UV, optical and infra-red emission. Figure appears in Chomiuk et al. (2021a, Figure 13) ['New Insights into Classical Novae', Chomiuk et al., Ann. Rev. A&A, 59, 2021 DOI `https://doi.org/10.1146/annurev-astro-112420-114502` Used with permission of Annual Reviews, Inc., permission conveyed through Copyright Clearance Center, Inc.]

Early studies suggested that the γ-ray and optical emission could show correlated peaks, with the shocks driving the optical emission (Ackermann et al., 2014; Metzger et al., 2015). As more γ-ray novae were studied, the evidence to support the link between the γ-ray and optical emission grew. Aydi et al. (2020a) demonstrated that shock-powered emission was responsible for the bulk of the luminosity of V906 Car, with multiple simultaneous γ-ray and optical flares.

1.10.3 Hadronic and leptonic emission models

In the hadronic scenario for γ-ray emission, relativistic ions collide with ambient ions such as protons, and produce pions, either neutral as in Equation 1.2, or charged as in Equation 1.3. The pions then decay into γ-rays (Chomiuk et al., 2021a). Approximately 1/3 of the proton-proton interactions result in the production of a neutral pion, with the remainder producing a charged pion. The charged pions then decay to leptons, which can in turn emit γ-rays via the leptonic scenario.

$$p + p \rightarrow \pi^0 \rightarrow \gamma + \gamma \tag{1.2}$$

$$p + p \rightarrow \pi^{\pm} \rightarrow \mu^{\pm} + \nu_{\mu} \rightarrow e^{\pm} + \nu_e + \nu_{\mu} \tag{1.3}$$

In the leptonic scenario, γ-ray emission occurs due to the interaction of relativistic electrons with ambient protons (see Equation 1.4) or electrons (see Equation 1.5), causing bremsstrahlung emission (Ackermann et al., 2014; Chomiuk et al., 2021a).

$$e^{\pm} + p \rightarrow e^{\pm} + p + \gamma \tag{1.4}$$

$$e^{\pm} + e^{-} \rightarrow e^{\pm} + e^{-} + \gamma \tag{1.5}$$

Leptonic γ-rays are also produced when optical photons undergo inverse Compton scattering, as in Equation 1.6:

$$e^{\pm} + \gamma_{opt} \rightarrow e^{\pm} + \gamma \tag{1.6}$$

Ackermann et al. (2014) modelled the γ-ray spectrum measured by Fermi-LAT for the four novae V407 Cyg, V1324 Sco, V959 Mon and V339 Del with both hadronic and leptonic models.

For the hadronic model, Ackermann et al. (2014) assumed an exponentially cut-off power law distribution of protons in the form

$$N_P(p_p) = N_{p,0}(p_p c)^{-S_p} e^{-W_p/E_{cp}} \quad \text{protons}\,\text{GeV}^{-1} \tag{1.7}$$

where p_p and W_p are the momentum and kinetic energy of protons respectively, $N_{p,0}$ the normalization, S_p the slope and E_{cp} the cutoff energy. They fitted E_{cp} and s_p with the LAT spectra to obtain the best-fit π^0 models.

The leptonic model used by Ackermann et al. (2014) had a similar form to the hadronic model:

$$N_e(W_e) = N_{e,0} W_e^{-S_e} e^{-W_e/E_{ce}} \quad \text{electrons}\,\text{GeV}^{-1} \tag{1.8}$$

where the normalization $N_{e,0}$, slope S_e, and cutoff energy E_{ce} were fitted to the LAT

data for each nova, and W_e was the kinetic energy of electrons.

For the classical novae, the hadronic and leptonic models could not be distinguished between (Ackermann et al., 2014).

Later studies found that the X-ray to γ-ray luminosity ratio, L_X/L_γ is a good diagnostic of whether leptonic or hadronic processes dominate in the accelerated particles (Vurm & Metzger, 2018). Lower limits of $L_X/L_\gamma \gtrsim 10^{-3}$ and $L_X/L_\gamma \gtrsim 10^{-4}$ apply respectively in the leptonic and hadronic scenarios. In the leptonic scenario, there are far fewer electron-positron pairs with energies significantly below the pion rest mass $\sim 100\,\mathrm{MeV}$, therefore the X-ray luminosity is lower.

Hadronic processes are now favoured for the production of γ-rays in novae. The hadronic model predicts a turnover at the low-energy end of the spectrum because the neutral pion rest mass energy provides a lower bound on the energy of proton-proton interactions (Chomiuk et al., 2021a). We would expect both processes to take place simultaneously, as in a plasma the electrons and ions would both be accelerated.

1.11 Photoionization

Since hydrogen is the most abundant element in both the WD envelope and the donor star, in the absence of shocks, the main mechanism by which energy is input into the post-ejection gas in the nova ejecta is by the photoionization of hydrogen (Osterbrock & Ferland, 2006, Chapter 1). Photoionization occurs when ultraviolet - or more energetic - photons are emitted from a hot star, with surface temperature $T_{\mathrm{eff}} \gtrsim 10^4\,\mathrm{K}$. Hydrogen atoms are ionized by absorbing photons carrying more energy than the ground-state ionization potential of hydrogen, 13.6 eV, with the release of a further photoelectron with kinetic energy equal to the surplus of

energy over the ionization potential. This energy is redistributed throughout the gas due to collisions between electrons, or between ions and electrons, leading to a Maxwellian distribution of particle energies, corresponding to a temperature in the range $5000\,\mathrm{K} < T < 20000\,\mathrm{K}$ in many nebulae.

Collisional rates have a large influence on the ionization conditions at electron densities higher than $n_e \sim 10^8\,\mathrm{cm}^{-3}$, which are commonly found in nova shells at early times. At lower densities, the low energy levels of the thermal ions are collisionally excited by thermal electrons, and almost all excitations lead to the emission of a photon. This is because in the low density environment of many nebulae, the probability of collisional de-excitation is even lower than that of the transition to a lower energy level with the emision of a photon. This is the reason for the presence of many forbidden line transitions in the spectra of nebulae, including nova shells at later times.

Electron capture takes place in the gas alongside the photoionization, so the equilibrium between these two processes at any point in the nebula determines the ionization state of the gas. In the presence of a particularly hot ionizing source, many high energy photons will be emitted, so high ionization lines such as [Ne V] or [Fe VII] will be present. This does not automatically imply a high temperature of the nebula, corresponding to free electrons with high kinetic energy (Osterbrock & Ferland, 2006, Chapter 1). When electrons are captured via recombination, the free electrons are initially bound at excited energy levels. The atoms then emit photons as the electrons decay to lower and lower energy levels, until they reach the ground state (Osterbrock & Ferland, 2006, Chapter 1). Recombination is responsible for Balmer and Paschen line emission, which is observed from all nebulae. In the same way, recombination leads to He I and He II emission from neutral and singly ionized helium.

The ionizing source will photoexcite atoms in the nova shell, leading to the appearance of different emission and absorption lines in spectra. The species present will depend on the elemental abundance of the gas in the ejecta. According to the gas temperature and density, there will be a certain equilibrium between photoexcitation, photoionization and recombination. However, the balance of this equilibrium will evolve with time, causing different spectral lines to appear, strengthen, weaken and disappear as the eruption proceeds.

After a nova eruption, the photoionization of the nova ejecta can be modelled using a central ionizing source and a gas shell of a given initial density and radius. The ionizing source will change depending on whether nuclear burning is still ongoing on the surface of the WD, as this will affect the black-body effective temperature of the WD. The shell parameters will evolve as the nova ejecta expands. As the radius of the shell increases, the density of the shell will decrease accordingly (although the ejection of multiple shells could initially offset the decreasing density, somewhat). As the size of the shell increases, we would expect its temperature to decrease due to adiabatic cooling.

Shocks in the ejecta heat and ionize the gas, as well as compressing it, thereby increasing its density (Osterbrock & Ferland, 2006, Chapter 12) - perhaps to densities higher than those typically found within nebulae. As discussed in Section 1.10.2, the shocked gas is radiative, so cools rapidly by emitting UV and X-rays. The UV and X-ray photons can then photoionize the gas in the vicinity of the shock.

The filling factor is a parameter that accounts for the presence of clumps in the gas. The shell is considered to consist of clumps of high density gas (electron density n_e) surrounded by either vacuum or much lower density gas. The filling factor $f < 1$ denotes the fraction of the total volume of the shell that is filled by clumps (Osterbrock & Ferland, 2006, Chapter 5). The covering factor is the fraction

of the surface area of a sphere centred on the ionizing source that contains gas, i.e., it is $\Omega/4\pi$, where $0 \leq \Omega/4\pi \leq 1$ (Osterbrock & Ferland, 2006, Chapter 5).

Plots comparing observed and theoretical line ratios of various species have regularly been used as diagnostic tools to identify or constrain nebular temperatures and densities in nova shells (see e.g., Ferland & Shields (1978), Morisset & Pequignot (1996), Shore (2013), Takeda et al. (2018), Harvey et al. (2018), Mason et al. (2018), and Mondal et al. (2019), among others). In addition to nova shells, this tool has been applied to diverse astrophysical systems, such as H II regions in interstellar gas (Morisset et al., 2016), planetary nebulae (Boumis et al., 2006), supernova remnants (Osterbrock et al., 1992), and active galactic nuclei (Vogt et al., 2014). Different elements respond to given gas temperature and density conditions in different ways. Their ionization state occupation, and the relative likelihood of transitions between those states (by means of ionization, excitation and radiative emission), will depend on temperature and density. The equilibrium between these processes - and hence the intensity of emission lines - will respond to changes in temperature and density, and this will happen at a different rate for different elements. Hence the utility of line ratio plots as a diagnostic tool.

1.12 Systems known to exhibit both DN and CN outbursts

A number of CVs have been observed to undergo both CN eruptions and DN outbursts. GK Per (Bianchini et al., 1986; Zemko et al., 2017), V446 Her (Honeycutt, Robertson & Kafka, 2011), RR Pic, V1047 Cen, and V606 Aql (Kato & Kojiguchi, 2021) are CNe that subsequently underwent DN outbursts. Z Cam, AT Cnc, and 2MASS J17012815-4306123 (Nova Sco 1437) are known DNe surrounded by proposed

ancient CN shells (Shara et al., 2007, 2012, 2017a). V1213 Cen and V1017 Sgr exhibited DN outbursts six and eighteen years, respectively, before a CN; V1017 Sgr also showed post-nova DN outbursts (Mróz et al., 2016). The nebula Te 11, with a DN at its centre, was proposed to be the shell of an ancient nova eruption, rather than a planetary nebula (Miszalski et al., 2016).

1.13 V392 Persei

V392 Persei was a known CV with a few observed DN outbursts, with quiescent magnitudes of $15.0 < m_{\rm pg} < 17.0$ (Downes & Shara, 1993) and $V > 17$ (Zwitter & Munari, 1994). Its CN eruption was discovered on 2018 Apr 29 (UT) by Y. Nakamura, with an unfiltered brightness of 6.2 mag (Wagner et al., 2018). The following day, γ-ray emission was detected from V392 Per ($> 6\sigma$; Li, Chomiuk & Strader, 2018b), with detections continuing for 11 days (Gordon et al., 2021; Albert et al., 2022). Non-thermal synchrotron emission during early radio observations (Chomiuk et al., 2021b) provided further support for the presence of shocks during the eruption. The system is proposed to host an evolved donor similar to the sub-giant donors of U Sco and GK Per, or the low-luminosity giant donor of M31N 2008-12a (Darnley & Starrfield, 2018). Potential orbital periods of 3.4118 days (Munari, Moretti & Maitan, 2020a) and 3.21997 days (Schaefer, 2021) are consistent with an evolved donor.

On 29th April 2018, a CN eruption of magnitude 6.2 was discovered at the location of the DN V392 Per (Wagner et al., 2018). A post-discovery image of V392 Per is shown in Figure 1.8. V392 Per joins the growing number of novae that have experienced both CN and DN eruptions, supporting the nova-cycle (see, e.g., Warner, 1995; Mróz et al., 2016). The following day, Fermi-LAT detected γ-rays coincident with the position of V392 Per, finding a photon flux of $\mathrm{F}(0.1-300\,\mathrm{GeV}) =$

$8.9 \pm 2.9 \times 10^{-7}\,\mathrm{ph\,cm^{-2}\,s^{-1}}$ with a photon index of 1.9 ± 0.2 (Li et al., 2018b).

Spectra taken within 1 day of discovery (see Figures 1.9 and 1.10) show P Cygni type line profiles, broadened Hα lines with FWHM $\sim 5200\,\mathrm{km\,s^{-1}}$ and overlapping Fe II lines, resembling pre-maximum-light spectra of CNe (Wagner et al., 2018). The nova was already declining 1.3 days after discovery (Konyves-Toth et al., 2018).

A low resolution Liverpool Telescope FRODOSpec spectrum taken on May 2nd 2018 showed broad Balmer emission, Paschen lines 10–14, He I, O I, Fe II (multiplet 42) and Si II (multiplet 2). Balmer lines and O I lines showed significant structure, with a minimum of 3 individual peaks. Hα and Hβ had FWHMs of $4700 \pm 100\,\mathrm{km\,s^{-1}}$ and $4200 \pm 100\,\mathrm{km\,s^{-1}}$ respectively (Darnley et al., 2018a).

Gaia (Data Release 2) parallax measurements estimate a distance of $3.9^{+1.0}_{-0.6}\,\mathrm{kpc}$ (Gaia Collaboration, 2018). Archival AAVSO observations of V392 Per from 2004 – 2018 reveal a quiescent magnitude of V $\sim 16 - 17$ mag, as well as 4 dwarf nova eruptions, most recently in 2016 where a peak of $V \sim 13.57$ mag was reached. With a published quiescent magnitude of $15.0 \leq \mathrm{m_{pg}} \leq 17.0$ (Downes & Shara, 1993) and V > 17 (Zwitter & Munari, 1994), the eruption amplitude is ≤ 12 mag. This is rather small for a CN eruption, hinting at a possible evolved donor. The eruption had an absolute magnitude of $\mathrm{M_V} = -9.5^{-0.8}_{+0.7}$ mag or $\mathrm{M_V} = -10.1^{-0.8}_{+0.7}$ mag, assuming a peak magnitude of 6.2 mag or 5.6 mag respectively (Darnley & Starrfield, 2018). The initial high ejecta velocities, low eruption amplitude and prompt detection of γ-rays suggest that V392 Per could be a recurrent nova, possibly with a symbiotic donor (Darnley & Starrfield, 2018).

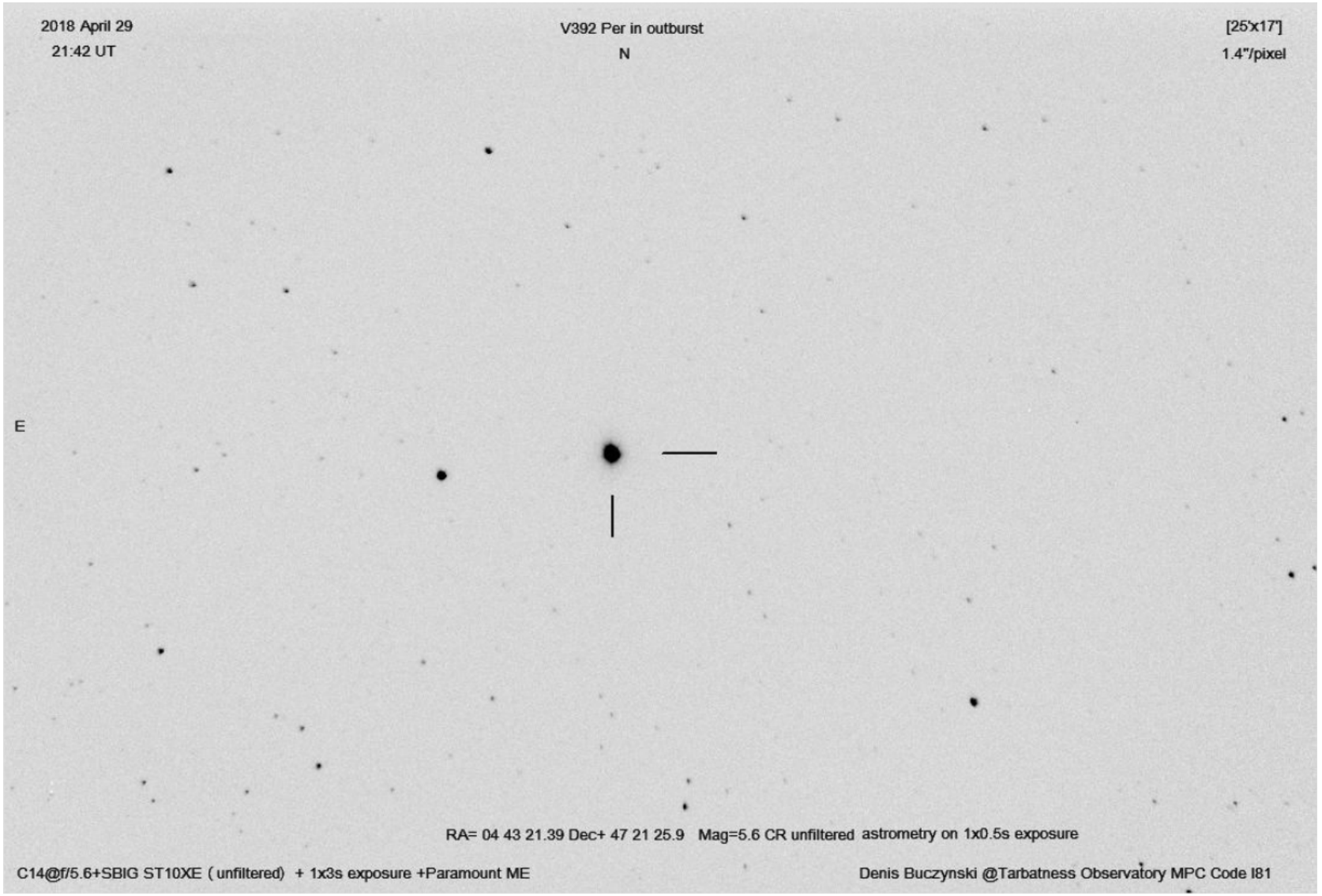

Figure 1.8: Image of V392 Per taken by Denis Buczynski on April 29th 2018, shortly after the nova discovery, with a reported unfiltered magnitude of 5.6.

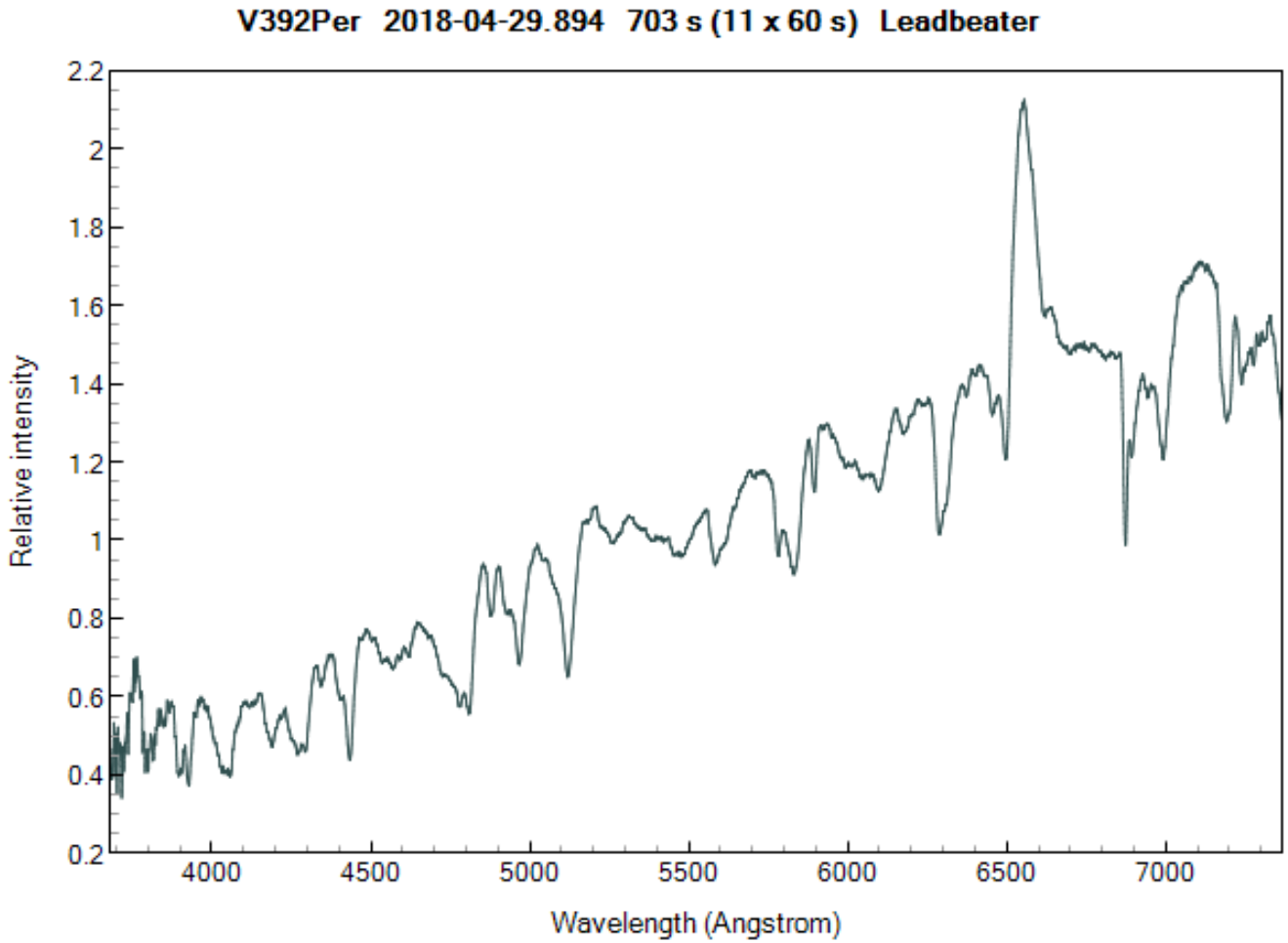

Figure 1.9: The first spectrum of the CN eruption of V392 Per, taken by Robin Leadbeater (2018) is shown.

Darnley & Starrfield (2018) discuss the possible progenitor system of V392 Per, comparing its initial spectral energy density (SED) with those of some CNe and RNe with known progenitors (see Figure 1.11). The progenitor SED is significantly different to those of the symbiotic novae RS Oph and T CrB, but bears a strong resemblance to the SEDs of GK Per and U Sco with their evolved sub-giant companions, or possibly to the rapid RN M31N 2008-12a – with its suggested low luminosity giant/ red clump donor.

Two high resolution spectra from May 1st and 2nd 2018 showed Hα and Hβ emission with complex line profiles and a FWHM of $5600 \pm 200\,\mathrm{km\,s^{-1}}$ (Stoyanov et al., 2020). From All-Sky Automated Survey for SuperNovae (ASAS-SN) and AAVSO photometry, Stoyanov et al. (2020) determined t_2 and t_3 to be ~ 3 days and ~ 11 days respectively, classifying V392 Per as a very fast nova (Payne-Gaposchkin, 1957). Stoyanov et al. (2020) used line intensities to determine the extinction towards V392 Per, finding a peak absolute magnitude of $M = -10.3 \pm 0.3$ mag.

Another group produced a high resolution echelle spectrum (R $\sim$ 7400) on May 1st 2018, finding a FWHM of $4600 \pm 250\,\mathrm{km\,s^{-1}}$ and identifying absorption at the Na I 5890 & 5896 Å doublet (Mugrauer et al., 2018), producing simultaneous photometry of the decline of the nova.

Radio observations taken with the Karl G Jansky Very Large Array (VLA) and the Arcminute Microkelvin Imager Large Array (AMI-LA) were reported on May 16th by Linford et al. (2018). The nova was detected clearly at 5.0, 7.0 and 15.5 GHz, with flux density increasing at all frequencies. The estimated brightness temperature of $T_B \sim 10^5$ K was 10 times higher than expected for a nova emitting thermal Bremsstrahlung radiation, suggesting a large contribution from synchrotron radiation. This could have been produced in the shocks which accelerated the leptons or protons, causing γ-ray emission (Linford et al., 2018).

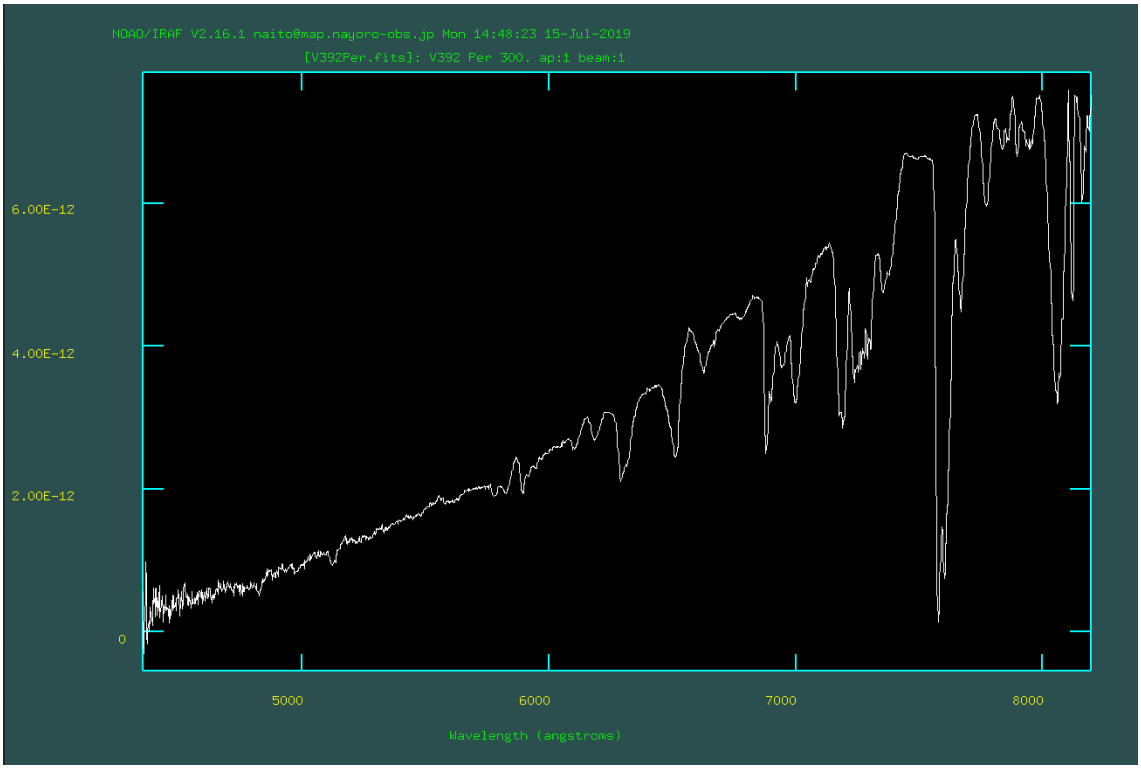

Figure 1.10: Spectrum of the CN eruption of V392 Per, taken by Naito and Ono (2018) is shown. This spectrum was published in CBET 4515 `http://www.cbat.eps.harvard.edu/unconf/followups/J04432130+4721280.html`

On July 13th 2018, the first post-Sun-constraint FRODOSpec spectrum was taken, revealing that the shape of the three visible emission lines (Hα, He I 6678 Å and He I 7065 Å) had similar structures, but had changed dramatically from their pre-Sun-constraint profiles (Darnley, 2018a). The line profiles showed a narrow, bright spike of emission, surrounded on either side by fainter, broader emission features.

The Liverpool Telescope SPRAT spectrum taken on July 19th 2018, 82.2 days post-discovery, showed that V392 Per had entered its nebular phase (Darnley, 2018b), with the appearance of strong, double-peaked forbidden lines of [O III] at 4363 Å, 4959 Å and 5007 Å. The nebular line of He II 4686 Å appeared and, like [O III] 4363, is more intense than Hβ, whereas [O III] 5007 is similar in brightness to Hα.

The first *Neil Gehrels Swift Observatory* observations were taken post-Sun-

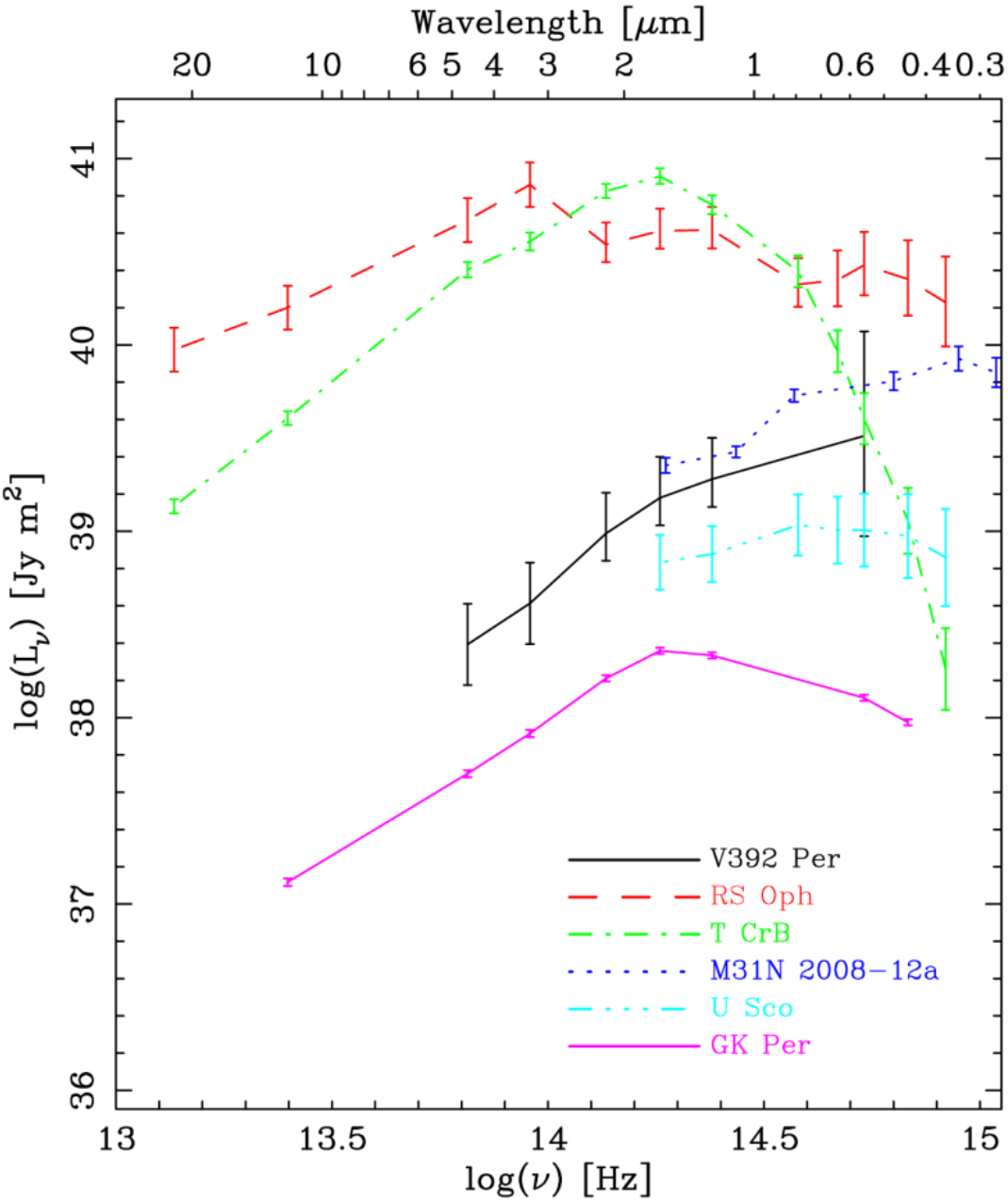

Figure 1.11: SED of the quiescent nova V392 Per compared with other classical and recurrent novae. Figure appears in Darnley & Starrfield (2018) ['On the Progenitor System of V392 Persei', Darnley & Starrfield, Research Notes of the American Astronomical Society, 2, 24, 2018 DOI `https://doi.org/10.3847/2515-5172/aac26c` ©AAS. Reproduced with permission.]

constraint (Darnley et al., 2018b), using UVOT filters v, b, u, uvm2, uvw1 and uvw2, with photometry suggesting high extinction towards V392 Per. An X-ray spectrum taken with the *Swift* XRT is best fitted with three temperature components, including a soft model atmosphere component (as we would expect supersoft source emission from V392 Per). A hydrogen column of $N_H = (1.9 \pm 0.3) \times 10^{22}\,cm^{-2}$ was found, with an X-ray count of $0.060 \pm 0.006\,counts\,s^{-1}$.

The August 9th 2018 spectrum taken with the Asiago 1.22 m telescope ($R \sim 1100$; see central spectrum in Figure 1.12) shows the presence of neon, with a [Ne V] 3426 Å velocity of $\sim 4500\,km\,s^{-1}$ (Munari & Ochner, 2018). [Ne V] 3426 and Hα had similar intensity, with a lower intensity of [Ne III] 3869 Å also detected. Munari & Ochner (2018) suggest V392 Per is a neon nova, i.e., it has a super-solar abundance of neon in the ejecta (Austin et al., 1996). Since neon is not produced in significant quantities in the hot-CNO cycle, this suggests that the neon was already present in the core (see Chomiuk et al., 2021a, and references therein). This in turn implies the primary had a high Zero Age Main Sequence mass, in order to proceed to the production of neon in its helium-burning. Some of the neon from the core would have been dredged up and mixed with the accreted hydrogen envelope, and ejected in the eruption. The abundance relative to solar composition should be determined before making statements about the WD type.

1.14 This thesis

The aim of this thesis was to conduct a comprehensive, multiwavelength study of the known DN V392 Persei following its eruption as a classical nova, and its subsequent detection as a source of γ-rays.

In Chapter 2, the facilities and instruments used to observe V392 Per are described, along with the data reduction processes applied. Chapter 3 covers the photometric results and analysis. The spectroscopic results and analysis are discussed in Chapter 4, as well as the UV and X-ray observations and analysis. The preliminary photoionization analysis is discussed in Chapter 5. A discussion of the research is presented in Chapter 6, with the conclusions and future work presented in Chapter 7.

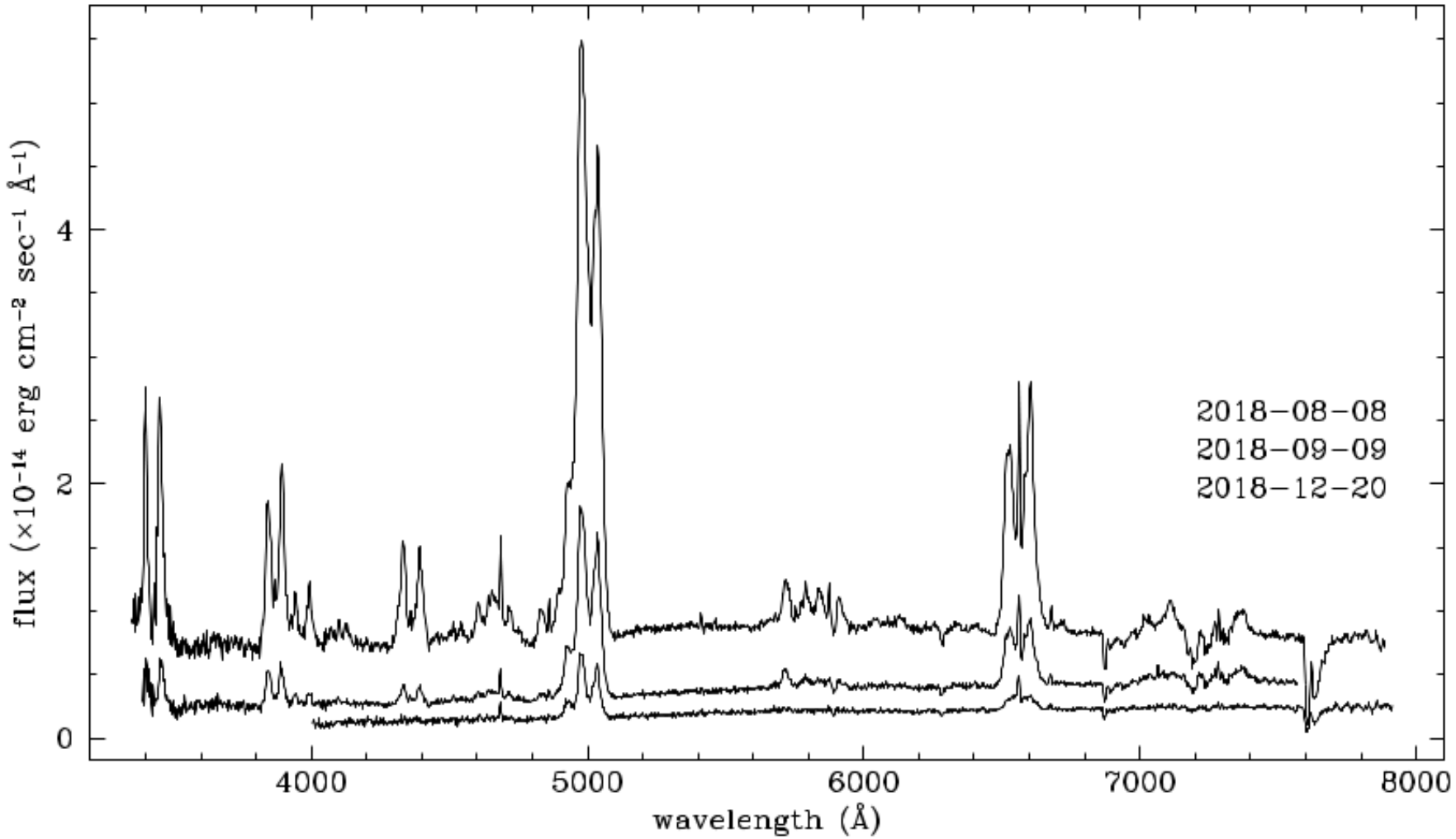

Figure 1.12: Low resolution spectra of V392 Per showing the evolution with time of the spectral lines of the nova. Plot produced and provided by Ulisse Munari (private communication).

Chapter 2

Facilities and Data Reduction

In this chapter, the facilities and instruments used to observe V392 Per are described, along with the data reduction processes applied. This chapter is an expanded version of Section 2 of Murphy-Glaysher et al. (2022). Dr Kim Page, *Swift* Data Centre Scientist, University of Leicester, provided the UV photometry and provided guidance on the X-ray data reduction and analysis.

Optical photometric data used in this project were collected using the Liverpool Telescope and two telescopes at the Las Cumbres Observatory. In addition, a large number of observations used were taken by the American Association of Variable Star Observers. The *Neil Gehrels Swift Observatory* provided UV photometry and a small number of optical U-band observations.

Spectroscopic data were collected using the Liverpool Telescope, the Hiltner telescope at the Michigan-Dartmouth-MIT (MDM) Observatory, and the Large Binocular Telescope, with additional optical spectra provided by the Astronomical Ring for Access to Spectroscopy (ARAS).

X-ray observations with *Neil Gehrels Swift Observatory* provided counts and spectra. γ-ray observations were carried out with the Fermi Large Area Telescope.

Images of all facilities used in this research are shown in Figure 2.1.

2.1 Liverpool Telescope

The Liverpool Telescope (LT; Steele et al., 2004) is a fully robotic, autonomous 2.0 m telescope, located at the Observatoio del Roque de Los Muchachos on the island La Palma, the westernmost Canary Island. The LT is owned and operated by the Astrophysics Research Institute at Liverpool John Moores University, and is financially supported by the United Kingdom Research and Innovation Science and Technology Facilities Council (UKRI/STFC).

Photometric observations of V392 Per were taken with the IO:O instrument (Smith & Steele, 2017) through $u'BVr'i'z'$ filters (see Section 2.1.1). Spectroscopic observations utilized both the low-resolution SPRAT and the higher resolution FRODOSpec.

2.1.1 LT Photometry

Photometry was taken using the Infrared–Optical (IO) suite of instruments: primarily using the optical wide-field camera IO:O. The filters used regularly for IO:O were Bessell-B and Bessell-V, along with the sloan-like filters *u'*, *r'*, *i'* and *z'*. [1]

[1] Initial observations were taken using Hα-6566 and the sloan-like *g'* filters. These observations are not used in this analysis.

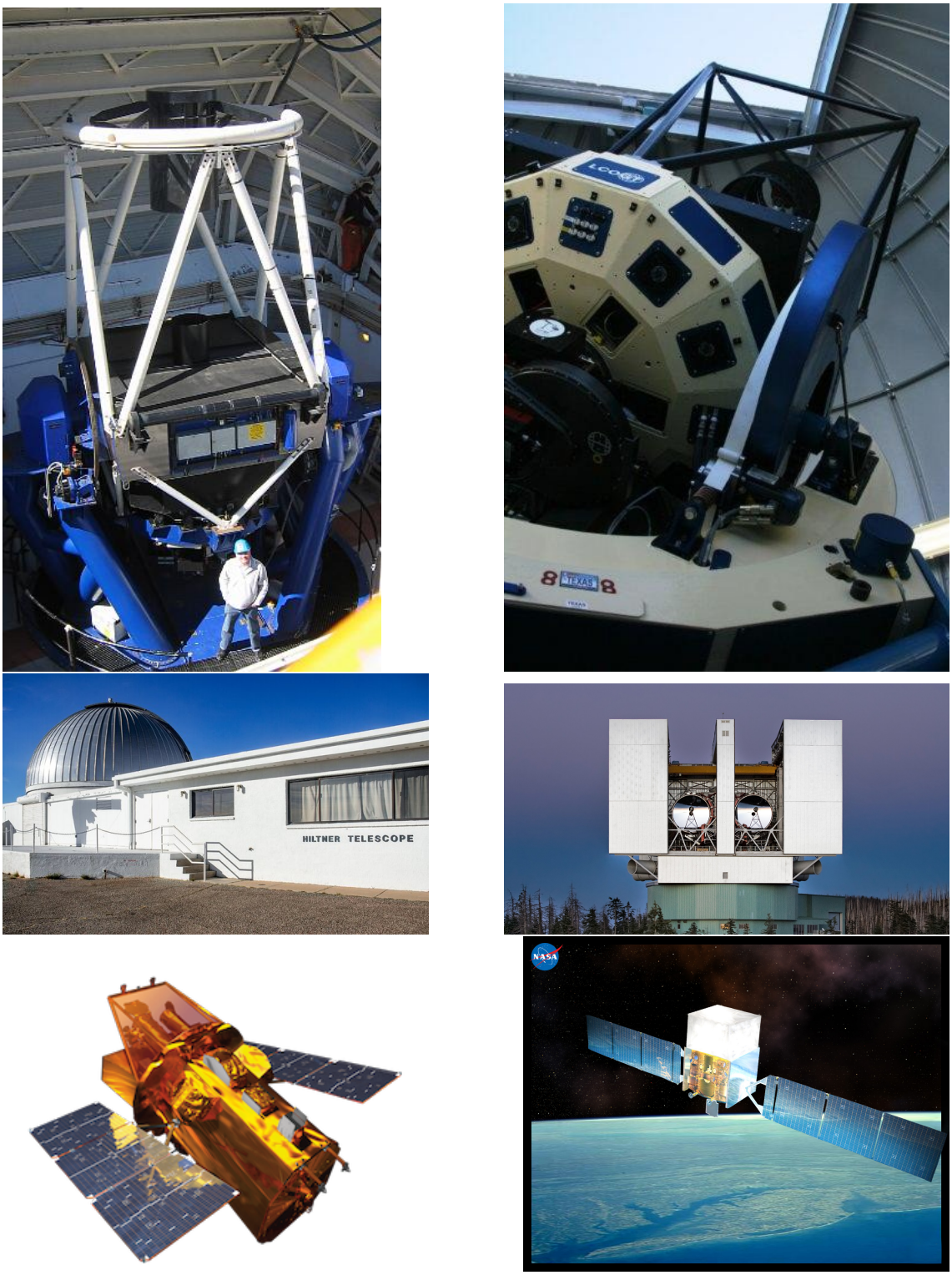

Figure 2.1: Facilities used to observe V392 Per. Clockwise from top left: Liverpool Telescope at La Palma [Image Credit: Liverpool Telescope]; LCOGT telescope at Fort Davis, Texas [Image Credit: Las Cumbres Observatory]; Large Binocular Telescope [Image Credit: NASA/JPL-Caltech]; the *Fermi* Space Telescope [Image Credits: NASA E/PO, Sonoma State University, Aurore Simonnet]; *Swift* Telescope [Image Credits: NASA E/PO, Sonoma State University, Aurore Simonnet]; and Hiltner Telescope, MDM Observatory [Image Credit: NOIRLab/AURA/NSF].

2.1.2 LT Spectroscopy

High-resolution LT spectra were taken using the Fibre-fed RObotic Dual-beam Optical Spectrograph (FRoDOSpec; Barnsley, Smith & Steele, 2012). In the low resolution mode the blue arm covers the wavelength range $3900 \leq \lambda \leq 5700\,\text{Å}$ with a resolution of $R \approx 2600$, and the red arm covers $5800 \leq \lambda \leq 9400\,\text{Å}$ with a resolution of $R \approx 2200$. In the high resolution mode the blue arm covers the wavelength range $3900 \leq \lambda \leq 5100\,\text{Å}$ with a resolution of $R \approx 5500$, and the red arm covers $5900 \leq \lambda \leq 8000\,\text{Å}$ with a resolution of $R \approx 5300$.

The low-resolution LT spectra used the high-throughput instrument SPectrograph for the Rapid Acquisition of Transients (SPRAT; Piascik et al., 2014, blue-optimised mode), covering the wavelength range $4000 \leq \lambda \leq 8000\,\text{Å}$ with a spectral resolution of $R \approx 350$. The blue-optimised mode was selected to maximise the throughput at the blue end of the spectrum, where $\lambda = 5600\,\text{Å}$ is the wavelength at which the red- and blue-optimised modes have equal efficiency. Classical novae have hot, blue continuua, and many of their emission lines of interest lie at wavelengths of $4000 \leq \lambda \leq 5600\,\text{Å}$, including H$\beta$ and subsequent Balmer lines, He II 4686, and nebular and auroral [O III] 4363, 4959, 5007 Å.

Groups of three or five exposures were taken at each epoch. Spectra were reduced using the LT pipeline; producing bias subtracted, flat-fielded, wavelength calibrated, sky-subtracted products. Cosmic rays were removed by a two-stage process involving interactive interpolation and exposure combination with the IRAF routine `scombine` (Tody, 1986).

2.2 American Association of Variable Star Observers

The American Association of Variable Star Observers (AAVSO; Kafka, 2021) is an international organization of amateur and professional astronomers that share an interest in variable stars. It has observers active in over 100 countries around the world, with archives spanning more than 34 million observations of variable stars. Amateur astronomers make their observations of variable stars and submit them to an online database, where they are checked and processed, and made available for download. The AAVSO provides target-of-opportunity notification to enable observers to coordinate with satellite observations, as well as intensive monitoring of interesting variable stars.

An alert notice requesting observations of V392 Per, posted on 2018 April 30 and submitted by Matt Darnley and Stella Kafka, resulted in many observations of the system. Observations of V392 Per were downloaded from the AAVSO archives [2] in the following bands: *B*, *TB*, *V*, *CV*, *Vis*, *SG*, *TG*, *I*, *SI*, *R*, *SR*, and *TR*. The earliest observations of V392 Per recorded in the AAVSO online database date back more than 5000 days before the detection of the classical nova eruption, with more than 1500 observations taken prior to this date. The most recent download from the AAVSO database was on 1st May 2019.

2.3 Las Cumbres Observatory

Las Cumbres Observatory (LCOGT; Brown et al., 2013) operates a fully robotic network of 25 telescopes from 7 global locations, capable of performing as a single instrument. There are three sizes of telescope in the network: 0.4 m, 1.0 m and 2.0 m.

[2](https://www.aavso.org/)

The LCO network covers both hemispheres, with observatories located in Hawaii, Texas, Chile, Tenerife, South Africa, Israel and Australia, with a new site under development in Western Tibet.

Additional i'-band photometry of V392 Per was collected using both 1.0 m Telescopes at the LCO McDonald Observatory in Fort Davis, Texas.

2.4 Michigan-Dartmouth-MIT Observatory

The Michigan-Dartmouth-MIT (MDM) Observatory is located at the Kitt Peak National Observatory, on Kitt Peak in the Quinlan Mountains. The Quinlan Mountains lie in the Arizona-Sonoran desert, in the Tohono O'odham Nation. MDM is operated by a consortium of educational institutions, comprising Dartmouth College, University of Michigan, Ohio State University, Ohio University and Columbia University. The name of the Observatory originated when Massachusetts Institute of Technology was still a member of the consortium.

The 2.4 m Hiltner telescope at the MDM Observatory utilizes the Ohio State Multi-Object Spectrograph (OSMOS; Martini et al., 2011). This instrument has a 1.2 arcsec wide entrance to the long-slit and high-efficiency, low-resolution blue- and red-optimized grisms. The slit position can be altered to adjust the wavelength coverage between 3980–6860 Å and 3200–9000 Å , with a spectral resolution of $R \simeq 1600$ at 6000 Å. The Hiltner telescope was used to obtain many spectroscopic observations of V392 Per.

2.5 Large Binocular Telescope

The Large Binocular Telescope (LBT; Hill et al., 2008) consists of two identical 8.4 m diameter telescopes co-pointing on a shared altitude-azimuth mounting, acting as binoculars, with an effective aperture of 11.8 m. The LBT is located on Emerald Peak in the Pinaleno Mountains in Arizona. LBT is operated by a large collaboration, with partners in Italy, the United States and Germany [3].

We obtained optical spectra of V392 Per at two epochs with LBT and the Multi Object Double Spectrograph (MODS; Pogge et al., 2010). MODS utilizes separate and optimized blue and red channel spectrographs. MODS takes simultaneous blue and red spectra with R $\sim$ 1850 and R $\sim$ 2300 respectively, covering the wavelength range 3249–10100 Å .

2.6 *Neil Gehrels Swift Observatory*

The *Neil Gehrels Swift Observatory* (*Swift*; Gehrels et al., 2004) is a space-based facility that was designed to detect and perform multi-wavelength observations of long and short duration gamma ray bursts and their afterglows. *Swift* has three instruments onboard, each optimised for a different wavelength range. The Burst Alert Telescope (BAT; Barthelmy et al., 2005)) detects gamma rays of energy $15 - 50$ keV, the X-Ray Telescope (XRT; Burrows et al., 2005) detects X-rays of energy $0.3 - 10$ keV, and the Ultraviolet/Optical Telescope (UVOT; Roming et al.,

[3]The collaborating institutions are: the Italian Istituto Nazionale de Astrofisica (INAF); the US Arizona State University, University of Arizona, Northern Arizona University, Ohio State University, and the Research Corporation (representing the University of Notre Dame, University of Minnesota and University of Virginia); and the German LBT Beteiligungsgesellschaft (LBTB). The LBTB consists of the Max Planck Institute for Astronomy, the University of Heidelberg Center for Astronomy, the Leibniz Institute for Astrophysics Potsdam, the Max Planck Institute for Extraterrestrial Physics and the Max Planck Institute for Radio Astronomy.

2005) covers the wavelength range $1700 - 6000\,\text{Å}$. Although *Swift* is optimised for observing GRBs, it is extremely useful for observations of other transients due to its rapid slewing capabilities and the fact it can detect X-rays and UV radiation.

2.7 Fermi Large Area Telescope

The Fermi Gamma-ray Space Telescope (Fermi) was launched into Low Earth Orbit in 2008 as the Gamma-ray Large Area Space Telescope (GLAST Facility Science Team et al., 1999), but was renamed to honour the high-energy physicist Enrico Fermi shortly thereafter. Fermi probes the extreme environments in the Universe, detecting photons in the energy range 10 keV to 300 GeV, addressing questions about diverse topics such as black holes, γ-ray bursts and cosmic rays, as well as searching for dark matter.

There are two instruments mounted on Fermi, the Large Area Telescope (LAT; Atwood et al., 2009) and the Gamma-ray Burst Monitor (GBM; Meegan et al., 2009). LAT is a powerful imager that detects γ-rays in the energy range 20 MeV to 300 GeV, and represents a sensitivity improvement of a factor of 30 over the previous generation of γ-ray telescopes, due to its larger collecting area, field of view and angular resolution. GBM has a wider field of view than LAT and covers the energy range 10 keV to 25 MeV. The LAT field of view covers approximately 20 % of the sky, allowing the whole sky to be observed every three hours. In contrast, the GBM field of view covers the whole sky except the part occulted by Earth.

Fermi-LAT detected γ-rays from V392 Per the day after the optical detection of the eruption (Li et al., 2018b). However, solar panel issues between 2018 April 4–30 prevented observations prior to that day (Albert et al., 2022). The γ-ray light

curve used in this research (see Chapter 3) and Murphy-Glaysher et al. (2022) was published in a review of Classical Novae by Chomiuk et al. (2021a), and received by private communication from L. Chomiuk. The light curve has since been published in a paper combining data from Fermi and the High Altitude Water Cherenkov Observatory (HAWC; Albert et al., 2022).

2.8 Photometric Data Reduction

LT data were reduced using the LT pipeline. LT and LCOGT data were stacked and aligned using standard tools within PyRAF (Science Software Branch at STScI, 2012), and aperture photometry was performed using `qphot`. The data were calibrated against 25 reference stars in the field (see Section 3.2 and Table A.2), selected from the Pan-STARRS catalogue (DR1; Chambers & Pan-STARRS Team, 2016). The reference stars had $g'r'i'z'$ magnitudes $14 < m < 22$, and were sufficiently distant from other stars. Pan-STARRS photometry was converted to Johnson BV and Sloan-like $r'i'z'$ using relations in Tonry et al. (2012). A single star in a *Swift* observation of the field was utilised to calibrate the u'-band photometry.

For comparison with the LT/LCOGT data, the AAVSO photometry was converted to the AB system using relations from Blanton & Roweis (2007). More details of the conversion to the AB system are given in Section 3.2. Due to the typically larger or unknown uncertainties on the AAVSO data and the large number of independent observers, we opted not to apply colour corrections to these data.

All photometry is recorded in Table A.3, and near-UV and optical light curves of V392 Per are presented in Figures 3.3–3.6. An analysis of the photometric data is presented in Chapter 3.

2.9 Spectroscopic Data Reduction

As mentioned in Section 2.1.2, the LT pipeline produces bias subtracted, flat-fielded, wavelength calibrated, sky-subtracted products. Relative flux calibration of the SPRAT spectra was conducted with 78 observations of the spectrophotometric standard Hiltner 102 (Stone, 1977). Relative flux calibration of the FRODOSpec spectra was performed using observations of the spectrophotometric standard stars Hiltner 102 and BD+33 2642 (Oke, 1990) for the higher and lower resolution modes, respectively.

The Hiltner and LBT spectra were provided by Mark Wagner, and were already wavelength calibrated, flat-fielded and relative flux calibrated using the standard stars Hiltner 102 or G191-B2B (Stone, 1977). The wavelength scale of the 2019 LBT data was shifted by 2 Å post-reduction to ensure that the position of the Hα emission lines coincided.

All aforementioned spectra from LT, Hiltner and LBT were absolute flux calibrated using interpolated $BVr'i'$ photometry (see Section 4.1). Spectra were corrected for heliocentric velocity and dereddened using $E\,(B-V) = 0.7$ (see Section 3.8).

Additional spectra were retrieved from the Astronomical Ring for Access to Spectroscopy database[4] (ARAS; Teyssier, 2019). Some of the spectra were relative flux calibrated by the ARAS observers, but I did not perform absolute flux calibration on these spectra. These spectra were primarily used to measure the P Cygni velocities from the Balmer lines.

All spectra used in this work are listed in Table A.1. Analysis of the spectra is presented in Chapter 4.

[4] `http://www.astrosurf.com/aras/Aras_DataBase/DataBase.htm`

2.10 UV and X-ray data collection and reduction

XRT and UVOT observations of V392 Per were taken using the target of opportunity programme on *Swift*, with target IDs 10734 and 10773. The UVOT filters used were uvw1, uvm2 and uvw2. An initial observation on 2018 July 20, upon the emergence of V392 Per from its first Sun constraint, was taken to ascertain the suitability of the target for the UVOT UV-grism: it was too faint. Subsequent observations were taken approximately weekly with XRT, initially in automatic mode, before switching to XRT in photon counting (PC) mode. Observations switched to every two weeks from October 2018 until April 2019, and from July 2019 observations moved to a four-weekly cadence. Monthly observations took place from 2020 January–April, and a final observation was taken in 2020 August. *Swift* data were processed and analysed using the standard HEASoft tools and relevant calibration files.

XRT analysis utilised all X-ray photon detection events with good detection grades, i.e., those in the range 0–12, as is standard for photon counting mode. The count rate was not high enough to cause the data to suffer from pile-up, where two or more X-ray photons are detected as a single event. A circular extraction region of 10–15 pixels ($2.36''\,\mathrm{pixel}^{-1}$) was used, depending on the source brightness; the background was estimated from a 60 pixel radius circle, offset from, but close to, the source. Upon examination of the hardness ratio (HR), it was clear that there was no rapid spectral evolution. The on-line XRT product generator[5] (Evans et al., 2009) was used to extract spectra over a number of intervals. The HR remained approximately constant throughout each interval.

UVOT analysis utilised the updated sensitivity calibrations released in 2020. Magnitudes were estimated using `uvotsource`, with a $3''$ radius source extraction

[5] `https://www.swift.ac.uk/user_objects`

region to avoid possible low-level contamination from a nearby source, and 20″ background circle.

All photometry is recorded in Table A.3, and near-UV and optical light curves of V392 Per are presented in Figures 3.3–3.6. An analysis of the X-ray and UV data is presented in Chapter 4.

This chapter described the facilities and instruments used to observe V392 Per, along with the data reduction processes applied. The next chapter outlines the photometric analysis of the observations of V392 Per.

Chapter 3

Photometric Evolution

This chapter is an extended version of Section 3 of Murphy-Glaysher et al. (2022).

3.1 Alignment and stacking of images

The Liverpool Telescope automated pipeline produces reduced images where the bias and flat field frames have been subtracted pixel by pixel from the science images. The reduced images for each observation were downloaded from the data archive via the Liverpool Telescope website. IO:O images for a given filter were taken in groups of 3 or 5 images, centred on the location of V392 Per, taken during the same pointing.

All Bessell-V and *r'* images were examined to identify the clearest image, which was selected to use as a reference in the alignment of all images. The PyRAF command `wcsmap` was used to find the transformation between each reduced image and the reference image (h_e_20180821_40_1_1_1.fits). Then `geotran` was used to

perform the transformation to align each image with the reference image. The alignment was initially applied to one image as a test, and then applied to all images.

Once the images were aligned, the images within each group, i.e. taken during the same pointing, were stacked. The `imcombine` routine was used to combine the images within the group. The routine works by comparing the three images pixel by pixel and adopting the median value for each pixel, thereby removing the effect of cosmic rays on the stacked image.

3.2 Standard stars for photometric calibration

Aladin Sky Atlas was used to overlay the reference image with assorted catalogues of standard stars around the sky coordinates of the image. Data from the following catalogues were downloaded, and the corresponding number of objects from each catalogue found in the reference image are shown: PanSTARRS (322), AllWISE (99), WISE (84), 2MASS (87), IPHAS2 (179) and AAVSO (5). The Panoramic Survey Telescope and Rapid Response System (PanSTARRS) catalogue (Chambers & Pan-STARRS Team, 2016) was selected as it included the highest number of potential reference stars in the vicinity of V392 Per, and contained standard magnitudes in five broadband filters (grizy).

PanSTARRS magnitudes for the reference stars were converted to the Sloan-like and Bessell magnitudes (*g'r'i'z'y'*,Bessell-B and Bessell-V) using relations determined by Tonry et al. (2012). The basic form of the conversion is shown in Equation 3.1, where both linear and quadratic versions are given, and the constants A_n and B_n differ according to the filter. The linear form of the conversion was used because this would give sufficiently accurate magnitudes, given the relatively large number of

reference stars to be used.

$$y = A_0 + A_i x + A_2 x^2 = B_0 + B_1 x \tag{3.1}$$

The Bessell B and V magnitudes are assumed to be equivalent to those in the Johnson-Cousins system. The conversions used to find the Sloan-like and Bessell magnitudes are shown in Equations 3.2 to 3.7, where the subscripts P1 and SDSS indicate PanSTARRS and Sloan-like magnitudes and colours respectively.

$$\mathrm{g_{SDSS}} = \mathrm{g_{P1}} + 0.014 + 0.162(\mathrm{g} - \mathrm{r})_{\mathrm{P1}} \tag{3.2}$$

$$\mathrm{r_{SDSS}} = \mathrm{r_{P1}} - 0.001 + 0.011(\mathrm{g} - \mathrm{r})_{\mathrm{P1}} \tag{3.3}$$

$$\mathrm{i_{SDSS}} = \mathrm{i_{P1}} - 0.004 + 0.020(\mathrm{g} - \mathrm{r})_{\mathrm{P1}} \tag{3.4}$$

$$\mathrm{z_{SDSS}} = \mathrm{z_{P1}} + 0.013 - 0.050(\mathrm{g} - \mathrm{r})_{\mathrm{P1}} \tag{3.5}$$

$$\mathrm{B} = \mathrm{g_{P1}} + 0.213 + 0.587(\mathrm{g} - \mathrm{r})_{\mathrm{P1}} \tag{3.6}$$

$$\mathrm{V} = \mathrm{r_{P1}} + 0.006 + 0.474(\mathrm{g} - \mathrm{r})_{\mathrm{P1}} \tag{3.7}$$

The field around V392 Per was examined, and 25 suitable reference stars chosen, that were initially assumed to be of constant magnitude. The PanStarrs identifier for each reference star was found using the Aladin Sky Atlas, and the relevant data extracted from the PanSTARRS catalogue. The reference stars were sorted in order of their right ascension, and then renumbered from 1 to 25.

The field of V392 Per is shown in Figure 3.1, with the reference stars circled and labelled. Further details for each reference star are shown in Table 3.1, which shows the PanSTARRS grizy magnitudes and their associated errors. Table 3.2 shows the Sloan-like and Bessell magnitudes *g'r'i'z'BV* for the reference stars, calculated using the data in Tonry et al. (2012).

3.3 Initial photometry

Aperture photometry was performed using STARLINK `gaia` on V392 Per in the aligned V-band reference image aligned_h_e_20180821_40_1_1_1.fits, using the 25 reference stars to calibrate the photometry. The aperture selected was 3.5 pixels, with the inner and outer annuli set to 10.5 pixels and 14.0 pixels respectively. The `photometry` function found the centroid of each star's position and the coordinates were recorded. The relative zero point for each reference star was found, and then the mean was applied to the instrumental magnitude of the nova, yielding a calibrated magnitude of $V = 14.2217 \pm 0.0504$ mag.

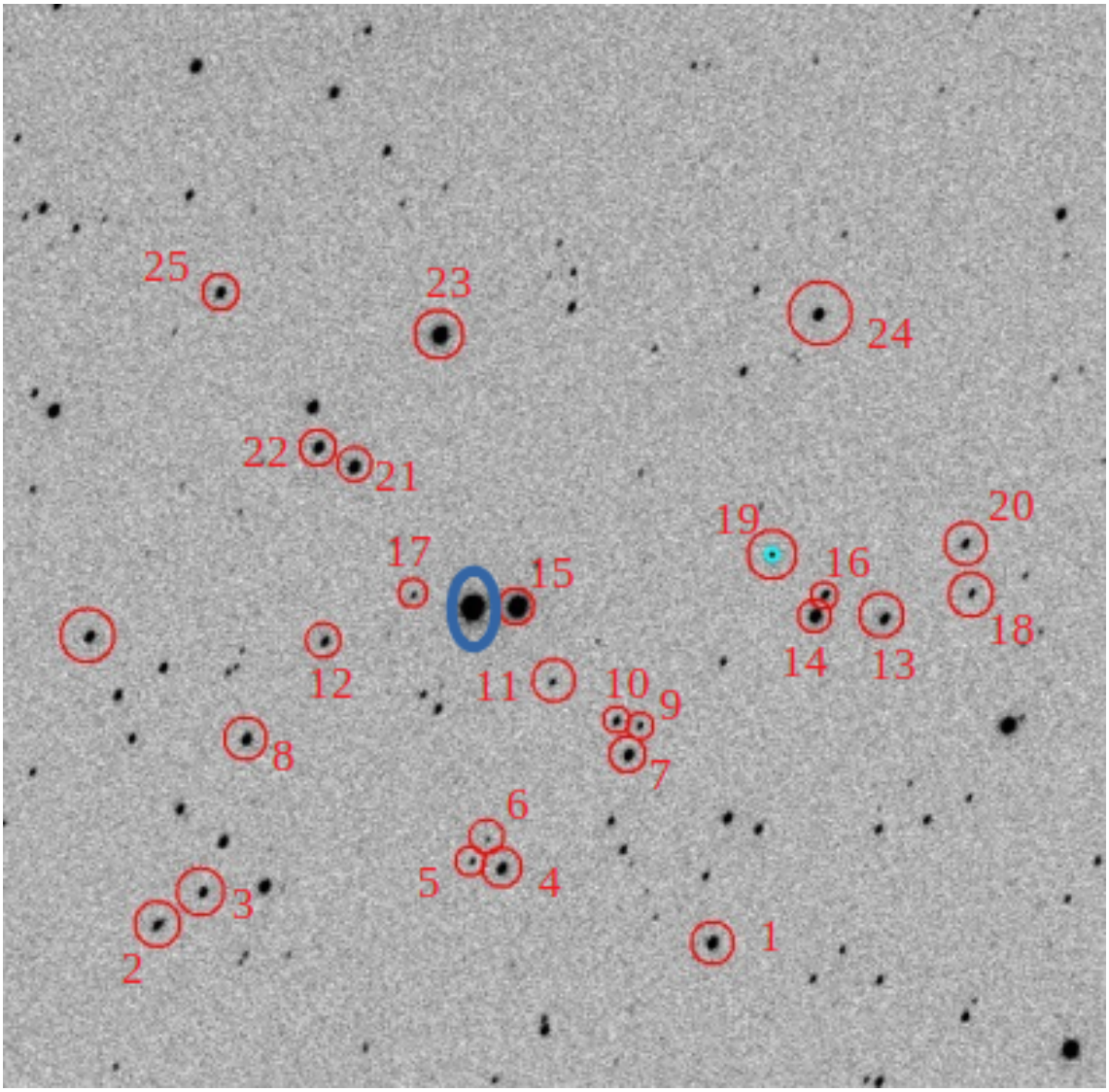

Figure 3.1: The field around V392 Per is shown. A blue ellipse surrounds V392 Per, and the reference stars used to perform photometry on the nova are shown circled in red, labelled with the reference star number. The small cyan circle surrounding reference star 19 has no significance.

Star no	R.A. (J2000)	Dec. (J2000)	Object ID.	g/mag	$\delta\,g$/mag	r/mag	$\delta\,r$/mag	i/mag	$\delta\,i$/mag	z/mag	$\delta\,z$/mag	y/mag	$\delta\,y$/mag
1	70.81249209	47.37007015	164840708125355000	18.1996	0.0066	17.2783	0.0038	16.8080	0.0032	16.5464	0.0067	16.3534	0.0060
2	70.81383005	47.34026310	164800708138869000	19.4267	0.0141	18.5334	0.0122	18.0682	0.0095	17.7333	0.0021	17.4308	0.0242
3	70.81645958	47.34276040	164810708164722000	19.1637	0.0096	18.0720	0.0050	17.4510	0.0050	17.0716	0.0124	16.8305	0.0102
4	70.81837435	47.35878305	164830708184131000	18.5872	0.0012	17.5938	0.0039	17.0115	0.0029	16.6768	0.0039	16.4413	0.0038
5	70.81894658	47.35717717	164820708189789000	20.8281	0.0197	19.6675	0.0086	19.0011	0.0044	18.6029	0.0080	18.3308	0.0310
6	70.82066808	47.35800618	164830708206900000	21.6254	0.0885	20.4448	0.0129	19.7522	0.0141	19.2737	0.0159	18.9737	0.0246
7	70.82737554	47.36556815	164830708274029000	18.6378	0.0043	17.3717	0.0063	16.6876	0.0047	16.2888	0.0053	15.9979	0.0062
8	70.82860289	47.34506741	164810708286245000	18.5086	0.0121	17.5342	0.0060	16.9937	0.0035	16.6613	0.0053	16.4154	0.0036
9	70.82969930	47.36617769	164840708297440000	20.4520	0.0395	19.3966	0.0188	18.7389	0.0053	18.3681	0.0171	18.1098	0.0142
10	70.83006169	47.36491612	164830708300909000	19.9856	0.0176	18.6229	0.0089	17.8968	0.0026	17.4693	0.0128	17.2006	0.0110
11	70.83312893	47.36146279	164830708331564000	20.6393	0.0344	19.4030	0.0104	18.7326	0.0146	18.3334	0.0092	18.1156	0.0235
12	70.83635760	47.34927241	164810708363800000	19.4262	0.0116	18.2787	0.0037	17.6414	0.0041	17.2571	0.0095	17.0004	0.0178
13	70.83816407	47.37927311	164850708381906000	18.8836	0.0134	17.5161	0.0039	16.7298	0.0035	16.2676	0.0048	15.9614	0.0041
14	70.83840148	47.37556334	164850708384241000	17.6462	0.0030	16.9136	0.0020	16.5180	0.0039	16.2832	0.0046	16.0462	0.0039
15	70.83911851	47.35957369	164830708391402000	15.4344	0.0018	14.7889	0.0020	14.5037	0.0025	14.3481	0.0002	14.2402	0.0036
16	70.84002441	47.37608219	164850708400482000	19.5950	0.0091	18.5693	0.0102	17.9982	0.0109	17.6277	0.0153	17.3654	0.0117
17	70.84002473	47.35403355	164820708400455000	20.9870	0.0387	19.6647	0.0101	18.9598	0.0147	18.5197	0.0051	18.2594	0.0272
18	70.84018790	47.38395890	164860708402161000	20.2112	0.0165	19.0219	0.0119	18.3469	0.0031	17.9591	0.0089	17.6840	0.0132
19	70.84312884	47.37324886	164840708431519000	18.0998	0.0072	17.2341	0.0042	16.7577	0.0058	16.4777	0.0071	16.2596	0.0031
20	70.84410873	47.38361085	164860708441271000	19.6501	0.0087	18.7600	0.0103	18.2130	0.0049	17.8788	0.0036	17.6188	0.0125
21	70.85017773	47.35083154	164820708501862000	18.1518	0.0042	17.2433	0.0035	16.7310	0.0016	16.4441	0.0060	16.1891	0.0065
22	70.85170105	47.34893444	164810708517219000	18.1877	0.0026	17.2433	0.0068	16.7271	0.0028	16.4184	0.0046	16.1897	0.0070
23	70.86059215	47.35543692	164820708606127000	16.4221	0.0027	15.5078	0.0024	15.0888	0.0046	14.8687	0.0067	14.7238	0.0055
24	70.86226330	47.37572836	164850708622792000	18.2517	0.0079	17.1450	0.0066	16.5161	0.0027	16.1808	0.0032	15.9253	0.0034
25	70.86395183	47.34367003	164810708639843000	18.8058	0.0111	17.7934	0.0111	17.2571	0.0029	16.9342	0.0063	16.6745	0.0076

Table 3.1: Table showing the 25 reference stars used in the photometry of V392 Per along with their position in RA and Dec, PanSTARRS object ID, PanSTARRS g,r,i,z and y magnitudes and errors.

Star no	R.A. (J2000)	Dec (J2000)	Object ID	g'/mag	r'/mag	i'/mag	z'/mag	B/mag	V/mag
1	70.81249209	47.37007015	164840708125355000	18.3628506	17.2874343	16.822426	16.513335	18.9534031	17.7209962
2	70.81383005	47.34026310	164800708138869000	19.5854146	18.5422263	18.082066	17.701635	20.1640671	18.9628242
3	70.81645958	47.34276040	164810708164722000	19.3545554	18.0830087	17.468834	17.030015	20.0175279	18.5954658
4	70.81837435	47.35878305	164830708184131000	18.7621308	17.6037274	17.027368	16.64013	19.3833258	18.0706716
5	70.81894658	47.35717717	164820708189789000	21.0301172	19.6792666	19.020312	18.557870	21.7223722	20.2236244
6	70.82066808	47.35800618	164830708206900000	21.8306572	20.4567866	19.771812	19.227670	22.5314122	21.0104044
7	70.82737554	47.36556815	164830708274029000	18.8569082	17.3846271	16.708922	16.238495	19.5940007	17.9778314
8	70.82860289	47.34506741	164810708286245000	18.6804528	17.5439184	17.009188	16.625580	19.2935728	18.0020656
9	70.82969930	47.36617769	164840708297440000	20.6369748	19.4072094	18.756008	18.328330	21.2845198	19.9028596
10	70.83006169	47.36491612	164830708300909000	20.2203574	18.6368897	17.920054	17.414165	20.9985049	19.2748198
11	70.83312893	47.36146279	164830708331564000	20.8535806	19.4155993	18.753326	18.284585	21.5780081	19.9950062
12	70.83635760	47.34927241	164810708363800000	19.6260950	18.2903225	17.660350	17.212725	20.3127825	18.8286150
13	70.83816407	47.37927311	164850708381906000	19.1191350	17.5301425	16.753150	16.212225	19.8993225	18.1702950
14	70.83840148	47.37556334	164850708384241000	17.7788812	16.9206586	16.528652	16.259570	18.2892362	17.2668524
15	70.83911851	47.35957369	164830708391402000	15.5529710	14.7950005	14.512610	14.328825	16.0263085	15.1008670
16	70.84002441	47.37608219	164850708400482000	19.7751634	18.5795827	18.014714	17.589415	20.4100859	19.0614818
17	70.84002473	47.35403355	164820708400455000	21.2152126	19.6782453	18.982246	18.466585	21.9761901	20.2974702
18	70.84018790	47.38395890	164860708402161000	20.4178666	19.0339823	18.366686	17.912635	21.1223191	19.5916282
19	70.84312884	47.37324886	164840708431519000	18.2540434	17.2426227	16.771014	16.447415	18.8209659	17.6504418
20	70.84410873	47.38361085	164860708441271000	19.8082962	18.7687911	18.226802	17.847295	20.3855887	19.1879074
21	70.85017773	47.35083154	164820708501862000	18.3129770	17.2522935	16.745170	16.411675	18.8980895	17.6799290
22	70.85170105	47.34893444	164810708517219000	18.3546928	17.2526884	16.741988	16.384180	18.9550628	17.6969456
23	70.86059215	47.35543692	164820708606127000	16.5842166	15.5168573	15.103086	14.835985	17.1717941	15.9471782
24	70.86226330	47.37572836	164850708622792000	18.4449854	17.1561737	16.534234	16.138465	19.1143329	17.6755758
25	70.86395183	47.34367003	164810708639843000	18.9838088	17.8035364	17.273348	16.896580	19.6130788	18.2792776

Table 3.2: Table showing the 25 reference stars used in the photometry of V392 Per along with their position in RA and Dec, PanSTARRS object ID, Sloan-like magnitudes g,r,i and z and Bessell magnitudes B and V.

Using the coordinates found using `gaia photometry`, the PyRAF routine `qphot` was used to perform aperture photometry on the same image, yielding $V = 14.2249 \pm 0.0559$ mag. The `gaia` photometry was consistent with that produced by `qphot`, so I developed a programme to automate the photometry, allowing more efficent analysis of sets of images gathered during the observing campaign for V392 Per.

3.4 Ongoing photometry

The photometry code takes a list of stacked, aligned images and performs aperture photometry on the nova and reference stars for each image. Multiple apertures are used, ranging from 1 to 10 pixels, with a step size of 0.5 pixels. The annulus surrounding the aperture has inner and outer radii of 10.5 pixels and 14 pixels respectively.

For a given image and for each aperture, the zeropoint correction Z for each reference star was calculated by subtracting the star's standard magnitude m_{std} (as described in Section 3.2) from the instrumental magnitude m_{inst} obtained by using `qphot`.

$$Z = m_{inst} - m_{std} \tag{3.8}$$

The mean reference star zeropoint $\bar{Z}$ and standard deviation σ_Z were calculated, including only those reference stars meeting the error criteria in Equation 3.9, where $m_{cut} = 0.3$ mag was the initial error cut-off. The zeropoint correction Z and instrumental magnitude error σ_{inst} for any reference star that was not detected in a given image were set to zero to simplify the calculation of $\bar{Z}$.

$$0 < m_{err} < m_{cut} \tag{3.9}$$

The mean zeropoint was subtracted from the instrumental nova magnitude $m_{nova,inst}$, yielding the calibrated nova magnitude $m_{nova,cal}$.

$$m_{nova,cal} = m_{nova,inst} - \bar{Z} \tag{3.10}$$

The error on the nova magnitude, σ_{nova}, was calculated for each aperture by combining in quadrature the standard deviation of the zeropoint σ_Z with the error on the instrumental magnitude for the nova $\sigma_{nova,inst}$.

$$\sigma_{nova} = \sqrt{\sigma_Z^2 + \sigma_{nova,inst}^2} \tag{3.11}$$

The aperture size yielding the lowest overall error on the nova magnitude was selected as the optimal aperture for that image. The code produced a file showing the modified julian date (MJD) of the observation, the size of the optimal aperture, the calibrated nova magnitude using that aperture and the overall error on the calibrated nova magnitude, which could be used to plot light curves.

The instrumental magnitudes of the reference stars, $m_{ref,inst}$, were calibrated for each aperture by subtracting the mean zeropoint $\bar{Z}$ calculated previously.

$$m_{ref,cal} = m_{ref,inst} - \bar{Z} \tag{3.12}$$

If the error on the instrumental magnitude for a given reference star did not meet the error criterion in Equation 3.9, the calibrated magnitude of the reference star was set to -1 to identify reference stars with large instrumental errors, and those which were too faint to be detected in a given image. For each reference star and for each aperture, the overall error on the calibrated magnitude σ_{ref} was calculated by combining in quadrature the instrumental error $\sigma_{ref,inst}$ and the standard deviation

of the zeropoints $\sigma_{\rm Z}$.

$$\sigma_{\rm ref} = \sqrt{{\sigma_{\rm ref,inst}}^2 + {\sigma_{\rm Z}}^2} \tag{3.13}$$

3.4.1 u' photometry

In the case of observations taken in the u' passband, the process for performing photometry differed, because the only reference star visible was the nearby field star, reference star 15. The PanSTARRS catalogue did not include u magnitudes, and the Tonry et al. (2012) relations did not include a conversion to the Sloan-like u'. Instead, I used a *Swift U* observation of V392 Per to calibrate the LT u' photometry of V392 Per in the u' image taken closest in time to the *Swift* observation. The reference star was assumed to have a constant u' magnitude, which was used to calibrate all other LT u' images. For the final two u' images, the error criterion had to be increased to $m_{\rm cut} = 0.7$, whereas in all other filters, $m_{\rm cut} = 0.3$ was sufficient.

3.4.2 Stability of reference stars

The $BVr'i'z'$ light curves for each of the 25 reference stars from $84 - 157$ days after eruption are shown in Figure 3.2. In producing the light curves for each reference star, photometry was performed as described in Section 3.4, except the optimal aperture size was chosen to be the one which minimized the overall error for that reference star (rather than for the nova).

We can see that the light curves are fairly stable, with greater variability due to noise in the dimmer light curves. In particular, the B-band light curve exhibits

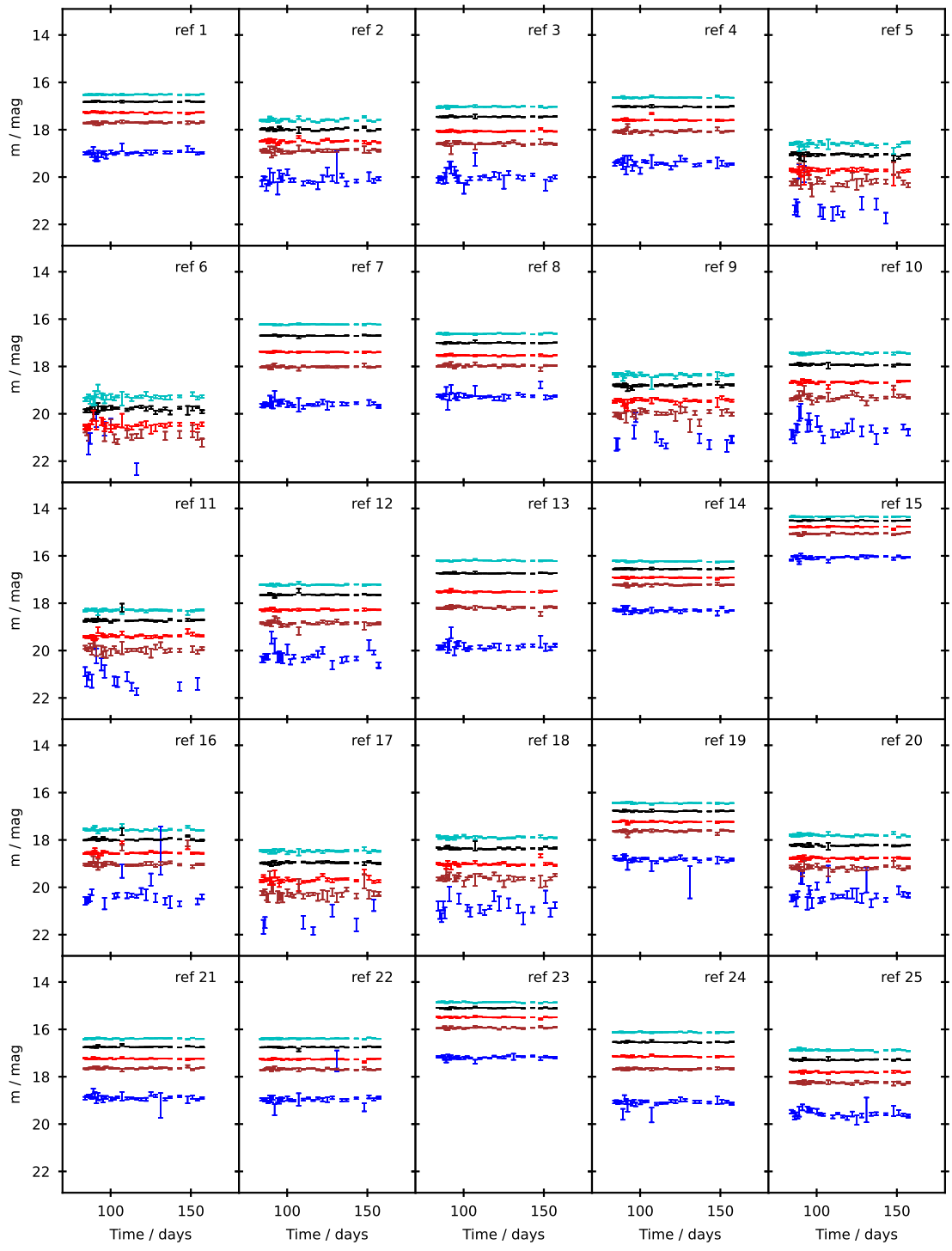

Figure 3.2: Light curves of the 25 reference stars used to calibrate the photometry of V392 Per. $BVr'i'z'$ photometry is shown in blue, brown, red, cyan and black respectively.

greater noise, since the reference stars are red in colour. However, when the zeropoints in a given filter for all of the reference stars are combined, the mean zeropoint value yields a stable light curve for V392 Per. This illustrates why a relatively large number of reference stars were used to calibrate the nova photometry.

In order to reduce the total error on the nova magnitude $\sigma_{\rm nova}$, an additional stage was added to the photometry process. For a given aperture, any reference star with a zeropoint that varied by more than 3σ from the mean zeropoint was removed, and the new mean zeropoint calculated. Reference stars satisfying Equation 3.14 at each stage were retained.

$$\bar{\rm Z} - 3\sigma_Z \leq \ Z \ \leq \bar{\rm Z} + 3\sigma_Z \tag{3.14}$$

This process was carried out three times in total for each aperture, improving the zeropoint used to calibrate the nova photometry.

3.5 Light Curves

All photometry of the V392 Per CN eruption and post-nova phase is presented in Figures 3.3 – 3.6, with the details recorded in Table A.3. The bottom panel of Figure 3.6 shows the de-reddened colour evolution of the nova eruption. Details of all fits to the light curves in Figures 3.3 – 3.6 are given in Table 3.3. The process used to determine the time of eruption and fit the light curves is described in Sections 3.7 and 3.9.

The light curves show an apparent periodic modulation around the fitted power laws, that is particularly noticeable in the post-nova phase of the light curve, when the brightness has reached a long-lasting plateau. In order to check that this signified

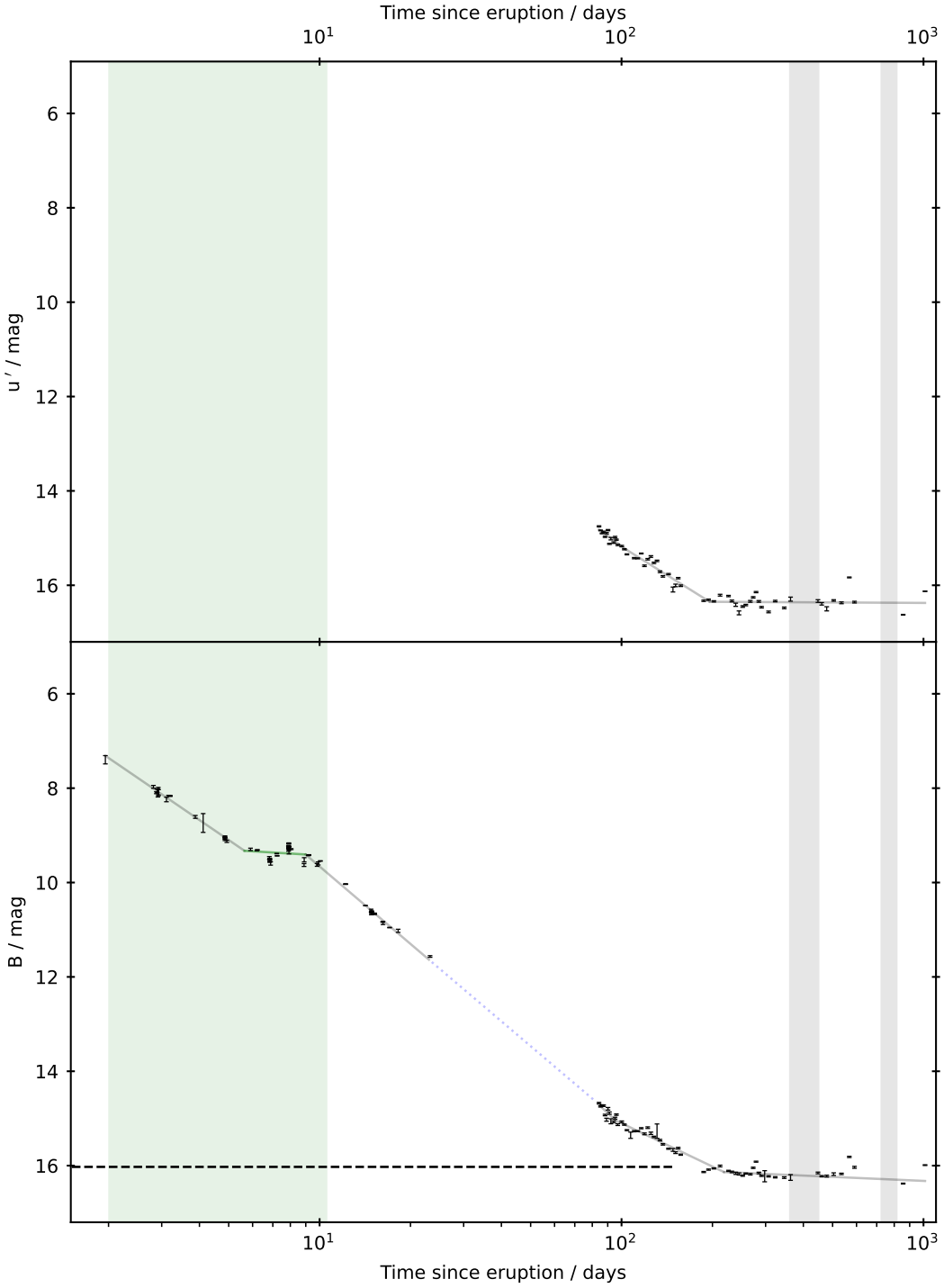

Figure 3.3: u' and B light curves of the nova eruption of V392 Per from LT, LCOGT, AAVSO, and *Swift* observations. Grey regions indicate the *Swift* Sun constraints, and the green region demarks the epoch of γ-ray detection by *Fermi*-LAT. Broken power laws have been fitted to each light curve (see Section 3.9). The horizontal dashed line indicates photometry of a nearby (9″ away) star in the field. Modified from Figure 1 in Murphy-Glaysher et al. (2022) ['V392 Persei: A γ-ray bright nova eruption from a known dwarf nova', Murphy-Glaysher et al., Mon. Not. R. Astron. Soc., 514, 6183, 2022 DOI `https://doi.org/10.1093/mnras/stac1577`].

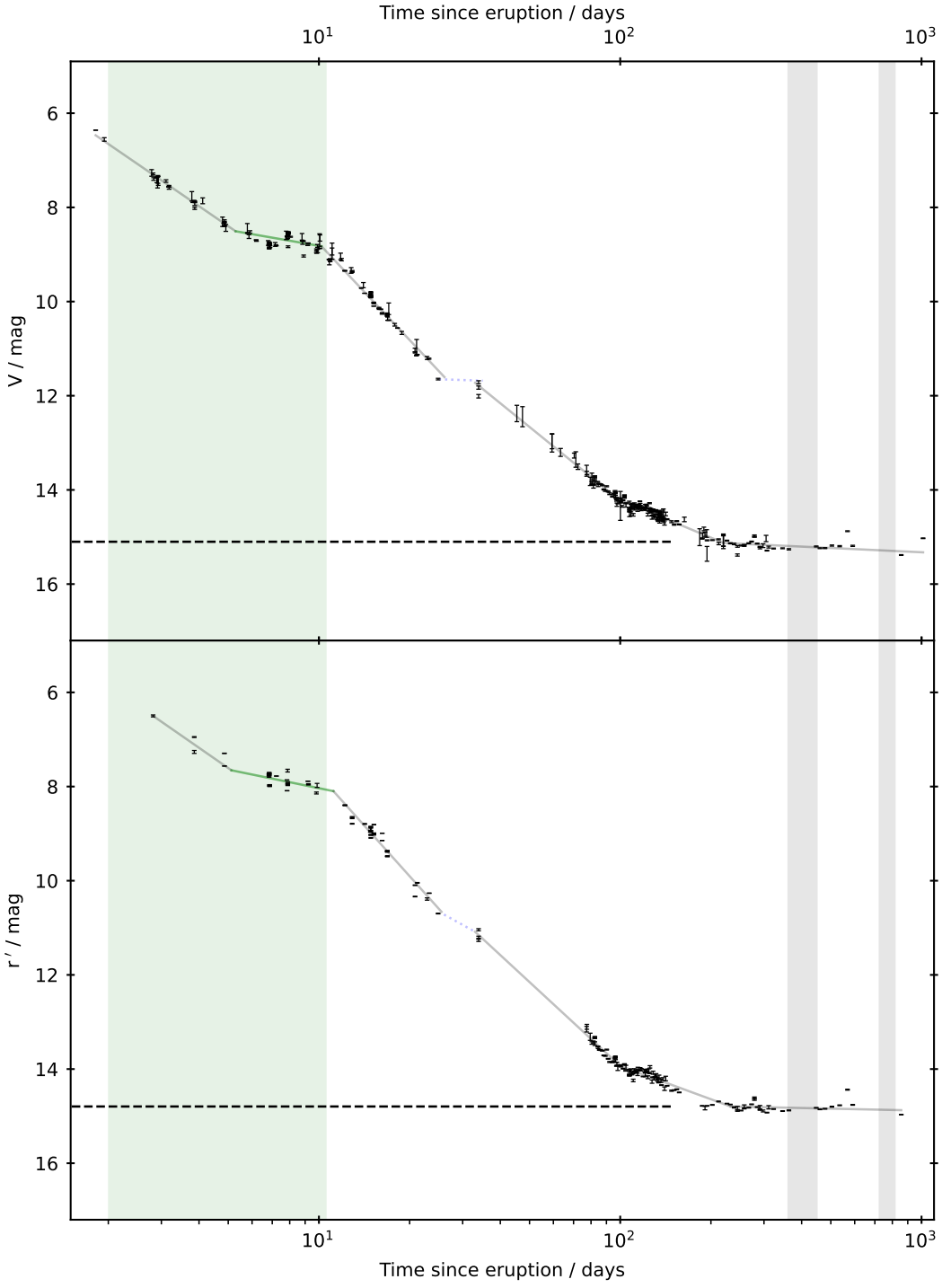

Figure 3.4: As in Figure 3.3, but showing V and r' light curves. Modified from Figure 1 in Murphy-Glaysher et al. (2022) ['V392 Persei: A γ-ray bright nova eruption from a known dwarf nova', Murphy-Glaysher et al., Mon. Not. R. Astron. Soc., 514, 6183, 2022 DOI `https://doi.org/10.1093/mnras/stac1577`].

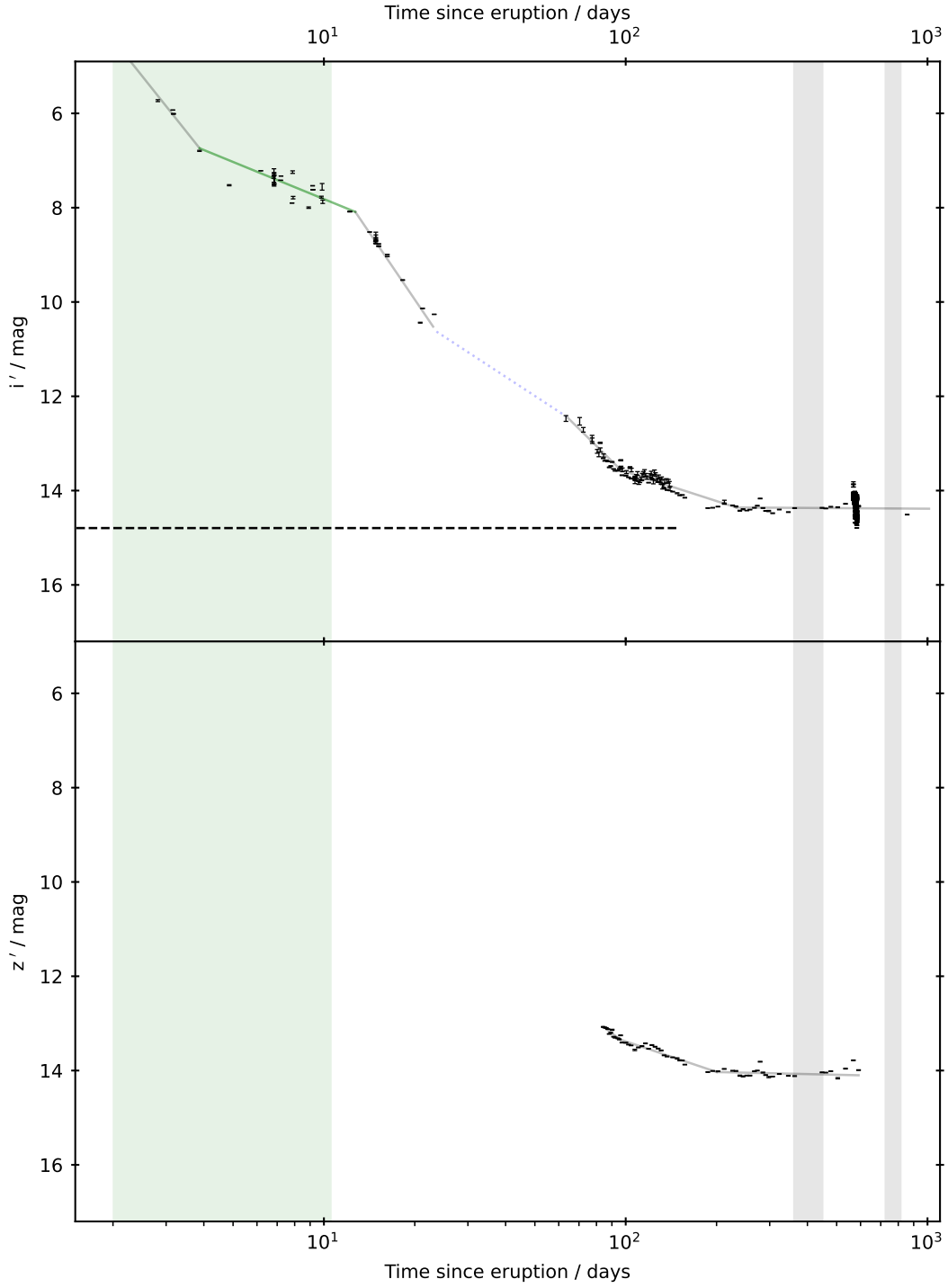

Figure 3.5: As in Figure 3.3, but showing i' and z' light curves. Modified from Figure 1 in Murphy-Glaysher et al. (2022) ['V392 Persei: A γ-ray bright nova eruption from a known dwarf nova', Murphy-Glaysher et al., Mon. Not. R. Astron. Soc., 514, 6183, 2022 DOI `https://doi.org/10.1093/mnras/stac1577`].

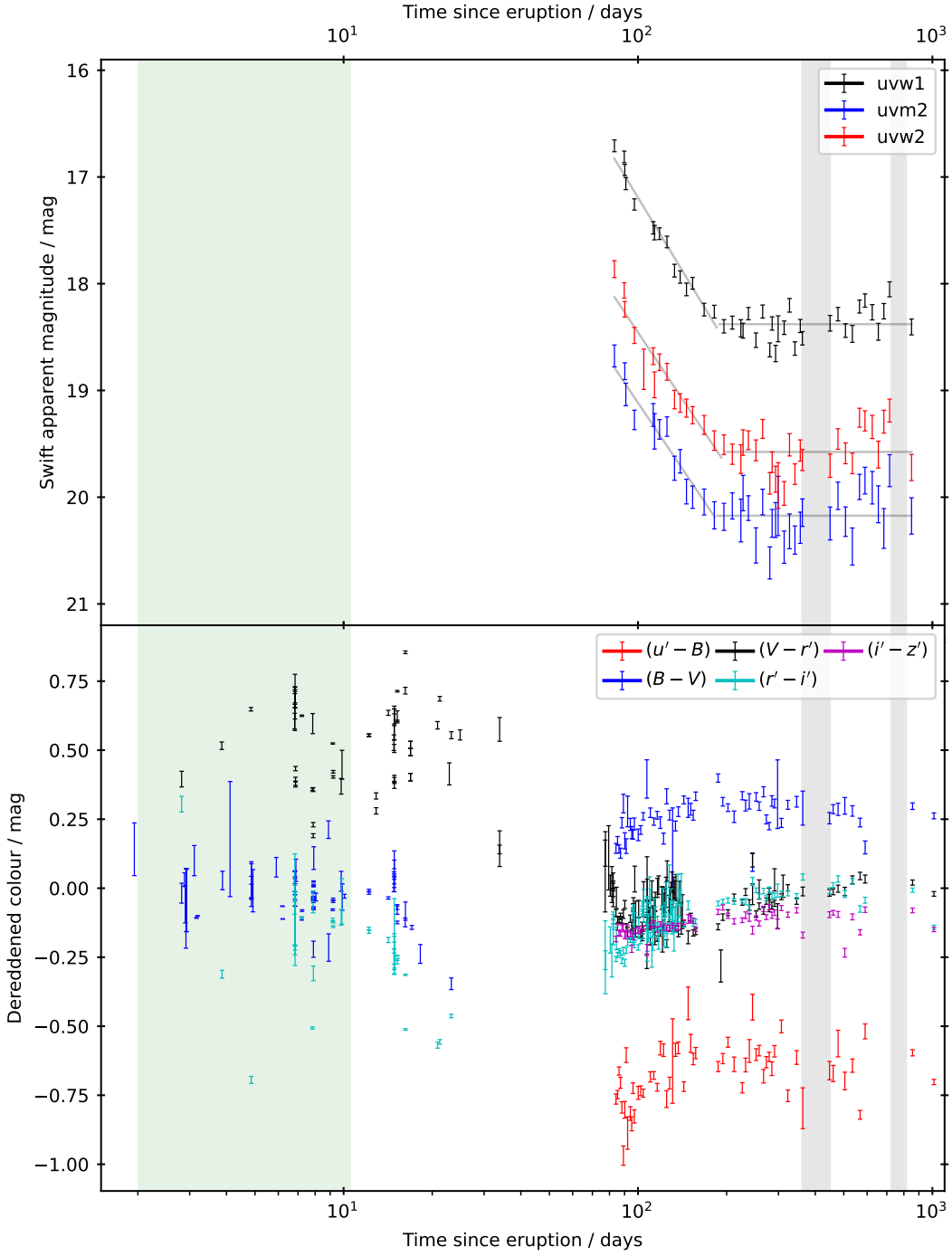

Figure 3.6: As in Figure 3.3, but showing *Swift* uvw1, uvm2, and uvw2 light curves, and the dereddened colour evolution using $E(B-V) = 0.7$ mag. Modified from Figure 1 in Murphy-Glaysher et al. (2022) ['V392 Persei: A γ-ray bright nova eruption from a known dwarf nova', Murphy-Glaysher et al., Mon. Not. R. Astron. Soc., 514, 6183, 2022 DOI `https://doi.org/10.1093/mnras/stac1577`].

Table 3.3: V392 Per light curve parameters, under the assumption that each can be modelled by up to six broken power laws of form $f \propto t^{\alpha}$, where $t_{\rm i}$ and $t_{\rm f}$ denote the initial and final extent of each power law, respectively, and D is the duration of each power law's dominance. Appears as Table A5 in Murphy-Glaysher et al. (2022) ['V392 Persei: A γ-ray bright nova eruption from a known dwarf nova', Murphy-Glaysher et al., Mon. Not. R. Astron. Soc., 514, 6183, 2022 DOI `https://doi.org/10.1093/mnras/stac1577`].

w2	α	$t_{\rm i}$ [d]	$t_{\rm f}$ [d]	D [d]	m2	α	$t_{\rm i}$ [d]	$t_{\rm f}$ [d]	D [d]
5	-1.66 ± 0.14	70.0	186.4	116.4	5	-1.64 ± 0.11	70.0	181.0	111.0
6	0	186.4	849.4	663.1	6	0	181.0	849.4	668.4
w1	α	$t_{\rm i}$ [d]	$t_{\rm f}$ [d]	D [d]	u'	α	$t_{\rm i}$ [d]	$t_{\rm f}$ [d]	D [d]
4	...	-	...	-	4	-1.93 ± 0.42	70.0	103.5	33.5
5	-1.82 ± 0.09	70.0	182.2	112.2	5	-1.60 ± 0.10	103.5	195.9	92.3
6	0	182.2	849.4	667.2	6	-0.01 ± 0.09	195.9	1011.9	816.0
B	α	$t_{\rm i}$ [d]	$t_{\rm f}$ [d]	D [d]	V	α	$t_{\rm i}$ [d]	$t_{\rm f}$ [d]	D [d]
1	-1.75 ± 0.04	0.0	5.6	5.6	1	-1.76 ± 0.07	0.0	5.3	5.3
2	-0.15 ± 0.18	5.6	9.0	3.3	2	-0.45 ± 0.09	5.3	10.2	4.9
3	-2.18 ± 0.08	9.0	58.2	49.2	3	-2.72 ± 0.05	10.2	14.6	4.4
4	-2.42 ± 0.53	70.0	95.3	25.3	4	-2.08 ± 0.04	14.6	98.5	84.0
5	-1.22 ± 0.07	95.3	218.4	123.2	5	-1.07 ± 0.05	98.5	220.4	121.8
6	-0.11 ± 0.10	218.4	1011.9	793.5	6	-0.12 ± 0.05	220.4	1011.9	791.5
r'	α	$t_{\rm i}$ [d]	$t_{\rm f}$ [d]	D [d]	i'	α	$t_{\rm i}$ [d]	$t_{\rm f}$ [d]	D [d]
1	-1.78 ± 0.80	0.0	5.1	5.1	1	-3.22 ± 0.37	0.0	3.9	3.9
2	-0.52 ± 0.18	5.1	11.2	6.1	2	-1.05 ± 0.27	3.9	12.7	8.8
3	-2.86 ± 0.12	11.2	24.9	13.7	3	-3.78 ± 0.18	12.7	23.2	10.5
4	-2.37 ± 0.05	33.9	100.1	66.2	4	-2.52 ± 0.20	63.4	96.5	33.1
5	-0.94 ± 0.09	100.1	232.5	132.4	5	-0.83 ± 0.10	96.5	232.6	136.1
6	-0.06 ± 0.04	232.5	1011.9	779.4	6	-0.017 ± 0.04	232.6	1011.9	779.3
z'	α	$t_{\rm i}$ [d]	$t_{\rm f}$ [d]	D [d]					
4	-1.92 ± 0.27	70.0	96.0	26.0					
5	-0.86 ± 0.06	96.0	200.5	104.5					
6	-0.06 ± 0.08	200.5	1011.9	811.5					

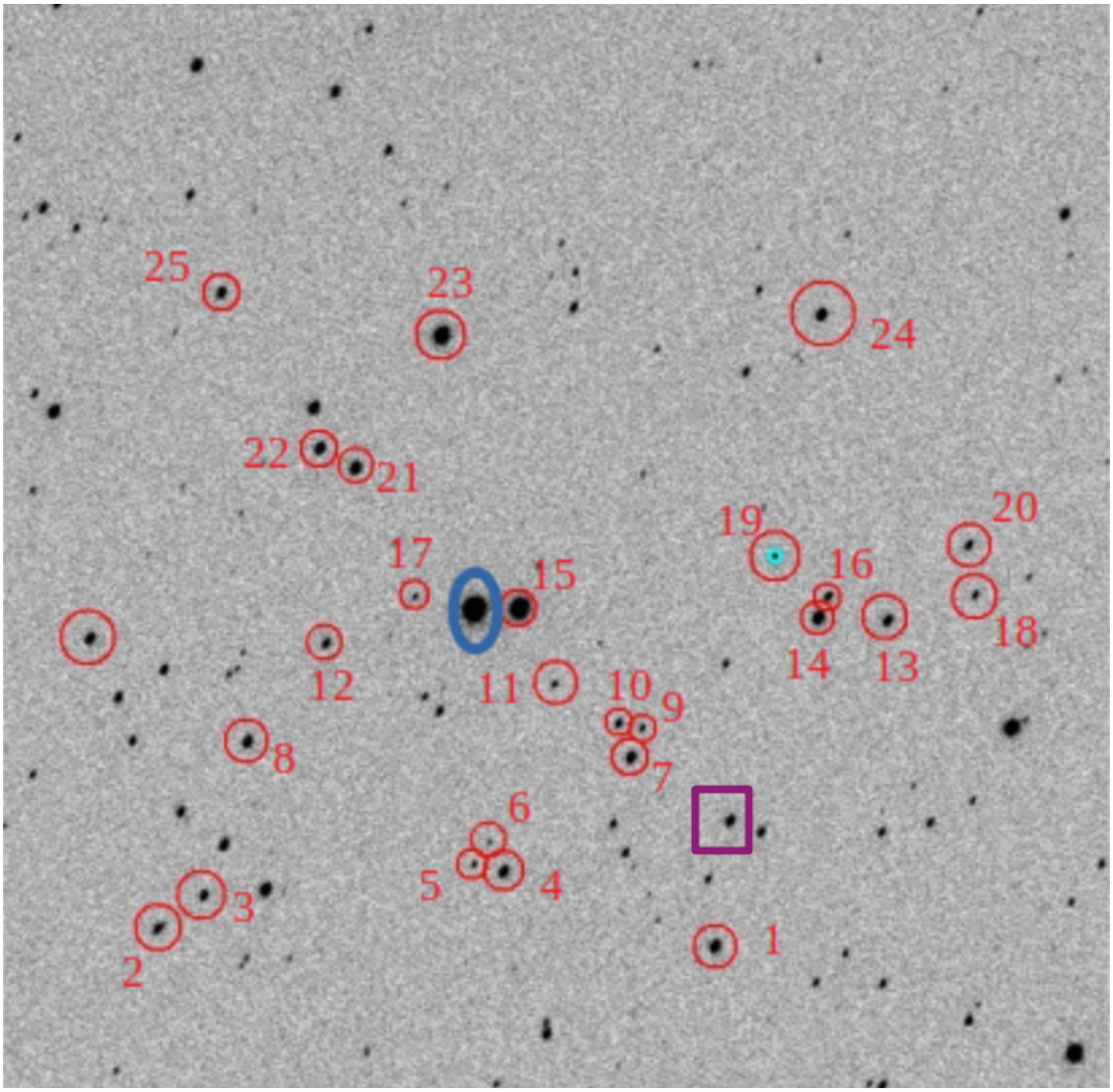

Figure 3.7: The position of the comparison star, indicated by the purple square, relative to V392 Per, with the reference stars labelled.

a real variation in the nova light curve, I adapted my photometry code to measure the brightness of a comparison star. The comparison star was chosen to be a star in the field that was not used as a reference star, as indicated by the purple square in Figure 3.7. Figures 3.8–3.10 compare the $BVr'i'z'$ photometry of this comparison star with that of V392 Per, showing that the comparison star has a flat light curve. Therefore, the variation in the nova light curve is real.

Additional rapid i'-band photometry was obtained of V392 Per, where multiple

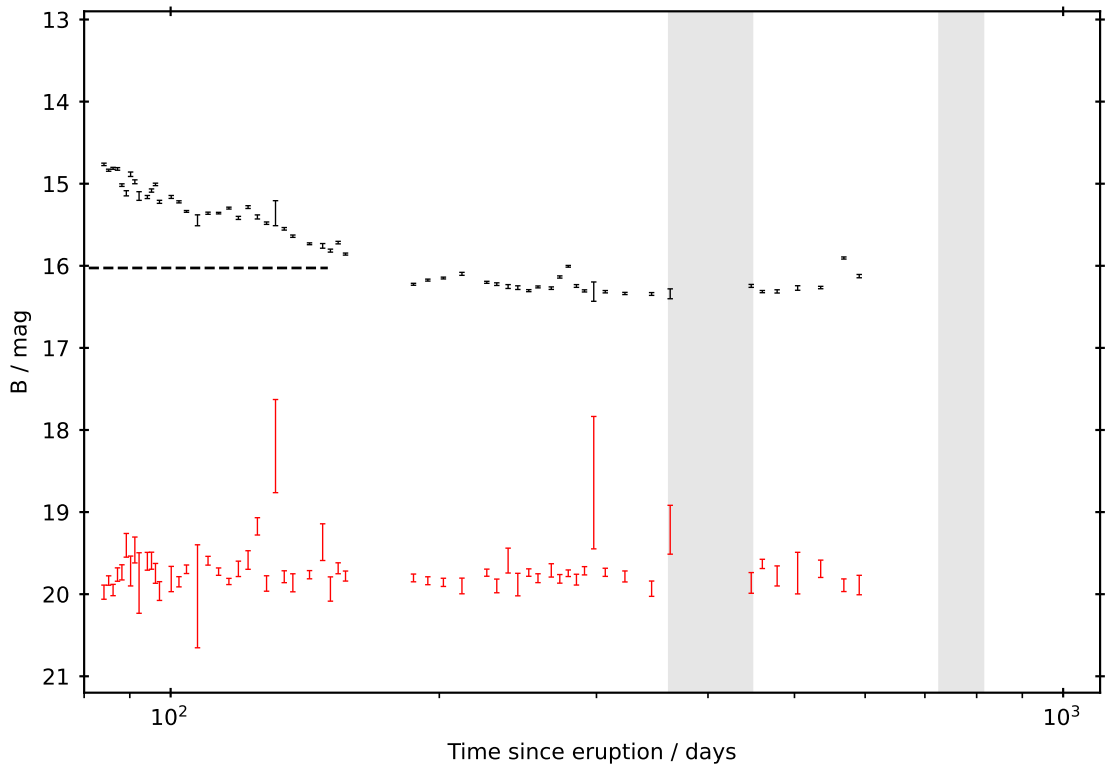

Figure 3.8: Photometry of nova (shown in black) vs comparison star (in red) in B

observations per night were carried out. Photometry was performed on individual images, with no stacking, to maximise the time resolution. Figure 3.11 contains the light curves of V392 Per and the companion star using the LT (in black and red, respectively) and the LCOGT (in blue and magenta, respectively). The light curves of the companion star in this figure clearly illustrate that photometry is consistent between the two telescopes, as expected. Analysis of the periodic modulation of the nova light curve is presented in Section 3.11.

3.6 Sun constraints

Observation of V392 Per was heavily impacted by on-sky proximity to the Sun at the time of its eruption. Our early ground-based observations focussed on spectroscopic

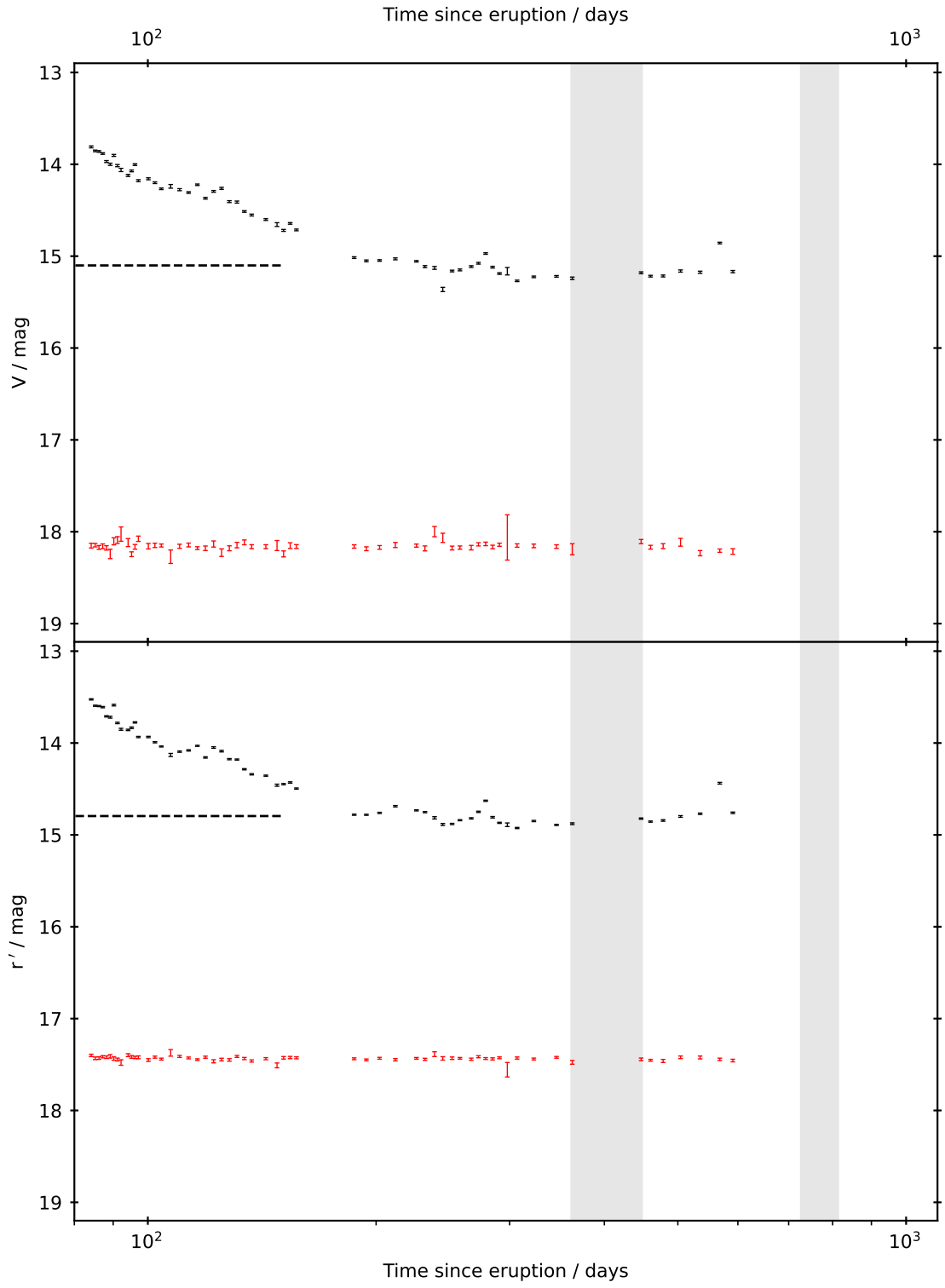

Figure 3.9: Comparison between photometry of nova (shown in black) and comparison star (in red) in V and r'.

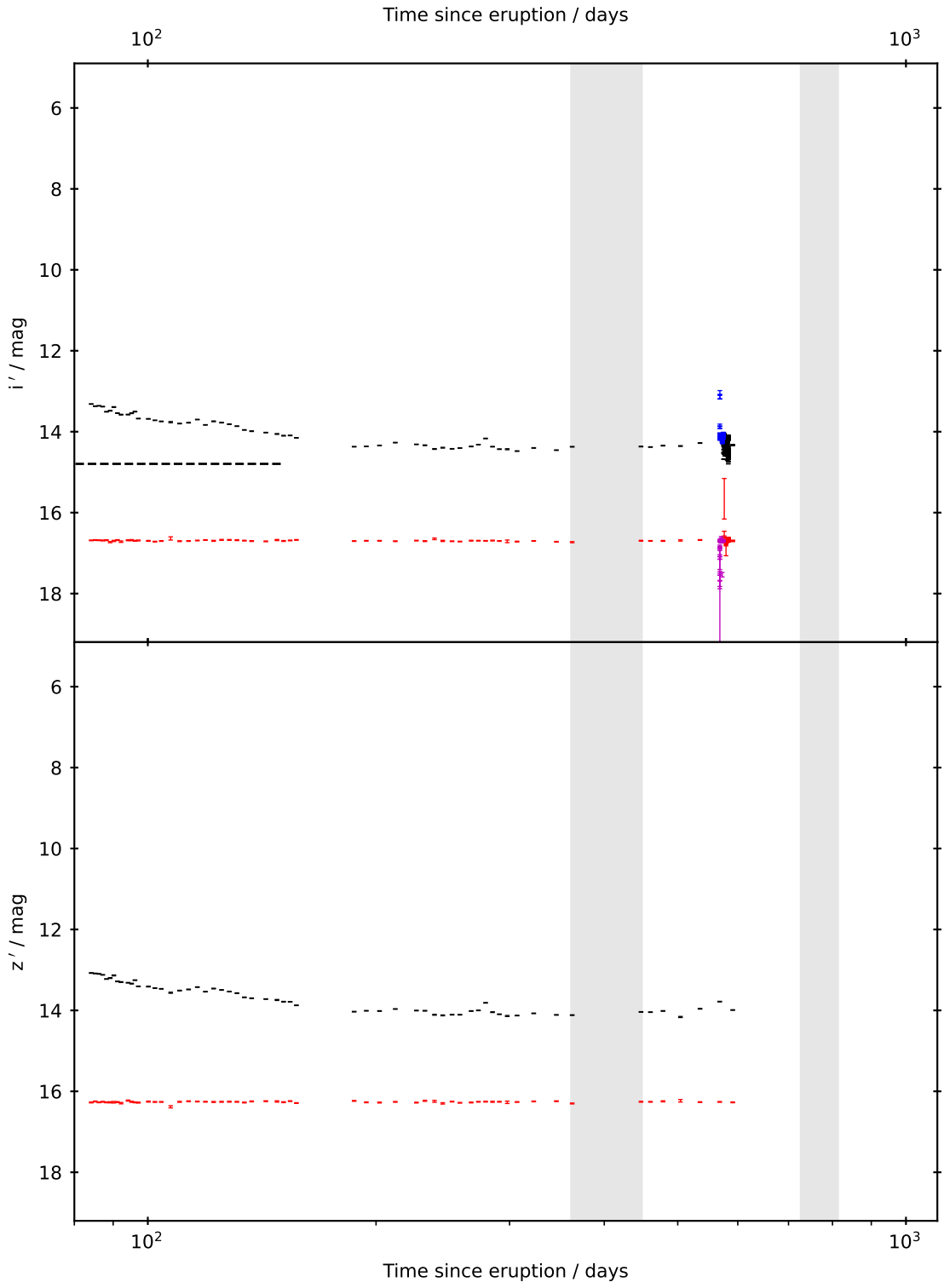

Figure 3.10: Comparison between photometry of nova and comparison star in i' and z'. LT photometry of V392 Per and the comparison star are shown in black and red, respectively. LCOGT photometry of V392 Per and the comparison star are shown in blue and magenta, respectively. A zoomed-in version of the i' photometry, focussing on the period of rapid photometric observation, is shown in Figure 3.11.

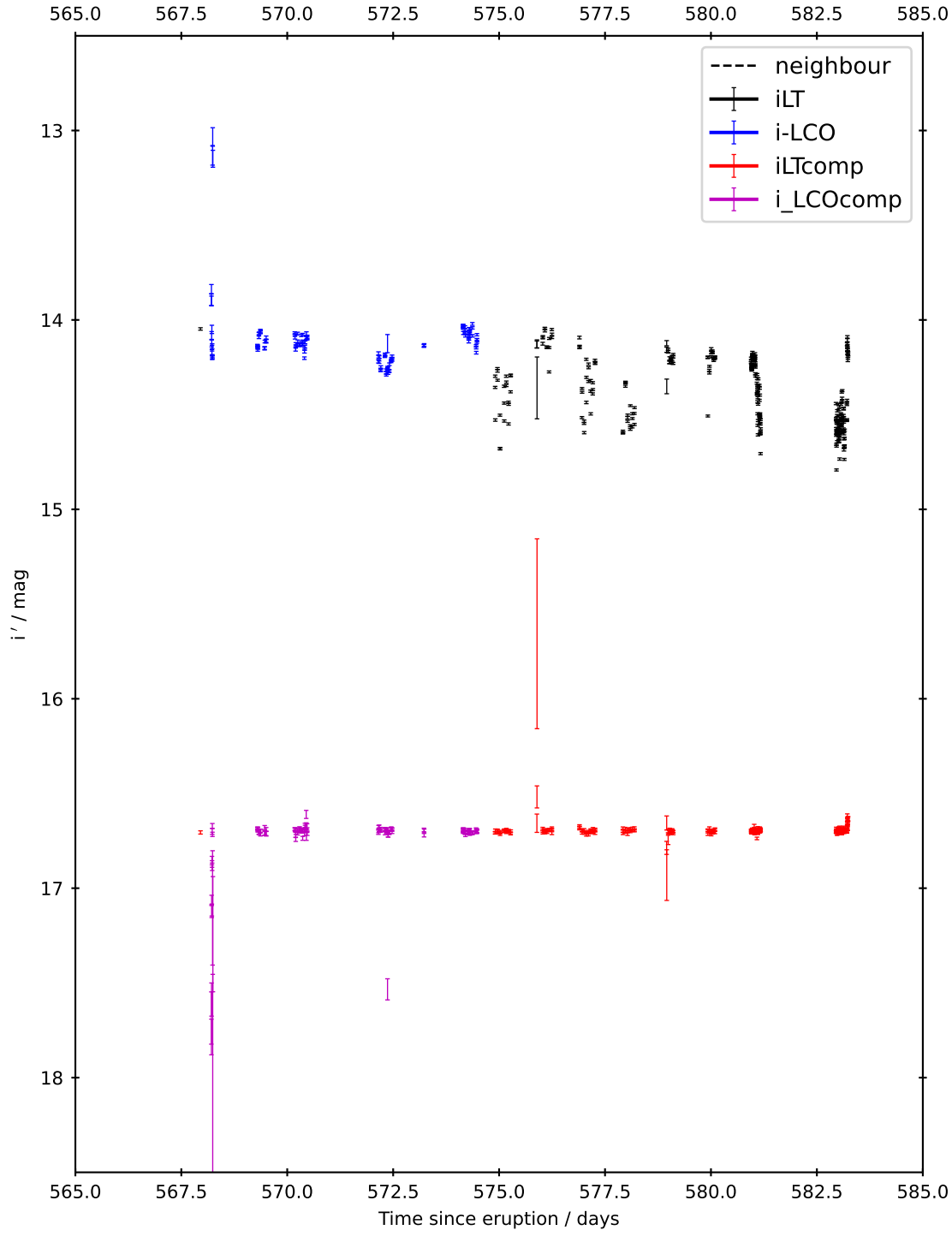

Figure 3.11: Comparison between rapid photometry of nova and comparison star in i'. LT photometry of V392 Per and the comparison star are shown in black and red, respectively. LCOGT photometry of V392 Per and the comparison star are shown in blue and magenta, respectively.

data until the system entered its Sun constraint. *Swift* was constrained more severely than ground-based telescopes, due to the requirement to protect the Observatory from the Sun. The *Swift* Sun constraints covered the periods from discovery up to 2018 Jul 18; 2019 Apr 25 to Jul 20; and 2020 Apr 24 to Jul 19. The *Swift* constraints are shown by the vertical shaded regions in Figures 3.3 – 3.6.

3.7 Time of eruption

The eruption of V392 Per was discovered on 2018 April 29 by Yuji Nakamura in Kameyama (Wagner et al., 2018); who also collected the last pre-eruption observation on April 21.4627[1], 8.01 days earlier.

3.7.1 Assuming maximum light at time of discovery

The brightest observation of V392 Per was the discovery observation, and one could assume that this coincides with onset of the eruption (T_0), or with maximum light ($T_{\rm max}$). Thus, we used the V-band light curve (see top panel of Figure 3.4) to estimate t_2 and t_3 (the time to decline from peak by two and three magnitudes, respectively), and the rise time Δt_0 (using Equation 3.15, which is Equation 16 from Hachisu & Kato, 2006).

$$t_3 = 1.69 t_2 + 0.69 \Delta t_0 \tag{3.15}$$

The onset of the nova eruption was initially assumed to occur at the midpoint between the last pre-eruption observation and the discovery observation, and the MJD corresponding to this time was set to T_0. All observation times were expressed

[1] `http://www.cbat.eps.harvard.edu/unconf/followups/J04432130+4721280.html`

as the time in days since this assumed onset.

Using observation times calculated from this initial assumption, regression analysis was applied to fit broken power laws to the V-band light curve. The gradients and intercepts of the fitted power laws were used to calculate the intersection coordinates of the two fits, to identify the time period where each fit was valid. So if the first and second fits were represented by $y = m_1x + c_1$ and $y = m_2x + c_2$, respectively, then Equation 3.16 was used to find x and y.

$$y = m_1 \frac{c_2 - c_1}{m_1 - m_2} + c_1 \tag{3.16}$$

Equation 3.17 expresses the time in days between the onset of eruption and the nova reaching maximum light at $T_{\max}$ (corresponding to the discovery observation of the nova).

$$t_{\text{peak}} = \mathrm{T}_{\max} - T_0 \tag{3.17}$$

I used the first fit to the light curve to calculate the magnitude at the time of discovery, which was defined to be m_{peak}. Therefore, when the light curve had declined by 2 and 3 magnitudes respectively, the brightness was given by Equation 3.18.

$$\begin{aligned} m_{\text{peak+2}} &= m_{\text{peak}} + 2\,\text{mag} \\ m_{\text{peak+3}} &= m_{\text{peak}} + 3\,\text{mag} \end{aligned} \tag{3.18}$$

The fits to the light curve were used to calculate the times at which the nova reached these magnitudes, $t_{\text{peak+2}}$ and $t_{\text{peak+3}}$. The time of the peak, t_{peak}, was then subtracted to find the t_2 and t_3 times, as shown in Equation 3.19.

$$\begin{aligned} t_3 &= t_{\text{peak+3}} - t_{\text{peak}} \\ t_2 &= t_{\text{peak+2}} - t_{\text{peak}} \end{aligned} \tag{3.19}$$

Table 3.4: Key parameters of the V392 Per eruption. Appears as Table 1 in Murphy-Glaysher et al. (2022) ['V392 Persei: A γ-ray bright nova eruption from a known dwarf nova', Murphy-Glaysher et al., Mon. Not. R. Astron. Soc., 514, 6183, 2022 DOI `https://doi.org/10.1093/mnras/stac1577`].

Methodology:	Discovery at $T_{\max}$	Plateau at t_3
Discovery (MJD)	58237.474	
Eruption: T_0 (MJD)	58233^{+3}_{-2}	58236.0 ± 0.2
Maximum light: $T_{\max}$ (MJD)	58237.474	58237.1 ± 0.3
Rise time: Δt_0 / days	4^{+2}_{-3}	1.1 ± 0.2
t_2 / days	3.1 ± 0.2	2.0 ± 0.1
t_3 / days	8^{+1}_{-2}	4.2 ± 0.3
Plateau onset / days	12 ± 1	$5.2^{+0.9}_{-1.1}$
Plateau duration / days	3 ± 2	5 ± 1
$m_{V,\max}$ / mag	$5.92^{-0.04}_{+0.3}$	5.51 ∓ 0.09
$E\,(B-V)$ / mag	$0.70^{+0.03}_{-0.02}$	
$M_{V,Gaia}$ / mag	$-9.0^{-0.6}_{+0.4}$	$-9.4^{-0.4}_{+0.3}$
$M_{V,\mathrm{MMRD}}$ / mag	-8.5 ∓ 0.2	-8.8 ∓ 0.2
d_{Gaia} / kpc	$3.5^{+0.6}_{-0.5}$	
d_{MMRD} / kpc	2.7 ± 0.5	2.7 ± 0.3

Then Equation 3.15 was used to calculate the rise time, Δt_0, which was then used to find the new estimate for the time of onset of the eruption, $T_{0,\mathrm{new}}$. The process was then repeated until the eruption parameters (T_0, Δt_0, t_2, t_3, and $T_{\max}$) were constant to at least 3 decimal places.

A Monte Carlo analysis was performed to constrain the uncertainties on the parameters, using the uncertainties on the gradients and intercepts from the fits. Eruption parameters computed via this approach are recorded in the second column of Table 3.4. The first and final attempts at fitting the light curve under the assumption that maximum brightness coincided with the time of discovery are shown in Figure 3.12.

However, the light curve follows the P-class morphology (Strope, Schaefer & Henden, 2010), exhibiting a pseudo-plateau in the early evolution (see Figure 3.4), where the otherwise smooth, steep decline has a relatively flat interval, typically 3–

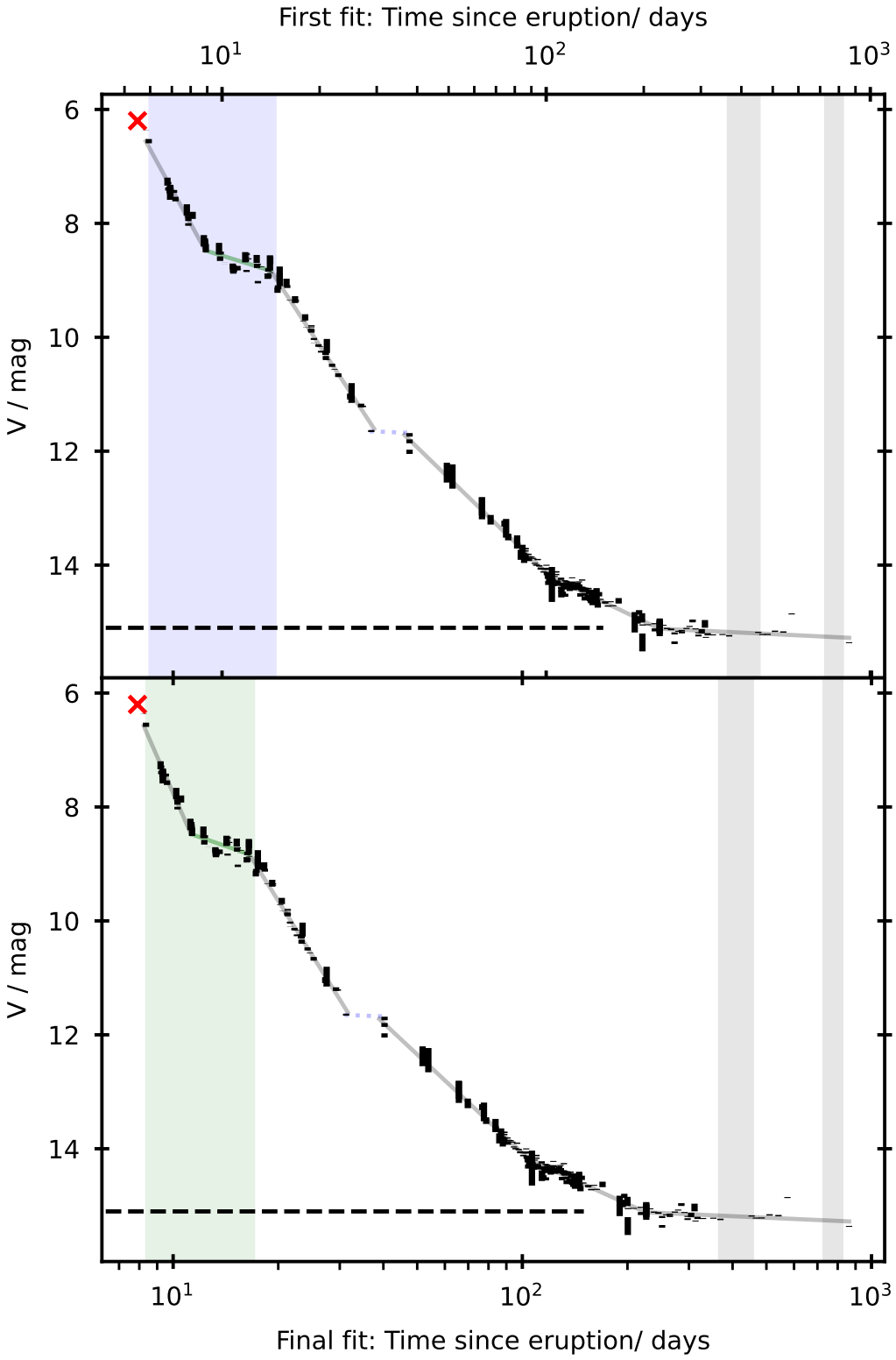

Figure 3.12: Comparison between first (top) and final (bottom) fits, assuming the maximum brightness coincided with the time of discovery. Note that T_0 differs between the two fits, so the zeroes on the time axes are not aligned.

6 mag below peak, followed by another steep decline. If we assume that $T_{\max}$ coincides with the earliest V-band observation ($V = 6.36$ mag), then plateau onset occurs after a decline of only 2.1 mag. Thus t_3 occurs during the plateau, interrupting the smooth decline, which leads to a relatively long rise time estimate ($\Delta t_0 = 4^{+2}_{-3}$ days) for such a rapidly evolving eruption. Here, poor constraint of the eruption time leads to large uncertainties on all light curve derived parameters.

3.7.2 Assuming plateau coincides with t_3

As an alternative, we assumed that plateau onset coincides with t_3. In the Strope et al. (2010) sample of 19 P-class novae, only V4021 Sgr entered a plateau earlier (2.4 mag below peak; it also had the slowest decline of the sample). Fixing plateau onset at t_3 provides a conservative estimate of the time of maximum: if the plateau onset occurs later there would have been an earlier and brighter peak. The light curve evolution of V392 Per is well described by a series of broken power-laws (see Figures 3.3–3.6), whose indices depend upon the assumed T_0. Hence, an iterative approach was used to fit the light curves (see Section 3.9) to determine $T_{\max}$ such that the plateau began at t_3. This leads to independent estimates of T_0, Δt_0, t_2, t_3, and $T_{\max} = 0.3 \pm 0.3$ days pre-discovery (see third column of Table 3.4).

As in Section 3.7.1, an initial assumption was made for the time of onset of the nova eruption, with the MJD at this time set as T_0. All observation times were expressed as the number of days since this assumed onset.

Using observation times calculated from this initial assumption, regression analysis was applied to fit broken power-laws to the V-band light curve. I found the intersection coordinates of the fit to the plateau and the fit to the initial decline of the light curve. By definition of the model applied, this intersection corresponded to the decline from

peak brightness by 3 magnitudes. I calculated the brightness, $m_{\mathrm{plat,onset}}$, and the time since the start of the eruption, $t_{\mathrm{plat,onset}}$.

I found the brightness at peak, m_{peak}, and when the nova had dimmed by two magnitudes from peak, $m_{\mathrm{peak+2}}$, using Equation 3.20.

$$\begin{aligned} m_{\mathrm{peak}} &= m_{\mathrm{plat,onset}} - 3\,\mathrm{mag} \\ m_{\mathrm{peak+2}} &= m_{\mathrm{plat,onset}} - 1\,\mathrm{mag} \end{aligned} \tag{3.20}$$

I used the fit to the initial decline to determine the time of peak brightness, t_{peak} (in days since the eruption), and the time when the nova had dimmed by two magnitudes, $t_{\mathrm{peak+2}}$. Using Equation 3.21 to calculate t_2 and t_3, I then determined the rise time $\Delta\, t_0$ using Equation 3.15.

$$\begin{aligned} t_3 &= t_{\mathrm{plat,onset}} - t_{\mathrm{peak}} \\ t_2 &= t_{\mathrm{peak+2}} - t_{\mathrm{peak}} \end{aligned} \tag{3.21}$$

The rise time was subtracted from T_{max} to find the new onset of eruption $T_{0,\mathrm{new}}$.

The observation times were recalculated using the new value of T_0, and the process was repeated until the values of T_0, t_2, and t_3 were consistent to at least 3 decimal places. As in Section 3.7.1, a Monte Carlo analysis was performed to constrain the uncertainties on the parameters, using the uncertainties on the fits. Eruption parameters computed via this approach are recorded in the third column of Table 3.4. Figure 3.13 compares the first and final fits to the light curves, under the assumption that the onset of the first plateau coincides with the decline by 3 magnitudes from peak brightness.

Regardless of the method employed, $t_2 < 4\,\mathrm{days}$: a very fast eruption (Payne-Gaposchkin, 1964), and V392 Per is one of the fastest evolving novae yet discovered.

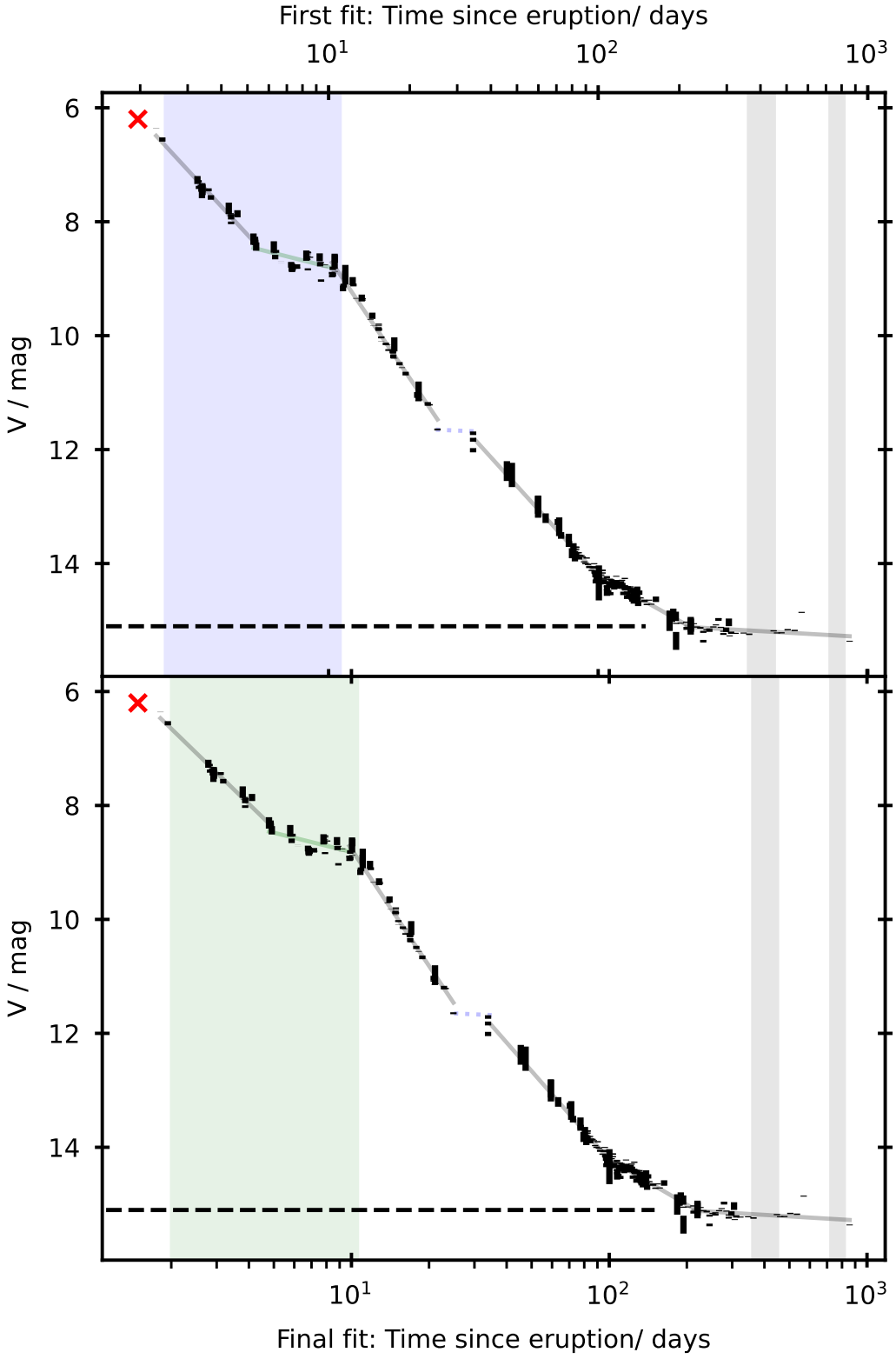

Figure 3.13: Comparison between first (top) and final (bottom) fits assuming the onset of the early plateau coincided with the decline by 3 mag from peak. Note that T_0 differs between the two fits, so the zeroes on the time axes are not aligned.

Based on the likelihood that maximum light was missed, the rapid evolution of the light curve, the γ-ray detection, and behaviour of similar P-class novae, we adopt the estimates determined by assuming the plateau onset coincides with t_3 throughout.

3.8 Distance, Extinction, and Astrometry

Stoyanov et al. (2020) measured radial velocities of diffuse interstellar bands and interstellar K I in their V392 Per spectra from 2018 May 1–2, deriving $E(B-V) = 1.2 \pm 0.1$. Munari et al. (2020a) compared the $(B-V)$ colour of V392 Per shortly after peak with the expected intrinsic colour at maximum to derive $E(B-V) = 0.72 \pm 0.06$. The Stoyanov et al. (2020) measurement was very early post-eruption and the ejecta may have added to the extinction column.

The equivalent width of the interstellar sodium doublet absorption line is often used to determine reddening. However, the interstellar Na I-D lines were saturated in our spectra. Stoyanov et al. (2020) also reported saturation of the Na doublet.

The astrometry of V392 Per, as reported by *Gaia* EDR3 (Gaia Collaboration et al., 2016, 2021) is $\alpha = 4^{\rm h}43^{\rm m}21^{\rm s}.369814 \pm 0.04$ mas, $\delta = 47°21'25''.84112 \pm 0.03$ mas (J2000). EDR3 reports a parallax measurement for V392 Per of $\varpi = 0.276 \pm 0.046$ mas. Following Bailer-Jones et al. (2021), this leads to a distance estimate of $d = 3.5^{+0.6}_{-0.5}$ kpc. Utilising the 3D dust maps of Green et al. (2019), we estimate the line of sight reddening toward V392 Per to be $E\,(B-V) = 0.70^{+0.03}_{-0.02}$. This follows the approach used by Darnley & Starrfield (2018)[2], however, both the distance and reddening estimates are smaller due to advances between *Gaia* DR2 and EDR3. This reddening estimate is in agreement with that by Munari et al. (2020a), and we adopt

[2]The parallax reported by Darnley & Starrfield (2018) was actually that of RS Oph, although their reported distance did relate to V392 Per.

$E\,(B-V) = 0.7$ throughout.

As such, and utilising the plateau method (see Section 3.7.2), we estimate a peak absolute magnitude $M_{V,Gaia} = -9.4^{-0.4}_{+0.3}$ mag. This large *Gaia* distance and resulting luminous M_V demonstrate that V392 Per is NOT a "faint-fast" nova, like those commonly seen in M 31 and in M 87 (Kasliwal et al., 2011; Shara et al., 2016). Thus the use of the MMRD, as discussed in Section 1.7, is justified to check on the *Gaia* distance. The 'S-shaped' MMRD for the Milky Way calibrated by Della Valle & Izzo (2020, see their Equation 15) is given by Equation 3.22.

$$M_V = -7.78(\pm 0.22) - 0.81 \times \arctan\left((1.32 - \log t_2)/0.23\right) \tag{3.22}$$

For a nova with $t_2 = 2.0 \pm 0.1$, the equation produces a consistent ($< 2\sigma$) estimate of $M_{V,\mathrm{MMRD}} = -8.8 \mp 0.2$, and an MMRD distance estimate of 2.7 ± 0.3 kpc (within 1.4σ of the *Gaia* distance). Equation 3.23 was used to calculate the distance, where m_V is the observed V-band magnitude, M_V is the absolute magnitude calculated using the MMRD calibration, and d is the distance in parsecs.

$$m_V - M_V = 5 \log d - 5 \tag{3.23}$$

3.9 Photometry and light curve fitting

Figures 3.3–3.6 present the u' and B, V and r', i and z', and *Swift*/UVOT uvw1, uvm2, and uvw2 light curves for V392 Per, respectively. The optical observations are shown with the same scale to aid comparison, and the $BVr'i'$ light curves include observations taken by AAVSO observers (all photometric data before the first Sun constraint: see Table A.4 for observer details). The colour evolution of the nova is also shown in Figure 3.6. The series of high-cadence i'-band photometry collected by

LT and LCOGT is included, and illustrates the high amplitude variations seen (see Section 3.11).

As shown in Figures 3.3–3.6, the optical and near-UV light curves of V392 Per can be broadly replicated by a series of up to six broken power-laws ($f \propto t^{\alpha}$) and a least-squares regression was employed to fit each light curve. For all passbands, T_0 was set to the value determined from fitting the V-band light curve, as described in Section 3.7.2, under the assumption that the onset of the early plateau coincided with the decline from maximum brightness by 3 magnitudes.

Key parameters from the best fits are shown in Table 3.3. In general, the light curve exhibits an initial decline from maximum before entering a quasi-plateau after $\sim$ 5 days. The plateau continues for a further $\sim$ 5 days after which the decline steepens further and the light curve follows three broken power-laws as it approaches an approximately flat luminosity $\sim$ 225 days post-eruption.

The onset, duration, and gradient of the plateau differs between the passbands; with a shallower gradient, later onset and longer duration with decreasing wavelength. Such plateaus have been proposed to be caused by a surviving, or reformed, accretion disk emerging from the optically thick photosphere as it recedes back toward the WD surface (Hachisu & Kato, 2006; Henze et al., 2018). The behaviour here is compatible with a cooler outer disk emerging from the receding photosphere earlier than the inner hotter regions.

There is a potential light curve discontinuity during the first Sun constraint. The B-band light curve is poorly sampled but appears continuous across the gap, but the $Vr'i'$ data point to a change in gradient during that Sun constraint, possibly hinting at a further plateau stage during the gap. Upon exiting the initial Sun constraint, the system had entered the nebular phase, with strong emission from [O III] 4363,

4959, and 5007 Å and He II 4686 Å present (see Sections 4.7–4.9). These emission lines began to appear before the end of the Sun constraint and, due to their strengths, may have driven the changes observed in the B and V light curves.

The power-law indices in the initial decline in the BVr'-bands are $\alpha = -1.75 \pm 0.04$, -1.76 ± 0.07, and -1.78 ± 0.80, respectively. This appears in good agreement with the expected continuum from free-free emission from an optically thin plasma (also see Section 6.1 for discussion about the nature of the early-decline light curve). Other than the initial power-law and the plateau, we do not ascribe any physical meaning to the power-laws. We simply utilise these as a tool to calibrate the optical spectroscopy (see Section 4.1).

The light curves have remained broadly static at the post-nova luminosity since ~ 225 days post-eruption, with $\bar{V} = 15.2 \pm 0.1$ mag. This is substantially brighter than the long-term quiescent minimum of ~ 17 mag, and was referred to by Munari et al. (2020a) as 'sustained post-(eruption) brightening', see Figure 3.14.

3.10 Spectral Energy Distribution

The evolution of the spectral energy distribution (SED) of V392 Per is shown in Figure 3.15. The SEDs are derived from dereddened photometry using LT $u'BVr'i'z'$, and *Swift* uvw2, uvm2 and uvw1 filters. We assumed the *Gaia* EDR3 determined distance of 3.45 kpc and $E(B-V) = 0.7$ mag. All plots include the SED averaged over the post-nova period, $t \geq 223$ days post-eruption.

The shape of the first SED, produced from photometry taken 23 days after eruption, shows that there was a bump in luminosity in the r'-band, which was not present in the quiescent average SED (shown in black in all panels), or any of the

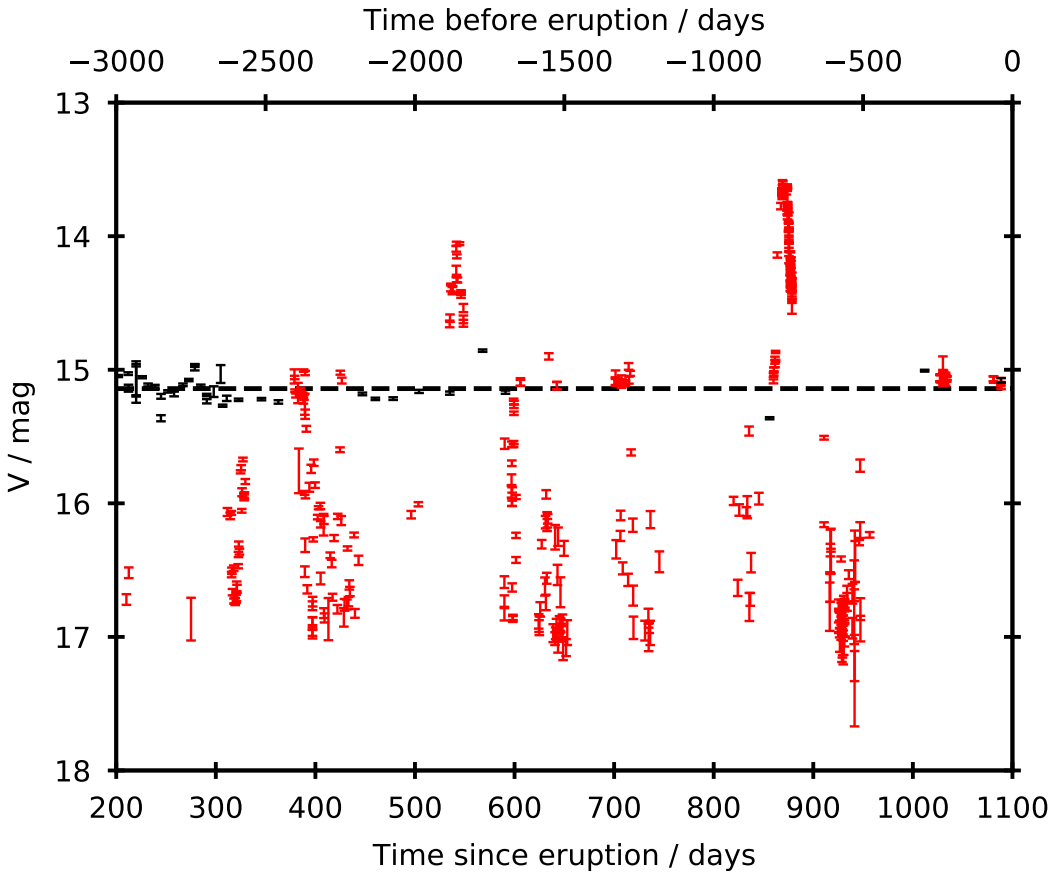

Figure 3.14: Comparison of post-nova (black) and pre-nova (red) V-band brightness of V392 Per. The average post-nova magnitude $\bar{V} = 15.2 \pm 0.1$ mag is shown by the dashed line. The time-scale for the pre-eruption AAVSO data from March 2004 to March 2018, which covers around 3 times the duration of the post-nova observations, is shown by the top time axis. Appears as Figure 2 in Murphy-Glaysher et al. (2022) ['V392 Persei: A γ-ray bright nova eruption from a known dwarf nova', Murphy-Glaysher et al., Mon. Not. R. Astron. Soc., 514, 6183, 2022 DOI `https://doi.org/10.1093/mnras/stac1577`].

others shown in Figure 3.15. The bump was driven by the high Hα line emission (see, e.g., Figures 4.1 and 4.2). By the time V392 Per emerged from its Sun constraint, the $BVr'i'$ luminosity was much lower, and the shape of the SED had changed.

Figure 3.16 shows only the post-Sun-constraint SEDs. Since V392 Per emerged from the first Sun constraint, the SED shape has remained broadly constant, with the overall luminosity fading toward the post-nova average (black line), although the overall SED slope has gradually decreased: the SED has become redder. From day 194 post-eruption, the SED luminosity has remained very close to the average post-nova value. From day 84, the SED shows a persistent V-band bump, which seems to be driven by [O III] 4959+5007 Å emission (see, e.g. Figures 4.2 and 4.3). We propose that the SED from the u'-band and bluer is that of an accretion disk (see Chapter 6).

3.11 Orbital Period

The post-nova light curve of V392 Per shows clear and significant variation, see Figure 3.11 (i'-band) and Figure 3.14. There are three prior published periods for V392 Per, as detailed in Section 3.11.1.

3.11.1 Prior Published Orbital Periods

Schmidt (2020) used Cousins I-band photometry collected over 78 days between 2019 December 22 and 2020 March 9 (effectively the same observing period as Munari et al., 2020a). The data were detrended by subtracting the nightly mean magnitude. Schmidt (2020) performed a discrete Fourier transform and Lomb-Scargle

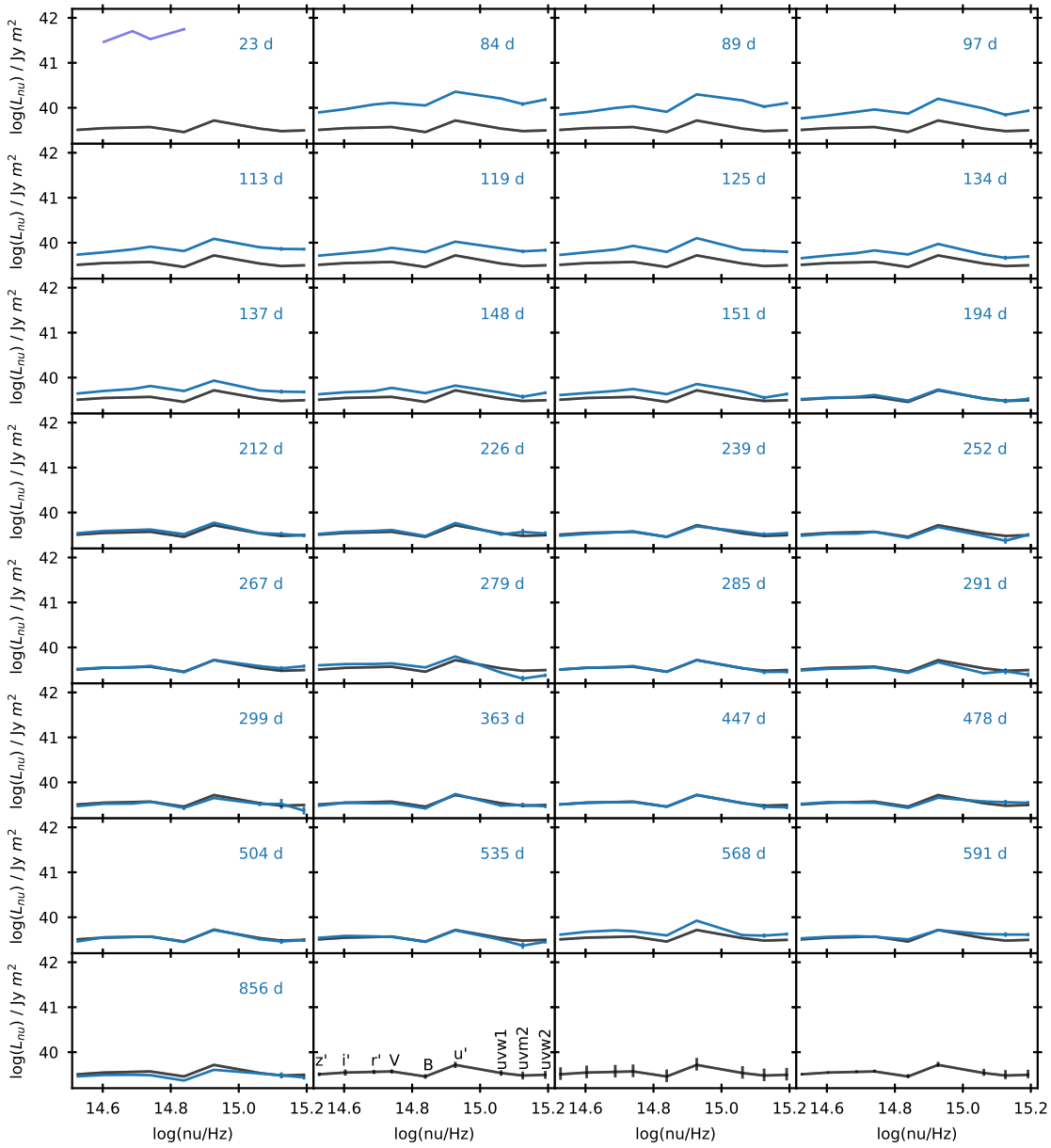

Figure 3.15: Spectral energy distribution evolution for V392 Per based on $d = 3.45^{+0.67}_{-0.46}$ kpc and $E(B-V) = 0.70^{+0.03}_{-0.02}$. The SED from each epoch is plotted in blue, with the average quiescent SED plotted in black. The top left panel shows the SED based on $BVr'i'$ observations 23.2 days after eruption, shortly before V392 Per entered its initial Sun constraint. In the bottom row: the second panel from the left shows the errors on the average quiescent SED, as well as the passbands corresponding to each frequency; the third panel from the left and the right panel show the systematic errors on the average quiescent SED due to the distance estimation and the interstellar extinction, respectively.

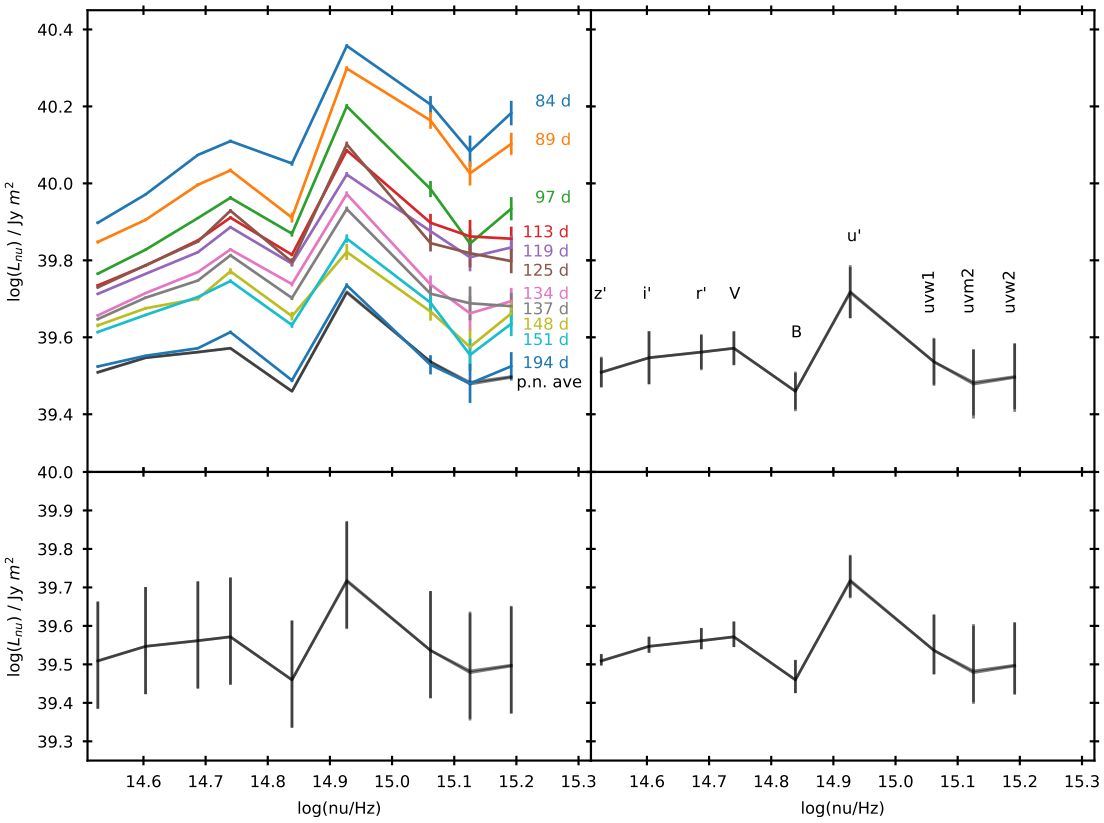

Figure 3.16: Spectral energy distribution (SED) evolution of V392 Per. **Top left**: Evolution between days 84–194, and the average post-nova (p.n. ave) SED, from day 220 and beyond, is shown in black at the bottom. **Top right**: Average post-nova SED, error bars indicate 1σ scattter. **Bottom left**: Distance uncertainty, $d = 3.5^{+0.6}_{-0.5}$ kpc **Bottom right**: Extinction uncertainties, $E\,(B-V) = 0.70^{+0.03}_{-0.02}$. Appears as Figure 3 in Murphy-Glaysher et al. (2022) ['V392 Persei: A γ-ray bright nova eruption from a known dwarf nova', Murphy-Glaysher et al., Mon. Not. R. Astron. Soc., 514, 6183, 2022 DOI `https://doi.org/10.1093/mnras/stac1577`].

periodogram analysis, yielding a period of $P = 0.06600 \pm 0.00002$ days.

The Munari et al. (2020a) period was calculated using ANS Collaboration VRI data taken over 17 nights between 2019 December 30 and 2020 March 11. The Fourier power spectrum of these data revealed two significant, potentially linked peaks, $P = 3.4118$ days and $P = 1.4107$ days (both illustrated in Figure 3.18). Consideration of the pre-nova photometry and derived system parameters led them to favour the longer period. Munari et al. notes that their R and I-band data show similar periodic modulation.

Schaefer (2021) utilised 1150 TESS observations from 2019, with 28725 supplementary AAVSO observations from 2019–2021, and, following cleaning and detrending, employed a Fourier technique and folded light curve fitting to estimate $P = 3.21997 \pm 0.00039$ days, with an amplitude of 0.122 magnitudes. However, the TESS CCD scale ($21''$ pixel^{-1}) would prohibit the disentanglement of signals from V392 Per and the nearby, similar luminosity, field star (standard #15; $9''$ distant). Some AAVSO observers were unable to separate these two sources as the nova faded. Munari, Moretti & Maitan (2020b) find the neighbour star shows no variability; our photometry of this source concurs.

3.11.2 Orbital Period from LT and LCOGT data

We collected 423 high-cadence observations in the i'-band using LT and LCOGT between 2019 November 17 and December 2. These data show variation with amplitude up to ~ 0.7 mag over the course of a night (see Figure 3.17), much greater than reported by Munari et al. or Schaefer.

Figure 3.18 shows the Lomb-Scargle power spectrum for our i'-band observations

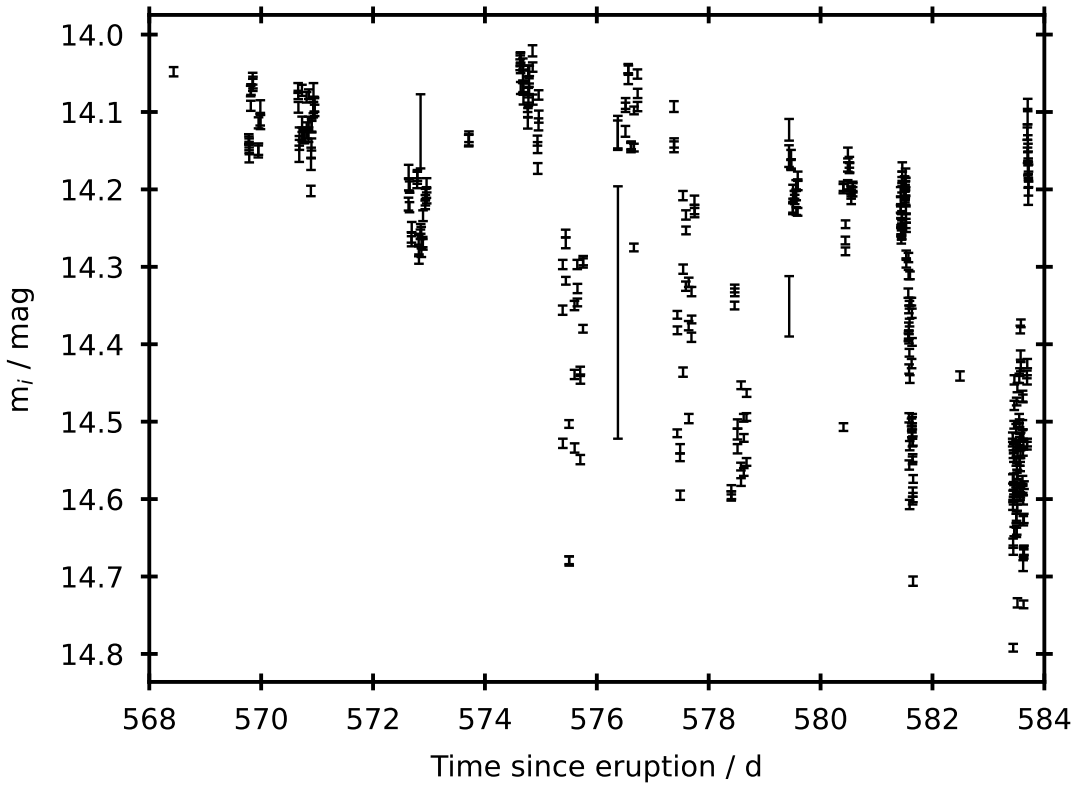

Figure 3.17: Rapid photometry i'-band light curve of V392 Per.

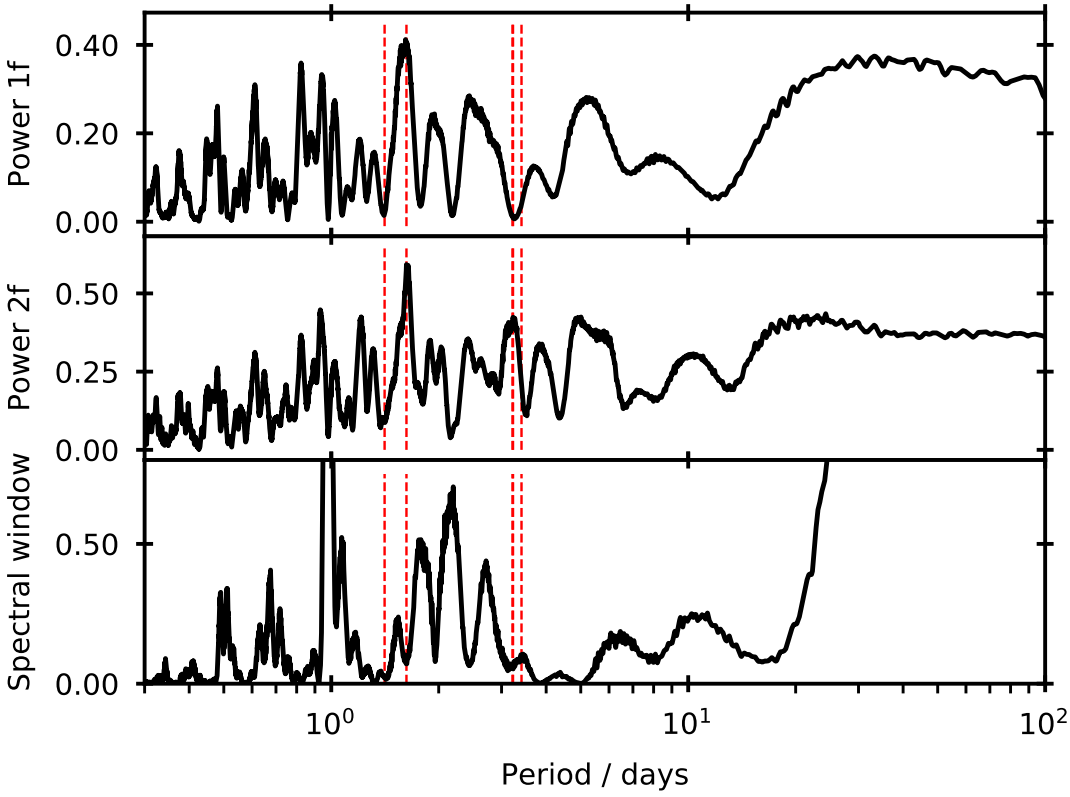

Figure 3.18: **Top panel:** Power spectrum of post-nova i'-band observations using a single Fourier sinusoidal term. **Middle panel:** As top, but utilising two Fourier terms. **Bottom panel:** Window function power spectrum. In all three panels the vertical red dashed lines indicate the reported periods, from left to right: $P = 1.4107$ days (Munari et al., 2020a); $P = 1.62419 \pm 0.00069$ d (this work); $P = 3.21997 \pm 0.00039$ days (Schaefer, 2021); $P = 3.2297 \pm 0.0027$ days (this work; indistinguishable from Schaefer, 2021); and $P = 3.4118$ days (Munari et al., 2020a). Appears as Figure 4 in Murphy-Glaysher et al. (2022) ['V392 Persei: A γ-ray bright nova eruption from a known dwarf nova', Murphy-Glaysher et al., Mon. Not. R. Astron. Soc., 514, 6183, 2022 DOI `https://doi.org/10.1093/mnras/stac1577`].

taken after day 252, during the roughly consistent brightness post-nova phase. The top panel uses a single Fourier sinusoidal term, whereas the middle panel uses two Fourier components. The observations were cleaned to remove any data points that were not statistically significant. Observations from the first night of rapid photometry with LCOGT were anomalous, suffered with poor seeing and as a result a seemingly varying comparison star, so were removed. We also show the associated window function, in the bottom panel. This is the power spectrum corresponding to the timing of the observations only, with all observations set to a constant magnitude and error.

The periods reported by Munari et al. (2020a) and Schaefer (2021) are indicated on the power spectrum. The strongest significant peak is found at $P = 1.62419 \pm 0.00069$ d, when utilising a single (sinusoidal) Fourier term; this is very close to half the Schaefer (2021) value. Adding a second sinusoidal term reveals an additional peak at $P = 3.2297 \pm 0.0027$ days, very close to Schaefer's.

The top panel of Figure 3.19 presents our i'-band data folded around $P = 3.2297$ days. Here, upon visual inspection, there does appear to be a plausible phase-folded light curve that is compatible with a double-dipping CV, i.e., one where dips in the optical light curve are visible due to each binary component passing in front of the other. In a single-dipping CV, by contrast, the WD and accretion disk do not emit significantly in the optical, so we observe a dip in the light curve when the accretion disk and WD obscure optical light from the secondary star, but not when the secondary occults the WD and accretion disk.

The folded light curve in the top panel of Figure 3.19 appears 'noisy', and we suggest that this may be due to different periodic, or other, activity from the system. The bottom panel of Figure 3.19 presents our i'-band data folded around the shorter period found, $P = 1.6242$ days. The light curve appears 'noisier', or less coherent,

when folded on this shorter period.

We favour the longer orbital period of $P = 3.2297 \pm 0.0027$ days. The phase folded light curve is less 'noisy', i.e., more coherent, than that for $P = 1.62419 \pm 0.00069$ days. The quiescent SED of the donor star, shown in Figure 1.11 and discussed further in Section 6.4, supports the idea that the companion is an evolved star but not a giant. According to Munari et al. (2020a)'s fits to stellar isochrones, for a system with an evolved companion and an extinction of $E(B-V) = 0.72$ (i.e., very similar to the extinction value determined in Section 3.8), a reasonable estimate for the orbital period is 3.4 to 3.6 days, depending on the WD mass. A shorter orbital period of $P \sim 1.4$ days would require a much higher extinction $E(B-V) \geq 1.8$ and a very young age (< 0.3 Gyr) for the binary system (Munari et al., 2020a). Similar arguments would apply to an orbital period of $P \sim 1.6$ days.

In this chapter, we described how the photometry was calculated and calibrated, and we presented light curves and colour curves. In addition, we discussed the determination of the likely time of eruption, fits to the light curve evolution, and determination of the likely extinction towards V392 Per. The evolution of the spectral energy distribution was presented, and compared to the quiescent average SED of the system. Furthermore, analysis of the post-nova light curve hinted at a detection of the orbital period of V392 Per, and was in close agreement to the periods found by other researchers. In the next chapter, we will present the spectroscopic analysis of V392 Per. In addition, the *Swift* X-ray and UV observations are presented and analysed.

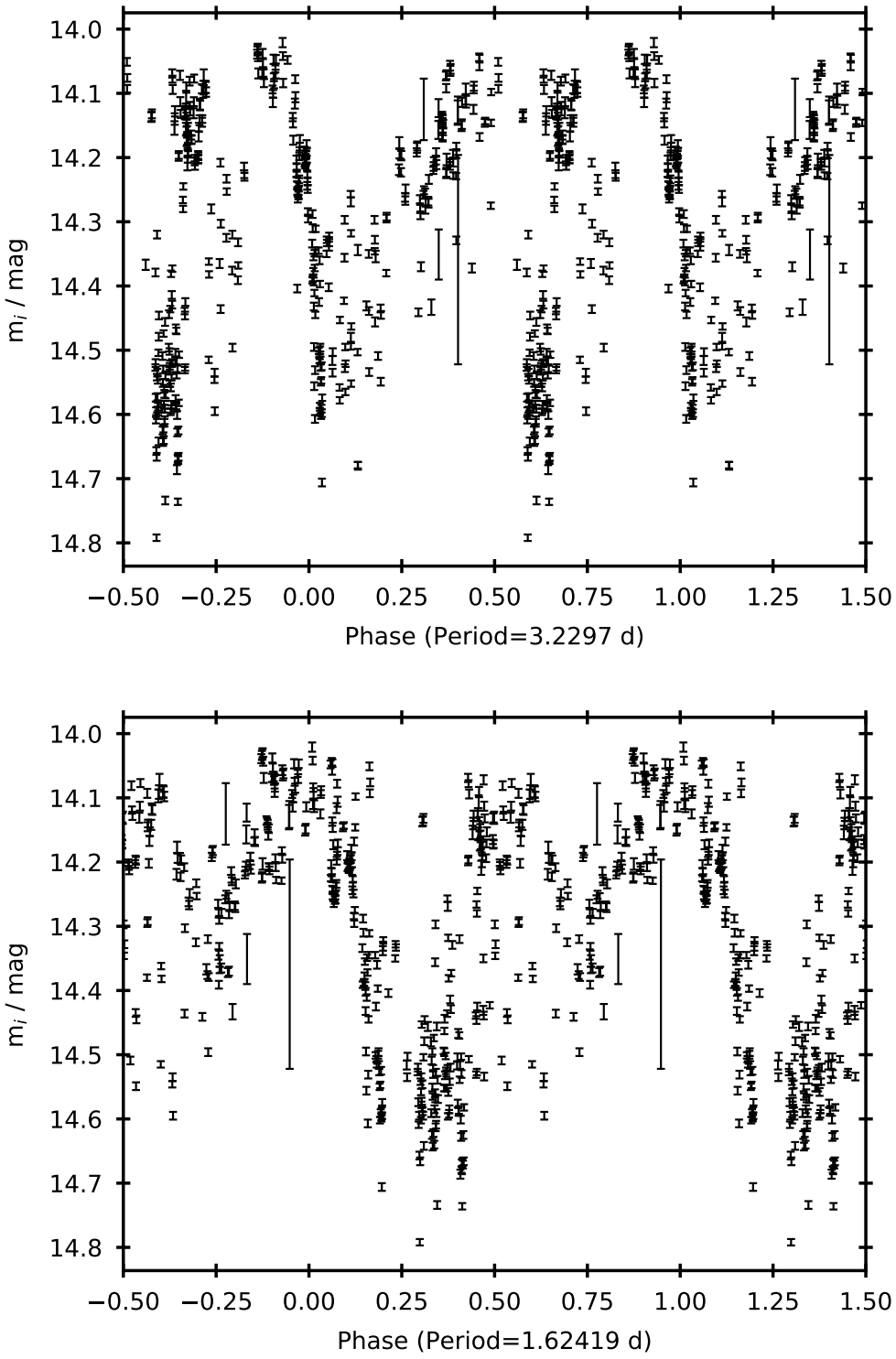

Figure 3.19: Post-eruption i'-band light curves, folded on **top:** the best fit period of $P = 3.2297\,(\pm 0.0027)$ days, and **bottom:** a period of $P = 1.6242\,(\pm 0.0007)$ days. The top panel appears as Figure 4 in Murphy-Glaysher et al. (2022) ['V392 Persei: A γ-ray bright nova eruption from a known dwarf nova', Murphy-Glaysher et al., Mon. Not. R. Astron. Soc., 514, 6183, 2022 DOI `https://doi.org/10.1093/mnras/stac1577`].

Chapter 4

Spectroscopic Evolution and *Swift* Observations

This chapter is an extended version of Sections 3.7, 3.8 and 4 from Murphy-Glaysher et al. (2022).

4.1 Absolute flux calibration of spectra

As discussed in Section 2.9, all spectra were relative flux calibrated using observations of standard stars with the respective spectrograph. An additional step was applied to calibrate the spectra to the photometry. For a given spectrum, the MJD at the midpoint of the observation was found, and T_0 subtracted to find the time of the observation, in days since the eruption onset. This time was then used in conjunction with the fits to the $BVr'i'$ photometry to calculate the magnitude in each passband at the time of the observation. The magnitude was then converted to a flux F_{Jy} in

Janskys using Equation 4.1, where m is the magnitude in a given passband.

$$F_{\mathrm{Jy}} = 3631 \times 10^{-m/2.5} \tag{4.1}$$

The flux in Janskys was converted into the corresponding flux F in $\mathrm{erg\,cm^{-2}\,s^{-1}}$ using Equation 4.2, where λ_c is the central wavelength of the passband in Angstroms, i.e. 4250 Å, 5150 Å, 6535 Å and 7623 Å respectively for $BVr'i'$.

$$F = \frac{F_{\mathrm{Jy}}/\lambda_c^2}{33400} \tag{4.2}$$

The PyRAF function `sbands` was used to measure the flux within each of the passbands $BVr'i'$ for the spectrum. A scaling factor between the flux predicted by the light curve fits and the measured flux was calculated for each passband: $S_B, S_V, S_{r'}, S_{i'}$ for $BVr'i'$, respectively. The geometrical average S of the scaling factors was calculated for each spectrum according to Equation 4.3.

$$S = (S_B S_V S_{r'} S_{i'})^{1/4} \tag{4.3}$$

Each spectrum was rescaled using the PyRAF function `imarith` so that the sbands flux would match the flux from the photometry, i.e. the flux predicted from the fits to the light curves. This was done to minimize the systematic effect of slit losses on the fluxes measured, both for the observations of the nova and of the spectrophotometric standards. This is particularly useful for those spectral lines on the boundary between passbands. Since the spectroscopic observations did not, in general, coincide with the photometric observations, we used the light curve fits rather than matching to the photometric observation made closest in time.

The spectra were also dereddened and the heliocentric correction was applied using the PyRAF functions `deredden` and `rvcorrect`.

4.2 Optical spectra

Our LT and Hiltner 2.4 m flux calibrated and dereddened spectra are shown in Figures 4.1–4.3. Those shown in Figure 4.1 were taken before V392 Per entered the initial Sun constraint, and cover the period of early spectral evolution, while the spectra were declining in optical thickness. The strongest features in the earliest spectrum (2.1 days post-eruption; 1 day post-maximum) are H I Balmer series lines, with Hα–Hδ exhibiting broad, optically thick, P Cygni profiles. All lines attributable to the eruption have P Cygni shapes. We see strong lines from He I 4471 Å, in particular, and from He I 4388 Å and 4438 Å. Lines from Fe II multiplet 42 are dominant features. A broad Na I-D profile is punctuated by saturated interstellar absorption lines (see Section 3.8). In the second spectrum (4.9 days post-eruption), we also see He I 6678 Å, 7065 Å, and 7281 Å. In addition, lines from O I 7774 Å, 8227 Å, and 8446 Å were present (but not shown in Figure 4.1). All spectra before the initial Sun constraint exhibit these lines, but their intensity and optical depth diminishes over this first week of evolution, and the line profiles evolve from P Cygni profiles to triple-peaked structures (also see Darnley et al., 2018a; Mugrauer et al., 2018; Tomov et al., 2018; Wagner et al., 2018). Based on the spectral morphology, we would place this eruption in the Fe II taxonomic class, although the inferred ejecta velocities are higher than normally seen in spectra from this class.

Once V392 Per became visible following the first Sun constraint (76 days post-eruption), the spectra had transitioned to the nebular phase (see Figure 4.2; Darnley, 2018a). We see the continued presence of Balmer and He I emission; however, the spectra are dominated by nebular [O III] 4959+5007 Å and auroral [O III] 4363 Å lines, with He II emission (particularly at 4200 Å and 4686 Å) now also present. As reported by Darnley (2018b), the [O III] 5007 Å line rivals Hα in brightness, and [O III] 4363 Å and He II 4686 Å are stronger than Hβ. The forbidden lines are double-peaked,

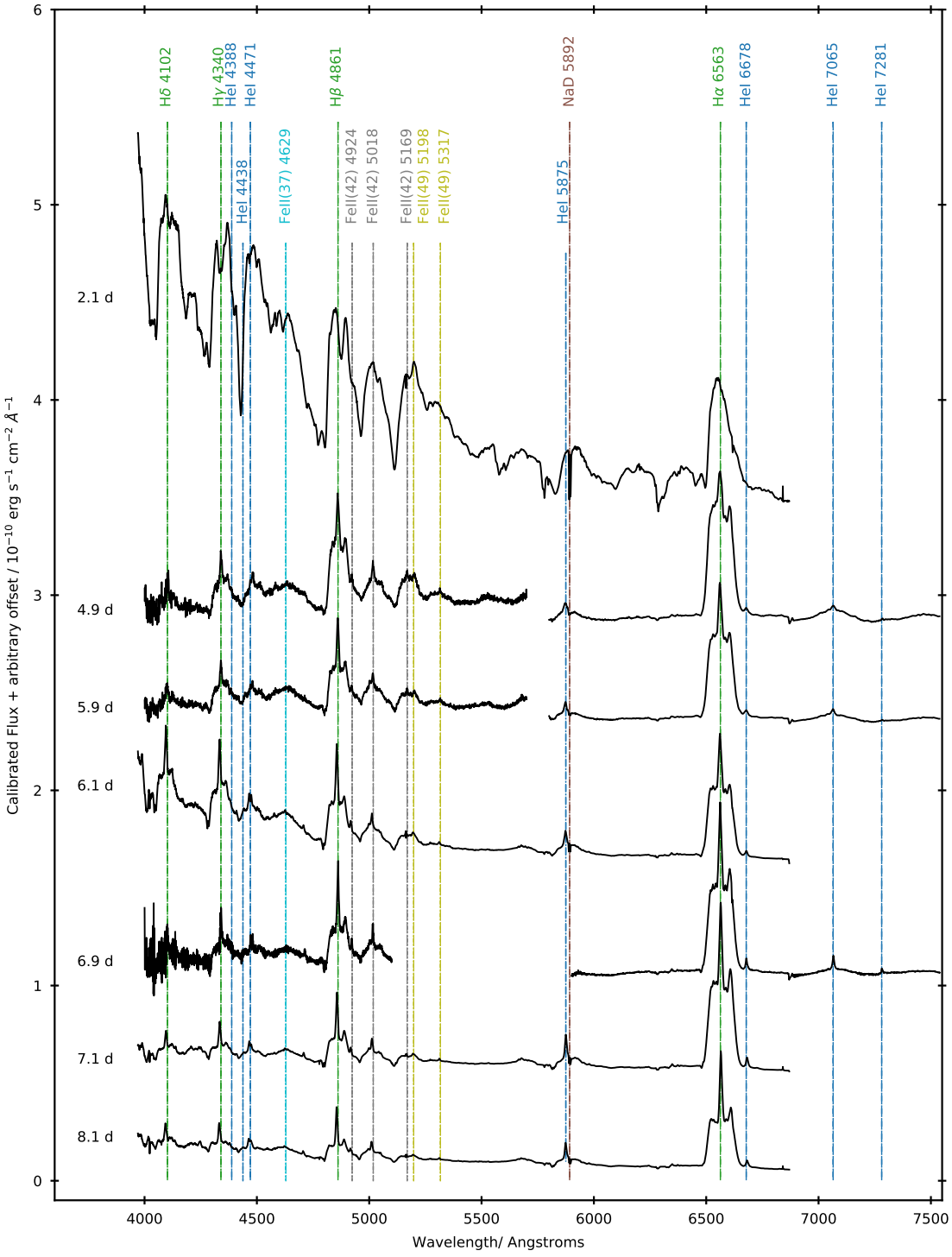

Figure 4.1: Pre-first-Sun constraint spectra of V392 Per, from 2.1–8.1 days post-eruption. Here we present flux calibrated (but offset) dereddened spectra from the LT (SPRAT and FRODOSpec) and the Hiltner 2.4 m. These early spectra are becoming progressively less optically thick. Prominent spectral features are labelled. Appears as Figure 5 in Murphy-Glaysher et al. (2022) ['V392 Persei: A γ-ray bright nova eruption from a known dwarf nova', Murphy-Glaysher et al., Mon. Not. R. Astron. Soc., 514, 6183, 2022 DOI `https://doi.org/10.1093/mnras/stac1577`].

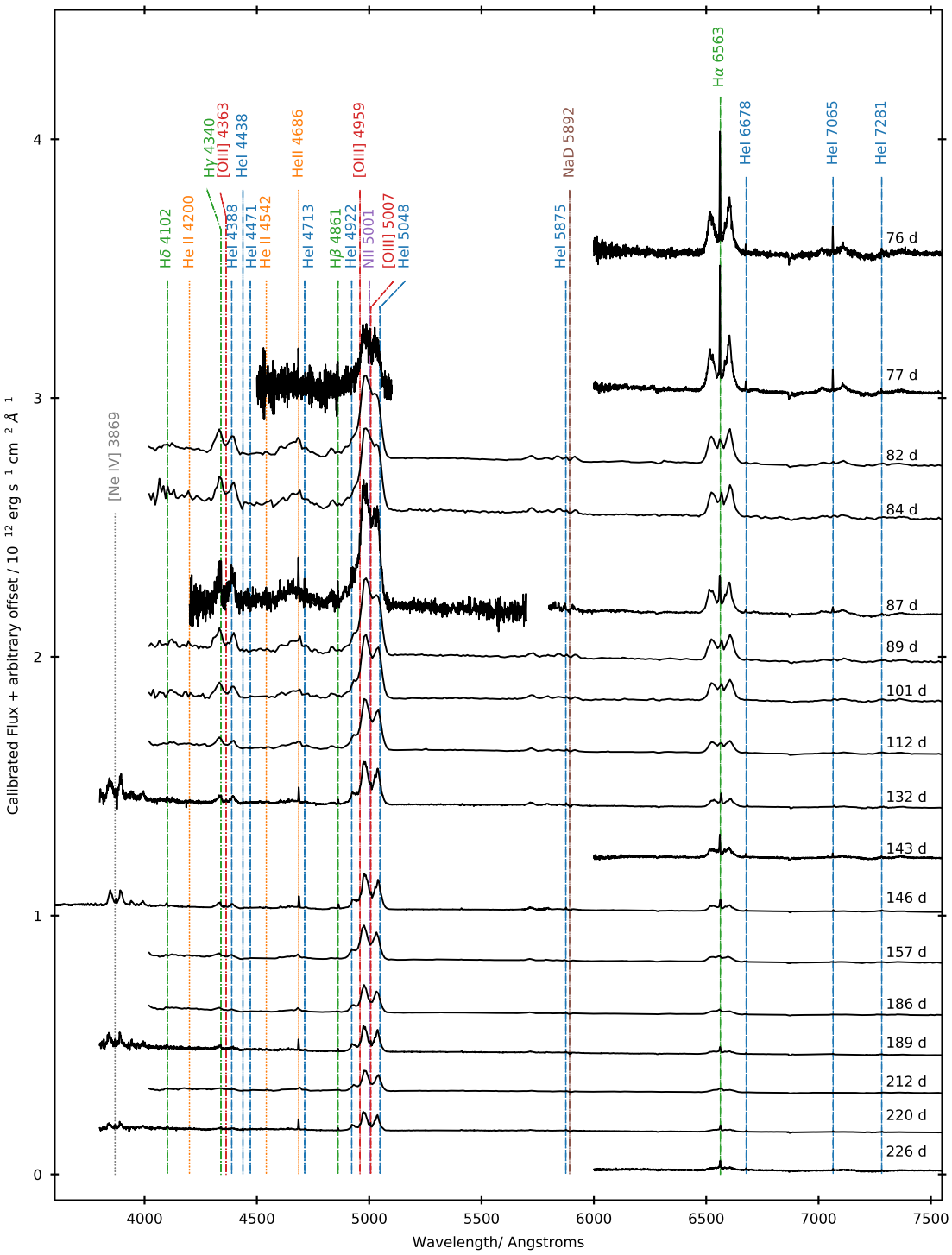

Figure 4.2: As Figure 4.1, displaying spectra from 76–226 days post-eruption and the nebular phase. Appears as Figure 6 in Murphy-Glaysher et al. (2022) ['V392 Persei: A γ-ray bright nova eruption from a known dwarf nova', Murphy-Glaysher et al., Mon. Not. R. Astron. Soc., 514, 6183, 2022 DOI `https://doi.org/10.1093/mnras/stac1577`].

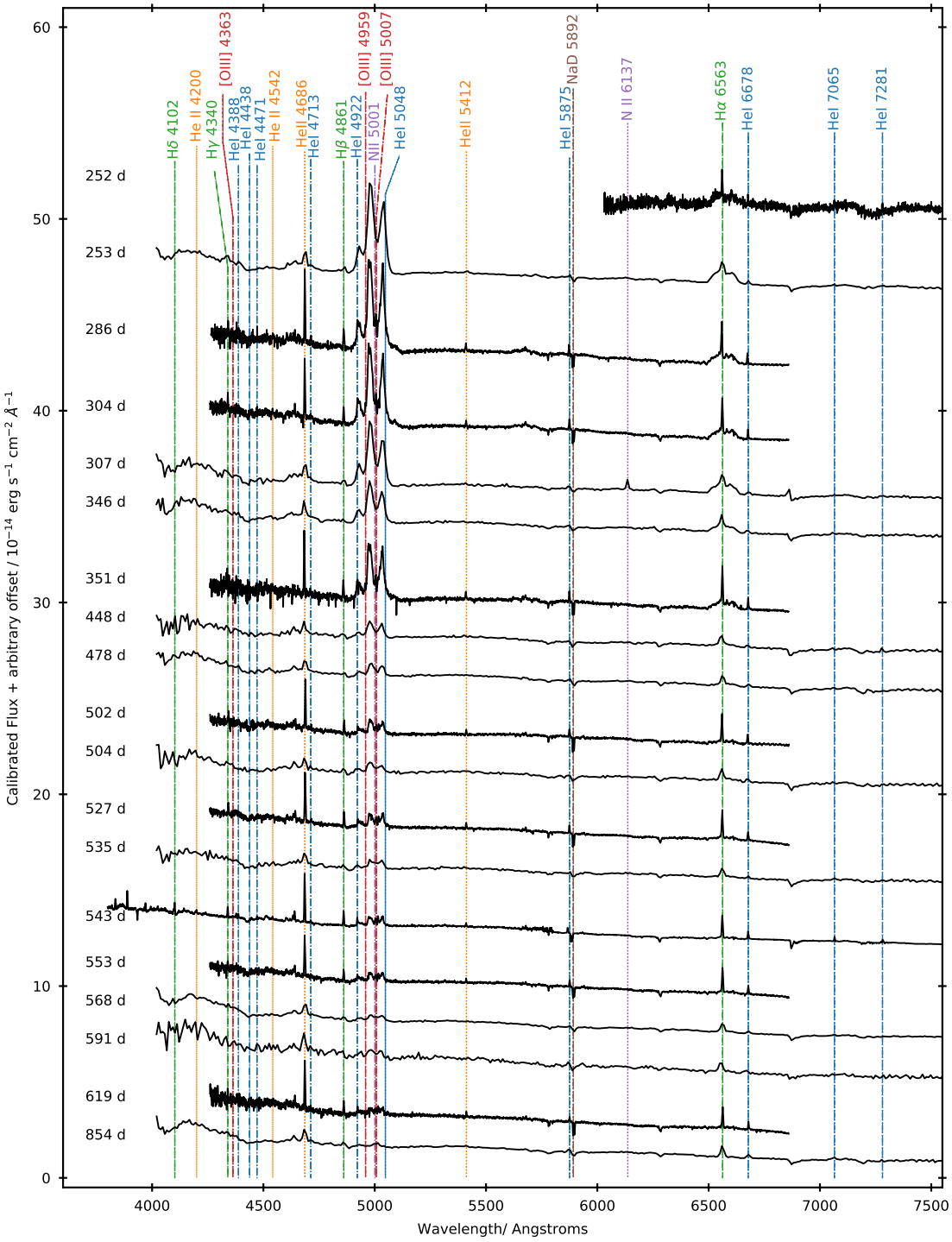

Figure 4.3: As Figure 4.1, displaying spectra from 252–854 days post-eruption, showing the transition from the late-nebular phase to the post-nova phase. Appears as Figure 7 in Murphy-Glaysher et al. (2022) ['V392 Persei: A γ-ray bright nova eruption from a known dwarf nova', Murphy-Glaysher et al., Mon. Not. R. Astron. Soc., 514, 6183, 2022 DOI `https://doi.org/10.1093/mnras/stac1577`].

whereas the H I and He I lines retain the triple-peaked structure, and the widths of the forbidden lines are consistent with those of H I. The final set of spectra are shown in Figure 4.3. Here we witness the decline of the nebular emission and the transition to the post-nova spectrum. Emission from the [O III] lines fades relative to that from He II 4686 Å and H I.

As first reported by Munari & Ochner (2018), we also see evidence for [Ne III] 3869 Å in the Hiltner and LBT spectra taken on days 132, 146, 189 and 220 post eruption. However, we do not see evidence for [Ne IV] 4715 Å. This line might blend with the He II 4686 Å profile, but we link the structure seen at $\sim \pm 2000\,\mathrm{km\,s^{-1}}$ around He II to a contribution from the ejecta (see Section 4.7).

4.3 Model used to measure fluxes

Line profiles for a given spectral species were plotted showing velocity against flux. Velocities were calculated relative to the rest wavelength of the species (or of the central peak for multi-peaked species), λ_c, using Equation 4.4. For convenience, we used $c = 3 \times 10^5\,\mathrm{km\,s^{-1}}$ to express velocities in units of $\mathrm{km\,s^{-1}}$.

$$v(\lambda) = \frac{\lambda - \lambda_c}{\lambda_c}\, c \tag{4.4}$$

First, a linear function h(x), of the form shown in Equation 4.5, was fitted to the continuum of the spectrum.

$$h(x) = ax + b \tag{4.5}$$

Then, each individual emission peak was modelled using a Gaussian function $g_n(x)$,

of the form shown in equation 4.6, where $n \in \{1, 2, 3\}$, depending on how many Gaussian components are required, and A_n, μ_n and σ_n are the amplitude, velocity corresponding to the central wavelength, and width, respectively, of the Gaussian component. Since some emission lines were double- or triple-peaked, they were modelled using two or three Gaussian components.

$$g(x) = \sum^{n} g_n(x) = \sum^{n} A_n \exp\left(-0.5\left(\frac{x - \mu_n}{\sigma_n}\right)^2\right) \tag{4.6}$$

The line profile was modelled as shown in Equation 4.7, as the sum of the continuum and the Gaussian components.

$$f(x) = h(x) + g(x) \tag{4.7}$$

The flux of a single-peaked emission line was found by calculating the area of the Gaussian component, as expressed in Equation 4.8.

$$F_n(x) = A_n \sigma_n \sqrt{2\pi} \tag{4.8}$$

The corresponding error in the flux of a single-peaked emission line was found using Equation 4.9.

$$F_{n,\mathrm{err}}(x) = A_n \sigma_n \sqrt{2\pi} \sqrt{\left(\frac{A_{n,\mathrm{err}}}{A_n}\right)^2 + \left(\frac{\sigma_{n,\mathrm{err}}}{\sigma_n}\right)^2} \tag{4.9}$$

Figure 4.4 shows two examples of fitting the Hα line profile with three individual Gaussian components. The top and bottom panels show low resolution and high

resolution line profiles, respectively. Both spectra were from early in the nebular phase, when V392 Per had just left its first Sun constraint.

The total flux of a double- or triple-peaked emission line was then found by summing over the fluxes of the individual Gaussian components, as in Equation 4.10.

$$F_{\mathrm{tot}}(x) = \sum^{n} F_n \tag{4.10}$$

The error on the total flux was then found by combining the errors of the individual components in quadrature, as shown in Equation 4.11.

$$F_{\mathrm{tot,err}}(x) = \sqrt{\sum^{n} (F_{n,\mathrm{err}})^2} \tag{4.11}$$

4.4 Balmer lines

High resolution Hα line profiles are shown in Figure 4.5, which presents Hiltner 2.4 m and the LT/FRODOSpec data. Our earliest spectrum (2.1 days post-eruption; Figure 4.5 top-left) reveals a single-peaked, optically thick, broad and asymmetric Hα line, with P Cygni absorptions at $-2560\,\mathrm{km\,s^{-1}}$ and $-4550\,\mathrm{km\,s^{-1}}$, and emission on the red side out to $\sim 5000\,\mathrm{km\,s^{-1}}$. By the next spectrum (4.9 days post-eruption) the profile has developed a stronger and narrower central peak, and additional secondary peaks have started to develop at $\sim\pm2500\,\mathrm{km\,s^{-1}}$, the P Cygni absorption elements have weakened and possibly merged (see Section 4.5), and the high velocity redward wing has gone. Over the next week, as V392 Per approached the first Sun constraint, the central peak increased in intensity relative to the red- and blue-shifted secondary

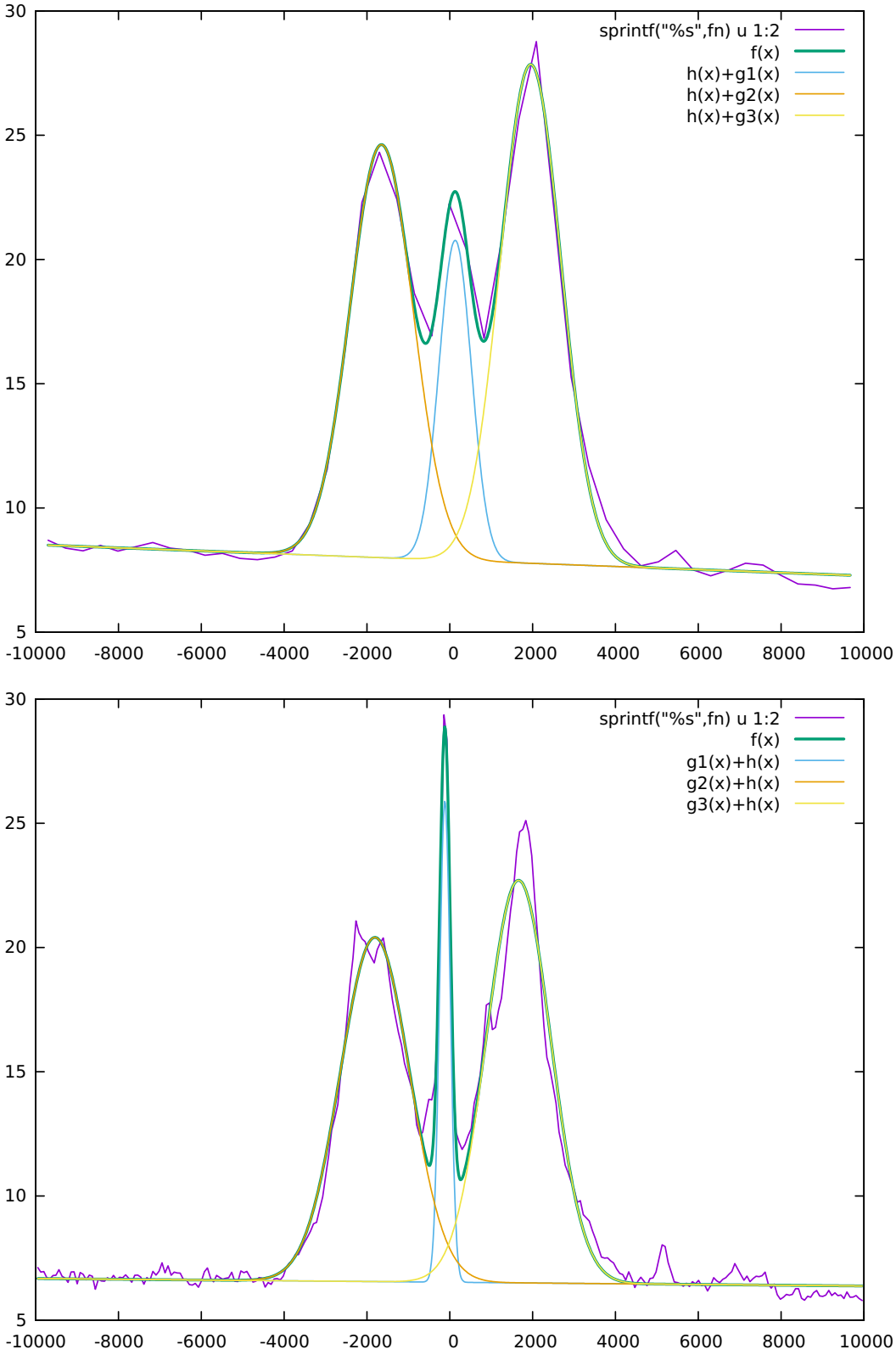

Figure 4.4: Fitting the Hα line profile with a linear fit to the continuum (not shown) and multiple Gaussian components. The horizontal axes show velocity in units of $\mathrm{km\,s^{-1}}$, and the vertical axes show flux. The top and bottom panels show fits to early nebular SPRAT and FRODOSpec spectra, respectively.

peaks, with the redward peak more sharply defined than its blue counterpart.

The subsequent spectrum was taken once V392 Per emerged from the first Sun constraint, on day 76 (Figure 4.5 top-right). By this time the system had evolved to the nebular phase and the Hα line profile transitioned to a clear three-peaked structure with a bright, very narrow, central peak with measured FWHM of 57 km s^{-1}. The velocity structure of the outer peaks are symmetric, but the redward peak is brighter. This morphology persisted until 220 days post-eruption, but the outer peak amplitude continued to weaken relative to the central peak.

From day 226 post-eruption (Figure 4.5 bottom-left), the amplitude of the central peak began to dominate and emission from the outer peaks began to wane more rapidly at higher velocities: the outer peaks appear to move inward toward the central peak – most likely an effect of decreasing emissivity as the ejecta thin. The fastest moving ejecta thin the fastest. As the outer peak flux decreased, nearby lines became more prominent, e.g., He I 6678 Å (+5165 km s^{-1}). Between days 351–448 (see Figure 4.3) all high velocity elements had disappeared, leaving just the narrow central line (Figure 4.5 bottom-right) — the post-nova profile.

In Figure 4.6 we compare the Hα profile with those of Hβ and Hγ. As expected, the Balmer line profiles evolve broadly similarly. The P Cygni absorptions persist for longer in Hβ and Hγ, possibly up to day 7.1 (see Section 4.5). The central peak is stronger relative to the outer peaks in Hβ and Hγ than in Hα. This suggests there may be different recombination conditions in different ejecta components or stronger self-absorption in those components – both indicative of a complex geometry. During the nebular phase, Hβ and Hγ are severely blended with, and dominated by, the nebular and auroral [O III] lines, respectively. By the post-nova phase all three Balmer lines simply show a very narrow peak.

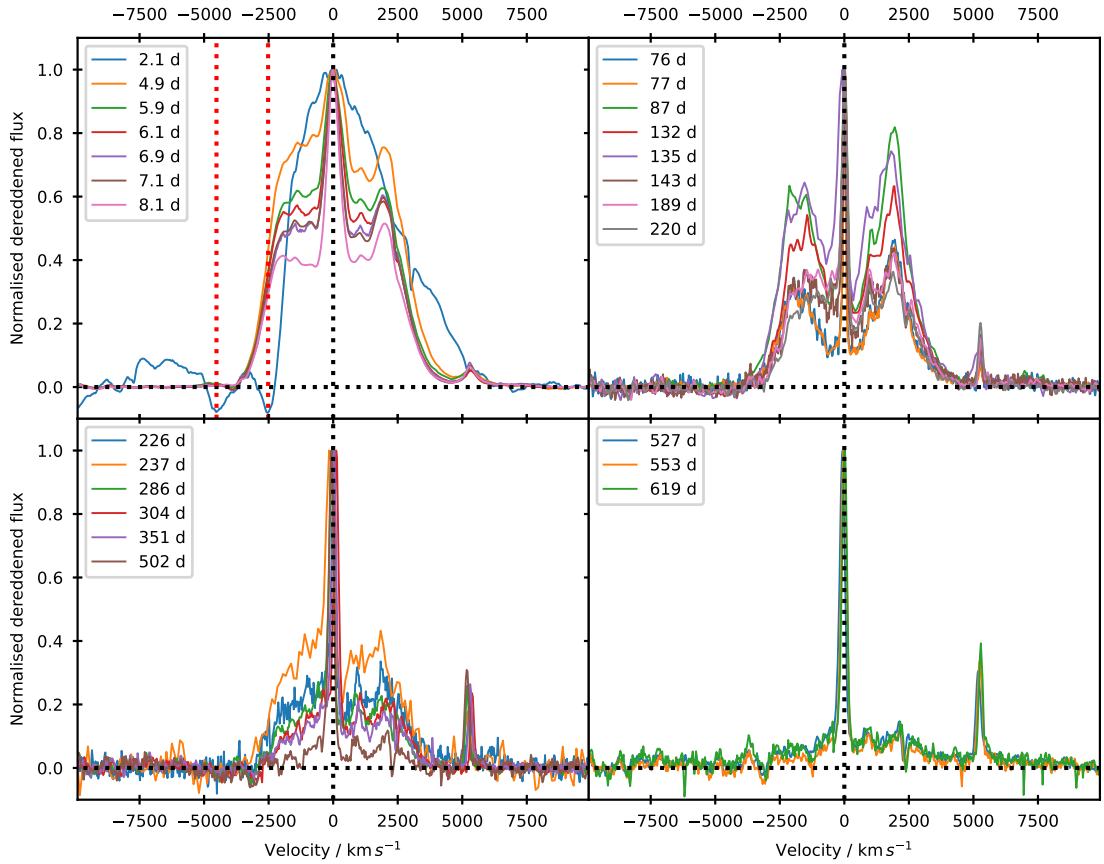

Figure 4.5: High resolution Hα line profiles from Hiltner OSMOS and FRODOSpec spectra. The spectra have been normalised to the flux of the Hα central peak. The horizontal dotted lines indicate a normalised dereddened flux value of 0. The vertical black dotted line shows the rest wavelength of Hα, and the vertical red dotted lines in the top left panel indicate the P Cygni absorption features. Modified from Figure 9 in Murphy-Glaysher et al. (2022) ['V392 Persei: A γ-ray bright nova eruption from a known dwarf nova', Murphy-Glaysher et al., Mon. Not. R. Astron. Soc., 514, 6183, 2022 DOI `https://doi.org/10.1093/mnras/stac1577`].

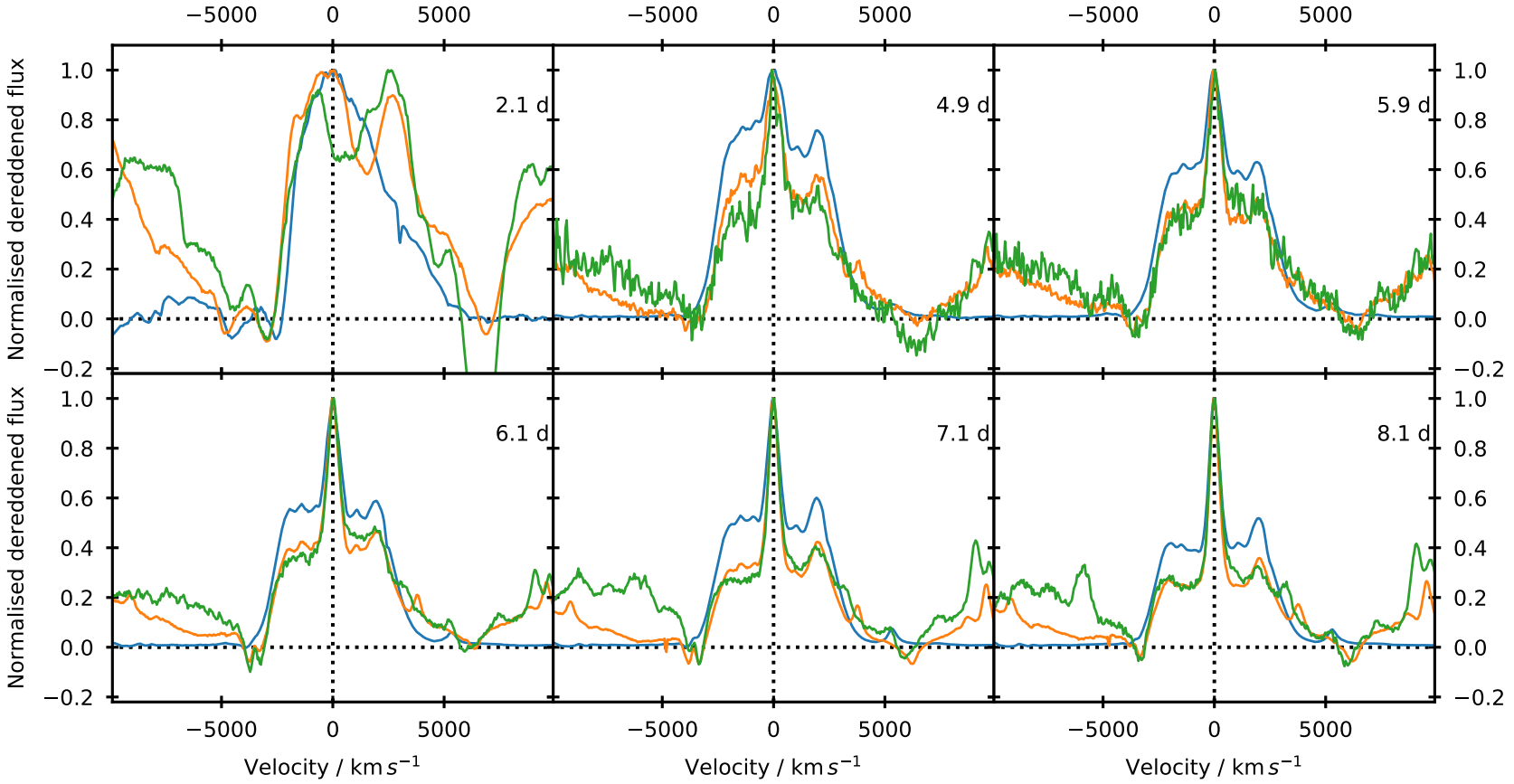

Figure 4.6: Comparison of Hα (blue), Hβ (orange), and Hγ (green) line profiles for pre-first Sun constraint epochs. Spectra have been normalised to the central peak flux. Appears as Figure 10 in Murphy-Glaysher et al. (2022) ['V392 Persei: A γ-ray bright nova eruption from a known dwarf nova', Murphy-Glaysher et al., Mon. Not. R. Astron. Soc., 514, 6183, 2022 DOI `https://doi.org/10.1093/mnras/stac1577`].

The Hα profile remains isolated from other lines and is one of the strongest lines in the spectra at all times, whereas other bright lines, e.g., other H I, He I-II, and [O III], were often severely blended. Thus, to measure the flux of the emission lines we used a triple-Gaussian profile, modelled around the Hα profile at each epoch, to estimate line fluxes and, where necessary, de-blend lines. The model used the same offsets from the rest wavelength, and the same widths and amplitudes for the three peaks as the Hα line profile. This model was than multiplied by a scaling factor to find the flux of Hβ and Hγ, and incorporated into the fitting process to find the flux of the [O III] line profiles, to take into account the blending which occurred. Line fluxes are tabulated in Tables A.7 and A.8.

Figure 4.7 shows how the central velocities (μ, or mu) of the three components used to model the Hα line profile change over the course of the eruption. Figure 4.8 shows the change in σ, or sig, which is a measure of the width of the Gaussian profiles used to model the emission lines. Figures 4.7 and 4.8 are based solely on measurements of the SPRAT spectra, which were taken during the nebular and post-nova phase of the eruption. We see that the central velocity of the central peak remains fairly stable, close to the velocity corresponding to the rest wavelength of H α, but becomes increasingly blue-shifted. The width of the central peak also remains fairly stable, at around $300\,\mathrm{km\,s^{-1}}$. In contrast, the outer peaks exhibit a more marked change in their central velocities, which were offset $\sim$ 1500 - 2000 $\mathrm{km\,s^{-1}}$ from the rest wavelength for H α when SPRAT observations began, but then demonstrated a decreasing offset, as the centres of the peaks approached the rest wavelength. The widths of the outer peaks increased from $\sim 750\,\mathrm{km\,s^{-1}}$ when SPRAT observations began, to $\sim 1400\,\mathrm{km\,s^{-1}}$ when the flux of the outer peaks decreased to the extent that measurements of the outer peaks became too noisy to be detected at a significant level.

The flux evolution of the Hα line profile is shown in Figure 4.9. Although the

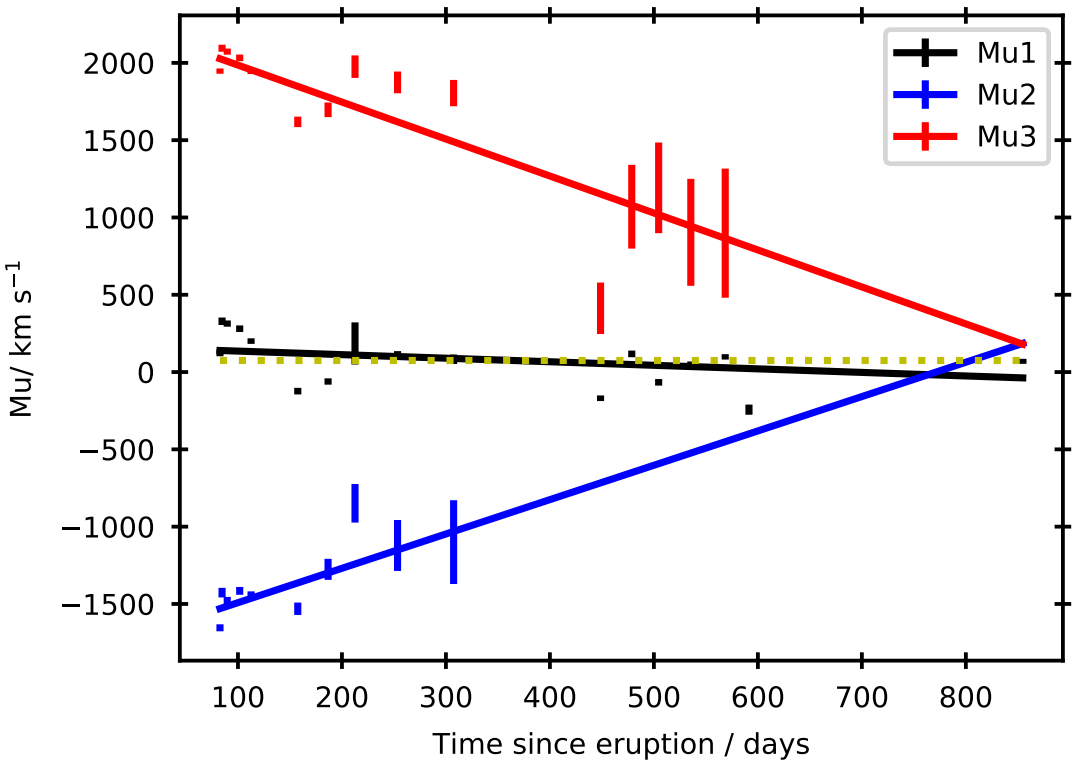

Figure 4.7: Mu evolution for H α line profiles from SPRAT spectra. The mu values show the velocity at the centre of the Gaussian fitted to each component. The black data points correspond to the central peak, the red and blue data points correspond to the centre of the red-shifted and blue-shifted peaks respectively. The solid black line shows the best fit to all of the mu values for the central peak, whereas the yellow dotted line shows the best fit of a horizontal line to the mu values. The solid black line shows the fit that was used in modelling the H α line profiles.

high amplitude of the central peak had appeared to dominate from day 226, here we see that the integrated emission from the outer peaks (blue and red) dominates the overall line flux (brown) until day $\sim$600. The decline of the outer peak fluxes are well described by a power-law with index -2.32 ± 0.04. The decay of the central peak (black) is steeper than the outer peaks and power-law-like until day ~ 100, however, from this point the central peak tends towards a constant flux of $(2.90 \pm 0.42) \times 10^{-12}\,\mathrm{erg\,s^{-1}\,cm^{-2}}$. Here we suggest that there are two system components contributing to the Hα line, a triple-peaked ejecta profile, that decays as a power-law, and a constant single narrow peaked contribution from the central system. While the Hβ line is strong and isolated during the early spectra, once in the nebular phase the line is severely blended and dominated by [O III] 4959+5007 Å. As such, we can only reliably estimate the Hβ flux until day $\sim$350. As shown in Figure 4.10, the Hβ flux declines following a similar power-law to Hα.

4.5 Multiple ejections?

In Figure 4.11 we show the velocity evolution of detected P Cygni absorption components from the Balmer lines. For illustrative purposes, we also show the Fermi-LAT γ-ray light curve and 95th percentile upper limits (Chomiuk et al., 2021a; Albert et al., 2022). Here we also utilise the ARAS spectra, some of which included very high resolution data for the Balmer lines. The first Hα P Cygni measurement is 1.9 days post-eruption and yielded two components $\sim -3000\,\mathrm{km\,s^{-1}}$ and $\sim -5000\,\mathrm{km\,s^{-1}}$. The H$\alpha$ P Cygni absorptions appear to shift further blueward over the next three spectra. By day 3.85, the Hα profile only revealed a single P Cygni absorption at $\sim -4000\,\mathrm{km\,s^{-1}}$, with subsequent measurements showing similar P Cygni velocities. Most of the later Hα line profiles only contain a single P Cygni absorption, but a higher resolution spectrum taken 7.8 days post-eruption indicated that the absorp-

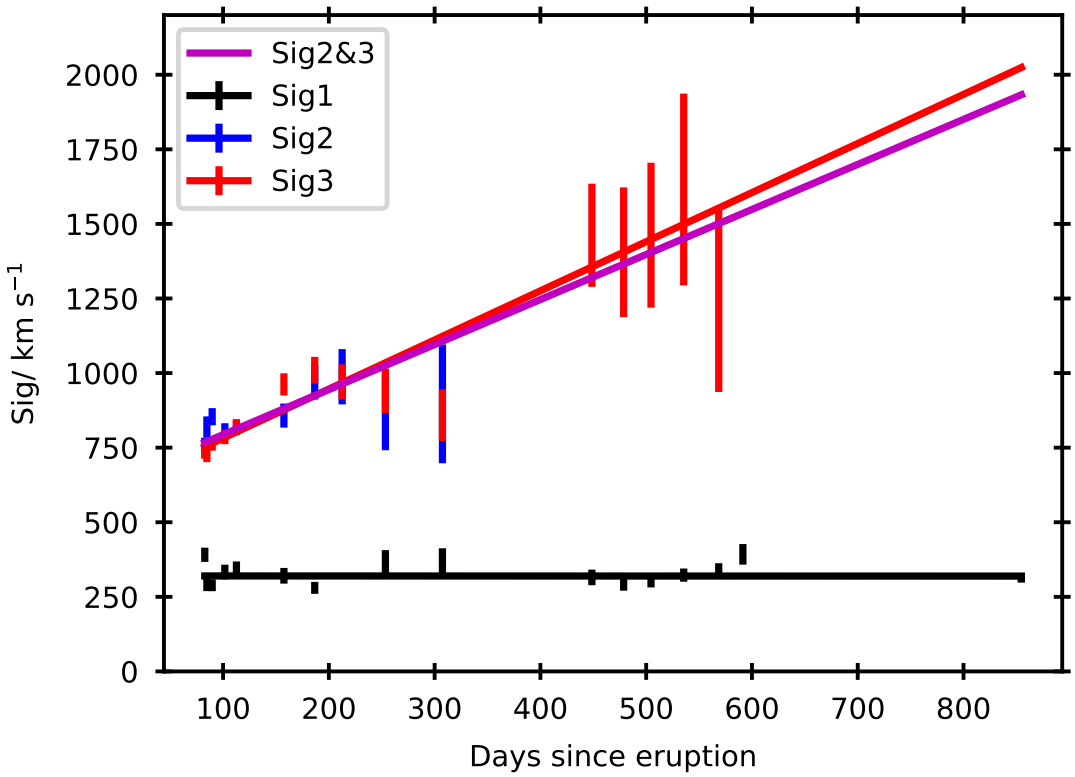

Figure 4.8: Sig evolution for H α line profiles from SPRAT spectra. The sig values show the width of the Gaussian fitted to each component. The black, blue and red data points correspond to the central peak, the blue-shifted peak and the red-shifted peak respectively. The black solid line shows the best fit to the sig values of the central peak. The red solid line shows the best fit to the red-shifted sig values, whereas the magenta solid line shows the best fit to the sig values for both the blue-shifted and red-shifted peaks.

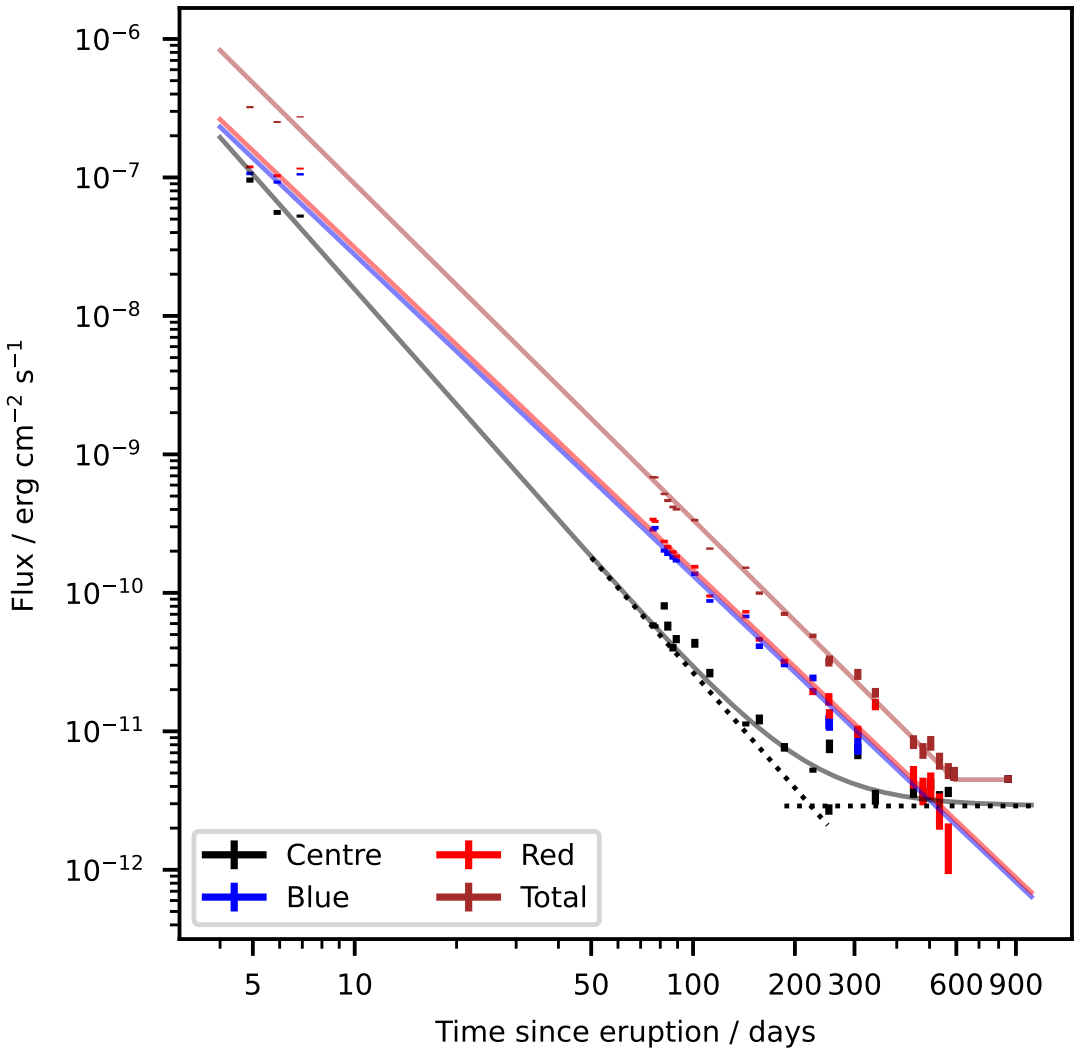

Figure 4.9: Hα flux evolution from SPRAT and FRODOSpec spectra. The fluxes of the central, blueward and redward components are shown in black, blue and red, respectively. The total flux is shown in brown. Appears as Figure 11 in Murphy-Glaysher et al. (2022) ['V392 Persei: A γ-ray bright nova eruption from a known dwarf nova', Murphy-Glaysher et al., Mon. Not. R. Astron. Soc., 514, 6183, 2022 DOI `https://doi.org/10.1093/mnras/stac1577`].

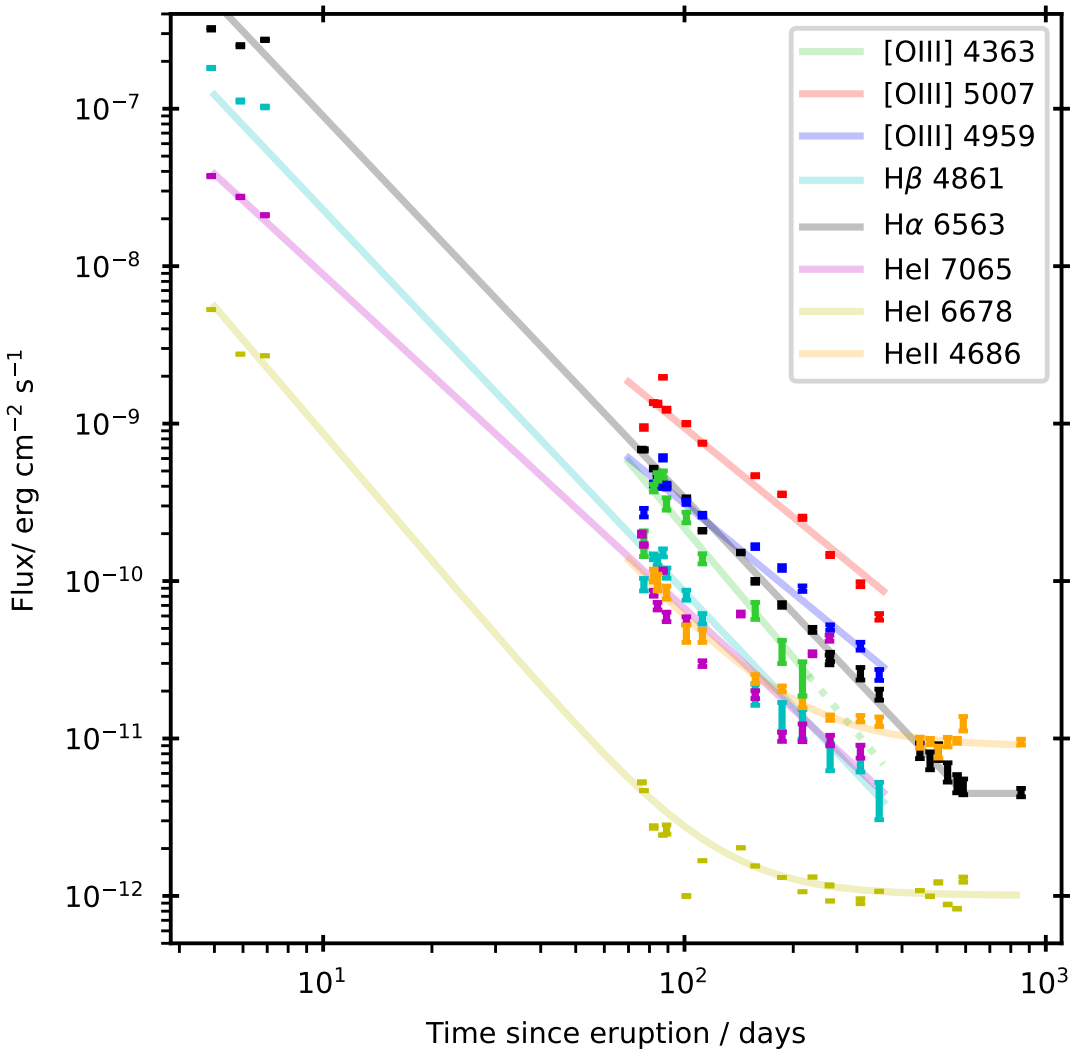

Figure 4.10: Flux evolution of prominent lines in the V392 Per spectra. Data for [O III] 4959 Å, [O III] 5007 Å, and Hβ are only shown up to day 346. The Hα flux from day 346 onward only includes the central and redward component, and for day 591 onward only the central component. Power law fits to these data are indicated by the solid lines, dotted lines are extrapolations of fits beyond the available data. Appears as Figure 11 in Murphy-Glaysher et al. (2022) ['V392 Persei: A γ-ray bright nova eruption from a known dwarf nova', Murphy-Glaysher et al., Mon. Not. R. Astron. Soc., 514, 6183, 2022 DOI `https://doi.org/10.1093/mnras/stac1577`].

tion contained sub-structure with similar nearby minima of $\sim -3800\,\mathrm{km\,s^{-1}}$ and $\sim -4000\,\mathrm{km\,s^{-1}}$. The overall structure of the Balmer lines is complex and this led to systematic difficulties in the P Cygni measurement, and as such the scatter seen in the Hα measures from day 5 onward, is indicative of the associated systematic errors.

The first Fermi-LAT γ-ray detection occurred 2.5 days post-eruption (one day post-discovery), the second detection a day later had less than half the flux of the first detection, and the γ-ray flux had almost halved again by day 4.5. During this period of rapid γ-ray fading, we observe the apparent merger of two P Cygni absorptions, leaving a single absorption line with a velocity intermediate to the two.

This scenario is consistent with that reported in Aydi et al. (2020a,b) for V906 Car and other CNe, where two constituents of a multi-component ejecta merge, with the associated shocks driving γ-ray emission. Here, we propose that an initial $\sim 3000\,\mathrm{km\,s^{-1}}$ ejection merges with a subsequent $\sim 5000\,\mathrm{km\,s^{-1}}$ ejection, leaving a single component travelling at $\sim 4000\,\mathrm{km\,s^{-1}}$. Given the timing of the initial γ-ray detection, this merger seemingly occurred 2.5 ± 0.5 days after the onset of eruption. Assuming the initially ejected material travelled at a constant velocity $v_{\mathrm{ej},1} \sim 3000\,\mathrm{km\,s^{-1}}$ (there were no signs of deceleration) for 2.5 ± 0.5 days, it covered a distance of $(6.5 \pm 1.3) \times 10^8$ km, or 4.3 ± 0.9 au, before the merger occurred. Therefore, the second ejection, travelling at velocity $v_{\mathrm{ej},2} \sim 5000\,\mathrm{km\,s^{-1}}$, would take 1.5 ± 0.3 days to cover the same distance. This corresponds to 1.0 ± 0.3 days post-eruption, i.e. around the time of optical maximum. Assuming that kinetic energy is largely conserved during the merger, the second ejection could have a mass up to 80% that of the first.

The equivalent Hβ and Hγ data appear richer, both showing evidence for the initial merger that drove the strong γ-ray peak. From day 5, there remains evidence for two absorption features at lower velocities ($\sim -3750\,\mathrm{km\,s^{-1}}$ and $\sim -3250\,\mathrm{km\,s^{-1}}$).

These are markedly lower than P Cygni velocities seen in the Hα profile during the same epochs, but we note that the Hα line was already transitioning to an optically thin emission profile at this time. These data are admittedly noisy, but they hint at a second or on-going merger event; which may be driving the flat γ-ray emission during this time. The spectral coverage ends at day 10, but in this final spectrum there is a hint of a single, merged, P Cygni at $\sim -3550\,\mathrm{km\,s^{-1}}$. We note that this corresponds to the final Fermi-LAT detection, although V392 Per remained visible to Fermi beyond this time.

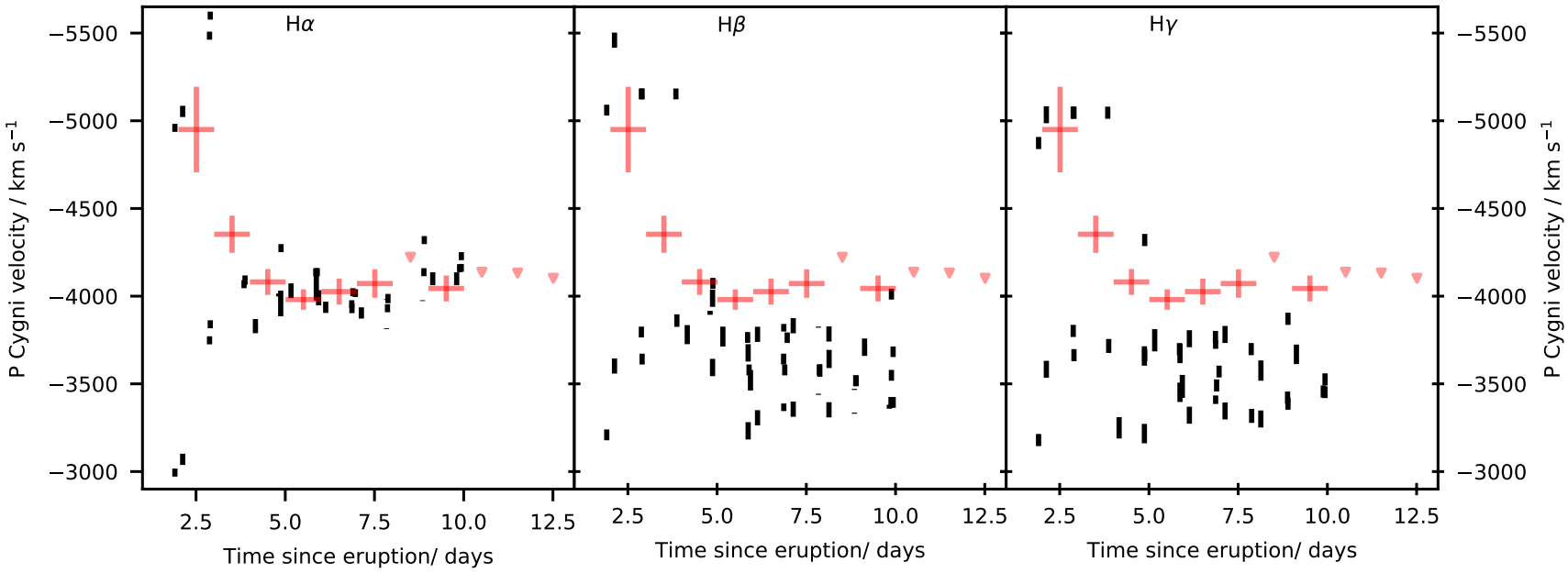

Figure 4.11: Velocity evolution of the Balmer line (left: Hα, centre: Hβ, right: Hγ) P Cygni absorption features (black). The red data points show the Fermi-LAT light curve for comparison, the red arrowheads are 95th percentile upper limits. Appears as Figure 12 in Murphy-Glaysher et al. (2022) ['V392 Persei: A γ-ray bright nova eruption from a known dwarf nova', Murphy-Glaysher et al., Mon. Not. R. Astron. Soc., 514, 6183, 2022 DOI `https://doi.org/10.1093/mnras/stac1577`].

4.6 He I 6678 Å and 7065 Å

The He I 6678 Å profiles were fitted simultaneously with the Hα, and are shown in Figures 4.5 and 4.6 at $\sim 5250\,\mathrm{km\,s^{-1}}$. The flux evolution of He I 6678 Å is shown in Figure 4.10. Due to its proximity to Hα, only the central peak of the He I 6678 Å was measured, and emission peaked 4.9 days post-eruption at $(5.30 \pm 0.01) \times 10^{-9}\,\mathrm{erg\,s^{-1}\,cm^{-2}}$. The He I 6678 Å flux follows a power law with index -2.69 ± 0.16, declining to a plateau of around $(1.01 \pm 0.03) \times 10^{-12}\,\mathrm{erg\,s^{-1}\,cm^{-2}}$, from day 253 post-eruption.

As He I 7065 Å is isolated from other strong lines, the profile was modelled using a three component Gaussian, as for Hα. The evolution of the total flux of He I 7065 Å is shown in Figure 4.10. The first flux measurement of He I 7065 Å was $(3.74 \pm 0.04) \times 10^{-8}\,\mathrm{erg\,s^{-1}\,cm^{-2}}$, 4.9 days post-eruption. The He I 7065 Å broadly follows a power law with index -2.12 ± 0.05, but there is no evidence for a flux plateau from the central component, as was seen in Hα and He I 6678 Å.

4.7 He II 4686 Å

He II 4686 Å normalized line profiles are shown in Figure 4.12. The top panel shows profiles from the nebular phase following emergence from the initial Sun constraint 83–212 days post-eruption. During this stage, the He II emission strengthened relative to neighbouring permitted lines. The low resolution spectra are suggestive of broad He II emission associated with the nova ejecta, due to blending from neighbouring lines. However, the higher resolution data indicate that the He II emission is dominated by a narrow central peak, with hints of a faint, broad, contribution from the ejecta ($\pm 2300\,\mathrm{km\,s^{-1}}$) in spectra from days 132 and 189. The He II profiles toward the end

of the nebular phase and throughout the post-nova period, show only the narrow central peak.

Given the simplicity of the He II profile, we fitted the line using a single Gaussian. The flux evolution of He II 4686 Å is shown in Figure 4.13. There is no significant detection of He II before the first Sun constraint. The first clear detection of He II occurs after emergence from this Sun constraint, on day 82. Here, the flux is $(1.09 \pm 0.10) \times 10^{-10}\,\mathrm{erg\,s^{-1}\,cm^{-2}}$. The evolution of the line flux is best described by the combination of a power law of index -2.54 ± 0.16 and a plateau of around $(9.02 \pm 0.37) \times 10^{-12}\,\mathrm{erg\,s^{-1}\,cm^{-2}}$. The flux evolution is compared with that of other species in Figures 4.10, shown in Figure 4.13, and discussed further in Section 6.2.

4.8 Nebular [O III] 4959+5007 Å

The combined [O III] 4959+5007 Å nebular emission complex was visible from the initial post-first Sun constraint spectrum, and dominant throughout the nebular phase (see Figures 4.2 and 4.3). Although appearing to mirror the triple-peaked Hα profile, the [O III] complex consists of a pair of overlapping double-peaked line profiles, the brighter centred at 5007 Å the fainter at 4959 Å (see Figures 4.14 and 4.15). There is no evidence for a central component and, by this time, the central component seen in the permitted lines was only $\sim$60 km s^{-1} wide and therefore not associated with the ejecta.

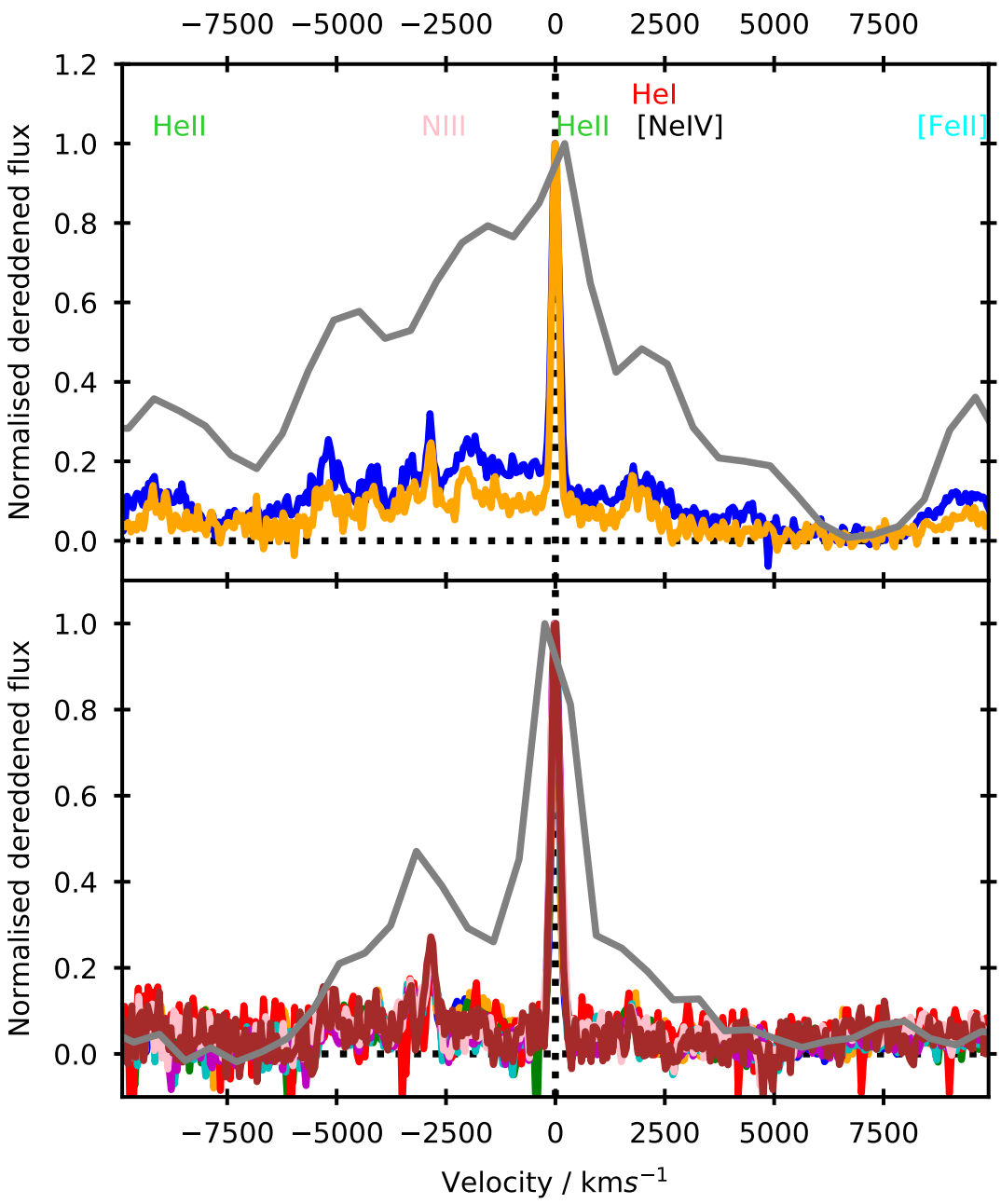

Figure 4.12: He II 4686 Å line profile evolution: high resolution profiles are compared with time-averaged low resolution data (grey) from the same time interval. **Top:** spectra from 83–212 days post-eruption, high resolution data from 132 (blue) and 189 (orange) days post-eruption. **Bottom:** spectra from 253–854 days post-eruption. Modified from Figure 13 in Murphy-Glaysher et al. (2022) ['V392 Persei: A γ-ray bright nova eruption from a known dwarf nova', Murphy-Glaysher et al., Mon. Not. R. Astron. Soc., 514, 6183, 2022 DOI `https://doi.org/10.1093/mnras/stac1577`].

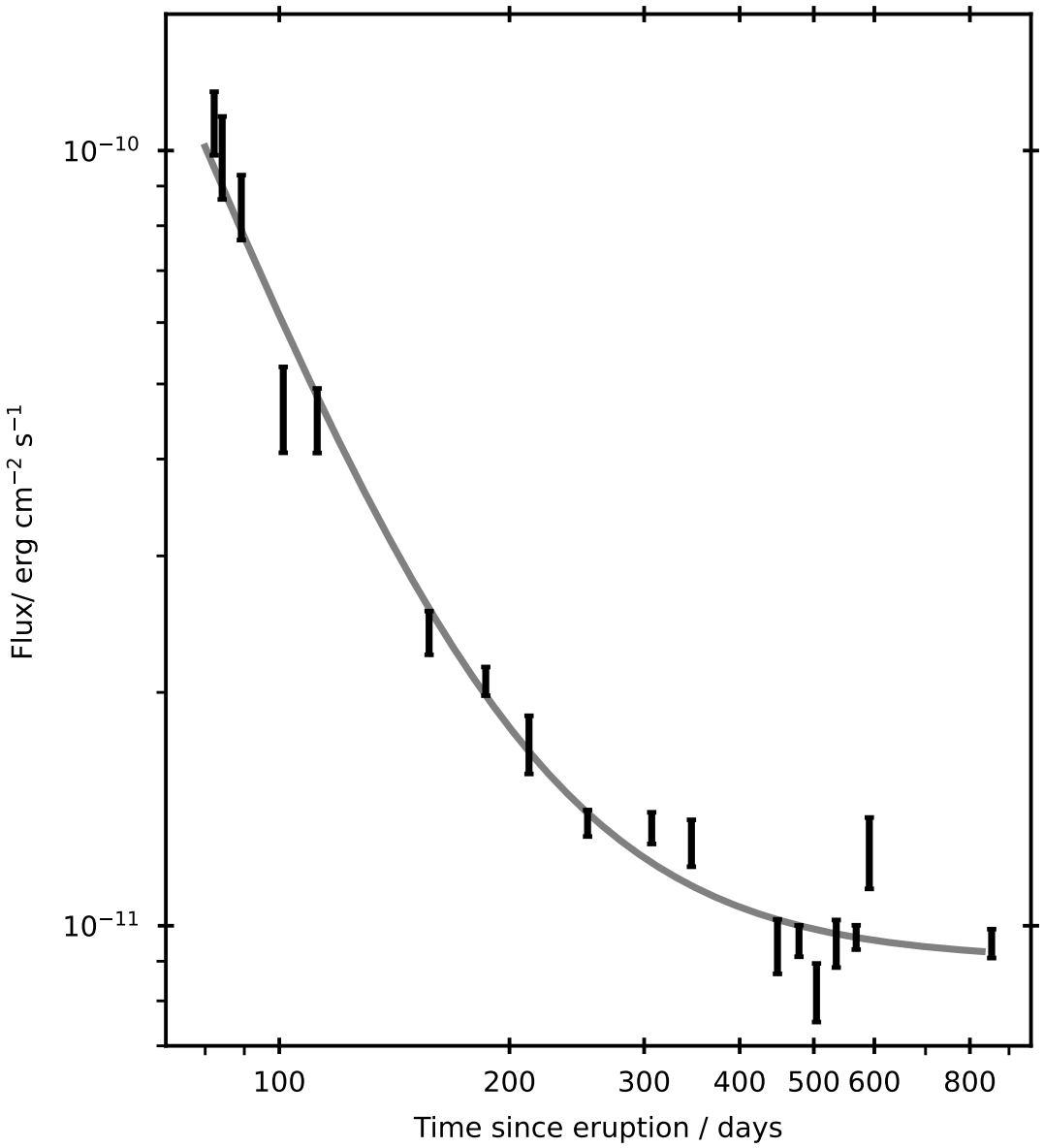

Figure 4.13: He II 4686 Å flux evolution, where the solid line indicates a power-law plus plateau fit to the data. Appears as Figure 13 in Murphy-Glaysher et al. (2022) ['V392 Persei: A γ-ray bright nova eruption from a known dwarf nova', Murphy-Glaysher et al., Mon. Not. R. Astron. Soc., 514, 6183, 2022 DOI `https://doi.org/10.1093/mnras/stac1577`].

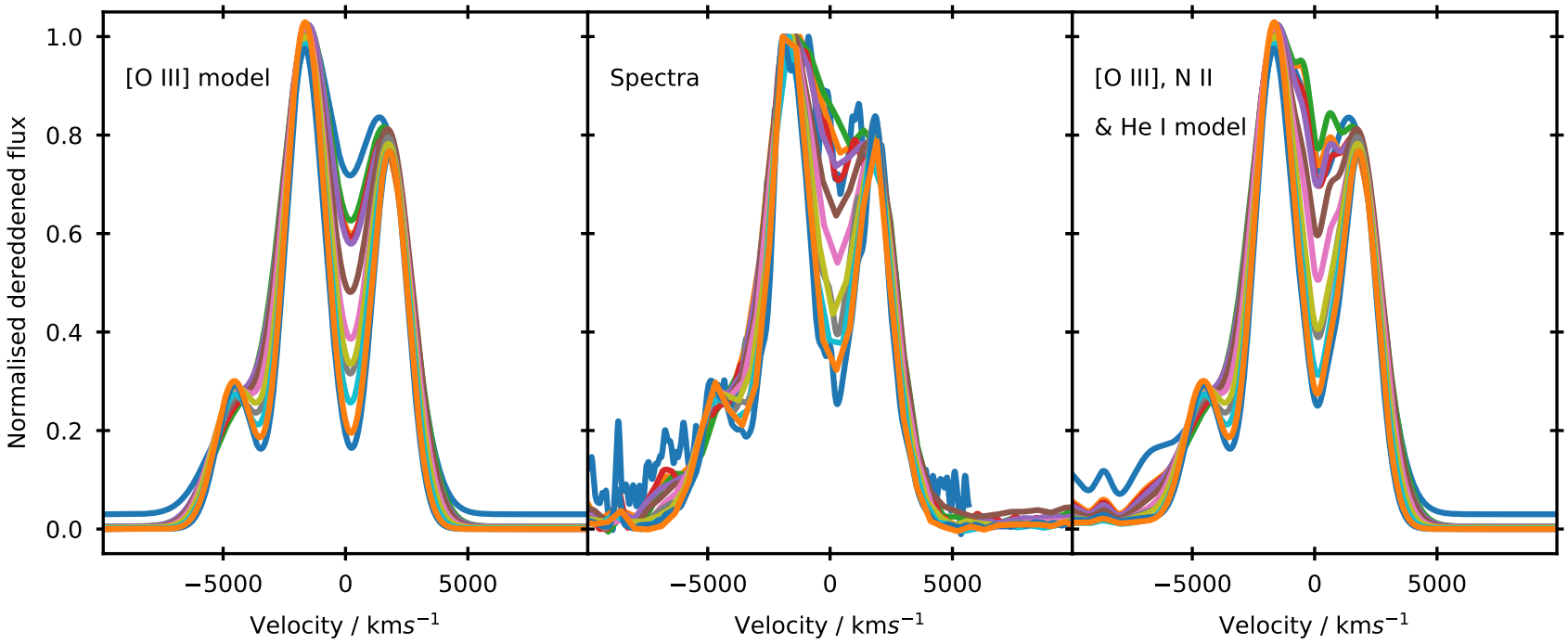

Figure 4.14: Evolution of the [O III] 4959+5007 Å profile from days 77–212 post-eruption. **Centre:** observed line profiles. **Left:** [O III] line profile models. **Right:** [O III] models including emission from N II 5001 Å, He I 5016 Å, and Hβ ($-8727\,\mathrm{km\,s^{-1}}$). Appears as Figure 14 in Murphy-Glaysher et al. (2022) ['V392 Persei: A γ-ray bright nova eruption from a known dwarf nova', Murphy-Glaysher et al., Mon. Not. R. Astron. Soc., 514, 6183, 2022 DOI `https://doi.org/10.1093/mnras/stac1577`].

The nebular [O III] flux was measured by modelling the 5007 Å component with a symmetric pair of Gaussians offset equally either side of the rest wavelength. The 4959 Å was simultaneously modelled by scaling the 5007 Å profile. The blueward peak from the 4959 Å profile overlaps with the redward outer peak of Hβ. Thus, to de-blend [O III] and Hβ, we included Hβ (based on the Hα profile) in the nebular [O III] model (see Section 4.4). In addition, we incorporated N II 5001 Å and He I 5016 Å lines using single Gaussians with widths matching the central Hα peak.

Figure 4.14 shows the evolution of the nebular [O III] 4959+5007 Å profile (days 77–212 post-eruption) as it transitions toward the 'frozen-in' state. Initially, the space between the two 5007 Å peaks was 'filled' by emission from N II 5001 Å and He I 5016 Å. As the relative strength of [O III] increased the impact of N II and He I diminished.

The left hand panel of Figure 4.15 presents the nebular [O III] profile in higher resolution. The top plot shows the pre-frozen evolution seen in Figure 4.14. The middle plot shows the frozen-in phase between days 220–351. The bottom plot (days 448–854) shows weakened [O III] (blue; with N II, He I, and Hβ again evident). Here, the orange line shows the low resolution profile obtained 854 days post-eruption, when [O III] was no longer detectable.

The flux evolution of [O III] 4959 Å and [O III] 5007 Å is shown in Figure 4.10. The first flux measurements are from day 77, yielding $(2.72 \pm 0.17) \times 10^{-10}\,\mathrm{erg\,s^{-1}\,cm^{-2}}$ and $(9.45 \pm 0.26) \times 10^{-10}\,\mathrm{erg\,s^{-1}\,cm^{-2}}$ for 4959 Å and 5007 Å, respectively (a ratio of 3.5 ± 0.2). We fit the flux of both the 4959 Å and 5007 Å contributions by linking both to a power law with index -1.88 ± 0.10. From day 346, the rate of decline steepened and the flux ratio between the components began to decrease.

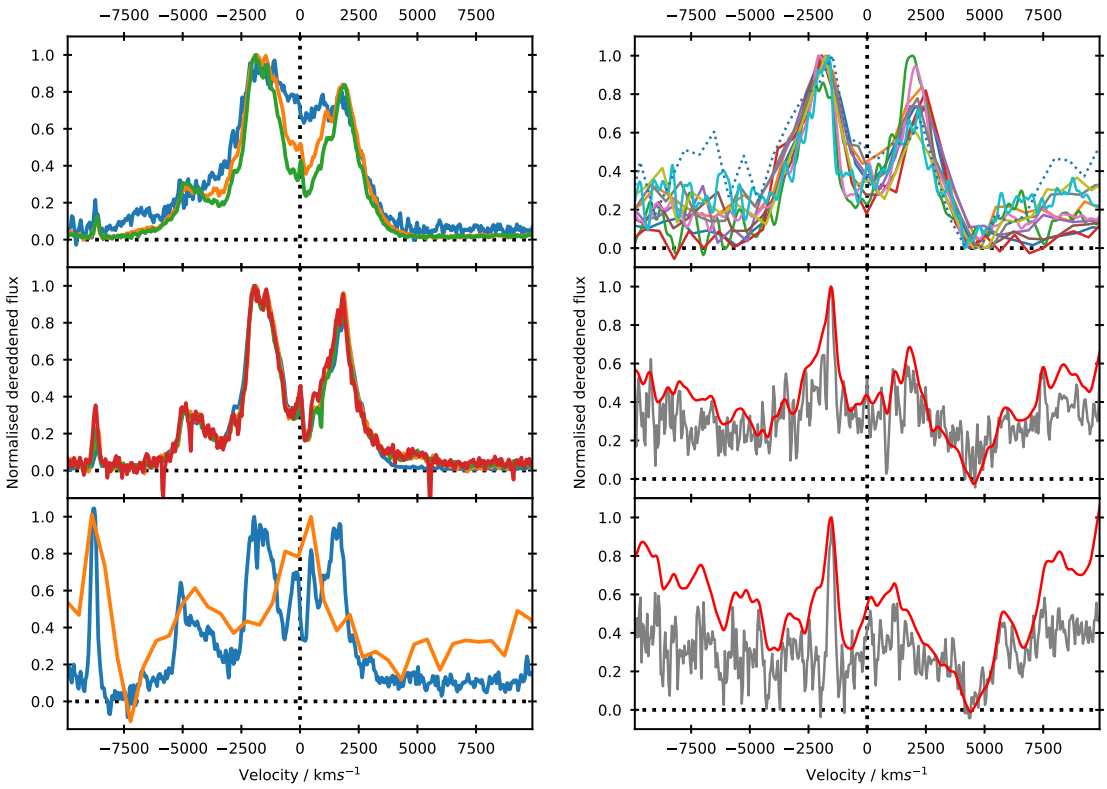

Figure 4.15: **Left:** Evolution of the high resolution [O III] 4959+5007 Å profile. Top panel, showing the transition to the 'frozen-in' state (as shown in low resolution in Figure 4.14). The middle panel shows profile 'frozen-in' between days 220-351 post-eruption. The bottom panel shows time-averaged data for the late nebular phase (blue), where Hβ ($-8727\,\mathrm{km\,s^{-1}}$) is now similar in strength to [O III] 5007 Å. The orange line shows the post-nova data from day 854, here only He I 5016 Å remains. **Right:** [O III] 4363 Å low resolution profile evolution, SPRAT data are shown at their native resolution, while Hiltner 2.4 m data have been Gaussian smoothed to match. The top panel shows data from days 82–212, where the profile is 'frozen-in'. The middle and bottom panels show the average profile between days 220–351 and 448–854, respectively for the low resolution (red) and high resolution (grey) spectra. By this time, Hγ has reasserted its dominance (at $\sim -1600\,\mathrm{km\,s^{-1}}$). Appears as Figure 15 in Murphy-Glaysher et al. (2022) ['V392 Persei: A γ-ray bright nova eruption from a known dwarf nova', Murphy-Glaysher et al., Mon. Not. R. Astron. Soc., 514, 6183, 2022 DOI `https://doi.org/10.1093/mnras/stac1577`].

4.9 Auroral [O III] 4363 Å

Similar to its nebular cousins, auroral [O III] 4363 Å was visible in the initial post-first Sun constraint spectra, and this emission rivalled the Hα line. The line profile evolution is shown in the right-hand panels of Figure 4.15. The top plot presents days 82-212 and, unlike the nebular lines, the auroral profiles are already frozen-in. The signal-to-noise for the auroral profile rapidly diminished, as such, the middle and bottom panels simply show time averaged low- (red) and high-resolution (grey) spectra between days 220–351 and 448–854, respectively. While the low-resolution spectra suggest changes in the relative intensity of the two components, in the high-resolution spectra (days 220–351) we see that the auroral structure has faded with narrow Hγ emission becoming more dominant. By the post-nova phase, evidence for auroral [O III] has largely disappeared leaving just the narrow Hγ line.

The [O III] 4363 Å flux was measured by fitting the profile with a similar model to [O III] 5007 Å combined with a Hα-based profile for Hγ. We also incorporated He I 4388 Å emission using a single Gaussian matched to the width of the Hα central peak. The flux measurements for [O III] 4363 Å are shown in Figure 4.10. The first measurement (day 77) yielded $(1.76 \pm 0.33) \times 10^{-10}\,\mathrm{erg\,s^{-1}\,cm^{-2}}$, with the flux evolution described by a power law with index -2.72 ± 0.46.

4.10 Other P-class neon novae

Four P-class novae listed in Strope et al. (2010), i.e., novae with a pseudo-plateau in their otherwise smoothly declining light curve, showed neon lines in their spectra. Their t_2 decline times ranged from 1 day (V838 Her) to 20 days (QU Vul). Fe II emission was present in the early spectra of QU Vul (Rosino et al., 1992) and

V1974 Cyg (Chochol et al., 1993; Rafanelli et al., 1995). There was no mention of Fe II in the spectra of V838 Her (Vanlandingham et al., 1996), and spectra of V351 Pup were only available from 136 days after eruption (Saizar et al., 1996). Expansion velocities decreased with decline time, and ranged from $1700 - 4200\,\mathrm{km\,s^{-1}}$, with double P Cygni profiles evident in the Balmer lines in early spectra of QU Vul, V1974 Cyg and V838 Her (Chochol et al., 1993; Rafanelli et al., 1995; Rosino et al., 1992; Vanlandingham et al., 1996). V1974 Cyg is a proposed magnetic CV, with $P = 0.08\,\mathrm{d}$ (Chochol et al., 1997). During the early evolution, there are no substantial differences between the spectra of these four and V392 Per. However, there is no evidence for similar late-time, narrow-line, behaviour in these systems (see Section 6.2).

4.11 *Swift* X-ray and UV observations

Swift observations commenced as soon as V392 Per emerged from the first Sun constraint on 2018 July 20 (Darnley et al., 2018b). The *Swift*/UVOT photometry is shown in Figure 3.6. Although starting much later, the near-UV light curves match the late decline and approximately flat post-nova phases seen in the optical. There is a slight upward trend in the near-UV brightness during the post-nova phase. The system is consistently fainter through the uvm2 filter (which lies between the uvw1 and uvw2 filters, and samples the 2175 Å 'bump' in the interstellar extinction curve), suggestive of high extinction. This is consistent with the reddening value of $E(B-V) = 0.7$ determined in Section 3.8.

The *Swift*/XRT light curve is presented in the left-hand panel of Figure 4.16. The plot at the top (black) shows the XRT count rate. A rapid decline in counts is seen from days 83–97, after which the counts remain approximately flat until entry into the second Sun-constraint. Upon exiting the second constraint, the XRT counts

remained slightly elevated. The X-ray HR [defined as counts (0.8–10 keV) / counts (0.3–0.8 keV)] is shown in the bottom panel (red). The HR is approximately constant (although slightly decreasing) from day 112 onward. However, the HR at day 83 is clearly lower (softer), and between days 83–97 there is a gradual hardening. Here we propose that the softer emission seen between days 83–97 is the tail of the super-soft source (SSS) phase of V392 Per.

The UVOT photometry was initially produced using an older calibration file, which over-corrected for the degradation of the UVOT detectors. The updated calibration was released in 2020. The right panel of Figure 4.16 presents a comparison between the *Swift*/UVOT uvw2 lightcurve and the XRT light curve; here the final decline in the near-UV is particularly evident. From $\sim$ 300 days post-eruption, the XRT count rate and uvw2 photometry appear roughly correlated. This suggests that the post-nova near-UV and X-ray emission have a similar origin.

4.11.1 X-ray spectral modelling

X-ray spectral modelling was performed independently but checked against modelling performed by Dr Kim Page. Figures 4.17 and 4.18 show *Swift*/XRT spectra from four epochs. For each epoch the upper panel shows the data (black) and best fit model (red), while the lower panel shows model residuals as a ratio. The XRT spectra were fitted using a combination of a black-body and collisionally excited plasma (Astrophysical Plasma Emission Code, or APEC: Smith et al., 2001) components, where appropriate. All spectra were modelled using a fixed column ($N_{\rm H} = 4.8 \times 10^{21}\,{\rm cm}^{-2}$; equivalent to $E(B-V) = 0.7$, converted using Equation 4.12, Equation 1 from Güver & Özel, 2009). Table 4.1 summarises the results of the fitting. We note that if $N_{\rm H}$ were permitted to vary freely, larger values ($\sim 10^{22}\,{\rm cm}^{-2}$) were obtained (see Section 6.2). The choice of column makes little difference to the resulting findings.

$$N_H = (2.21 \pm 0.09) \times 10^{21}\, A_V\, \mathrm{cm}^{-2} \tag{4.12}$$

The spectra in Figure 4.17 show the XRT data taken 83 days post-eruption (top) and the combined spectra between days 89–97 (bottom), both taken after exiting from the first Sun constraint. On day 83, the count rate was $0.06 \pm 0.01\,\mathrm{s}^{-1}$ and the spectrum was relatively soft, with a HR of 2.7. By days 89–97 the count rate had dropped to $0.035 \pm 0.003\,\mathrm{s}^{-1}$, and the HR had hardened to 4.4 and then to 6.3. These spectra correspond to the first three data points in Figure 4.16 and are the softest X-ray spectra taken of V392 Per. These first two spectra show clear count rate excesses at low energies and, as such, we fitted the earliest spectrum using the combination of a black-body ($k_\mathrm{B}T = 62^{+17}_{-14}\,\mathrm{eV}$) and hot plasma, APEC, component.

The day 89–97 spectra required an additional and hotter APEC component to account for the emission $> 5\,\mathrm{keV}$ that is not seen in the day 83 spectrum, likely due to the shorter integration. Given these spectra, the declining soft X-ray flux during this period, and the optical spectra at the time, we conclude that we are observing the tail of the super-soft source stage of V392 Per, and that the SSS ended at $97\,\mathrm{d} < t_\mathrm{SSS,off} < 112\,\mathrm{d}$. The spectra in Figure 4.18 show the XRT data between days 112–361 (top) and 449–849 (bottom). These are harder and clearly lack the SSS component. Here, both spectra are modelled using a pair of APEC components, with the best fit temperatures unchanged between the two epochs, although the count rate is higher at later times.

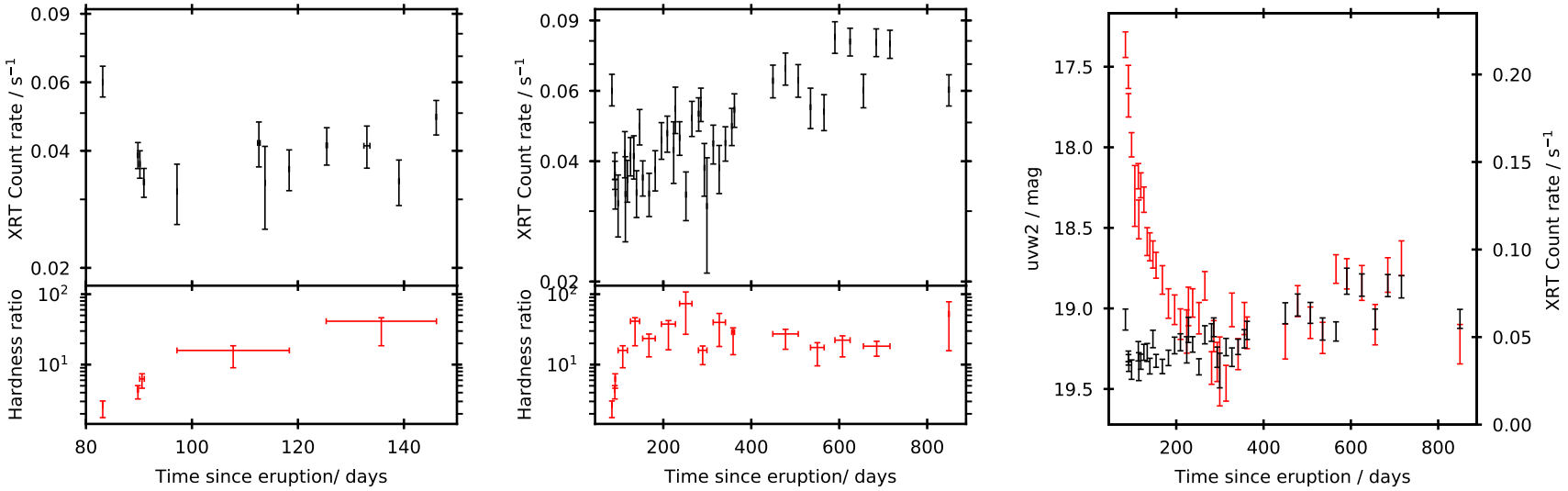

Figure 4.16: **Left and centre:** *Swift*/XRT observations of V392 Per. The upper panel shows the count rate, the lower panel shows the hardness ratio: counts(0.8–10 keV) / counts(0.3–0.8 keV). **Right:** *Swift*/XRT count rate (black) compared to the *Swift*/UVOT uvw2 photometry (red). Appears as Figure 8 in Murphy-Glaysher et al. (2022) ['V392 Persei: A γ-ray bright nova eruption from a known dwarf nova', Murphy-Glaysher et al., Mon. Not. R. Astron. Soc., 514, 6183, 2022 DOI `https://doi.org/10.1093/mnras/stac1577`].

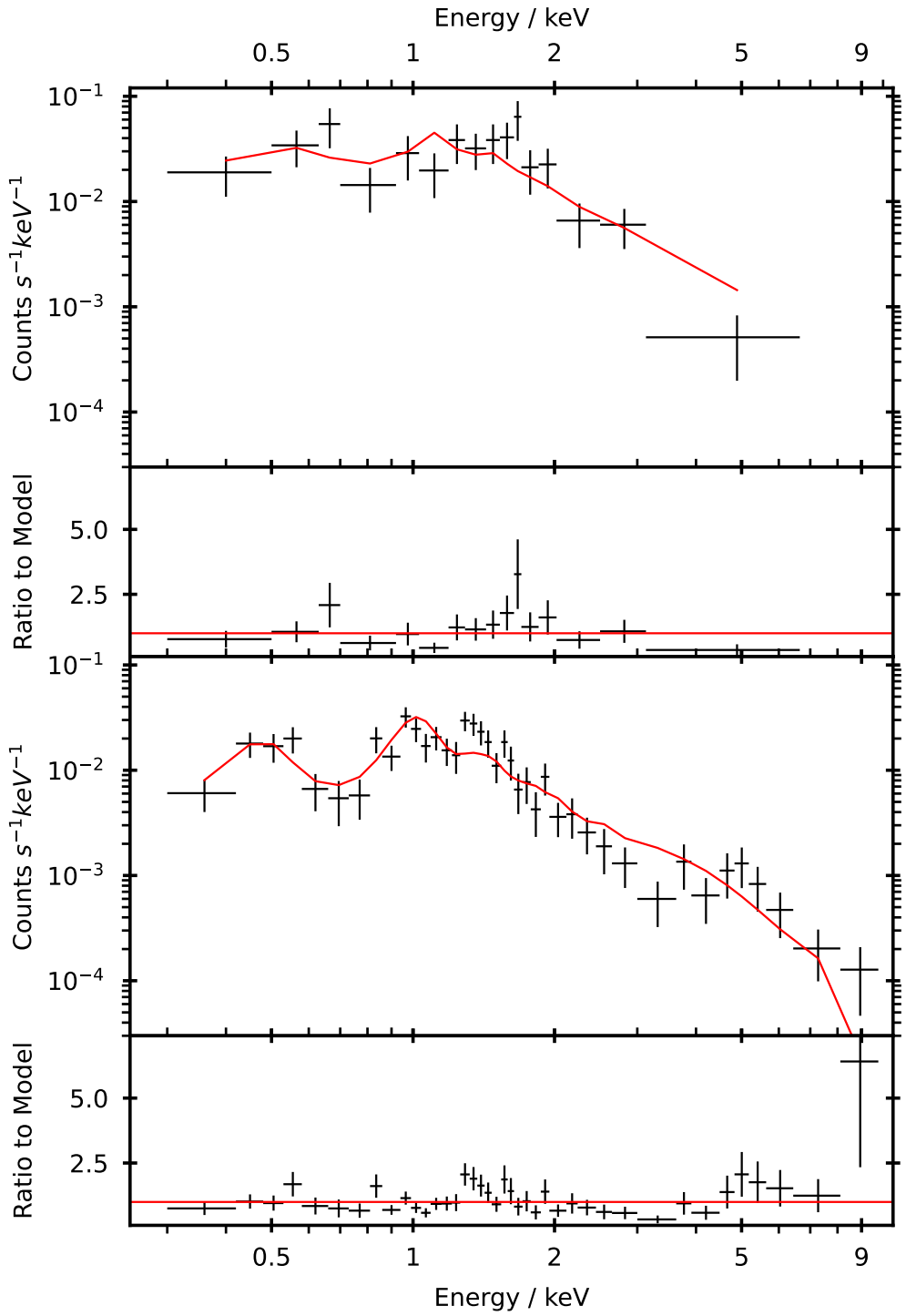

Figure 4.17: *Swift*/XRT spectra of V392 Per (black) and best-fit models (red), residuals included underneath. **Top:** single observation, 83 days post-eruption. **Bottom:** combination of observations 89–97 days post-eruption. Modified from Figure 16 in Murphy-Glaysher et al. (2022) ['V392 Persei: A γ-ray bright nova eruption from a known dwarf nova', Murphy-Glaysher et al., Mon. Not. R. Astron. Soc., 514, 6183, 2022 DOI `https://doi.org/10.1093/mnras/stac1577`].

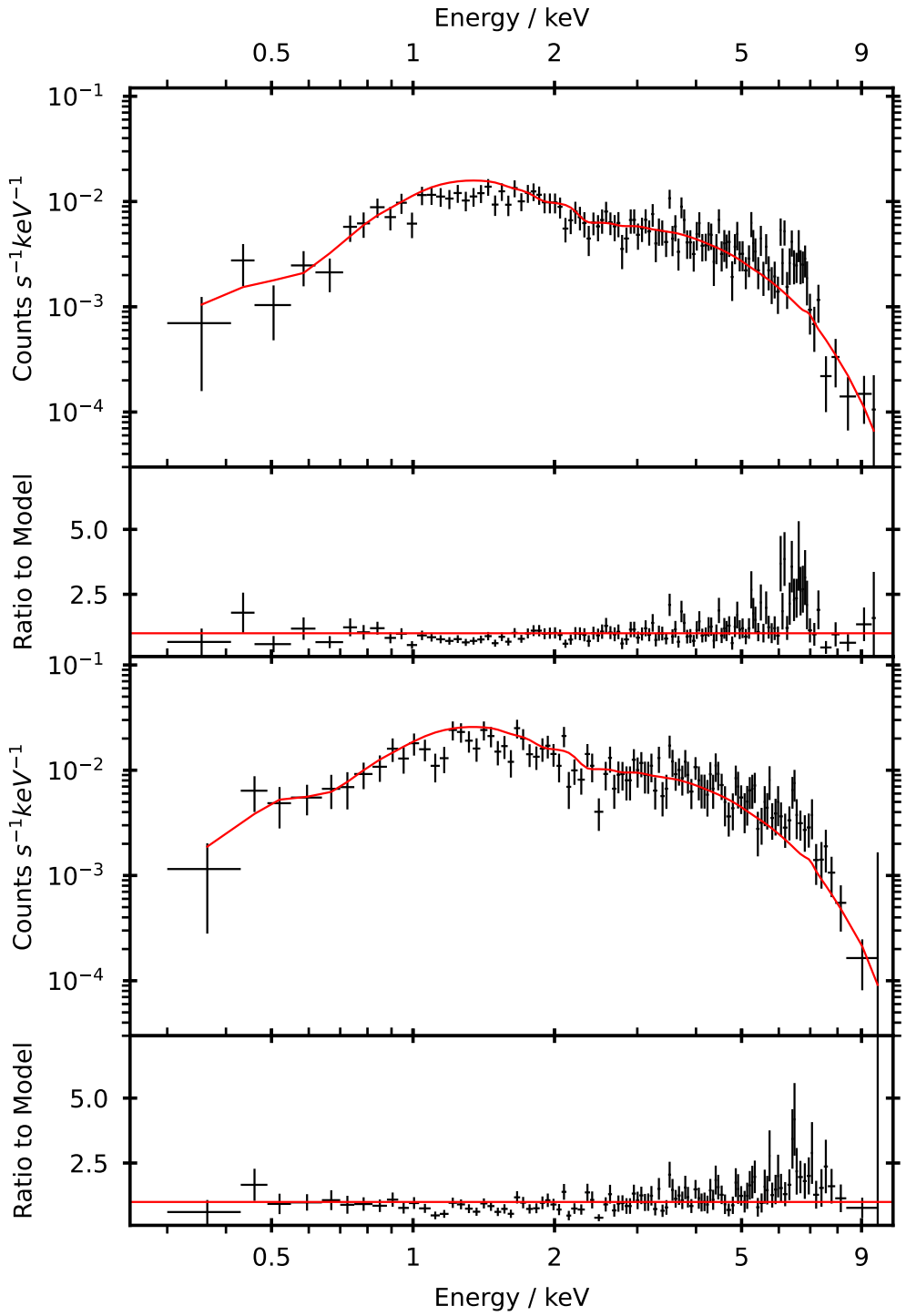

Figure 4.18: *Swift*/XRT spectra of V392 Per (black) and best-fit models (red), residuals included underneath. **Top:** 112–361 days post-eruption. **Bottom:** combination of observations 449–849 days post-eruption. Modified from Figure 16 in Murphy-Glaysher et al. (2022) ['V392 Persei: A γ-ray bright nova eruption from a known dwarf nova', Murphy-Glaysher et al., Mon. Not. R. Astron. Soc., 514, 6183, 2022 DOI `https://doi.org/10.1093/mnras/stac1577`].

Table 4.1: Fits to *Swift*/XRT spectra with $N_{\rm H} = 4.8 \times 10^{21}\,{\rm cm}^{-2}$. The third column shows the required model components. Subsequent columns record the temperature and normalisation of the required components, black-body, first APEC, and second APEC, respectively. The final column reports the goodness of fit, the (modified) Cash statistic per degree of freedom (C stat / d.o.f.). Appeared as Table 2 in Murphy-Glaysher et al. (2022) ['V392 Persei: A γ-ray bright nova eruption from a known dwarf nova', Murphy-Glaysher et al., Mon. Not. R. Astron. Soc., 514, 6183, 2022 DOI `https://doi.org/10.1093/mnras/stac1577`].

Time / days	Exp. time / ks	Components	$kT_{\rm BB}$ / eV	Norm$_{\rm BB}$ / 10^{-3}	$kT_{\rm APEC1}$ / keV	Norm$_{\rm APEC1}$ / 10^{-3}	$kT_{\rm APEC2}$ / keV	Norm$_{\rm APEC2}$ / 10^{-3}	C stat / d.o.f.
83	1.6	bb+apec	62^{+17}_{-14}	$0.8^{+3.0}_{-0.6}$	$2.3^{+1.2}_{-0.5}$	$2.0^{+0.4}_{-0.4}$	...	...	87 / 74
89–97	12.0	bb+apec+apec	48^{+10}_{-8}	2^{+5}_{-1}	$1.2^{+0.2}_{-0.1}$	$0.5^{+0.2}_{-0.1}$	> 4.2	$0.5^{+0.2}_{-0.1}$	208 / 192
112–361	43.6	apec+apec	...	...	< 0.06	< 2000	> 58.3	$1.93^{+0.08}_{-0.08}$	667 / 587
449–849	19.8	apec+apec	...	...	$0.08^{+0.08}_{-0.05}$	14^{+757}_{-14}	> 57.2	$3.0^{+0.1}_{-0.1}$	548 / 537

4.12 Summary

In this chapter, we discussed the method by which the spectra were absolute flux calibrated (and dereddened). We presented flux calibrated, dereddened spectra from the LT and the Hiltner 2.4 m telescope. We discussed the Balmer line evolution, and the presence of the P Cygni absorption components in Balmer lines. We presented the P Cygni velocities and the Fermi-LAT light curve as potential evidence of multiple ejections occurring during the eruption, with the ejection components colliding and shocking to produce γ-ray emission. The evolution of the He I 6678 Å and 7065 Å line fluxes and the He II 4686 Å line flux were discussed, as well as the flux evolution of nebular and auroral [O III]. V392 Per was compared with other P-class neon novae. Finally, we presented the X-ray and UV observations of the V392 Per eruption. The XRT count rate and *Swift*/UVOT uvw2 photometry are roughly correlated from $\sim$ 300 days post-eruption, suggesting the origin of the emission is similar. We were able to observe the tail of the super-soft source stage of the eruption, but most of this stage was missed due to the Sun constraint. The X-ray light curve and spectra indicate the presence of ongoing hard X-ray emission. In the next chapter, we present preliminary photoionization diagnostics of the early nebular spectra of V392 Per.

Chapter 5

Photoionization

5.1 Nova Shells

The material ejected during a nova eruption forms an expanding shell centred on the position of the nova system. After sufficient time has passed, the shell can be resolved in images of the nova. The time required for the shell to be resolved depends on the distance to the nova and the ejecta expansion velocity, as these factors will determine the angular size, and the resolving power of the telescope used to observe the shell.

Many nova shells have been identified due to directed follow-up observations at known nova eruptions. Cohen (1985) found nova shells around 8 of the 17 novae observed in their study of the brightest and closest known novae, whereas in their study of novae in the Southern sky, Gill & O'Brien (1998) were able to resolve shells around 4 of the 17 systems imaged. Similarly, Downes & Duerbeck (2000) used ground-based and space-based observations, and resolved shells around 14 out of 30 systems targeted. However, they were unable to find the shell of RW Umi, which

was previously resolved, as it had faded below the limits of detectability in the five years since it was last observed by Slavin et al. (1995). Expansion parallax of nova shells is regularly used to determine or refine distance estimates to nova systems, including by the researchers mentioned above. However,the distance estimates are necessarily dependent on the assumed (usually spherical) geometry.

Similar searches of the sky around 15 cataclysmic variables (dwarf novae and VY Scl systems) yielded no detected shells (Schmidtobreick et al., 2015). An in-depth search of the sky around 101 cataclysmic variables found one shell around the 24 nova-like variables studied, and tentative evidence of a shell around one dwarf nova, as well as a possible light echo from the 2001 eruption of the nova V2275 Cyg, hinting at the presence of a nebula from a previous nova eruption (Sahman et al., 2015).

Harvey et al. (2020) conducted a search of archival multiband Wide-field Infrared Survey Explorer satellite images of 12 reasonably bright nova eruptions that had no known nova shell, but which reached their optical peak 15 or more years prior to the start of the study in 2016. They found two previously undiscovered nova shells, around V4362 Sgr (Sagittarii, 1994) and DO Aquilae, which erupted in 1925.

5.1.1 Imaging and spectroscopy of nova shells

Nova shell imaging and spectroscopy have provided a wealth of information on the morphology and kinematics of the nova ejecta. Imaging has been carried out across the electromagnetic spectrum, covering broadband optical, UV, infrared and radio. Furthermore, narrowband filters such as [O III] and Hα + [N II] have been used to identify the shapes of the gas shells of those species. Some shells have been identified with clumps or knots of denser material set amongst areas of less dense material. Spectroscopic observations of nova shells can be used to find velocities of different

clumps within the ejecta, or of different regions of a more uniform appearing shell.

Payne-Gaposchkin (1957) produced a summary of earlier speculation on whether the shape of the ejecta could be inferred from the shape of emission lines. Since then, the approach has been utilized by other researchers (e.g., Ribeiro et al. (2009, 2013), Munari et al. (2011), Harvey et al. (2016, 2018, 2020) and Pavana et al. (2020)).

Figure 5.1 shows a selection of nova remnants, exhibiting different geometries. The top left panel shows an NIR image of V1280 Sco, revealing a bipolar morphology (Chesneau et al., 2012). The top right panel is a Nordic Optical Telescope (NOT) image of QU Vul, with a simple spherical shell (Santamaría et al., 2020), which had a measured radius of 2.1arcsec (Santamaría et al., 2022). The middle left and right panels show the remnants of T Aur and DQ Her (Santamaría et al., 2020), respectively. Both remnants have prolate, ellipsoid shells with clumpy equatorial waists and polar cones. T Aur and DQ Her measured 25.4 arcsec × 18.6 arcsec and 32.0 arcsec × 24.2 arcsec, respectively (Santamaría et al., 2022). The bottom left panel shows a composite image of GK Per, combining radio, X-ray and optical images (Takei et al., 2015). This remnant has a cylindrical structure with polar cones, with the dense purple region at the bottom right of the remnant corresponding to one of the polar cones (Harvey et al., 2016). The bottom right panel presents a Hubble Space Telescope image of the remnant of T Pyx. This image was used in the news release regarding a paper by Shara et al. (1997), as well as appearing as an Astronomy Picture Of the Day on the NASA website[1]. Modelling of the ionization structure of T Pyx by Pavana et al. (2019) implied the presence of bipolar conical shells and an equatorial ring.

[1] `https://apod.nasa.gov/apod/ap970925.html`

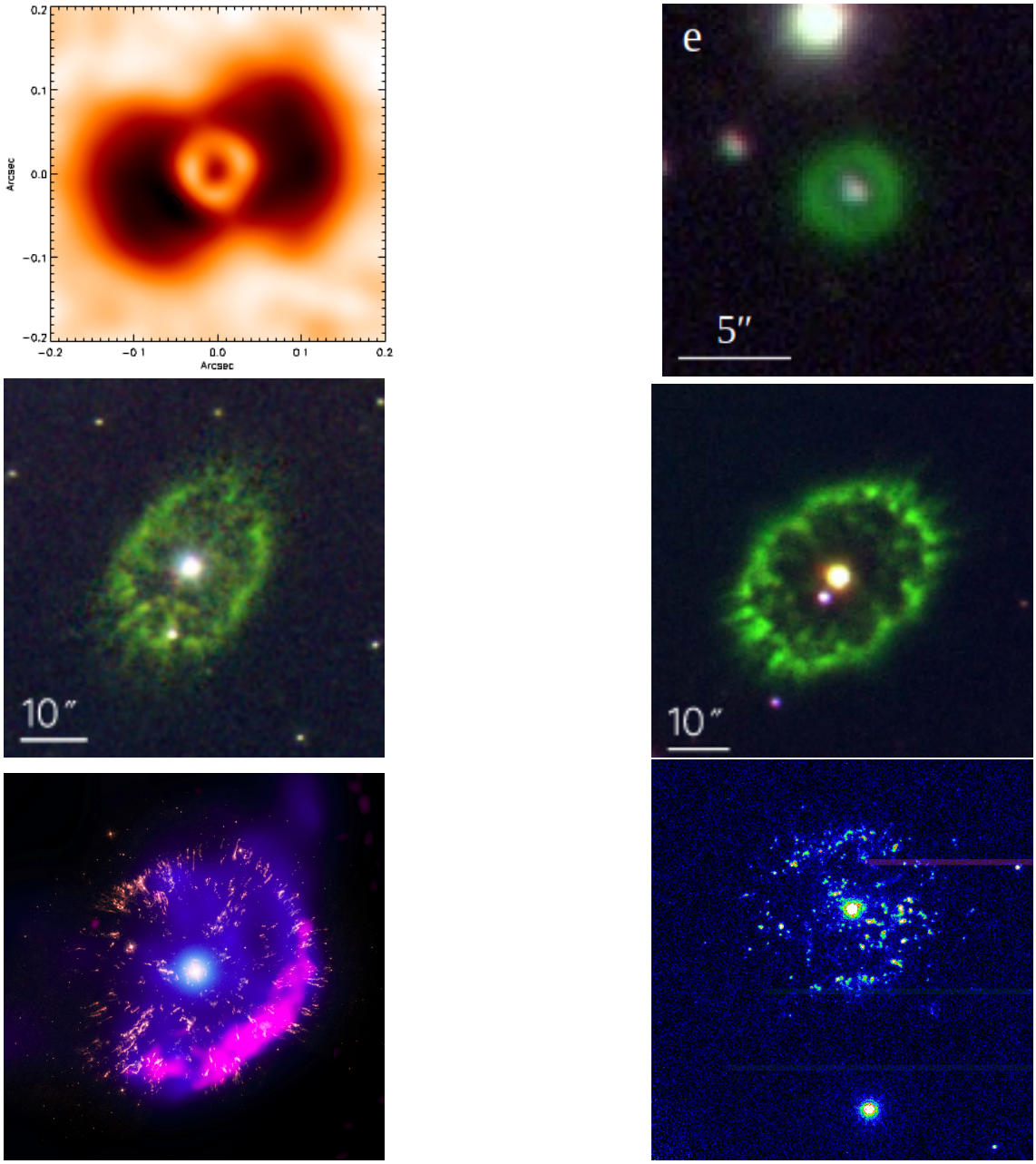

Figure 5.1: Top row: Bipolar shell of V1280 Sco (left: Chesneau et al., 2012) ['The expanding dusty bipolar nebula around the nova V1280 Scorpi', Credit: Chesneau O., et al., A&A, 545, A63, 2012, https://doi.org/10.1051/0004-6361/201219825 reproduced with permission ©ESO], QU Vul (right: Santamaría et al., 2022)['Spatiokinematic models of five nova remnants: correlations between nova shell axial ratio, expansion velocity, and speed class', Santamaria et al., Mon. Not. R. Astron. Soc., 512, 2003, 2022 DOI https://doi.org/10.1093/mnras/stac563]. Middle row: shells of T Aur (left) and DQ Her (right, both from Santamaría et al., 2020) 'Angular Expansion of Nova Shells', Santamaria et al., Astrophys. J., 892, 60, 2020 DOI https://doi.org/10.3847/1538-4357/ab76c5. Bottom row: GK Per (left: Takei et al., 2015) [Image Credit: X-ray: NASA/CXC/RIKEN/D.Takei et al; Optical: NASA/STScI; Radio: NRAO/VLA] and T Pyx (right: Shara et al., 1997). [Image credit: M. Shara, R. Williams, (STScI), R. Gilmozzi (ESO), NASA].

5.1.2 Shaping of ejecta

The shape of the ejected shell provides information about the nova eruption, including any shaping mechanisms that may occur, and about interactions with any earlier ejections of material, or with the interstellar medium. There appears to be a relationship between nova speed class and the morphology of the ejecta, with faster evolving eruptions approaching spherical symmetry (Slavin et al., 1995). In contrast, slower evolving systems have been found to have more of an ellipsoidal shape, with some systems having an equatorial ring, giving a bipolar appearance. However, Ribeiro (2011) found that this relationship does not always apply, particularly in the case of RN or potential RN systems with long orbital periods. The mechanism of shell formation is expected to be different for RNe, due to interaction with the pre-existing wind from the red giant.

Hutchings (1972) was one of the first to suggest that nova shells could be shaped in the form of polar cones of emission and an equatorial waist. There have also been indications of the presence of tropical rings in some systems (e.g. DQ Her Slavin et al., 1995). The orientation of the nova shell is linked to that of the binary. Depending on the orbital period and the ejecta velocity, the binary kinematics may play a greater or lesser role in the morphology of the ejecta, as the dynamical time over which the binary can influence the material ejected will vary. Systems in which the ejected material spends more time interacting with the secondary will experience a greater degree of 'mixing', which will act to smooth out any intrinsic asymmetry in the geometry of the ejecta. Therefore, systems with low ejection velocities and small binary separations produce a greater impact on the shape of their ejecta. In contrast, material ejected from systems with high ejection velocities and large orbital separations will experience less interaction and 'mixing', so the intrinsic asymmetry of the ejecta will persist after the shell has expanded beyond the orbital radius (Balick

& Frank, 2002; Frank et al., 2018).

Figure 5.2 illustrates different possible shell morphologies, viewed at an inclination of 90°, and produced using the 3D SHAPE[2] morpho-kinematic software (Steffen et al., 2011). The shell components presented are an ellipsoidal shell, equatorial ring or torus, tropical rings, polar rings, and different combinations of those components. Also presented are line profiles that would be produced by emission from the components shown, if viewed at that inclination.

Various groups have performed kinematic modelling of nova eruptions to see the likely shape of the shells, and how different interactions could affect the shape. A rotating WD reduces the shear between the envelope of the WD and the accreted material, as discussed in Porter et al. (1998). Shear velocities are highest in the plane of the orbit and can contribute to mixing between the accreted envelope and the WD material. The donor star imparts energy to the nova ejecta via the transfer of orbital angular momentum, which contributes to the asphericity of the ejecta, and the subsequent nova shell (Livio et al., 1990; Lloyd et al., 1997). However, early hydrodynamical models incorporating WD rotation predicted oblate shells (Fiedler & Jones, 1980; Lloyd et al., 1997), whereas observations revealed prolate nova shells (Slavin et al., 1995).

[2]https://wsteffen75.wixsite.com/website/

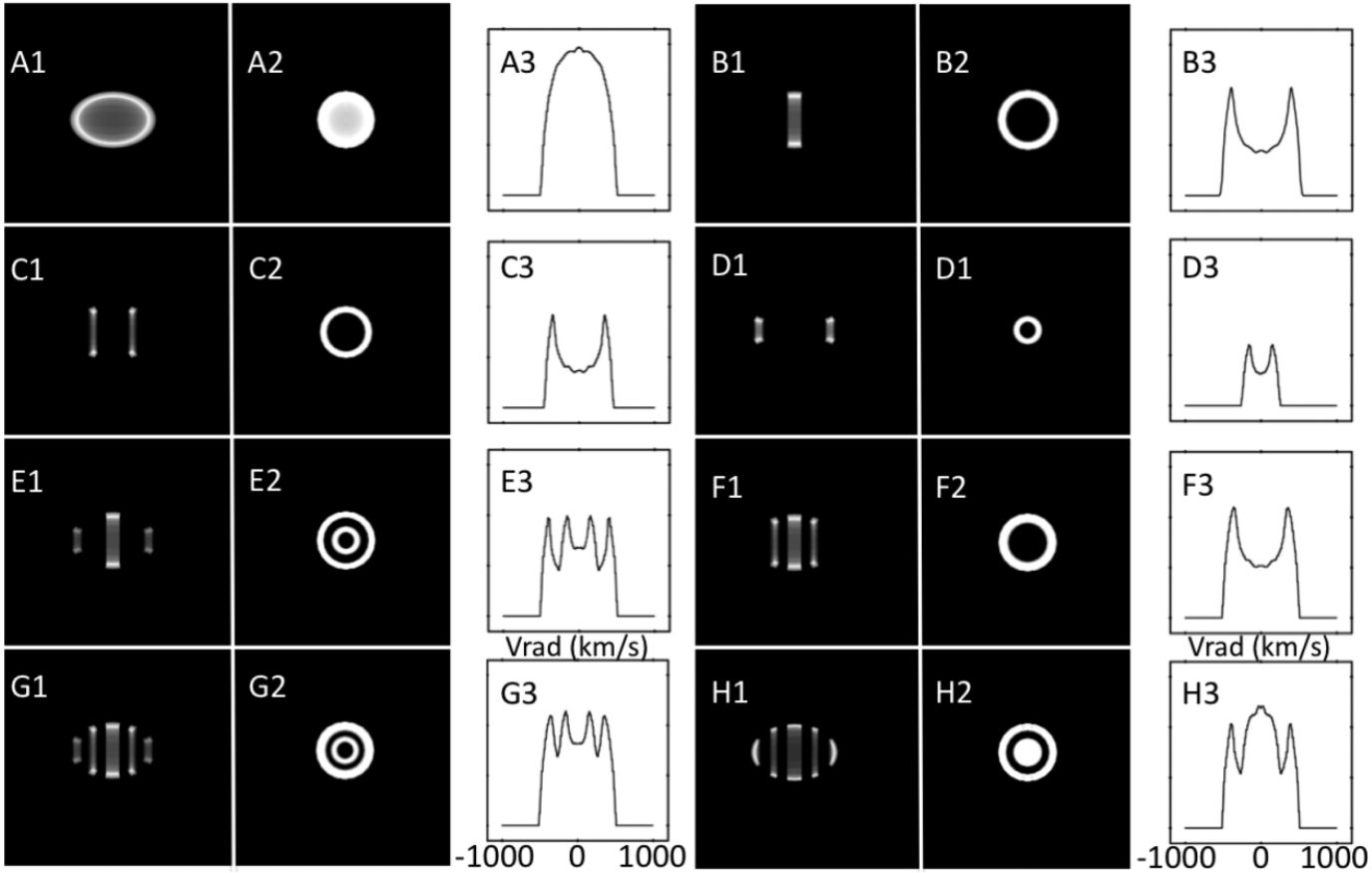

Figure 5.2: SHAPE models of possible nova shell morphologies, viewed at an inclination of 90 °. The models comprise combinations of one or more shell components, labelled A-H, representing A: an elliptical shell, B: an equatorial torus, C: tropical rings, D: polar rings, E: an equatorial torus and polar rings, F: an equatorial torus and tropical rings, G: equatorial torus, tropical rings and polar rings, and H: as G, but with polar caps rather than rings. The numbers 1 to 3 indicate the 2D image, the end-on view of the shell (with the velocity indicated by the brightness), and the 1D line profile predicted by the model, respectively. Figure appeared as Figure 6 in Harvey et al. (2020) ['Two new nova shells associated with V4362 Sagittarii and DO Aquilae', Harvey et al., Mon. Not. R. Astron. Soc., 499, 2959, 2020 DOI `https://doi.org/10.1093/mnras/staa2896`].

According to Porter et al. (1998), tropical cones can be formed as the ejecta sweeps up conical regions of relatively enhanced density around the WD. Indeed, the higher the rate of rotation of the WD, the more prolate will be the nova shell. The WD accretes stellar material and angular momentum from its donor, which is distributed around the WD envelope, and can increase its rotation. Rotation of the WD envelope reduces the effective gravity, thereby reducing the effective WD mass. The effective gravity (and mass) depends on the angle θ above or below the equator. The local radiative flux, and hence the local mass-loss rate driven by that flux, are θ-dependent, as the material within the envelope at the equator is less tightly-bound to the WD than that at the poles. More energy per unit mass is required to eject material with a given acceleration in the polar direction, so material is preferentially ejected in the orbital plane, rather than in the polar direction (Porter et al., 1998). For the three different rotation rates modelled, Porter et al. (1998) found that a cone formed around the donor star due to drag luminosity heating the ejecta, causing it to expand. Once the cones have formed, the faster moving ejecta sweeps the initial slow-moving ejecta into a shell, and the cones up into tropical rings, with the latitude of the rings increasing with the rate of rotation. The structure of the polar regions of the shell is not dependent on the rotation of the WD envelope, but the equatorial waist is narrower for higher rates of rotation, yielding a higher axial ratio.

The Richtmeyer-Meshkov instability is believed to be responsible for the clumping that occurs in ejecta (Toraskar et al., 2013). This instability relates to the mixing of two fluids of different density when they are accelerated, typically by a passing shock wave. Small perturbations develop, that grow with time, becoming more chaotic until the fluids mix. This process is also important for the formation of dust (Joiner, 1999; Gehrz et al., 2018), either silicate or carbonaceous.

5.2 Photoionization modelling of nova shells

Several groups have used spectral emission line flux ratios to constrain the ionization conditions within nova shells. For example, in their study of V5668 Sgr, Harvey et al. (2018) used CLOUDY (as described in Section 5.3: Ferland et al., 1998, 2013) to produce a grid of model oxygen to Hβ flux ratios, simulated using a range of different temperatures and densities. They compared the models with measurements of flux ratios from spectra taken 141 days after discovery of the eruption. The temperature and density estimates that best matched the measured flux ratios, along with an initial estimated structure, were used as input parameters for SHAPE to model the 3D morpho-kinematic structure of the gas in the nova shell. Harvey et al. (2018) compared observed line profiles with simulated spectra from SHAPE, based on the gas morpho-kinematic structure, to constrain the geometry of the shell. The modelled shell can be viewed from different angles to provide insight into inclination of the system.

In contrast, Mondal et al. (2019) produced a grid of 1792 nova shell models using CLOUDY, with free parameters of hydrogen density, effective temperature, ionizing luminosity, inner shell radius and shell thickness, from which they produced model spectra. Using their model spectra, they found ratios for various Balmer and helium emission lines (relative to Hβ) for all epochs between 5 and 120 days after eruption. Mondal et al. (2019) used observed spectra for several novae to estimate the effective temperature, shell size and thickness, and hydrogen and helium line ratios for each nova at a given epoch. By plotting Balmer line contour plots in the luminosity-hydrogen density phase space for models matching the parameters determined from the observed spectra, they used the intersection of the contours to provide estimates of the luminosity and N_H of the novae that were in good agreement with published values.

By allowing the relative abundance of key elements to vary within a grid of nova shell models, Pavana et al. (2019) used photoionization analysis at five epochs to identify relative abundances of those elements within the shell of T Pyx. In addition, the effective temperature, density of the gas, and the WD luminosity were determined. Furthermore, the evolution of the line profiles was used to produce pseudo-3D models to constrain the geometric evolution of the shell, including the evolving spatial distribution of individual ionized emission lines. As stated in Section 5.1.1, the overall structure of the shell of T Pyx was found to be a bipolar cone with equatorial rings. At the latest epoch, [O III] emission originated in the expanding ejecta, whereas hydrogen and helium lines were emitted from the inner region, consistent with emission from the accretion disk (Pavana et al., 2019).

5.3 Grid of nova shell models

In this section, we present a preliminary grid of models of nova shells, produced by varying three key parameters. We will compare these model shells and their predicted line ratios with measured line ratios from nebular spectra of V392 Per. The spectra, selected from those taken towards the end of the super-soft source phase, are the only two spectra that have flux measurements for all of the emission lines listed in Table A.7. The spectra were those taken 82 days and 89 days after eruption.

CLOUDY is an open-source code, developed to perform spectral synthesis and plasma simulation (Ferland et al., 1998, 2013, 2017). The version of CLOUDY used in this analysis was 17.02, as described by Ferland et al. (2017).

We used an array of models that varied the effective temperature $T_{\rm eff}$ of the ionizing source (i.e., the WD), the electron density n_e of the shell, and its metallicity.

Here, metallicity describes the abundances of different elements in the ejecta, relative to the abundance profile of the very fast nova V1500 Cyg (Ferland & Shields, 1978). The values considered for $T_{\rm eff}$, n_e and metallicity are shown in Table 5.1. The other parameter that determines the ionization state of the nova shell is the ionizing luminosity. However, during this preliminary analysis we did not vary the luminosity of the white dwarf in the grid of models. The ionizing luminosity at both epochs was set to $\log_{10}(L/L_{\odot}) = 4.25$, which is a standard luminosity used to model novae in CLOUDY.

To determine the inner radius of the ejecta shell at a given epoch, the average expansion velocity of $v = 4000\,{\rm km\,s^{-1}}$ was multiplied by the time since eruption. The inner radius was given by 2.84×10^{15} cm and 3.08×10^{15} cm, respectively, for 82 days and 89 days after eruption. The covering factor is the fraction of the surface area of a sphere centred on the ionizing source that contains gas, i.e., it is $\Omega/4\pi$, where $0 \leq \Omega/4\pi \leq 1$. In the grid of models, the covering factor was set to 0.3. The filling factor is a measure of the radial extent of clumping within the gas, and was set to 0.01 in the grid of models.

5.4 Emission lines evaluated

For each model in the grid, and for each epoch, three different line ratios were calculated in the preliminary analysis. The line ratios considered were various combinations of [O III], Hα and Hβ.

The ratio of [O III 5007] to [O III 4363] at a given epoch:

$$\mathrm{rO3} = \frac{\log_{10}\ F_{[\mathrm{O\,III}\,5007]}}{\log_{10}\ F_{[\mathrm{O\,III}\,4363]}} \tag{5.1}$$

Table 5.1: Input parameters for grid of CLOUDY models.

$T_{\rm eff}/K$	$\log_{10}(n_e)$	$\log_{10}$ (metallicity ratio)
1.0×10^4	4.0	-1.0
4.0×10^4	4.3	-0.5
7.0×10^4	4.7	0.0
1.0×10^5	5 .0	0.5
4.0×10^5	5.3	1.0
7.0×10^5	5.7	-
1.0×10^6	6.0	-
4.0×10^6	6.3	-
7.0×10^6	6.7	-
1.0×10^7	7.0	-
4.0×10^7	7.3	-
7.0×10^7	7.7	-
1.0×10^8	8.0	-
4.0×10^8	8.3	-
7.0×10^8	8.7	-
1.0×10^9	9.0	-
4.0×10^9	-	-
7.0×10^9	-	-

where $F_{[\rm O\,III\,5007]}$ is the flux of [O III 5007] and $F_{[\rm O\,III\,4363]}$ is the flux of [O III 4363].

The ratio of [O III 5007] to Hβ at a given epoch:

$$\mathrm{O3Hb} = \frac{\log_{10}\ F_{[\rm O\,III\,5007]}}{\log_{10}\ F_{\rm H\beta}} \tag{5.2}$$

where $F_{[\rm O\,III\,5007]}$ is the flux of [O III 5007] and $F_{\rm H\beta}$ is the flux of Hβ.

The ratio of Hα to Hβ at a given epoch:

$$\mathrm{HaHb} = \frac{\log_{10}\ F_{\rm H\alpha}}{\log_{10}\ F_{\rm H\beta}} \tag{5.3}$$

where $F_{\rm H\alpha}$ is the flux of Hα and $F_{\rm H\beta}$ is the flux of Hβ.

For each epoch, I produced plots comparing the line ratios rO3 with O3Hb, and comparing rO3 with HaHb. Two versions of each plot were produced, where colour

represented either temperature or density (with the other parameter represented by the size of the data point). Since it is much easier to distinguish the colour of the data points rather than their size, separate plots were used to emphasize either the temperature or the density. An additional version of each plot was produced that focuses on a smaller region surrounding the measured line ratios for the emission from V392 Per at that epoch. The black and red ellipses are centred on the measured line ratios for V392 Per, and indicate the 1σ and 3σ errors.

The shape of the data point symbol signifies the elemental abundances of metals in the nova ejecta for that model, relative to that of V1500 Cyg, which is the standard abundance used in CLOUDY photoionization models of nova ejecta. The metallicities range from 10 times higher ($\log_{10}(\text{metals}) = +1$, right-pointing triangles) to 10 times lower ($\log_{10}(\text{metals}) = -1$, stars). Circles represent the standard nova abundance ($\log_{10}(\text{metals}) = 0$). Left-pointing triangles represent 3.2 times the standard nova abundance ($\log_{10}(\text{metals}) = -0.5$), with diamonds representing abundances 32% of the standard metallicity ($\log_{10}(\text{metals}) = 0.5$).

PyNeb is a code developed to analyse emission lines in gaseous nebulae (Morisset et al., 2020; Luridiana et al., 2015). In addition to calculating physical conditions in nebulae, PyNeb also computes atomic and elemental abundances and can be used to produce diagnostic plots. PyNeb was used to plot theoretical contours on the temperature-density plane for the [O III] nebular to auroral line ratio:

$$\text{Ratio} = \frac{\log_{10}\left(F_{[\text{O III}\,5007]} + F_{[\text{O III}\,4959]}\right)}{\log_{10}\left(F_{[\text{O III}\,4363]}\right)} \tag{5.4}$$

where $F_{[\text{O III}\,4959]}$ is the flux of [O III 4959].

5.5 Diagnostic plots 82 days after eruption

Figure 5.3 contains four panels showing the ratios rO3, O3Hb and HaHb expected for each model, 82 days after eruption. All four panels show the ratio of nebular to auroral [O III], or rO3, on the x-axis. In the two left panels, the ratio of [O III] 5007 Å to Hβ (O3Hb) is shown on the y-axis. The two right panels show the ratio of Hα to Hβ (HaHb) on the y-axis. In the two top panels, the colour and size of each data point represents the effective temperature and electron density of the model, respectively. In contrast, for the two lower panels, the colour represents the electron density of the model, and the size of the data point represents the effective temperature.

5.5.1 Temperature dependence of rO3 and O3Hb ratios

The left panels of Figure 5.3 have a "wave-like" shape, and there appears to be a bimodal distribution, split around an effective temperature of 10^7 K to 10^8 K. From the top left panel we see that, in general, the higher the temperature, the higher the ratio of rO3, and the lower the ratio of O3Hb. This shows that at higher temperatures, the ionization conditions favour emission from nebular [O III], rather than auroral [O III], and that the emission from nebular [O III] 5007 Å increases more slowly than that from Hβ.

The highest rO3 ratio is obtained when the metallicity is 10 times higher than the standard nova metallicity. Figure 5.4 shows the same information as the top left panel of Figure 5.3 in its bottom right panel, but also includes a separate panel for each of the five different metallicities considered. For high temperature conditions, the novae with the lowest metallicity exhibit similar, relatively low rO3 ratios, as

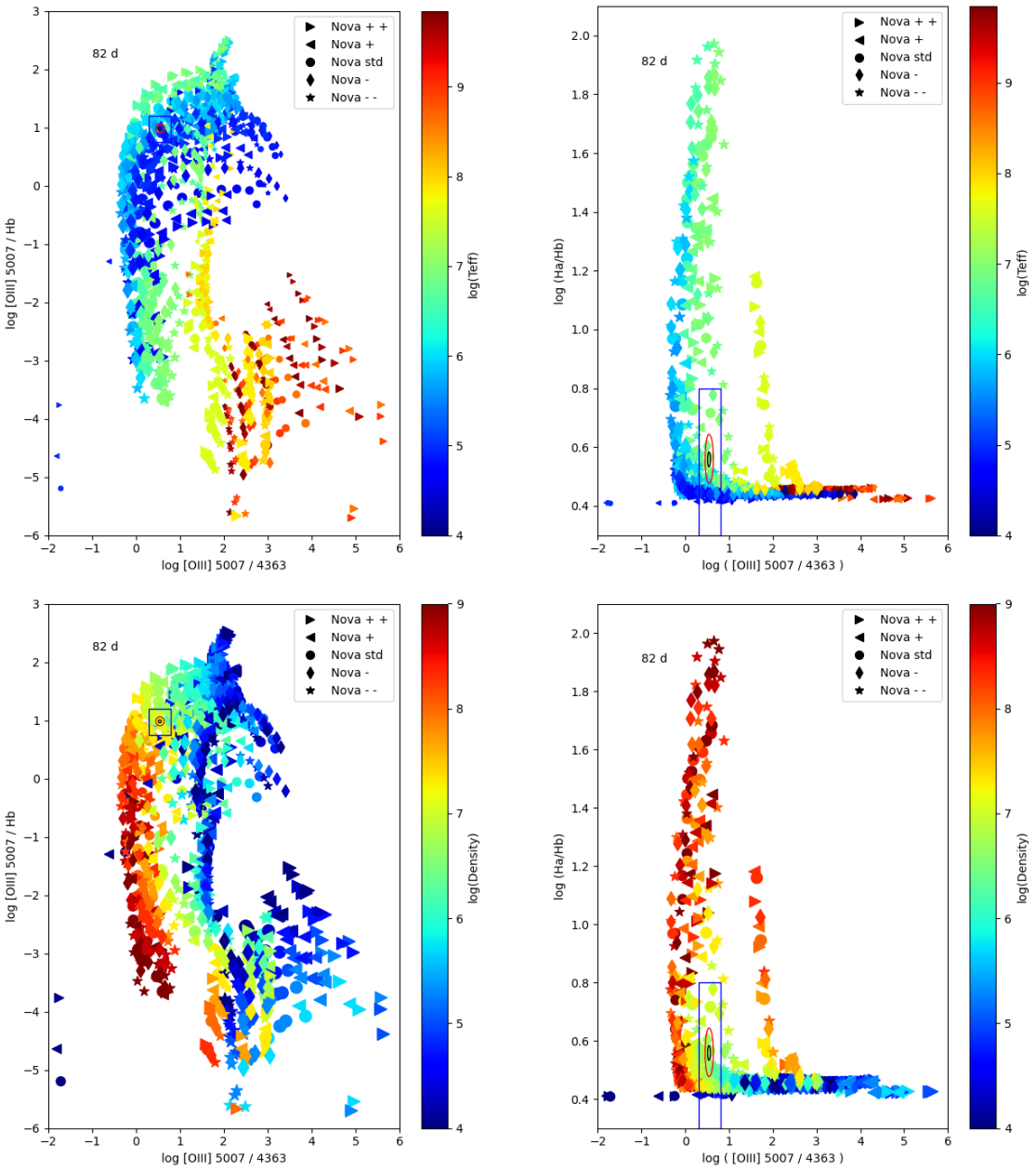

Figure 5.3: Comparison between O3Hb and rO3 ratios in the left panels, and between HaHb and rO3 ratios in the right panels, 82 days after eruption. In the top row, colour and size of the data points represent the temperature and density, respectively, of the models. In the bottom row, colour and size of the data points represent the density and temperature, respectively, of the models. In all panels, the blue rectangle shows the region in the vicinity of the ratios measured in the spectra of V392 Per, shown in Figure 5.8, with the 1σ and 3σ error ellipses shown in black and red.

shown by the number of stars and diamonds clustered around the rO3 ratio of 2–2.5 in Figure 5.4. As the metallicity of the model increases, so do the rO3 and HaHb ratios. That is, the higher the abundance of oxygen in the ejected gas, the more likely it is to be in nebular form, and by definition, the ratio of oxygen to hydrogen increases.

At slightly cooler temperatures (around 10^8 K), the rO3 ratio appears to be independent of metallicity, but as metallicity increases, the maximum ratio of O3Hb increases. For intermediate temperatures, as metallicity increases, so does the maximum O3Hb ratio. We can see lots of green triangles at the top of the left-most wave. There are also fewer branches at different O3Hb ratios. For the lowest temperatures, the maximum value of the rO3 ratio decreases as metallicity increases, whereas the ratio of O3Hb increases.

5.5.2 Density dependence of rO3 and O3Hb ratios

The bottom left plot of Figure 5.3 shows that the ratio rO3 decreases with increasing density. This is because nebular [O III] emission occurs in gas that was previously hot and dense, but has since cooled and expanded. The ratio O3Hb has relatively little dependence on density, as it covers a broad range of ratios, although the maximum ratio is lower for higher densities. The densest material, as shown by the dark red/ brown data points, has a ratio lower limit of around 10^{-4}. The high density points correspond to relatively low temperature points, and vice versa. At low densities, the higher metallicity models have higher rO3 ratios, as shown in Figure 5.5. This makes sense, as the lower overall gas density will compensate somewhat for the increased relative oxygen density due to the higher metallicity.

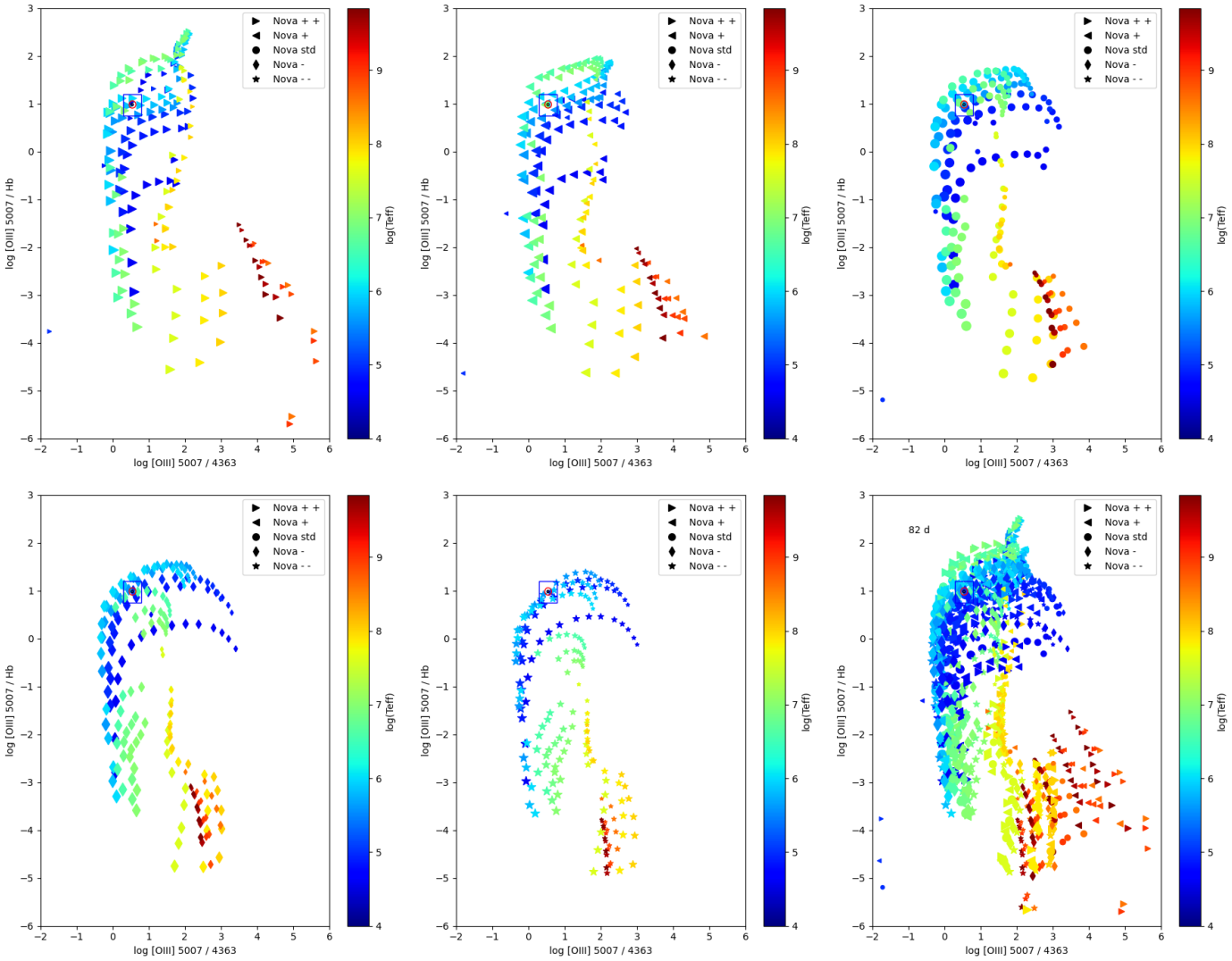

Figure 5.4: Comparison between O3Hb ratio and rO3 ratio 82 d after eruption, for different metallicity models. The metallicity is highest in the top left plot, then decreases along the top row, and then along the bottom row. The bottom right panel shows models of all metallicity values. Colour and size indicate the temperature and density of the model, respectively.

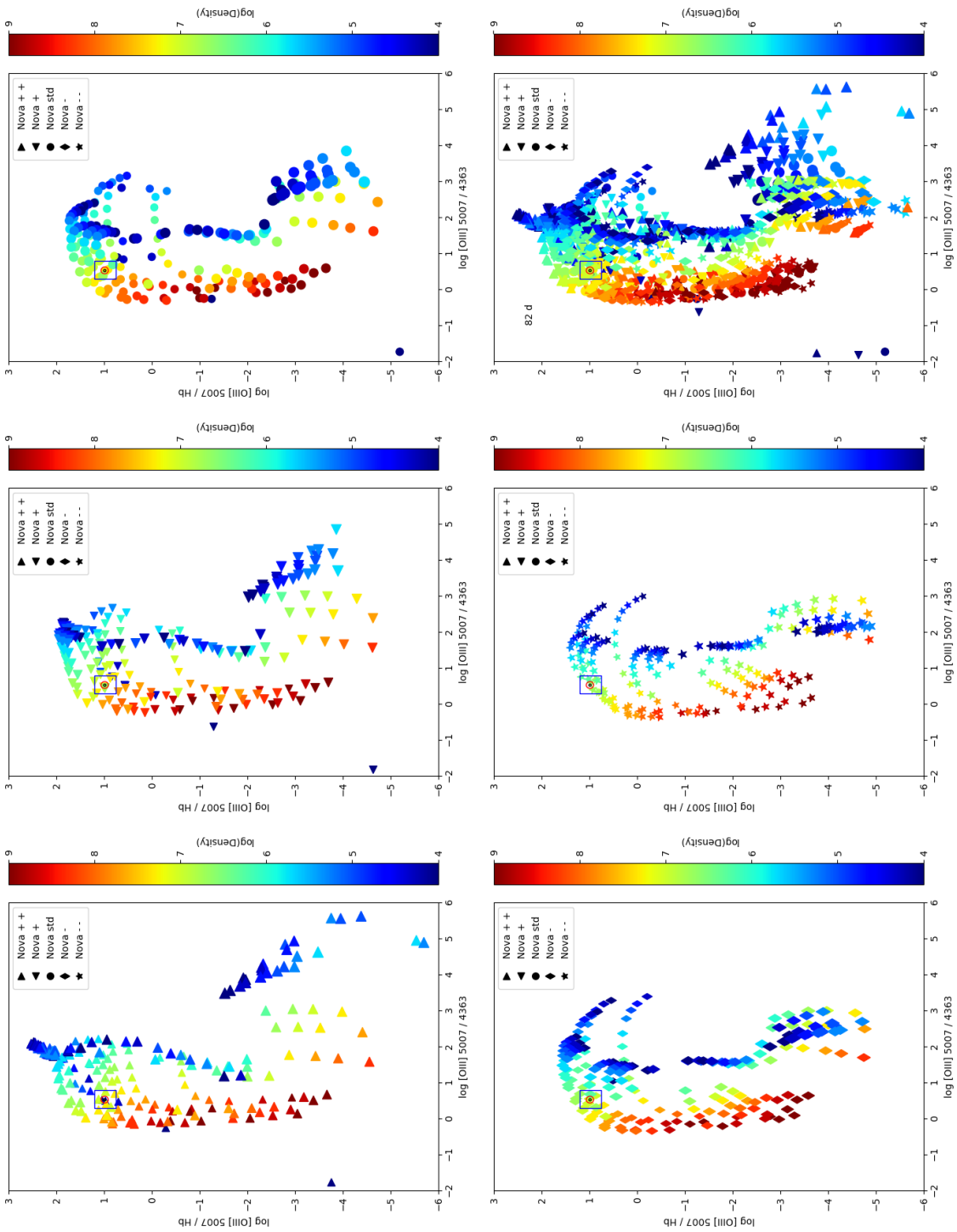

Figure 5.5: As in Figure 5.4, except colour indicates the density and size shows the temperature of the model.

5.5.3 Temperature dependence of rO3 and HaHb ratios

The right two panels of Figure 5.3 present the rO3 ratio against the HaHb ratio, as predicted by the grid of nova models. The overall shape of this relationship appears to be an "L" shape, although some temperatures and densities primarily occupy one branch of the "L". From the top right panel, we see that systems with higher temperatures have a higher rO3 ratio, and primarily occupy the horizontal branch of the "L" shape. Systems with the lowest temperatures, $\lesssim 10^{5.5}$ K, have very similar HaHb ratios, but can have quite varied rO3 ratios. In contrast, models with temperatures of the order $\sim 10^{6}$ K to $\sim 10^{7.5}$ K cover a relatively narrow range of rO3 ratios, but a broad range of HaHb ratios.

The very top of the vertical branch of the L is primarily occupied by models with lower metallicity than the standard nova model, as demonstrated by the star and diamond shaped symbols. In Figure 5.6, we see clearly that, for intermediate temperatures, as metallicity decreases, both the maximum HaHb ratio and the range of HaHb ratios increase. The total amount of hydrogen in the model shell increases with reducing metallicity.

5.5.4 Density dependence of rO3 and HaHb ratios

Similarly, we can see in the bottom right panel of Figure 5.3 that the lowest density models all have a low HaHb ratio, but cover a greater range of rO3 ratios. Below a temperature of around $\sim 10^{5.5}$ K, and for densities above $\sim 10^{6.5}$ cm^{-3}, the models cover a wide range of HaHb ratios. The widest range of HaHB ratios is covered by the high density, intermediate temperature models. As shown in Figures 5.6 and 5.7, the models with lower metallicity have higher HaHb ratios.

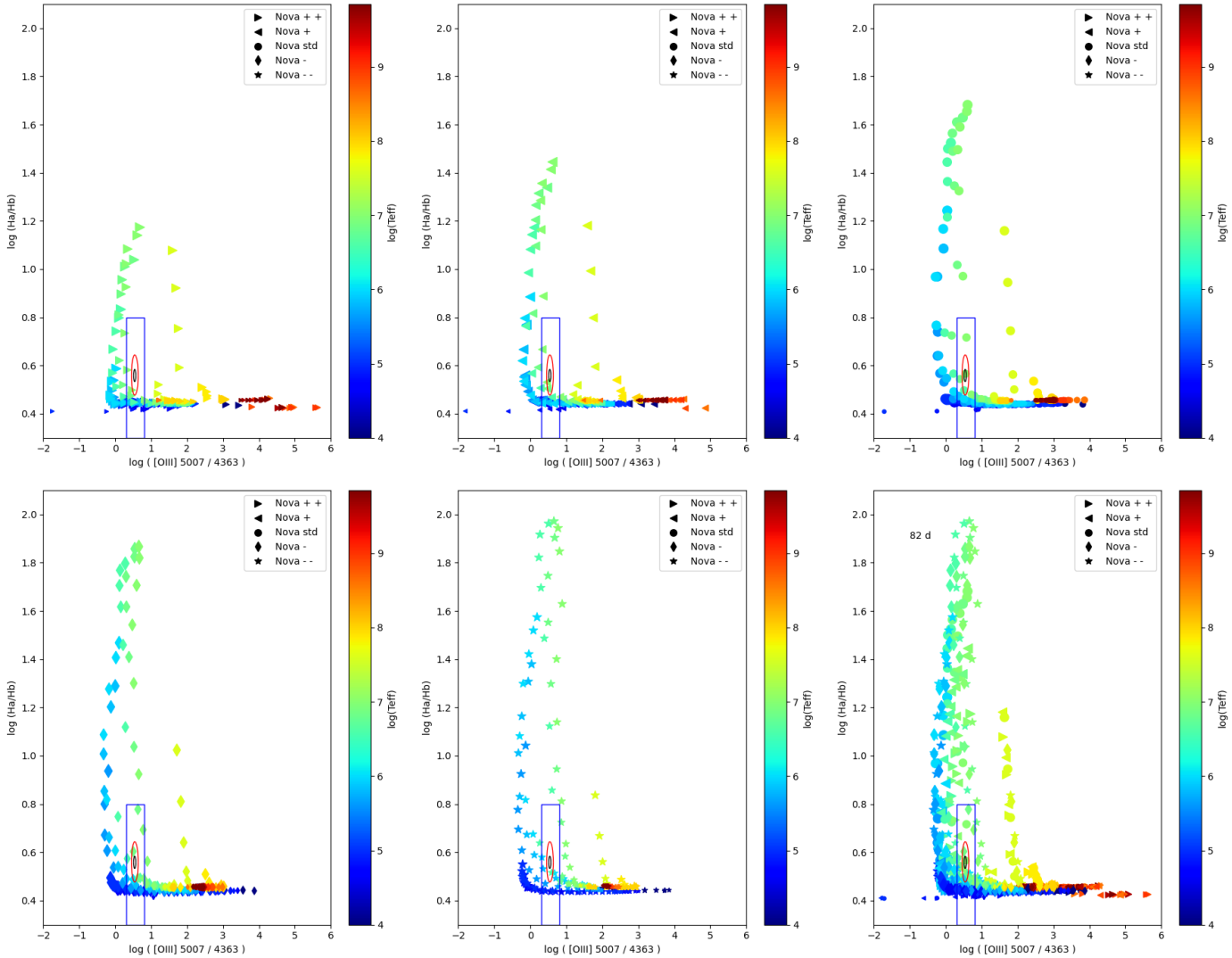

Figure 5.6: Comparison between HaHb ratio and rO3 ratio 82 d after eruption, for different metallicity models. The metallicity is highest in the top left plot, then decreases along the top row, and then along the bottom row. The bottom right panel shows models of all metallicity values. Colour and size indicate the temperature and density of the model, respectively.

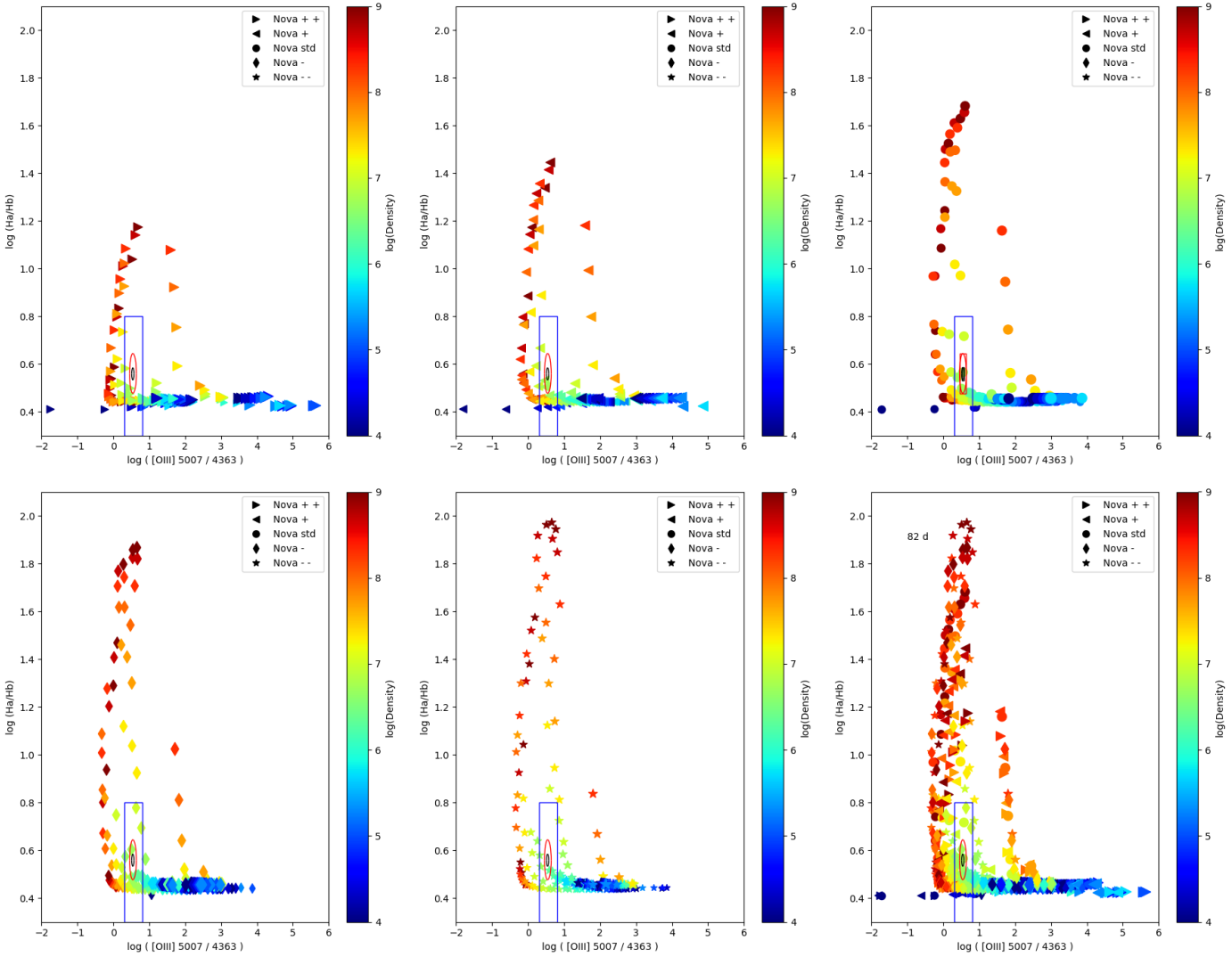

Figure 5.7: As in Figure 5.6, except here colour and size indicate the density and temperature of the model, respectively.

5.5.5 Comparison between ratios

The plots in Figure 5.8 focus on the regions of the diagnostic plots near to the measured ratios in the spectra of V392 Per, 82 days after eruption. The 1σ and 3σ error ellipses are centred on the measured flux ratios, and are shown in black and red, respectively. As in Figure 5.3, the top plots represent the effective temperature with colour, whereas in the bottom plots the colour of the data points shows the density.

In the top and bottom left panels, the central ellipse contains three data points, all with similar WD effective temperatures (between 4×10^4 K to 4×10^5 K). The right-pointing triangle has a low temperature and density (4×10^4 K and $10^{4.3}$ cm^{-3}), and a high metallicity. The circle represents the model with the highest temperature of the three models within 1σ of the measured ratios, albeit still a relatively low temperature of 4×10^5 K, and an intermediate density of $10^{7.3}$ cm^{-3}, with the standard nova metallicity. The diamond represents a model with relatively low metallicity, a relatively low temperature of 1×10^5 K, and an intermediate density of $10^{7.3}$ cm^{-3}.

The rO3 vs O3Hb ratio suggests that V392 Per could have a relatively low temperature. If it has a high metallicity, its density would be lower than if it has the standard metallicity. If V392 Per had a low metallicity, it could have a slightly cooler temperature, but would still have a lower density than a nova with the standard metallicity. Regardless of the metallicity, a relatively low temperature is implied.

In the right (top and bottom) panels of Figure 5.8, only one model is within the 1σ error ellipse of the measured ratios for V392 Per. This model has the standard nova metallicity and intermediate temperature and density, 1×10^7 K and $10^{6.7}$ cm^{-3}, respectively. However, this is hotter than any of the models within the 1σ error ellipse in the left two panels. The density is also lower than the density implied by the standard metallicity model within the 1σ error ellipse in the bottom left panel.

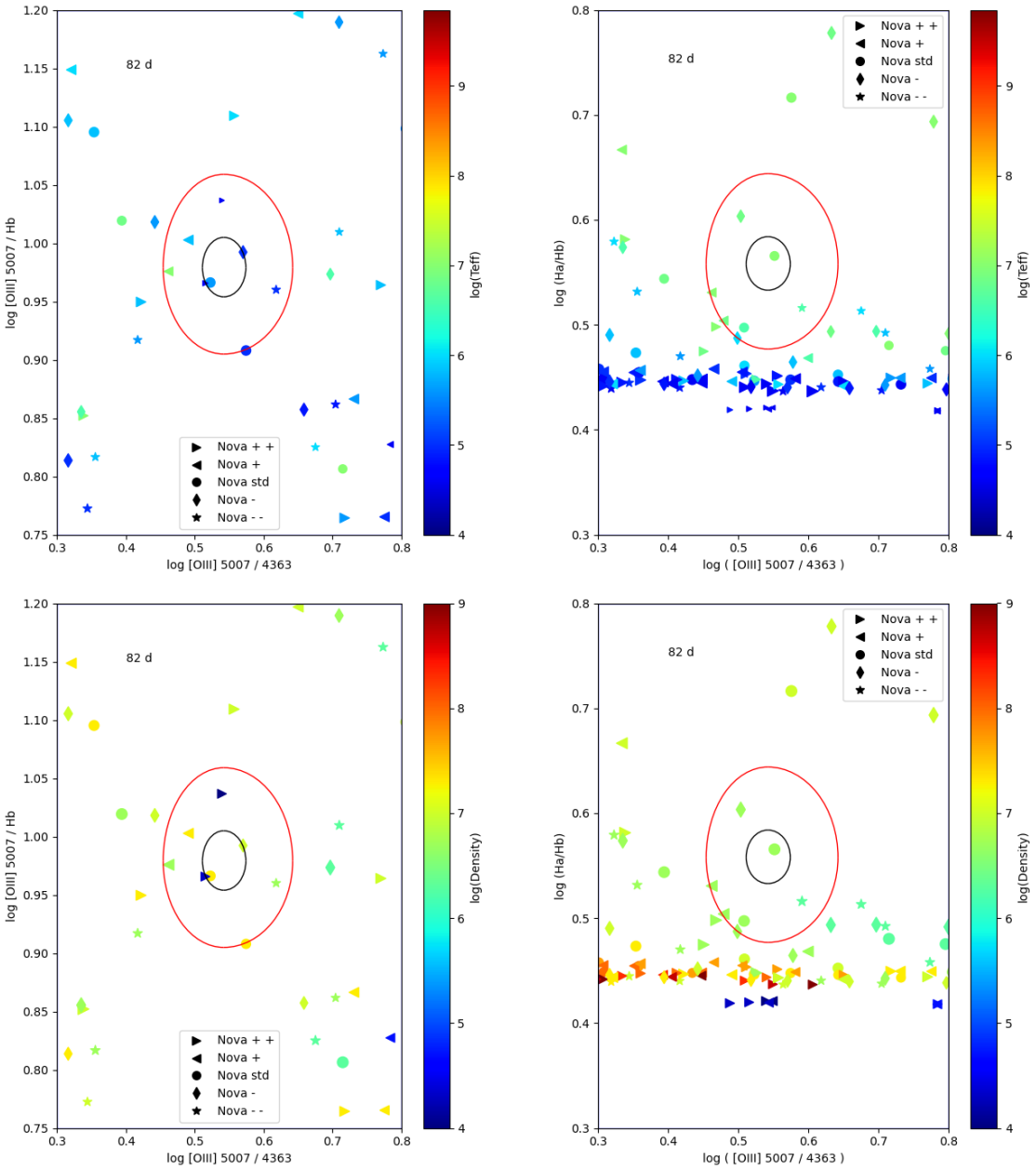

Figure 5.8: As Figure 5.3, focussing on the region around the measured ratios for V392 Per 82 days post-eruption.

If we consider the models within the 3σ error ellipse of the measured rO3 and O3Hb ratios for V392 Per (in the left panels of Figure 5.8), most of the temperatures are similar to those within the 1σ ellipse, although we also find one model with a higher temperature of 10^7 K. This model has a slightly enhanced metallicity, and an intermediate density of $10^{6.7}\,\mathrm{cm}^{-3}$. The models with the highest metallicity have the lowest temperatures (4×10^4 K) and densities ($\sim 10^4\,\mathrm{cm}^{-3}$ to $\sim 10^{4.3}\,\mathrm{cm}^{-3}$). However, the model with the lowest metallicity, represented by a star symbol, has a fairly low temperature (1×10^5 K) and an intermediate density ($10^{6.7}\,\mathrm{cm}^{-3}$). The highest density systems within the larger error ellipse are shown as yellow data points in the bottom left panel, and their metallicity is either that of the standard nova, or slightly enhanced. Systems with densities in excess of $10^{7.3}\,\mathrm{cm}^{-3}$ during the measured epoch do not produce ratios in the vicinity of those for V392 Per.

From the right panels of Figure 5.8, all models within the 3σ error ellipse have similar temperatures and densities to those of the model within 1σ of the measured flux ratios. The temperatures lie in the range 10^6 K to 10^7 K, and densities in the range $\sim 10^{6.3}\,\mathrm{cm}^{-3}$ to $\sim 10^{6.7}\,\mathrm{cm}^{-3}$. Three models have the same temperature and density (10^7 K and $10^{6.7}\,\mathrm{cm}^{-3}$), but they vary from enhanced or slightly enhanced metallicity, down to the standard nova metallicity. The lowest temperature model within 3σ (the blue diamond in the top right panel) had a slightly lower metallicity than standard, and the same density as the model within 1σ of the measured flux ratios, i.e. $10^{6.7}\,\mathrm{cm}^{-3}$.

5.5.6 Summary of comparison between ratios at 82 days

There is some disagreement between the temperatures and densities predicted by the different ratios. For example, the O3Hb ratio predicts a lower temperature, and generally a higher density than the HaHb ratio. Both ratios measured for

V392 Per could be produced by at least one model with the typical nova metallicity (represented by a circle) within 1σ of the measured ratios for V392 Per. However, the temperatures required are quite different (4×10^5 K vs 10^7 K), whereas the required densities are fairly similar ($10^{7.3}$ cm^{-3} vs $10^{6.7}$ cm^{-3}).

The model with slightly enhanced metallicity (a green left-pointing triangle in all four panels in Figure 5.8) is the only model that appears within the 3σ error ellipse at this epoch for all three ratios measured for V392 Per. This model has a temperature of 10^7 K and a density of $10^{6.7}$ cm^{-3}. Its rO3 ratio is just above the 3σ lower limit, its HaHb ratio is around the 1σ lower limit, and its O3Hb ratio is very close to that measured for V392 Per.

5.6 Comparison between 82 days and 89 days after eruption

The overall appearance of the plots showing the rO3 vs O3Hb ratios and those showing the rO3 vs HaHB ratios were very similar between the two epochs, as we might expect. Figure 5.9 provides a comparison of the model rO3 vs O3Hb ratios (in the top row), and the model rO3 vs HaHB ratios (in the bottom row), at 82 days after eruption with those seven days later. The figure focusses on the region in the vicinity of the ratios measured for V392 Per at each epoch. The left panels show the plots relating to 82 days post-eruption, and the right panels relate to 89 days post-eruption. All panels use colour and size to represent effective temperature and density, respectively. Although the measured ratios for rO3 and O3Hb and their corresponding errors increased between the two epochs, as reflected by the positions and sizes of the black and red error ellipses, the zoomed in regions cover the same range of ratios between epochs, to aid comparison.

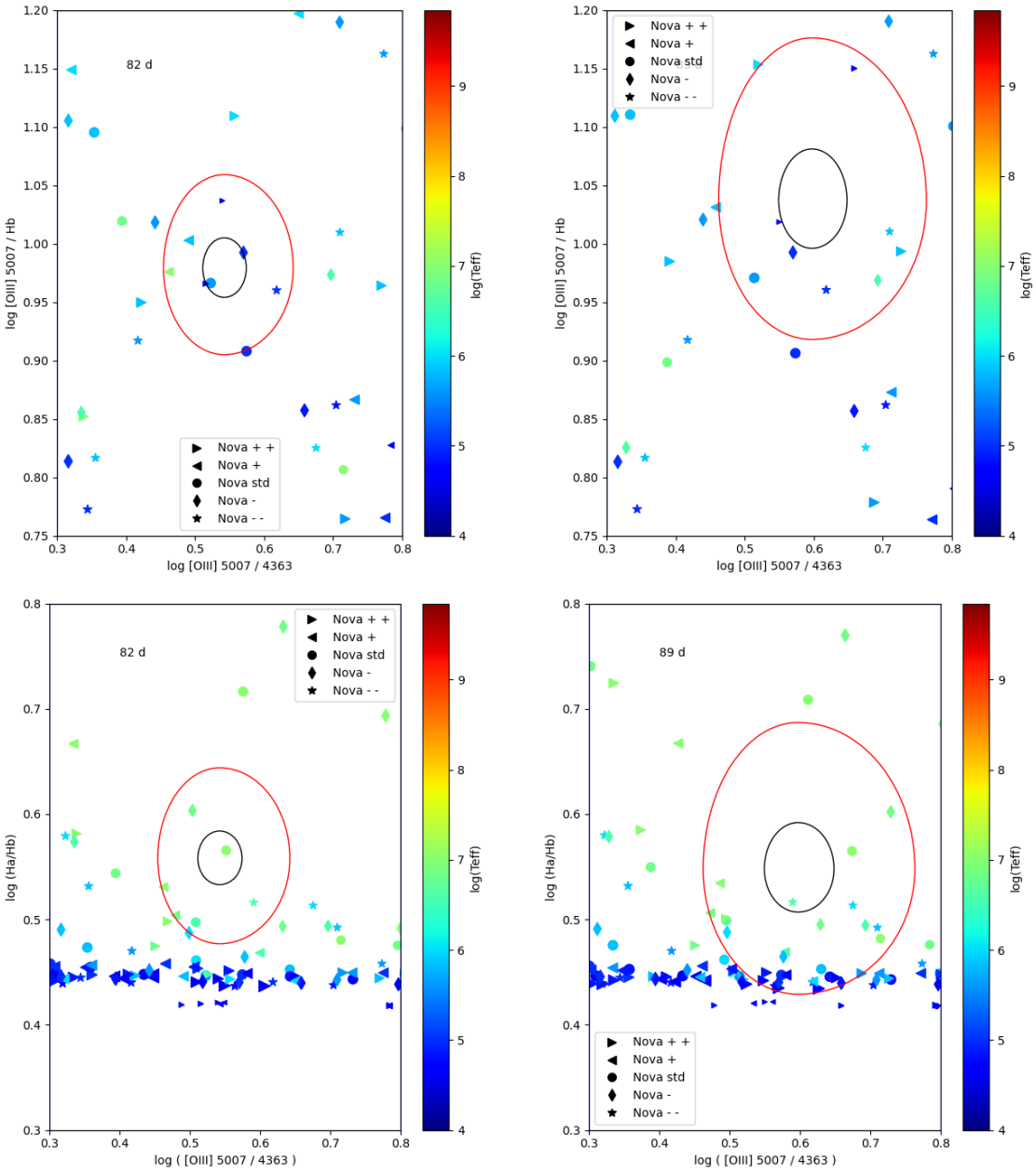

Figure 5.9: Comparison between model O3Hb ratio and rO3 ratio (top row), and between HaHb ratio and rO3 ratio (bottom row) for 82 d (left panels) and 89 d (right panels) - focussing on region around measured flux ratios for V392 Per. In all plots, colour represents the effective temperature of the WD.

When comparing the O3Hb and rO3 ratios in the top row, we see that the original and new 1σ error ellipses do not contain any identical points, although one model that was just within the original 1σ error ellipse is just outside it at 89 days. This is the model with slightly reduced metallicity (the dark blue diamond), a temperature of 10^5 K and a density of 10^7 cm^{-3}. This data point is very close to the edge of the 1σ error ellipse at both epochs. At first glance, it appears that the model with the highest metallicity (the dark blue right-pointing triangle) within the 1σ ellipse at 82 days, with a WD temperature and electron density of 4×10^5 K and $10^{4.3}$ cm^{-3}, is just outside the 1σ ellipse at 89 days. However, this model has effectively swapped places with the model with the same temperature and metallicity, but a slightly lower density (10^4 cm^{-3}), which was within the 3σ error ellipse at 82 days.

Regarding the comparison of the HaHb and rO3 ratios between epochs, the green circle that was the only data point within the 1σ error ellipse at 82 days, moves to the right of the new 1σ error ellipse, which is already at a higher rO3 ratio than the original one. For the HaHb vs rO3 plots, all of the data points within the 3σ error ellipse at 82 days still lie within the 3σ error ellipse at 89 days, so are plausible models to describe V392 Per. In particular, the green star within the 1σ error ellipse at 89 days post-eruption appears to be a good candidate model for V392 Per, as it was relatively close to the 1σ error ellipse at 82 days. This model has a metallicity 10 times lower than the standard nova, a temperature of 4×10^6 K and a density of $10^{6.3}$ cm^{-3}.

The seemingly promising candidate model from 82 days, that lay within the 3σ error ellipse for all three ratios, no longer appears on the zoomed in plot at 89 days, as its O3Hb ratio has decreased too much. This model, shown as a green left-pointing triangle in Figure 5.9, had a slightly enhanced metallicity, a temperature of 10^7 K and a density of $10^{6.7}$ cm^{-3}.

5.7 Comments regarding overall comparison

The diagnostic plots shown in the previous sections demonstrate that it is difficult to draw conclusions about the temperature, density and metallicity of the material ejected in the eruption of V392 Per. Depending on which ratios we consider, the model nova shells that best reproduce the measured line ratios have different parameters. The HaHb ratios indicate higher temperatures than the O3Hb ratios. The O3Hb ratio indicates a greater possible range of densities and metallicities than the HaHb ratio.

As we might have expected, the overall distribution of ratios predicted by the grid of models does not change significantly between the two epochs, as they are only separated by one week. Even though the eruption is fast evolving, in general, the ionization conditions within the ejecta do not change much within this short timeframe at this stage of the eruption. We do observe, however, that the ratios predicted by some individual models move a substantial distance within the plot, and some models no longer appear on the plot. These points are more affected by changes in the simulated local conditions, as the ionization states of the different elements change. The gas cools and expands between the two epochs,and the distance from the ionizing source to the inner radius of the gas shell increases. The rates of occupation of different energy levels, and the equilibrium between different energy transitions between those levels, change correspondingly. For some models, a small change in the gas conditions will correspond to a large change in the line ratios, as they were already close to a 'tipping point' between ionization states.

The range of temperatures and densities indicated by these diagnostic plots are consistent with those we would expect to find within a nova shell at this stage of its evolution, but the overall picture is complex and inconclusive. In order to gain a

better understanding of the temperature and density conditions within the ejecta, we will next consider oxygen line ratio contours produced using PyNeb.

5.8 Oxygen line ratio contours in the temperature-density plane

Figure 5.10 shows the PyNeb contours calculated for the nebular [O III] 4959 & 5007 Å to auroral [O III] 4363 Å ratio. The black dotted lines show the contour for the measured ratio in V392 Per 82 days after eruption, of $\log_{10}(4.547) \pm 5\% = 0.658 \pm 5\%$. The line ratios for several other novae included as a comparison are shown in Table 5.2.

From the top panel of Figure 5.10, we can see that for all electron densities higher than around $10^{5.6}\,\mathrm{cm}^{-3}$, the contours follow an asymmetrical "C" shape, where a given density will have two different electron temperatures that produce the same ratio of nebular to auroral [O III] emission. For electron temperatures in the approximate range $10^4\,\mathrm{K} \leq T_e \leq 10^5\,\mathrm{K}$, just above the ionization temperature of ground state H atoms, a range of densities can produce very similar [O III] line ratios. That is, for a given line ratio, a small range of temperatures corresponds to a large range of densities. For the contours exhibiting a "C" shape, higher line ratios correspond to lower densities.

In the bottom panel of Figure 5.10, we focus on a restricted range of temperatures and densities, only considering $10^4\,\mathrm{K} \leq T_e \lesssim 10^7\,\mathrm{K}$, and $10^5\,\mathrm{cm}^{-3} \leq n_e \lesssim 10^7\,\mathrm{cm}^{-3}$. This shows us more clearly where observed line ratios from different novae appear on this contour plot. The black dotted lines show the line ratio $\pm 5\%$ for V392 Per 82 days post-eruption. This is very close to the observed line ratios for V906 Car (yellow) and

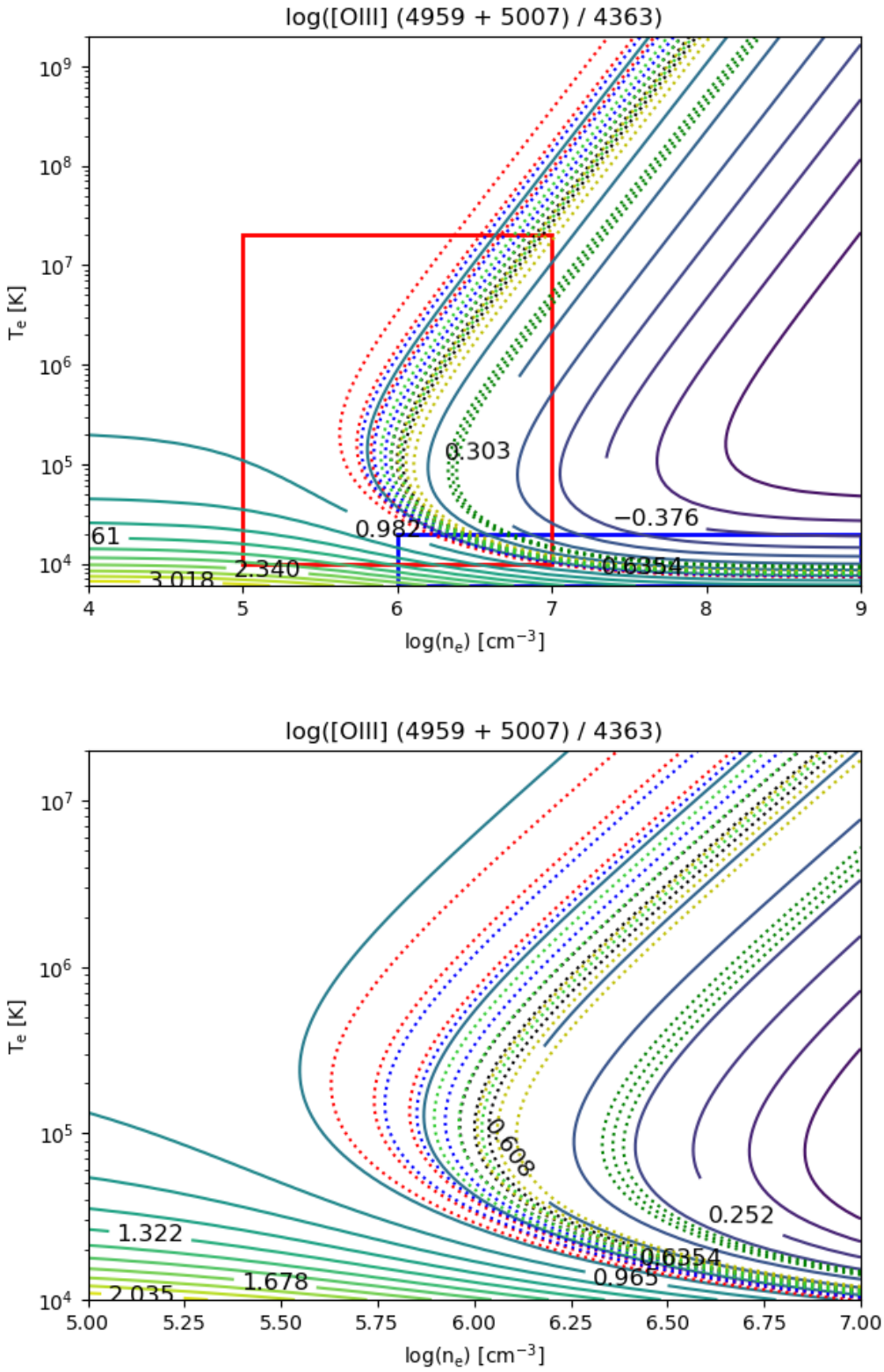

Figure 5.10: Contours for [O III] for different electron temperatures and electron densities 82 days after eruption. The top panel shows the contours for the full density and temperature range, whereas the bottom panel is zoomed in on the region between 10^4 K to 10^7 K and 10^5 cm^{-3} to 10^7 cm^{-3} (shown by the red rectangle). The region shown by the blue rectangle appears as Figure 5.11

Table 5.2: Comparison with [O III] nebular/ auroral ratios for other novae. The first column shows the name of the nova, the second column shows $\log_{10}$ of its ratio, and the third column shows the colour used to show the contour in Figures 5.10 and 5.11. For RS Oph and U Sco, two values of the ratio are given. In the case of RS Oph,the emission lines are quite asymmetrical, so the ratios for the red-ward and blue-ward sides of the emission lines are given separately. In the case of U Sco, the ratio is given separately at early and late times after the eruption.

Nova	Ratio (Neb/Aur)	Colour
V392 Per (82 d)	0.658	black
V392 Per (89 d)	0.720	black
RS Oph (red)	0.784	red
RS Oph (blue)	0.736	blue
V906 Car	0.622	yellow
U Sco (early)	0.415	green
U Sco (late)	0.680	lime green

late-time U Sco (lime green). The turning point for the "C"-shaped contours occurs at a higher temperature, and a lower density, as the line ratio increases. In this panel, the [O III] line ratio contours for temperatures above $\sim 10^{5.7}$ K and densities above $\sim 10^{5.6}\,\mathrm{cm}^{-3}$ have power law-like forms.

Figure 5.11 focuses on the lower temperature ranges ($T_\mathrm{e} < 2 \times 10^4$ K) covered in Figure 5.10. Figure 5.11 is shows densities in the range $10^6\,\mathrm{cm}^{-3} \leq n_e \lesssim 10^9\,\mathrm{cm}^{-3}$. If we only considered this contour plot, which shows typical electron temperatures and densities of planetary nebulae, we would think that (for a given line ratio) higher temperatures would imply lower densities. When we consider the higher temperatures shown in Figure 5.10, we see that the same line ratio at even higher temperatures would actually correspond to higher densities. Diagnostic line ratios are also applied to the study of supernova explosions, but as they occur in the high temperature ($T_\mathrm{e} > 10^6$ K), high density regime, the oxygen contours reveal simple relationships, with a given line ratio corresponding to a single temperature and density. Only novae reside in the part of the temperature-density phase-space where the line ratios exhibit a turning point.

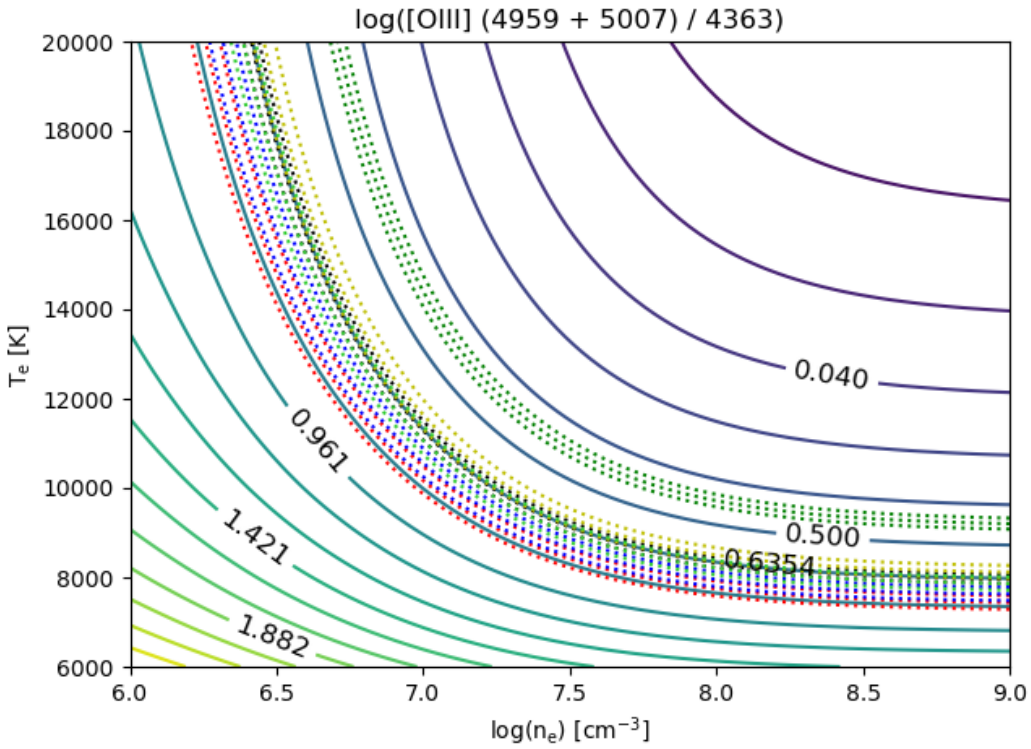

Figure 5.11: Contours for [O III] for different electron temperatures between 6000 K and 20000 K 82 days after eruption. Only electron densities in the region between $10^6\,\mathrm{cm}^{-3}$ to $10^9\,\mathrm{cm}^{-3}$ (indicated by the blue rectangle in Figure 5.10) are shown.

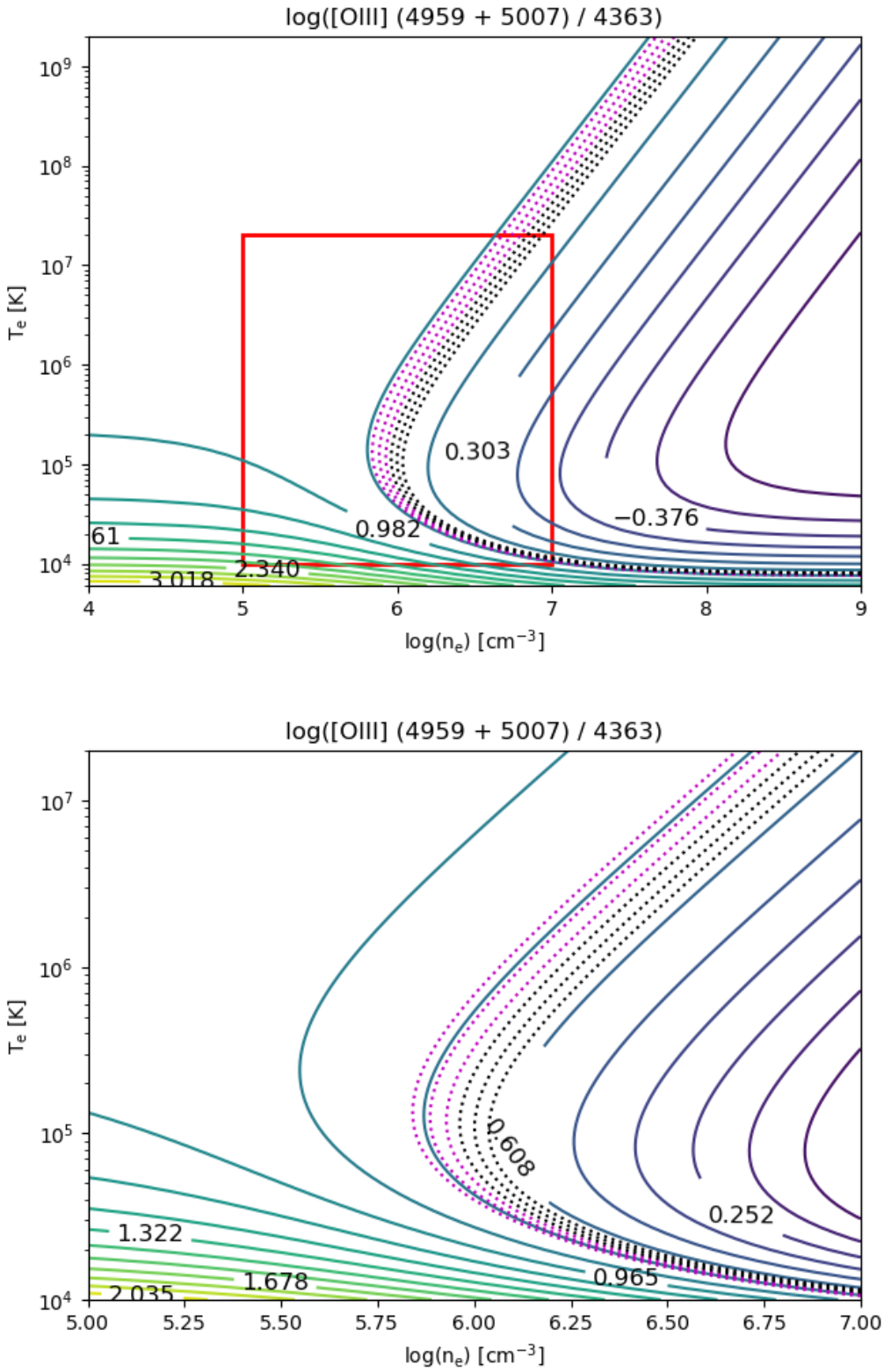

Figure 5.12: Contour plot for [O III] line ratios, comparing measured line ratios 82 days (black dotted line) and 89 days (magenta dotted line) after eruption. The top panel shows the contours for the full electron density and electron temperature range, whereas the bottom panel is zoomed in on the region between 10^4 K to 10^7 K and 10^5 cm^{-3} to 10^7 cm^{-3} (shown by the red rectangle in the top panel).

In Figure 5.12, we again present the oxygen line ratio contour plots covering a wider range of temperatures and densities. However, here we compare the measured line ratios from the V392 Per spectra at 82 days and 89 days, indicated by black and magenta dotted lines, respectively, and have removed the comparison line ratios for other novae. This shows that the measured line ratio at the later epoch, corresponds to a lower density, as we would expect given the ongoing expansion of the ejecta.

The shapes of the [O III] line ratio contours shown in this section illustrate the challenges implicit in applying photoionization analysis to nova ejecta. In the temperature and density ranges typically found in nova shells at relatively early times in their evolution, a small range of electron densities can correspond to two narrow temperature ranges centred on widely separated electron temperatures. Similarly, a small range in temperature can correspond to a large variety of different [O III] line ratios.

5.9 Summary

In this chapter we have applied diagnostic tools to measured line ratios from the spectra of V392 Per at two epochs towards the end of the super-soft source phase of the eruption. We have produced a suite of 1440 models covering a range of different possible ionizing source effective temperature, electron density and metallicity conditions, and compared three expected line ratios for those conditions with the measured line ratios for V392 Per. We have discussed possible temperatures and densities for the nova ejecta, depending on its metallicity, based on this preliminary analysis. In addition, we described the difficulty inherent in inferring photoionization conditions within the ejecta of a nova.

In the following chapter, we will present a discussion of all photometric and spectroscopic results from our observations of V392 Per. In Chapter 7, we include some suggestions for future development of this work.

Chapter 6

Discussion

This chapter is an extended version of Section 5 from Murphy-Glaysher et al. (2022).

V392 Per is the first pre-known DN to be observed as a γ-ray bright CN. Here, we aggregate our reported observations to present a plausible description of the underlying system.

6.1 A shock-powered light curve?

The Fermi-LAT detection of γ-ray emission from V392 Per (Albert et al., 2022) followed soon after the optical detection. However, γ-ray emission might have been detected earlier were it not for technical problems with Fermi. In Figure 6.1 we directly compare the Fermi-LAT flux (from Albert et al., 2022) with the V-band flux (see Section 3.9). As has been reported for other γ-ray novae (Ackermann et al., 2014; Aydi et al., 2020a), there appears to be a clear correlation between the γ-ray and optical emission during the early evolution.

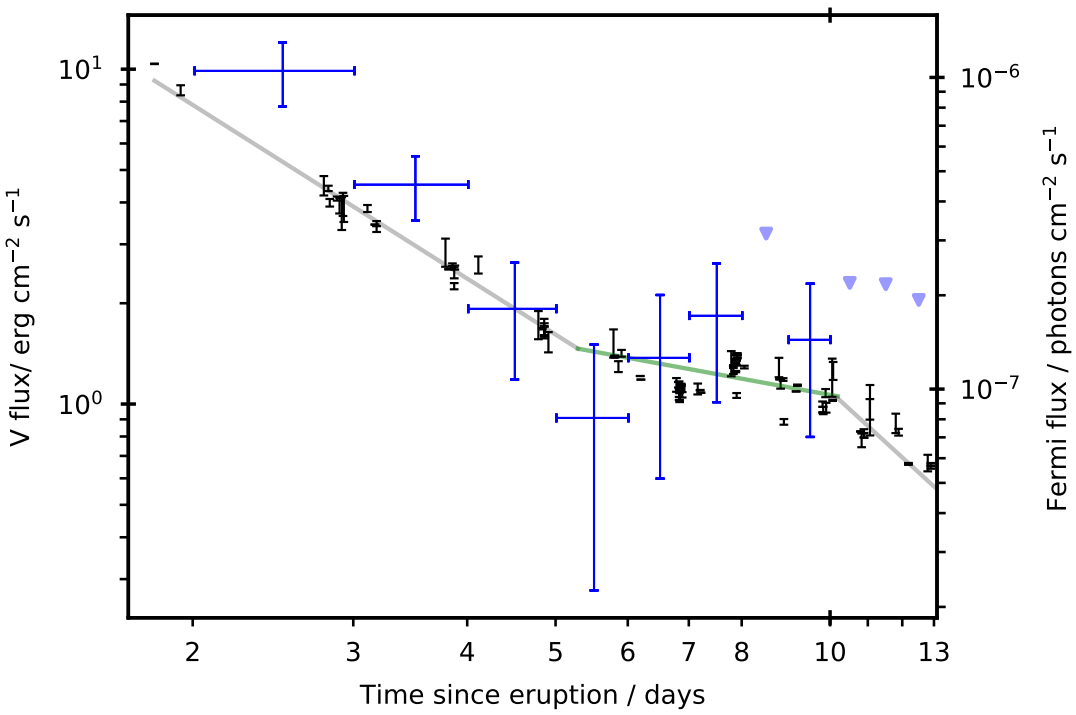

Figure 6.1: V-band light curve (in black), overlaid with Fermi-LAT γ-ray light curve (in blue). 1σ error bars are shown, and the blue arrowheads represent 95th percentile upper limits. Appears as Figure 17 in Murphy-Glaysher et al. (2022) ['V392 Persei: A γ-ray bright nova eruption from a known dwarf nova', Murphy-Glaysher et al., Mon. Not. R. Astron. Soc., 514, 6183, 2022 DOI `https://doi.org/10.1093/mnras/stac1577`]

The early γ-ray and optical declines both follow similar power-laws until day ~ 5, when both fluxes plateau. As the optical plateau ends (day ~ 10) and the decline resumes, the Fermi-LAT detections cease (although observations continued). Here, we propose that the early (pre-first Sun constraint) optical light curve is driven by the evolution of shocks between and within multiple mass ejection components (as discussed in Gordon et al., 2021):

As reported in Section 4.5, there is evidence for multiple mass ejections, an initial event with $v \sim 3000\,\mathrm{km\,s^{-1}}$ being swept up and shocked 2.5 d post-eruption by a faster ejecta at $v \sim 5000\,\mathrm{km\,s^{-1}}$ — corresponding with the initial Fermi-LAT detection. These shocks will have accelerated ions to relativistic velocities, which emitted γ-rays while interacting with particles or photons in the surroundings (Martin et al., 2018; Aydi et al., 2020a). While γ-ray emission from novae can also be linked to the ejecta shocking and sweeping up pre-existing circumbinary material (e.g., a red giant wind; Cheung et al., 2014), here we see no evidence for the associated coronal emission lines (Rosino & Iijima, 1987) or sustained bulk ejecta deceleration expected in such cases (Bode & Kahn, 1985; Darnley et al., 2016). As such, we propose that the most likely source of the initial γ-ray emission is inter-ejecta shocks between these two components. With the lack of very early optical data, evidence for an additional, earlier, light curve peak corresponding to the initial ejection is unavailable.

The spectral evolution during the initial plateau is complex, and is additionally challenging due to the decreasing optical depth likely to be simultaneously occurring. The light curves of many novae enter quasi-plateau phases around t_3. For the recurrents, this has been proposed to be driven by a surviving, or rapidly reformed, accretion disk emerging from the receding photosphere, with the unveiling of the SSS occurring toward the end of the plateau as the inner disk is revealed. However, unlike recurrent nova plateaus (e.g., Henze et al., 2018), here we see no evidence for He II emission during the plateau – which would be expected from a disk. Indeed,

He II emission is only seen after the first Sun constraint during the nebular phase. The plateau corresponds with the end of the clear 'bulk' ejecta merger, but there remains evidence for on-going 'minor' interaction. We tentatively propose that the γ-ray emission during the plateau is driven by intra-ejecta shocks following the major merger event.

6.2 X-ray emission and accretion

In Section 4.11.1 we presented evidence that the end of the SSS X-ray emission phase was caught just as V392 Per emerged from its first Sun-constraint. The relationships in Henze et al. (2014) predict a SSS turn-on time $t_{\rm SSS,on} = 13^{+6}_{-4}$ days (based on t_2), a corresponding turn-off $t_{\rm SSS,off} = 60^{+80}_{-40}$ days, and a SSS black-body parameterised temperature of $k_{\rm B}T \sim 90$ eV. A caveat here is that the Henze et al. (2014) relationships are defined for the M 31 nova population, where deep X-ray observations are prohibitive due to distance, and as such they may systematically predict later start and earlier end times than really occur for Galactic novae. Nonetheless, these predictions are compatible with the available X-ray observations of V392 Per. We again note that there was no associated optical spectral evidence of a SSS before the first Sun-constraint.

As is demonstrated in Figures 4.17 and 4.18, at all observed times, there is a substantial contribution to the X-ray luminosity by a harder component, that is well described by a single, or pair of, hot collisional plasma (APEC) models. Such emission is often associated with shocks. However, the consistency and longevity of the hard emission – from at least day 83 to beyond day 800 – reveals that this emission cannot be associated with an expanding ejecta. We do note that, unfortunately, there is no pre-eruption X-ray or UV data available for comparison.

During the post-nova phase, we see clear, strong, and very narrow emission from H I, He I, and especially He II, on top of a blue continuum – indicative of an accretion disk. However, the $< 100\,\mathrm{km\,s^{-1}}$ width of these lines might imply a disk very close to face-on and would seemingly contradict the orbital modulation observed (see Section 3.11), which suggests an inclination closer to edge-on. At the same time, the SED of V392 Per (see Figure 3.16) shows strong and consistent emission in the near-UV. As shown in Figure 4.16, the near-UV and X-ray emission appear correlated. We conclude from this that the UV and X-rays arise from the same system component and, given the shape of the SED, this will be from a reformed accretion disk. Most quiescent CNe do not show substantial X-ray emission, suggesting that the underlying binary system of V392 Per is a magnetic CV.

The potential orbital period ($P \simeq 3.2\,\mathrm{d}$; Section 3.11) is too long to be consistent with a tidally-locked polar configuration (Mukai, 2017), as would be the less-favoured orbital period of $P \simeq 1.6\,\mathrm{d}$. Therefore, V392 Per is likely to be an intermediate polar (IP); a CV with a WD magnetic field in the range $10^6 \lesssim B \lesssim 10^7\,\mathrm{G}$. With APEC temperatures, perhaps, in excess of 50 keV, the X-ray emission is similar to that expected to emanate from the standing/standoff shocks observed in the accretion environment surrounding IPs. The magnetic field of an IP is strong enough to truncate the inner part of the accretion disk, causing the accreted material to flow along the magnetic field lines in accretion curtains onto the WD. Truncation of the inner part of the accretion disk by the magnetic field of an IP could explain the apparent contradiction between the very narrow emission lines from H I, He I, and He II and the closer to edge-on inclination suggested by the orbital modulation of the light curve. The innermost circular orbit of gas in a truncated accretion disk is at a higher radius than that for a non-truncated disk. Therefore, the Keplerian velocity of the gas will be lower, and an inclination close to face-on is not required to explain the narrow emission lines observed.

Could the presence of an accretion curtain be behind the higher than expected column seen in the X-ray fits (see Section 4.11.1)? We note that neither our i'-band high cadence data, or *Swift* data, are suitable for searching for a signal from the WD spin period – a key diagnostic of an IP.

We have linked the narrow emission line spectrum in the post-nova phase to active accretion in the system. As such, we restate that this disk spectrum was already visible once the system had exited the first Sun-constraint (e.g. Figure 4.12), while the nova ejecta was still fading, and while the SSS was still on. As such, the disk must have (at least) partially survived the eruption, or reformed during the SSS phase. As discussed in Section 1.9.3, X-ray and optical observations of other novae have indicated the resumption of accretion took place within 35 days for U Sco (Ness et al., 2012), 65 days for HV Ceti (Beardmore et al., 2012), 117 to 241 days for RS Oph (Worters et al., 2007) and 150 days for V959 Mon (Page et al., 2013). Therefore, it seems reasonable for accretion to have resumed by the time V392 Per exited its initial Sun constraint, even if the accretion disk did not survive the eruption. From this we infer that there could have been active accretion during the SSS-phase, potentially 're-fuelling' the WD and prolonging the SSS phase (cf. Aydi et al., 2018a; Henze et al., 2018).

6.3 Pre-nova versus post-nova

In Figure 3.14, we directly compared the 'steady state' post-nova luminosity with the pre-nova AAVSO light curve. The pre-nova state shows a quiescent baseline at $V \sim 17$ mag (low-state), punctuated with several 2–3 mag amplitude DN outbursts (high-state). The timescale of these DN outbursts are more akin to those seen in longer orbital period systems, such as GK Per. As also discussed by Munari et al.

(2020a), V392 Per has not returned to its pre-nova quiescent level. The system has remained at an elevated high-state of $V \sim 15$ mag for (at least) two years post-eruption. During this time, the near-UV and X-ray luminosity continue to creep upwards (Figure 4.16) – i.e., there is no evidence so far that the system will return to the low-state. In DN systems, the majority of accretion onto the WD surface occurs when the disk is in a high state, i.e., during a DN outburst. Here, we infer that V392 Per is maintaining an elevated level of accretion post-nova, and that it is currently best classified as a nova-like variable, rather than a DN. It is unclear as to why V392 Per is remaining in this post-nova high-state. It may simply be that irradiation of the donor by the recent nova eruption is driving elevated mass loss from the companion (cf. T Pyx; Ginzburg & Quataert, 2021). We are not currently in a position to predict when, or even if, the system will revert to its pre-nova state.

6.4 The underlying system

With a t_2 as short as 2 days and a SSS turn-off of ~ 100 days, the indications are that the WD in this system is particularly massive (see, e.g., Schwarz et al., 2011). Indeed, the V392 Per nova eruption is one of the fastest evolving on record, and the SSS phase may have been unusually extended through refuelling by a surviving or rapidly reformed disk. Novae with similar parameters are expected to host WDs with masses in excess of 1.1 $M_\odot$, perhaps up to 1.3 $M_\odot$ (see Yaron et al., 2005; Osborne et al., 2011; Hillman et al., 2016, and references therein). The relatively high SSS black-body temperature ($k_B T \sim 50$ eV) seen even at the very end of the SSS phase is similarly suggestive of a massive WD. With strong forbidden Ne lines present in the spectra (see Section 4.2 and Munari et al., 2020b) there is a distinct possibility that V392 Per hosts a massive ONe WD.

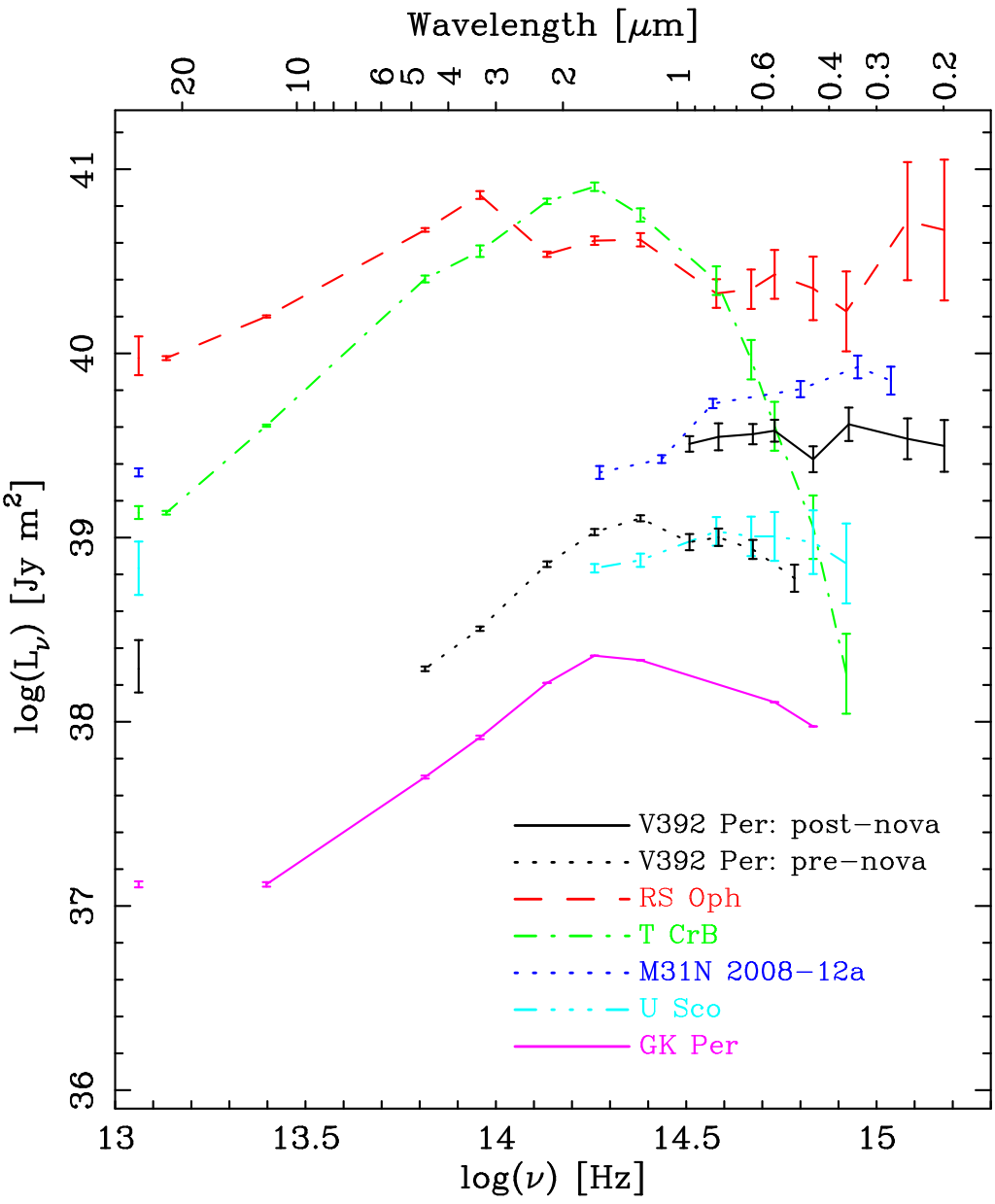

Figure 6.2: Distance and extinction corrected quiescent SEDs of V392 Per, RS Oph, T CrB, M31N 2008-12a, U Sco, and GK Per. Error bars include photometric and extinction uncertainties; distance uncertainties indicated to the left of the plot, lines are to aid the reader. Data from this work, Darnley et al. (2012, 2017), Evans et al. (2014), Gaia Collaboration et al. (2021), Munari et al. (2020a), Skrutskie et al. (2006), and Page et al. (2022). Appears as Figure 18 in Murphy-Glaysher et al. (2022) ['V392 Persei: A γ-ray bright nova eruption from a known dwarf nova', Murphy-Glaysher et al., Mon. Not. R. Astron. Soc., 514, 6183, 2022 DOI `https://doi.org/10.1093/mnras/stac1577`].

In Figure 6.2 we present an updated V392 Per SED (cf. Darnley & Starrfield, 2018). The dotted lower-luminosity black line shows the pre-nova SED, ranging from the Wise B2 band up to the g-band (data from Darnley & Starrfield, 2018; Munari et al., 2020a, and references therein). As extensively discussed by Munari et al. (2020a), these pre-nova data suggest a warm and cool component. Munari et al. utilised these data to constrain the donor, arriving at a similar (albeit more detailed) conclusion to Darnley & Starrfield that the donor is likely a sub giant or low luminosity giant (specifically: G9 IV-III; $5.34\,\mathrm{R}_\odot$; $1.35\,\mathrm{M}_\odot$; $15\,\mathrm{L}_\odot$; $T_{\rm eff} = 4875\,\mathrm{K}$; Munari et al., 2020a). With the addition of the Wise mid-IR data, we find that the pre-nova data are reasonably well represented by a single black-body, with $T_{\rm eff} = 5700 \pm 400\,\mathrm{K}$ (cf. $\simeq 5000\,\mathrm{K}$ for GK Per; Álvarez-Hernández et al., 2021), $R = 7.8 \pm 0.6\,\mathrm{R}_\odot$, and $L = 55^{+20}_{-18}\,\mathrm{L}_\odot$.

The pre-nova SED is remarkably similar to that of GK Per (magenta data), albeit ~ 10 times as luminous. It is easy to draw comparisons between the two systems: both novae have evolved companions and long orbital periods; DN outbursts characterised by their month-long longevity; and like GK Per, V392 Per may be an IP. However, their post-nova behaviour is very different. If the orbital period were much shorter than we have inferred, i.e., of the order hours rather than days, the ongoing hard X-ray emission observed could be indicative of the presence of a polar CV, rather than an IP. However, such a short orbital period is not supported by the pre-nova SED, which, as discussed above, indicates a sub-giant or low luminosity giant donor. Furthermore, the length of the DN outbursts indicates the presence of a large accretion disk, which would be incompatible with an orbital period of only a few hours.

The post-nova SED is indicated by the solid black line in Figure 6.2, here the data span the z'-band to the *Swift*/UVOT uvw2 near-UV filter. It is clear that the post-nova emission is substantially greater than that seen pre-eruption (in the low

states, at least). Here, the post-nova SED is reminiscent of, and indeed of similar luminosity to, the disk in M31N 2008-12a (Darnley et al., 2017). This implies that $\dot{M}$ during the post-nova phase may be very high, which may act to lessen the time toward the next eruption.

6.5 Preliminary photoionization analysis

The preliminary photoionization analysis of the early nebular spectra presented a slightly contradictory picture of the temperature and density of the gas in the nova ejecta. The line ratios that were evaluated and compared to the grid of nova shell models indicated plasma conditions broadly consistent with those we would expect in a nova shell. However, the O3Hb ratio implied lower temperatures and a broader range of densities and possible metallicities than the HaHb ratio, with a similar picture applying at both epochs.

However, we would expect the standard nova metallicity from CLOUDY to be a good approximation to that of V392 Per, as the V1500 Cyg system is similar to V392 Per. Both are fast evolving novae with neon in their spectra, and in the case of the intermediate polar V1500 Cyg, the abundance determination involved analysis of lots of UV as well as optical spectral lines (Ferland & Shields, 1978). The black-body temperature determined from the best-fitting model to the *Swift* X-ray spectrum from 83 days was $k_{\rm B}T = 62^{+17}_{-14}$ eV, or $T_{BB} = 7.2^{+2.0}_{-1.6} \times 10^5$ K. For the combined spectrum from 89 to 97 days, the best-fitting model indicated a black-body temperature of $k_{\rm B}T = 48^{+10}_{-8}$ eV, or $T_{BB} = 5.6^{+1.2}_{-0.9} \times 10^5$ K. Therefore, it seems reasonable to favour the CLOUDY models with similar temperatures, rather than those with temperatures $\sim 10^7$ K.

Furthermore, line ratios are more reliable when there is a smaller separation between the wavelengths of the emission lines. Therefore, the O3Hb ratio is more reliable than the HaHb ratio. This supports a lower black-body effective temperature, as the temperatures predicted by the O3Hb ratio are generally lower than those predicted by the HaHb ratio. The best-fitting CLOUDY models span a range of black-body effective temperatures between 4×10^4 K and 1×10^7 K, but these correspond to a much smaller range of electron temperatures of the shell at 82 days. The electron temperatures are in the range $3.3 \times 10^3\,\mathrm{K} \leq T_e \leq 2.8 \times 10^4\,\mathrm{K}$. The initial electron densities for these models are between $10^4\,\mathrm{cm}^{-3}$ and $10^{6.7}\,\mathrm{cm}^{-3}$, and the corresponding hydrogen densities are in the range $1 \times 10^4\,\mathrm{cm}^{-3} \leq \mathrm{H_{den}} \leq 2 \times 10^7\,\mathrm{cm}^{-3}$.

Most of the best-fitting models lie within narrow ranges of electron temperatures and hydrogen densities, i.e., $1.5 \times 10^4\,\mathrm{K} \leq T_e \leq 2.8 \times 10^4\,\mathrm{K}$ and $2 \times 10^6\,\mathrm{cm}^{-3} \leq \mathrm{H_{den}} \leq 2 \times 10^7\,\mathrm{cm}^{-3}$. This may suggest that these model electron temperatures and hydrogen densities are consistent with the dominant conditions within the nebula. The two best-fitting models which lie outside this relatively narrow range of conditions have electron temperatures of 3.3×10^3 K and 4.1×10^3 K, and the corresponding hydrogen densities are $1 \times 10^4\,\mathrm{cm}^{-3}$ and $2 \times 10^4\,\mathrm{cm}^{-3}$.

The emerging scenario is complicated, as explained using the [O III] line ratio contours in Section 5.8. At the temperatures and densities typically found in nova shells relatively early after the eruption, a small range of densities corresponds to two widely separated possible temperatures, so it can be difficult to constrain the ionization conditions.

One way in which this difficulty can be addressed is by using a variety of different line ratios, some of which will be more sensitive to temperature and some to density. There are a few different observed line ratios from the spectra of V392 Per that have not yet been compared to the ratios predicted by the model. Specifically, line

ratios involving He I 6678 Å and 7065 Å, and He II 4686 Å have not yet been analysed. However, due to the speed of the nova eruption and the corresponding high velocity of the ejecta, there was a high degree of Doppler broadening and blending of nearby spectral lines. This meant it was difficult to unambiguously identify some spectral lines, and to deblend the emission lines to reliably measure their fluxes. This reduced the number of diagnostic tools available to us, including some of the useful ratios involving [O I], [O II] and [N II]. Even though we were unable to reliably measure the flux of [N II] in the spectra of V392 Per, PyNeb diagnostic plots involving the line ratio of [N II] 5755 Å to [N II] 6584 Å flux were produced. The diagnostic plots present a very similar picture to the [O III] line ratio contour plots shown in Section 5.8.

6.6 Summary

In this Chapter, we discussed the evidence that the light curve was powered by shocks. The X-ray emission and accretion were discussed. We suggested the accretion disk at least partially survived the eruption, or had reformed during the SSS phase when the system was constrained by the Sun. V392 Per may be a magnetic CV, of the intermediate polar type. We compared the pre-nova and post-nova light curves, and found that V392 Per is currently in an elevated high state, inferring that the system is currently exhibiting nova-like behaviour. We discussed the underlying system, and how the very fast light curve evolution, early SSS turn-off time and relatively high SSS black-body temperature at the end of the SSS phase, and presence of forbidden Ne lines in the nebular spectra all indicate the presence of a high mass WD in the system. We presented the pre-nova and post-nova SEDs of V392 Per. The pre-nova SED is very similar to the quiescent SED of GK Per, whereas the post-nova SED is a similar shape and luminosity to the accretion disk in the RRN M31N 2008-12a,

which could be indicative of a very high mass accretion rate. We briefly discussed the preliminary photoionization analysis of the early nebular spectra of V392 Per. In the next chapter, we present our conclusions and suggest some ways in which the research could be developed in future work.

Chapter 7

Conclusions and Future Work

The Summary and Conclusions are based on Section 6 of Murphy-Glaysher et al. (2022).

7.1 Summary and Conclusions

V392 Per is a known CV, which exhibited month-long GK Per-like DN outbursts, and its only known classical nova eruption was discovered on 2018 April 29. Panchromatic photometric and spectroscopic follow-up took place, with optical observations intensifying after the reported detection of γ-rays by Fermi-LAT, although the system was already in *Swift* Sun constraint at eruption. Post-Sun constraint, the eruption had entered the nebular spectral phase and *Swift* observations began. Since ~ 250 days post-eruption, V392 Per has remained in a high-state, consistently ~ 2 mag brighter than the pre-eruption quiescent minimum. Here we summarise our key findings:

1. *Gaia* EDR3 astrometry indicates $d = 3.5^{+0.6}_{-0.5}$ kpc, and we derive $E\,(B-V) =$

$0.70^{+0.03}_{-0.02}$.

2. With $t_2 = 2.0 \pm 0.2$ days, the eruption is classed as 'very fast', indicative of a high mass WD.

3. The early spectra indicate that V392 Per is a rare Fe II-broad class, with ejection velocities up to 5000 km s^{-1}.

4. Evolution of early-time H I P Cygni profiles strongly suggest there were two distinct mass ejections, with the higher velocity second ejecta running into and shocking the first.

5. These inter-ejecta, and subsequent intra-ejecta, shocks drove the γ-ray emission.

6. Distinct similarities between the γ-ray and early-optical evolution suggest that the early luminosity was powered by the shock emission.

7. The X-ray observations indicate the SSS was turning off as V392 Per emerged from Sun constraint on day 83.

8. Inferred SSS parameters along with forbidden Ne lines also suggest a high mass, perhaps ONe, WD.

9. Optical spectra show two distinct contributions: a broad initially triple, then double peaked fading ejecta spectrum; and a narrow lined and persistent accretion disk spectrum.

10. Persistent hard X-ray emission, and post-nova near-UV luminosity, is consistent with continuing accretion, suggesting that V392 Per is an intermediate polar.

11. Post-nova high cadence i'-band data indicate an orbital period of $P = 3.230 \pm 0.003$ days.

12. The pre-nova mid-IR–optical SED suggests a sub-giant or low luminosity giant donor.

13. The post-nova optical–NUV SED is substantially more luminous and is akin to an accretion disk.

7.2 Future Work

7.2.1 Continuing photoionization analysis of V392 Per

In a follow-up work, we will use the extensive spectra published here to explore the underlying geometry and ionization structure of the V392 Per ejecta. We will build on the preliminary photoionization analysis presented in Chapter 5. We will extend the number of line ratios extracted for the model nova shells to include He I and He II to test if a clearer dependence on temperature and density are seen in their corresponding line strengths.

The ionization parameter used in all preliminary models was based on a typical ionizing luminosity for novae. However, V392 Per was a bright system, so it would be more appropriate to use a higher luminosity. The grid of nova shell models could be extended to include a range of different ionizing luminosities. The models only incorporated an inner radius, based on the average velocity of the post-shock P Cygni profiles. The shell thickness could be added as a parameter, based on the highest and lowest velocities measured in the spectra.

We will evolve the models to later epochs to compare with line ratios measured in later spectra to gain an understanding of the evolution of the ionization structure of the ejecta. We will use SHAPE to model different possible geometries of the ejecta and different viewing angles, and to produce synthetic spectra to compare with the observed spectra. In particular, we will compare the synthetic line profiles with

the observed profiles of different emission lines to constrain the morpho-kinematic structure of different lines.

7.2.2 Ongoing observations of V392 Per

The most recent observations of V392 Per presented in Murphy-Glaysher et al. (2022) revealed the system to be in a post-nova elevated high-state, with no indication that the system will return to its pre-nova low-state and DN behaviour. We will conduct a photometric monitoring campaign to see when the DN outbursts resume, or if V392 Per returns to its quiescent level. As part of the long term monitoring campaign, we would investigate whether the light curve revealed a change in the orbital period. A search of the online collection of digitised photographic plates from the Harvard Observatory via the Digital Access to a Sky Century at Harvard (DASCH: Laycock et al., 2010) revealed an extensive collection of images covering the region of the sky around V392 Per. It would be interesting to perform photometry on these images in order to extend the light curve of V392 Per, and to search for evidence of a prior nova eruption or dwarf nova outbursts. By conducting UV monitoring, we would aim to constrain the disk accretion rate by fitting stellar atmosphere models to the disk. Observations with HST would be particularly useful due to its superior UV capabilities. Regular observations would provide information on the long term accretion behaviour of V392 Per.

It would be interesting to undertake further investigation of V392 Per as a potential intermediate polar system. We aim to conduct polarimetric observations of V392 Per using the Multiocolour OPTimised Optical Polarimeter (MOPTOP: Shrestha et al., 2020) instrument mounted on the Liverpool Telescope, to see if we are able to detect a signal from the magnetic field, or of scattering from grains caused by late-time dust formation within the nova shell.

There are now publicly available radio observations of V392 Per. Analysis of these data could reveal evidence of ongoing shocks within the nova shell, which could provide information about potential interaction of the nova ejecta with the local ISM. An absence of such a signal would also be informative. It could imply a low density of material surrounding V392 Per, which in turn could possibly be the result of previous nova eruptions having "swept up" the nearby ISM and creating a "cavity" around the progenitor system. An extreme example of this process, repeated many times and very frequently, is provided by the nova super-remnant formed around the rapid RN M31N 2008-12a, as reported by Darnley et al. (2019).

High resolution optical spectroscopy of V392 Per would be helpful as it might reveal additional emission lines in the post-nova spectra, and would allow us to obtain more accurate and up-to-date line ratios and velocities to use in the photoionization and morpho-kinematic analysis of the nova shell. It would be useful to perform IR and NUV spectroscopic observations of V392 Per to extend the selection of line ratios available for analysis, in order to better constrain the electron temperature and density of the plasma in the nova shell. As discussed previously, some line ratios are more effective at probing temperature, whereas others are best suited to the diagnosis of density, but a more complete picture can be constructed using spectral features from different parts of the electromagnetic spectrum.

7.2.3 Similar system not constrained by Sun early in eruption

Another suggested development of this research is to apply the same analytical techniques to the study of a system similar to V392 Per, but where the Sun constraint does not occur so early in the evolution of the eruption. The ideal system would be closer to Earth than V392 Per, and subject to less extinction. An equivalent system that is nearer to Earth would appear brighter optically and in γ-rays. We would

seek to take early X-ray observations to check for evidence of correlation between the γ-ray, X-ray and optical luminosities, which would indicate that the luminosity was driven by shocks. In a more slowly evolving system, it may be easier to find stronger evidence supporting the correlation of γ-ray, X-ray and optical emission, as in the case of V906 Car, due to the longer timescales involved. We would use *Swift* to perform X-ray and NUV observations of the eruption. If the eruption was sufficiently bright, we would use the UV grism to observe spectroscopically.

We would take polarimetric observations with MOPTOP as soon as possible during the early stages of the eruption in order to investigate the potential signal of collimation of the ejecta due to magnetic fields. Absence of a signal would also provide useful information to constrain the physics of the eruption. As the ejecta expands and cools, dust formation could take place, in which case scattering from dust grains could introduce polarisation.

The photometric and spectroscopic data would be analysed in the same way as the data from the eruption of V392 Per. If the light curve of this system also exhibited a quasi-plateau during its early decline, we would examine the spectra to check for evidence of the appearance of He II, which we would expect to detect if the plateau was caused by the accretion disk being revealed as the photosphere recedes towards the WD surface, compensating to some extent for the decline in brightness as the ejecta expand.

X-ray observations of the SSS phase would be particularly interesting, as they would allow us to accurately determine the key SSS parameters $t_{\rm on}$ and $t_{\rm off}$. This would enable us to better estimate the WD mass. The observations would permit measurement of the X-ray luminosity and black-body temperature during the SSS phase. For a nearby system, the X-ray counts may be high enough to provide sufficient time resolution of the X-ray light curve to measure the periodicity due to

WD rotation in the case of a magnetic WD.

The SSS X-ray luminosity would provide a good estimate of the ionizing luminosity of the WD for use in the photoionization analysis. Just as we are in the process of doing for V392 Per, we would use the nebular optical spectra of the nova eruption to perform an analysis of the photoionization conditions. A more slowly evolving eruption would have lower ejection velocities, and therefore less line blending. This should enable us to perform flux measurements of a larger number of emission lines that are useful as temperature or density diagnostic tools. In addition, we would carry out morpho-kinematic modelling of the ejecta to gain information on the geometry of the system, as outlined in Chapter 5 and Section 7.2.1.

In order to build a pre-eruption SED and historic light curve if available, we would check for archival observations of the progenitor system. For a nearby system, there may be archival HST images available to identify or constrain the donor star of the progenitor system. We would also check to see if the progenitor system was previously detected in X-rays, or whether upper limits on the X-ray flux were available, as this would provide a useful benchmark for comparison with the ongoing X-ray measurements.

Appendix A

Appendix

Table A.1: Log of spectral observations of V392 Per. For FRODOSpec and LBT/MODS observations, the resolution of the red arm and the blue arm are both given. Appears as Table A1 in Murphy-Glaysher et al. (2022) ['V392 Persei: A γ-ray bright nova eruption from a known dwarf nova', Murphy-Glaysher et al., Mon. Not. R. Astron. Soc., 514, 6183, 2022 DOI `https://doi.org/10.1093/mnras/stac1577`].

Δt (d)	Date (UT)	Telescope/ instrument	Resolution ∼R	Exp. time (s)
1.9	2018-04-29.898	RLE /THO-UK	527	703
2.1	2018-04-30.116	Hiltner/OSMOS	1600	7×40
2.9	2018-04-30.868	RLE /THO-UK	530	636
2.9	2018-04-30.889	RLE /THO-UK	530	636
3.8	2018-05-01.836	EBE/SSO-FR	503	1235
3.9	2018-05-01.863	DDJ/LSS-FR	525	770
4.2	2018-05-02.154	JPE/DHO-US	...	838
4.8	2018-05-02.794	BER/BVO-IT	3975	484
4.8	2018-05-02.807	BER/BVO-IT	5713	1303
4.9	2018-05-02.863	LT/FRODOSpec	2200/2600	5×60

Continued on next page

Table A.1 – continued from previous page

Δt (d)	Date (UT)	Telescope/ instrument	Resolution ∼R	Exp. time (s)
4.9	2018-05-02.871	RLE /THO-UK	507	1820
5.2	2018-05-03.152	JPE/DHO-US	5713	763
5.9	2018-05-03.846	EBE/SSO-FR	514	1739
5.9	2018-05-03.860	LT/FRODOSpec	2200/2600	5×60
5.9	2018-05-03.886	CBO/OCT-FR	515	2111
5.9	2018-05-03.926	YBGM/OSM-FR	945	1821
6.1	2018-05-04.123	Hiltner/OSMOS	1600	4×75
6.9	2018-05-04.854	EBE/SSO-FR	521	2452
6.9	2018-05-04.859	LT/FRODOSpec	5300/5500	3×60
6.9	2018-05-04.886	CBO/OCT-FR	509	2111
7.0	2018-05-04.955	JMO/CAL-FR	646	3284
7.1	2018-05-05.123	Hiltner/OSMOS	1600	6×90
7.9	2018-05-05.830	OGA/OTO-FR	11000	2410
7.9	2018-05-05.868	DDJ/LSS-FR	522	4327
7.9	2018-05-05.855	EBE/SSO-FR	509	1817
8.1	2018-05-06.124	Hiltner/OSMOS	1600	7×90
8.1	2018-05-06.128	JPE/TEX-US	...	786
8.8	2018-05-06.838	OGA/OTO-FR	11000	3617
8.9	2018-05-06.874	CBO/OCT-FR	505	3016
8.9	2018-05-06.886	RLE /THO-UK	531	2982
9.1	2018-05-07.122	JPE/TEX-US	...	1253
9.8	2018-05-07.792	BER/BVO-IT	5915	1506
9.8	2018-05-07.816	BER/BVO-IT	3996	2013
9.9	2018-05-07.863	EBE/SSO-FR	506	1607

Continued on next page

Table A.1 – continued from previous page

Δt (d)	Date (UT)	Telescope/ instrument	Resolution ∼R	Exp. time (s)
9.9	2018-05-07.875	CBO/OCT-FR	506	3016
9.9	2018-05-07.922	JMO/CAL-FR	641	3696
9.9	2018-05-07.924	RLE /THO-UK	513	1517
76	2018-07-12.213	LT/FRODOSpec	5300/5500	3×180
77	2018-07-13.219	LT/FRODOSpec	5300/5500	3×300
82	2018-07-18.219	LT/SPRAT	350	3×600
84	2018-07-20.221	LT/SPRAT	350	3×300
87	2018-07-23.215	LT/FRODOSpec	2200/2600	3×600
89	2018-07-25.209	LT/SPRAT	350	3×300
101	2018-08-06.185	LT/SPRAT	350	3×300
112	2018-08-17.138	LT/SPRAT	350	3×300
132	2018-09-07.474	Hiltner/OSMOS	1600	2×300
143	2018-09-17.159	LT/FRODOSpec	5300/5500	3×600
146	2018-09-21.048	LBT/MODS	2300/1850	2×300
157	2018-10-01.036	LT/SPRAT	350	3×600
186	2018-10-30.166	LT/SPRAT	350	3×600
189	2018-11-03.257	Hiltner/OSMOS	1600	2×600
212	2018-11-25.082	LT/SPRAT	350	3×600
220	2018-11-28.237	Hiltner/OSMOS	1600	2×1200
226	2018-12-09.101	LT/FRODOSpec	5300/5500	3×900
252	2019-01-04.981	LT/FRODOSpec	5300/5500	5×1080
253	2019-01-05.984	LT/SPRAT	350	3×1200
286	2019-02-05.170	Hiltner/OSMOS	1600	3×1200
304	2019-02-23.119	Hiltner/OSMOS	1600	3×1200

Continued on next page

Table A.1 – continued from previous page

Δt (d)	Date (UT)	Telescope/ instrument	Resolution ∼R	Exp. time (s)
307	2019-02-28.852	LT/SPRAT	350	2×900
346	2019-04-08.890	LT/SPRAT	350	3×600
351	2019-04-10.121	Hiltner/OSMOS	1600	3×1200
448	2019-07-19.204	LT/SPRAT	350	3×600
478	2019-08-18.220	LT/SPRAT	350	3×600
502	2019-09-12.442	Hiltner/OSMOS	1600	3×1200
504	2019-09-13.087	LT/SPRAT	350	3×600
527	2019-10-07.435	Hiltner/OSMOS	1600	3×1200
535	2019-10-14.003	LT/SPRAT	350	3×600
543	2019-10-23.243	LBT/MODS	2300/1850	6×600
553	2019-11-02.342	Hiltner/OSMOS	1600	3×1200
568	2019-11-16.097	LT/SPRAT	350	3×600
591	2019-12-09.940	LT/SPRAT	350	3×900
619	2020-01-07.100	Hiltner/OSMOS	1600	3×1200
854	2021-02-01.206	LT/SPRAT	350	3×1200

ARAS Observers: BER: Paolo Berardi — CBO: Christophe Boussin — DDJ: Daniel Dejean — EBE: Etienne Bertrand — JMO: Jacques Montier — JPE: Jim Edlin — OGA: Olivier Garde — RLE: Robin Leadbeater — YBGM: Yolande Buchet & Gérard Martineau.

Table A.2: The Pan-STARRS reference stars used to calibrate the photometry of V392 Per. The *Swift*/UVOT U magnitude of #15 is included. Errors on magnitudes for $BVr'i'z'$ are ±0.034, ±0.012, ±0.004, ±0.005 and ±0.010, respectively. Appears as Table A2 in Murphy-Glaysher et al. (2022) ['V392 Persei: A γ-ray bright nova eruption from a known dwarf nova', Murphy-Glaysher et al., Mon. Not. R. Astron. Soc., 514, 6183, 2022 DOI `https://doi.org/10.1093/mnras/stac1577`].

Reference Star no	Pan-STARRS Object ID	U / mag	B / mag	V / mag	r' / mag	i' / mag	z' / mag
1	164840708125355000	...	18.95	17.72	17.29	16.82	16.51
2	164800708138869000	...	20.16	18.96	18.54	18.08	17.70
3	164810708164722000	...	20.02	18.60	18.08	17.47	17.03
4	164830708184131000	...	19.38	18.07	17.60	17.03	16.64
5	164820708189789000	...	21.72	20.22	19.68	19.02	18.56
6	164830708206900000	...	22.53	21.01	20.46	19.77	19.23
7	164830708274029000	...	19.59	17.98	17.38	16.71	16.24
8	164810708286245000	...	19.29	18.00	17.54	17.01	16.63
9	164840708297440000	...	21.28	19.90	19.41	18.76	18.33
10	164830708300909000	...	21.00	19.27	18.64	17.92	17.41
11	164830708331564000	...	21.58	20.00	19.42	18.75	18.28
12	164810708363800000	...	20.31	18.83	18.29	17.66	17.21
13	164850708381906000	...	19.90	18.17	17.53	16.75	16.21
14	164850708384241000	...	18.29	17.27	16.92	16.53	16.26
15	164830708391402000	16.70	16.03	15.10	14.80	14.51	14.33
16	164850708400482000	...	20.41	19.06	18.58	18.01	17.59
17	164820708400455000	...	21.98	20.30	19.68	18.98	18.47
18	164860708402161000	...	21.12	19.59	19.03	18.37	17.91
19	164840708431519000	...	18.82	17.65	17.24	16.77	16.45
20	164860708441271000	...	20.39	19.19	18.77	18.23	17.85
21	164820708501862000	...	18.90	17.68	17.25	16.75	16.41

Continued on next page

Table A.2 – continued from previous page

Reference Star no	Pan-STARRS Object ID	U / mag	B / mag	V / mag	r' / mag	i' / mag	z' / mag
22	164810708517219000	...	18.96	17.70	17.25	16.74	16.38
23	164820708606127000	...	17.17	15.95	15.52	15.10	14.84
24	164850708622792000	...	19.11	17.68	17.16	16.53	16.14
25	164810708639843000	...	19.61	18.28	17.80	17.27	16.90

Table A.3: u'BV$r'i'z'$ and *Swift*/UVOT photometry of V392 Per (AB magnitudes). Appears as Table A3 in Murphy-Glaysher et al. (2022) ['V392 Persei: A γ-ray bright nova eruption from a known dwarf nova', Murphy-Glaysher et al., Mon. Not. R. Astron. Soc., 514, 6183, 2022 DOI `https://doi.org/10.1093/mnras/stac1577`].

Date (UT)	Δ t / days	Telescope & Instrument	Filter	Exp. time /s	Photometry /mag
2018 Jul 21.192	84.202	LT IO:O	u'	3×30	14.751 ± 0.011
2018 Jul 22.217	85.227	LT IO:O	u'	3×30	14.838 ± 0.008
2018 Jul 23.194	86.204	LT IO:O	u'	3×30	14.900 ± 0.009
2018 Jul 24.185	87.195	LT IO:O	u'	3×30	14.865 ± 0.012
2018 Jul 25.182	88.192	LT IO:O	u'	3×30	14.973 ± 0.013
2018 Jul 26.190	89.200	LT IO:O	u'	3×30	14.898 ± 0.015
2018 Jul 27.182	90.192	LT IO:O	u'	3×30	14.832 ± 0.013
2018 Jul 28.175	91.185	LT IO:O	u'	3×30	15.122 ± 0.012
2018 Jul 29.174	92.184	LT IO:O	u'	3×30	15.013 ± 0.026
2018 Jul 31.169	94.179	LT IO:O	u'	3×30	15.096 ± 0.016
2018 Aug 01.184	95.194	LT IO:O	u'	3×30	14.980 ± 0.016
2018 Aug 02.159	96.169	LT IO:O	u'	3×30	15.034 ± 0.012
2018 Aug 03.157	97.167	LT IO:O	u'	3×30	15.144 ± 0.015
2018 Aug 06.148	100.158	LT IO:O	u'	3×30	15.170 ± 0.015
2018 Aug 08.164	102.174	LT IO:O	u'	3×30	15.237 ± 0.012
2018 Aug 10.171	104.181	LT IO:O	u'	3×30	15.345 ± 0.010
2018 Aug 16.122	110.132	LT IO:O	u'	3×30	15.426 ± 0.013
2018 Aug 19.165	113.175	LT IO:O	u'	3×30	15.430 ± 0.010
2018 Aug 22.217	116.227	LT IO:O	u'	3×30	15.326 ± 0.008
2018 Aug 25.097	119.107	LT IO:O	u'	3×30	15.587 ± 0.016
2018 Aug 28.107	122.117	LT IO:O	u'	3×30	15.448 ± 0.015
2018 Aug 31.085	125.095	LT IO:O	u'	3×30	15.391 ± 0.018
2018 Sep 03.073	128.083	LT IO:O	u'	3×30	15.525 ± 0.015
2018 Sep 06.066	131.076	LT IO:O	u'	3×30	15.483 ± 0.015
2018 Sep 09.054	134.064	LT IO:O	u'	3×30	15.714 ± 0.018
2018 Sep 12.062	137.072	LT IO:O	u'	3×30	15.811 ± 0.016
2018 Sep 18.086	143.096	LT IO:O	u'	3×30	15.763 ± 0.013
2018 Sep 23.018	148.028	LT IO:O	u'	3×30	16.090 ± 0.052

Continued on next page

Table A.3 – continued from previous page

Date (UT)	Δ t / days	Telescope & Instrument	Filter	Exp. time /s	Photometry /mag
2018 Sep 26.014	151.024	LT IO:O	u'	3×30	16.003 ± 0.027
2018 Sep 29.057	154.067	LT IO:O	u'	3×30	15.849 ± 0.014
2018 Oct 02.012	157.022	LT IO:O	u'	3×30	16.010 ± 0.016
2018 Nov 01.111	187.121	LT IO:O	u'	3×30	16.329 ± 0.014
2018 Nov 08.159	194.169	LT IO:O	u'	3×30	16.307 ± 0.014
2018 Nov 16.117	202.127	LT IO:O	u'	3×30	16.341 ± 0.014
2018 Nov 26.024	212.034	LT IO:O	u'	3×30	16.210 ± 0.019
2018 Dec 10.064	226.074	LT IO:O	u'	3×30	16.228 ± 0.014
2018 Dec 15.963	231.973	LT IO:O	u'	3×30	16.333 ± 0.019
2018 Dec 22.839	238.849	LT IO:O	u'	3×30	16.413 ± 0.034
2018 Dec 28.894	244.904	LT IO:O	u'	3×30	16.585 ± 0.041
2019 Jan 04.919	251.929	LT IO:O	u'	3×30	16.450 ± 0.017
2019 Jan 10.973	257.983	LT IO:O	u'	3×30	16.419 ± 0.015
2019 Jan 19.987	266.997	LT IO:O	u'	3×30	16.341 ± 0.019
2019 Jan 25.903	272.912	LT IO:O	u'	3×30	16.256 ± 0.015
2019 Jan 31.939	278.949	LT IO:O	u'	3×30	16.145 ± 0.013
2019 Feb 06.888	284.898	LT IO:O	u'	3×30	16.342 ± 0.018
2019 Feb 12.874	290.884	LT IO:O	u'	3×30	16.465 ± 0.016
2019 Feb 28.888	306.898	LT IO:O	u'	3×30	16.565 ± 0.018
2019 Mar 16.846	322.856	LT IO:O	u'	3×30	16.335 ± 0.016
2019 Apr 08.859	345.869	LT IO:O	u'	3×30	16.480 ± 0.018
2019 Apr 25.851	362.861	LT IO:O	u'	3×30	16.294 ± 0.043
2019 Jul 19.215	447.225	LT IO:O	u'	3×30	16.334 ± 0.028
2019 Aug 01.218	460.228	LT IO:O	u'	3×30	16.393 ± 0.026
2019 Aug 19.125	478.135	LT IO:O	u'	3×30	16.499 ± 0.044
2019 Sep 14.113	504.123	LT IO:O	u'	3×60	16.322 ± 0.016
2019 Oct 14.977	534.987	LT IO:O	u'	3×60	16.372 ± 0.019
2019 Nov 16.937	567.947	LT IO:O	u'	3×60	15.834 ± 0.009
2019 Dec 09.905	590.915	LT IO:O	u'	3×60	16.357 ± 0.018
2020 Aug 31.152	856.162	LT IO:O	u'	3×120	16.624 ± 0.007
2021 Feb 02.865	1011.875	LT IO:O	u'	3×180	16.127 ± 0.005

Continued on next page

Table A.3 – continued from previous page

Date (UT)	Δ t / days	Telescope & Instrument	Filter	Exp. time /s	Photometry /mag
2018 Apr 29.942	1.952	AAVSO MIW	B		7.398 ± 0.088
2018 Apr 30.807	2.817	AAVSO VMAG	B		7.972 ± 0.030
2018 Apr 30.870	2.880	AAVSO EHEA	B		8.097 ± 0.020
2018 Apr 30.889	2.899	AAVSO MIW	B		8.059 ± 0.036
2018 Apr 30.904	2.914	AAVSO BDG	B		8.099 ± 0.087
2018 Apr 30.913	2.923	AAVSO BDG	B		8.063 ± 0.079
2018 Apr 30.919	2.929	AAVSO BDG	B		8.095 ± 0.064
2018 May 01.101	3.110	AAVSO SDM	B		8.240 ± 0.048
2018 May 01.152	3.162	AAVSO SSTA	B		8.153 ± 0.001
2018 May 01.189	3.199	AAVSO STYA	B		8.157 ± 0.002
2018 May 01.190	3.200	AAVSO RBRB	B		8.171 ± 0.001
2018 May 01.867	3.877	AAVSO EHEA	B		8.609 ± 0.030
2018 May 02.106	4.115	AAVSO SDM	B		8.738 ± 0.199
2018 May 02.848	4.858	AAVSO ETOA	B		9.054 ± 0.027
2018 May 02.849	4.859	AAVSO ETOA	B		9.059 ± 0.012
2018 May 02.850	4.860	AAVSO ETOA	B		9.076 ± 0.034
2018 May 02.851	4.861	AAVSO ETOA	B		9.032 ± 0.020
2018 May 02.919	4.929	AAVSO MIW	B		9.127 ± 0.023
2018 May 03.896	5.906	AAVSO EHEA	B		9.297 ± 0.025
2018 May 04.192	6.202	AAVSO JDAD	B		9.326 ± 0.001
2018 May 04.210	6.220	AAVSO RBRB	B		9.306 ± 0.001
2018 May 04.808	6.818	AAVSO VMAG	B		9.480 ± 0.030
2018 May 04.827	6.837	AAVSO ETOA	B		9.504 ± 0.006
2018 May 04.828	6.838	AAVSO ETOA	B		9.529 ± 0.042
2018 May 04.829	6.839	AAVSO ETOA	B		9.537 ± 0.022
2018 May 04.830	6.839	AAVSO ETOA	B		9.520 ± 0.016
2018 May 04.874	6.884	AAVSO EHEA	B		9.596 ± 0.035
2018 May 05.204	7.214	AAVSO RBRB	B		9.387 ± 0.005
2018 May 05.225	7.235	AAVSO STYA	B		9.434 ± 0.003
2018 May 05.878	7.888	AAVSO OAR	B		9.229 ± 0.003
2018 May 05.878	7.888	AAVSO OAR	B		9.227 ± 0.003

Continued on next page

Table A.3 – continued from previous page

Date (UT)	Δ t / days	Telescope & Instrument	Filter	Exp. time /s	Photometry /mag
2018 May 05.878	7.888	AAVSO OAR	B		9.279 ± 0.003
2018 May 05.879	7.889	AAVSO OAR	B		9.260 ± 0.003
2018 May 05.879	7.889	AAVSO OAR	B		9.225 ± 0.003
2018 May 05.884	7.894	AAVSO MIW	B		9.315 ± 0.023
2018 May 05.893	7.903	AAVSO OAR	B		9.235 ± 0.003
2018 May 05.894	7.904	AAVSO OAR	B		9.183 ± 0.002
2018 May 05.895	7.905	AAVSO OAR	B		9.244 ± 0.002
2018 May 05.895	7.905	AAVSO OAR	B		9.246 ± 0.002
2018 May 05.896	7.906	AAVSO OAR	B		9.162 ± 0.002
2018 May 05.906	7.916	AAVSO EHEA	B		9.353 ± 0.040
2018 May 06.044	8.054	AAVSO LDJ	B		9.292 ± 0.010
2018 May 06.873	8.883	AAVSO EHEA	B		9.629 ± 0.030
2018 May 06.884	8.894	AAVSO MIW	B		9.518 ± 0.045
2018 May 07.180	9.190	AAVSO STYA	B		9.428 ± 0.003
2018 May 07.208	9.217	AAVSO RBRB	B		9.419 ± 0.003
2018 May 07.208	9.218	AAVSO RRIB	B		9.413 ± 0.003
2018 May 07.803	9.813	AAVSO VMAG	B		9.626 ± 0.030
2018 May 07.887	9.897	AAVSO MIW	B		9.595 ± 0.032
2018 May 08.050	10.060	AAVSO LDJ	B		9.543 ± 0.005
2018 May 10.185	12.195	AAVSO RBRB	B		10.033 ± 0.005
2018 May 10.185	12.195	AAVSO STYA	B		10.034 ± 0.004
2018 May 12.178	14.188	AAVSO SSTA	B		10.489 ± 0.003
2018 May 12.804	14.814	AAVSO VMAG	B		10.595 ± 0.030
2018 May 12.846	14.856	AAVSO ETOA	B		10.651 ± 0.032
2018 May 12.848	14.858	AAVSO ETOA	B		10.622 ± 0.023
2018 May 12.850	14.860	AAVSO ETOA	B		10.619 ± 0.003
2018 May 12.852	14.862	AAVSO ETOA	B		10.653 ± 0.030
2018 May 12.854	14.864	AAVSO ETOA	B		10.630 ± 0.026
2018 May 13.206	15.215	AAVSO RBRB	B		10.655 ± 0.005
2018 May 13.206	15.215	AAVSO LRCA	B		10.653 ± 0.004
2018 May 13.209	15.219	AAVSO STYA	B		10.673 ± 0.004

Continued on next page

Table A.3 – continued from previous page

Date (UT)	Δ t / days	Telescope & Instrument	Filter	Exp. time /s	Photometry /mag
2018 May 14.175	16.185	AAVSO STYA	B		10.833 ± 0.011
2018 May 14.210	16.219	AAVSO RBRB	B		10.858 ± 0.033
2018 May 15.042	17.051	AAVSO LDJ	B		10.954 ± 0.005
2018 May 16.194	18.204	AAVSO RBRB	B		11.024 ± 0.034
2018 May 21.212	23.221	AAVSO RBRB	B		11.567 ± 0.017
2018 Jul 07.363	70.373	AAVSO MRV	B		14.052 ± 0.098
2018 Jul 14.359	77.369	AAVSO MRV	B		14.362 ± 0.130
2018 Jul 14.479	77.488	AAVSO SGEA	B		13.892 ± 0.121
2018 Jul 17.474	80.484	AAVSO SGEA	B		14.152 ± 0.118
2018 Jul 17.501	80.511	AAVSO SGEA	B		14.452 ± 0.126
2018 Jul 18.479	81.489	AAVSO SGEA	B		14.302 ± 0.031
2018 Jul 18.497	81.507	AAVSO SGEA	B		14.128 ± 0.082
2018 Jul 19.352	82.362	AAVSO CDJA	B		14.422 ± 0.023
2018 Jul 19.353	82.363	AAVSO CDJA	B		14.453 ± 0.023
2018 Jul 19.355	82.365	AAVSO CDJA	B		14.452 ± 0.024
2018 Jul 21.189	84.199	LT IO:O	B	3×30	14.675 ± 0.015
2018 Jul 21.456	84.466	AAVSO SGEA	B		14.331 ± 0.056
2018 Jul 22.213	85.223	LT IO:O	B	3×30	14.746 ± 0.013
2018 Jul 23.190	86.200	LT IO:O	B	3×30	14.722 ± 0.012
2018 Jul 24.181	87.191	LT IO:O	B	3×30	14.730 ± 0.016
2018 Jul 25.178	88.188	LT IO:O	B	3×30	14.927 ± 0.016
2018 Jul 26.186	89.196	LT IO:O	B	3×30	15.027 ± 0.032
2018 Jul 27.178	90.188	LT IO:O	B	3×30	14.795 ± 0.027
2018 Jul 28.171	91.181	LT IO:O	B	3×30	14.887 ± 0.024
2018 Jul 29.170	92.180	LT IO:O	B	3×30	15.060 ± 0.053
2018 Jul 31.165	94.175	LT IO:O	B	3×30	15.072 ± 0.019
2018 Aug 01.179	95.189	LT IO:O	B	3×30	14.993 ± 0.020
2018 Aug 02.155	96.165	LT IO:O	B	3×30	14.918 ± 0.015
2018 Aug 02.345	96.355	AAVSO CDJA	B		14.902 ± 0.021
2018 Aug 02.347	96.357	AAVSO CDJA	B		14.895 ± 0.020
2018 Aug 02.348	96.358	AAVSO CDJA	B		14.878 ± 0.019

Continued on next page

Table A.3 – continued from previous page

Date (UT)	Δ t / days	Telescope & Instrument	Filter	Exp. time /s	Photometry /mag
2018 Aug 02.489	96.498	AAVSO SGEA	B		14.587 ± 0.054
2018 Aug 03.153	97.163	LT IO:O	B	3×30	15.131 ± 0.019
2018 Aug 03.486	97.496	AAVSO SGEA	B		14.818 ± 0.038
2018 Aug 04.152	98.162	AAVSO MRV	B		14.970 ± 0.110
2018 Aug 06.145	100.155	LT IO:O	B	3×30	15.071 ± 0.018
2018 Aug 06.419	100.429	AAVSO DKS	B		15.048 ± 0.047
2018 Aug 06.495	100.505	AAVSO SGEA	B		14.820 ± 0.023
2018 Aug 07.419	101.429	AAVSO DKS	B		15.175 ± 0.047
2018 Aug 08.160	102.170	LT IO:O	B	3×30	15.131 ± 0.013
2018 Aug 09.319	103.329	AAVSO BMSA	B		15.069 ± 0.028
2018 Aug 09.320	103.330	AAVSO BMSA	B		14.977 ± 0.025
2018 Aug 09.321	103.331	AAVSO BMSA	B		15.031 ± 0.026
2018 Aug 10.167	104.177	LT IO:O	B	3×30	15.247 ± 0.011
2018 Aug 10.483	104.493	AAVSO SGEA	B		14.822 ± 0.050
2018 Aug 13.169	107.179	LT IO:O	B	3×30	15.356 ± 0.066
2018 Aug 13.330	107.340	AAVSO BMSA	B		15.235 ± 0.033
2018 Aug 13.331	107.341	AAVSO BMSA	B		15.255 ± 0.033
2018 Aug 13.334	107.344	AAVSO BMSA	B		15.271 ± 0.032
2018 Aug 13.475	107.485	AAVSO SGEA	B		14.983 ± 0.031
2018 Aug 14.421	108.431	AAVSO SGEA	B		14.925 ± 0.034
2018 Aug 15.449	109.459	AAVSO SGEA	B		14.964 ± 0.027
2018 Aug 15.511	109.521	AAVSO SGEA	B		14.804 ± 0.030
2018 Aug 16.118	110.128	LT IO:O	B	3×30	15.270 ± 0.013
2018 Aug 16.451	110.461	AAVSO SGEA	B		15.112 ± 0.027
2018 Aug 17.444	111.454	AAVSO SGEA	B		14.999 ± 0.025
2018 Aug 17.503	111.512	AAVSO SGEA	B		14.800 ± 0.017
2018 Aug 18.412	112.421	AAVSO SGEA	B		14.978 ± 0.027
2018 Aug 18.503	112.513	AAVSO SGEA	B		14.863 ± 0.018
2018 Aug 19.161	113.171	LT IO:O	B	3×30	15.268 ± 0.010
2018 Aug 19.449	113.459	AAVSO SGEA	B		15.009 ± 0.026
2018 Aug 19.482	113.492	AAVSO SGEA	B		14.886 ± 0.018

Continued on next page

Table A.3 – continued from previous page

Date (UT)	Δ t / days	Telescope & Instrument	Filter	Exp. time /s	Photometry /mag
2018 Aug 20.190	114.200	AAVSO MRV	B		15.121 ± 0.058
2018 Aug 20.419	114.429	AAVSO SGEA	B		15.009 ± 0.025
2018 Aug 20.487	114.497	AAVSO SGEA	B		14.875 ± 0.016
2018 Aug 21.434	115.444	AAVSO SGEA	B		14.927 ± 0.026
2018 Aug 21.507	115.517	AAVSO SGEA	B		14.846 ± 0.017
2018 Aug 22.213	116.223	LT IO:O	B	3×30	15.207 ± 0.012
2018 Aug 22.443	116.453	AAVSO SGEA	B		14.934 ± 0.025
2018 Aug 22.522	116.532	AAVSO SGEA	B		14.897 ± 0.036
2018 Aug 23.474	117.484	AAVSO SGEA	B		15.029 ± 0.025
2018 Aug 23.510	117.520	AAVSO SGEA	B		14.905 ± 0.018
2018 Aug 25.094	119.104	LT IO:O	B	3×30	15.326 ± 0.019
2018 Aug 26.517	120.527	AAVSO SGEA	B		15.054 ± 0.034
2018 Aug 27.111	121.120	AAVSO MRV	B		15.176 ± 0.046
2018 Aug 27.517	121.527	AAVSO SGEA	B		15.010 ± 0.032
2018 Aug 28.104	122.113	LT IO:O	B	3×30	15.195 ± 0.017
2018 Aug 28.524	122.534	AAVSO SGEA	B		15.060 ± 0.044
2018 Aug 29.514	123.524	AAVSO SGEA	B		15.193 ± 0.034
2018 Aug 30.521	124.531	AAVSO SGEA	B		14.947 ± 0.041
2018 Aug 31.081	125.091	LT IO:O	B	3×30	15.315 ± 0.025
2018 Aug 31.517	125.527	AAVSO SGEA	B		14.978 ± 0.030
2018 Sep 01.528	126.538	AAVSO SGEA	B		15.049 ± 0.068
2018 Sep 02.518	127.528	AAVSO SGEA	B		15.109 ± 0.040
2018 Sep 02.520	127.530	AAVSO SGEA	B		15.110 ± 0.003
2018 Sep 03.069	128.079	LT IO:O	B	3×30	15.391 ± 0.015
2018 Sep 03.509	128.519	AAVSO SGEA	B		15.092 ± 0.033
2018 Sep 04.521	129.531	AAVSO SGEA	B		15.132 ± 0.032
2018 Sep 05.514	130.524	AAVSO SGEA	B		15.179 ± 0.033
2018 Sep 05.521	130.531	AAVSO SGEA	B		14.989 ± 0.022
2018 Sep 06.062	131.072	LT IO:O	B	3×30	15.269 ± 0.152
2018 Sep 06.504	131.514	AAVSO SGEA	B		15.155 ± 0.027
2018 Sep 06.511	131.521	AAVSO SGEA	B		14.971 ± 0.018

Continued on next page

Table A.3 – continued from previous page

Date (UT)	Δ t / days	Telescope & Instrument	Filter	Exp. time /s	Photometry /mag
2018 Sep 07.498	132.508	AAVSO SGEA	B		15.196 ± 0.030
2018 Sep 08.511	133.521	AAVSO SGEA	B		15.262 ± 0.028
2018 Sep 08.525	133.535	AAVSO SGEA	B		15.227 ± 0.023
2018 Sep 09.050	134.060	LT IO:O	B	3×30	15.459 ± 0.015
2018 Sep 09.532	134.542	AAVSO SGEA	B		15.153 ± 0.043
2018 Sep 09.535	134.545	AAVSO SGEA	B		15.018 ± 0.035
2018 Sep 11.532	136.542	AAVSO SGEA	B		15.268 ± 0.045
2018 Sep 12.058	137.068	LT IO:O	B	3×30	15.549 ± 0.014
2018 Sep 13.208	138.217	AAVSO MDYA	B		15.292 ± 0.033
2018 Sep 13.209	138.219	AAVSO MDYA	B		15.304 ± 0.033
2018 Sep 13.210	138.220	AAVSO MDYA	B		15.392 ± 0.033
2018 Sep 13.528	138.538	AAVSO SGEA	B		15.173 ± 0.032
2018 Sep 13.530	138.540	AAVSO SGEA	B		15.049 ± 0.022
2018 Sep 18.082	143.092	LT IO:O	B	3×30	15.642 ± 0.011
2018 Sep 23.014	148.024	LT IO:O	B	3×30	15.667 ± 0.028
2018 Sep 26.010	151.020	LT IO:O	B	3×30	15.725 ± 0.018
2018 Sep 29.053	154.063	LT IO:O	B	3×30	15.627 ± 0.015
2018 Oct 02.008	157.018	LT IO:O	B	3×30	15.767 ± 0.012
2018 Oct 08.283	163.293	AAVSO SGEA	B		14.987 ± 0.064
2018 Nov 01.107	187.117	LT IO:O	B	3×30	16.135 ± 0.012
2018 Nov 01.516	187.526	AAVSO SGEA	B		15.599 ± 0.067
2018 Nov 03.468	189.478	AAVSO SGEA	B		15.388 ± 0.047
2018 Nov 05.154	191.164	AAVSO MRV	B		16.026 ± 0.036
2018 Nov 07.566	193.576	AAVSO SGEA	B		15.405 ± 0.140
2018 Nov 08.156	194.165	LT IO:O	B	3×30	16.084 ± 0.012
2018 Nov 16.113	202.123	LT IO:O	B	3×30	16.059 ± 0.011
2018 Nov 26.020	212.030	LT IO:O	B	3×30	16.008 ± 0.018
2018 Nov 26.315	212.325	AAVSO MRV	B		16.038 ± 0.043
2018 Dec 10.061	226.071	LT IO:O	B	3×30	16.111 ± 0.012
2018 Dec 15.960	231.970	LT IO:O	B	3×30	16.133 ± 0.016
2018 Dec 22.836	238.846	LT IO:O	B	3×30	16.163 ± 0.024

Continued on next page

Table A.3 – continued from previous page

Date (UT)	Δ t / days	Telescope & Instrument	Filter	Exp. time /s	Photometry /mag
2018 Dec 28.890	244.900	LT IO:O	B	3×30	16.176 ± 0.022
2018 Dec 28.969	244.979	AAVSO MRV	B		16.053 ± 0.034
2019 Jan 04.916	251.926	LT IO:O	B	3×30	16.213 ± 0.012
2019 Jan 10.969	257.979	LT IO:O	B	3×30	16.167 ± 0.012
2019 Jan 11.075	258.085	AAVSO MRV	B		16.070 ± 0.029
2019 Jan 19.984	266.993	LT IO:O	B	3×30	16.182 ± 0.015
2019 Jan 25.899	272.909	LT IO:O	B	3×30	16.046 ± 0.013
2019 Jan 31.907	278.917	AAVSO MRV	B		15.811 ± 0.027
2019 Jan 31.935	278.945	LT IO:O	B	3×30	15.916 ± 0.011
2019 Feb 06.885	284.894	LT IO:O	B	3×30	16.156 ± 0.017
2019 Feb 12.870	290.880	LT IO:O	B	3×30	16.216 ± 0.013
2019 Feb 12.948	290.958	AAVSO MRV	B		16.124 ± 0.041
2019 Feb 19.895	297.905	LT IO:O	B	3×30	16.225 ± 0.118
2019 Feb 28.885	306.894	LT IO:O	B	3×30	16.226 ± 0.014
2019 Mar 04.966	310.976	AAVSO MRV	B		16.123 ± 0.024
2019 Mar 16.843	322.853	LT IO:O	B	3×30	16.247 ± 0.013
2019 Apr 08.855	345.865	LT IO:O	B	3×30	16.253 ± 0.017
2019 Apr 25.847	362.857	LT IO:O	B	3×30	16.251 ± 0.060
2019 Jul 19.211	447.221	LT IO:O	B	3×30	16.155 ± 0.018
2019 Aug 01.214	460.224	LT IO:O	B	3×30	16.224 ± 0.014
2019 Aug 19.122	478.131	LT IO:O	B	3×30	16.222 ± 0.020
2019 Sep 14.107	504.117	LT IO:O	B	3×60	16.180 ± 0.028
2019 Oct 14.971	534.981	LT IO:O	B	3×60	16.175 ± 0.015
2019 Nov 16.931	567.941	LT IO:O	B	3×60	15.815 ± 0.013
2019 Dec 09.899	590.909	LT IO:O	B	3×60	16.036 ± 0.020
2020 Aug 31.157	856.167	LT IO:O	B	3×120	16.380 ± 0.009
2021 Feb 02.851	1011.861	LT IO:O	B	3×120	15.989 ± 0.008
2018 Apr 29.806	1.816	AAVSO TRT	V		6.360 ± 0.002
2018 Apr 29.930	1.940	AAVSO MIW	V		6.557 ± 0.037
2018 Apr 30.775	2.785	AAVSO PMAK	V		7.268 ± 0.070
2018 Apr 30.807	2.817	AAVSO VMAG	V		7.290 ± 0.020

Continued on next page

Table A.3 – continued from previous page

Date (UT)	Δ t / days	Telescope & Instrument	Filter	Exp. time /s	Photometry /mag
2018 Apr 30.817	2.827	AAVSO VOL	V		7.397 ± 0.028
2018 Apr 30.870	2.880	AAVSO EHEA	V		7.366 ± 0.015
2018 Apr 30.888	2.898	AAVSO MIW	V		7.417 ± 0.057
2018 Apr 30.904	2.914	AAVSO BDG	V		7.472 ± 0.115
2018 Apr 30.913	2.923	AAVSO BDG	V		7.406 ± 0.083
2018 Apr 30.919	2.929	AAVSO BDG	V		7.439 ± 0.093
2018 May 01.099	3.109	AAVSO SDM	V		7.440 ± 0.026
2018 May 01.158	3.168	AAVSO SSTA	V		7.560 ± 0.001
2018 May 01.172	3.182	AAVSO RBRB	V		7.571 ± 0.001
2018 May 01.172	3.182	AAVSO STYA	V		7.574 ± 0.040
2018 May 01.777	3.787	AAVSO PMAK	V		7.765 ± 0.100
2018 May 01.807	3.817	AAVSO TRT	V		7.894 ± 0.002
2018 May 01.844	3.854	AAVSO NRNA	V		7.860 ± 0.010
2018 May 01.861	3.871	AAVSO ATE	V		8.020 ± 0.023
2018 May 01.861	3.871	AAVSO WKL	V		7.920 ± 0.040
2018 May 01.867	3.877	AAVSO EHEA	V		7.881 ± 0.015
2018 May 02.104	4.114	AAVSO SDM	V		7.860 ± 0.062
2018 May 02.778	4.788	AAVSO PMAK	V		8.306 ± 0.100
2018 May 02.825	4.835	AAVSO NRNA	V		8.338 ± 0.005
2018 May 02.848	4.858	AAVSO ETOA	V		8.323 ± 0.059
2018 May 02.849	4.859	AAVSO ETOA	V		8.356 ± 0.038
2018 May 02.851	4.861	AAVSO ETOA	V		8.352 ± 0.055
2018 May 02.852	4.862	AAVSO ETOA	V		8.358 ± 0.035
2018 May 02.900	4.910	AAVSO MIW	V		8.436 ± 0.073
2018 May 03.778	5.788	AAVSO PMAK	V		8.443 ± 0.100
2018 May 03.795	5.805	AAVSO TRT	V		8.540 ± 0.002
2018 May 03.798	5.808	AAVSO TRT	V		8.551 ± 0.002
2018 May 03.850	5.860	AAVSO WKL	V		8.620 ± 0.040
2018 May 03.896	5.906	AAVSO EHEA	V		8.521 ± 0.025
2018 May 04.181	6.191	AAVSO JDAD	V		8.691 ± 0.001
2018 May 04.193	6.203	AAVSO RBRB	V		8.718 ± 0.001

Continued on next page

Table A.3 – continued from previous page

Date (UT)	Δ t / days	Telescope & Instrument	Filter	Exp. time /s	Photometry /mag
2018 May 04.775	6.785	AAVSO PMAK	V		8.756 ± 0.050
2018 May 04.808	6.818	AAVSO VMAG	V		8.756 ± 0.020
2018 May 04.820	6.830	AAVSO ETOA	V		8.798 ± 0.067
2018 May 04.821	6.831	AAVSO ETOA	V		8.816 ± 0.030
2018 May 04.827	6.837	AAVSO ETOA	V		8.828 ± 0.040
2018 May 04.828	6.838	AAVSO ETOA	V		8.809 ± 0.010
2018 May 04.829	6.839	AAVSO ETOA	V		8.841 ± 0.032
2018 May 04.830	6.840	AAVSO ETOA	V		8.832 ± 0.051
2018 May 04.854	6.864	AAVSO AFSA	V		8.766 ± 0.008
2018 May 04.855	6.865	AAVSO AFSA	V		8.764 ± 0.006
2018 May 04.855	6.865	AAVSO AFSA	V		8.795 ± 0.006
2018 May 04.855	6.865	AAVSO AFSA	V		8.754 ± 0.006
2018 May 04.855	6.865	AAVSO AFSA	V		8.757 ± 0.005
2018 May 04.874	6.884	AAVSO EHEA	V		8.831 ± 0.020
2018 May 05.149	7.159	AAVSO GJED	V		8.787 ± 0.040
2018 May 05.193	7.203	AAVSO RBRB	V		8.797 ± 0.002
2018 May 05.208	7.218	AAVSO STYA	V		8.815 ± 0.002
2018 May 05.782	7.792	AAVSO PMAK	V		8.595 ± 0.090
2018 May 05.822	7.832	AAVSO NRNA	V		8.614 ± 0.004
2018 May 05.824	7.834	AAVSO VOL	V		8.653 ± 0.022
2018 May 05.873	7.883	AAVSO AFSA	V		8.598 ± 0.005
2018 May 05.873	7.883	AAVSO AFSA	V		8.658 ± 0.005
2018 May 05.873	7.883	AAVSO AFSA	V		8.529 ± 0.005
2018 May 05.880	7.890	AAVSO OAR	V		8.568 ± 0.001
2018 May 05.881	7.891	AAVSO OAR	V		8.564 ± 0.001
2018 May 05.881	7.891	AAVSO OAR	V		8.611 ± 0.001
2018 May 05.881	7.891	AAVSO OAR	V		8.575 ± 0.001
2018 May 05.882	7.892	AAVSO OAR	V		8.574 ± 0.001
2018 May 05.889	7.899	AAVSO MIW	V		8.836 ± 0.018
2018 May 05.897	7.907	AAVSO OAR	V		8.524 ± 0.001
2018 May 05.898	7.908	AAVSO OAR	V		8.559 ± 0.001

Continued on next page

Table A.3 – continued from previous page

Date (UT)	Δ t / days	Telescope & Instrument	Filter	Exp. time /s	Photometry /mag
2018 May 05.898	7.908	AAVSO OAR	V		8.537 ± 0.001
2018 May 05.898	7.908	AAVSO OAR	V		8.522 ± 0.001
2018 May 05.899	7.909	AAVSO OAR	V		8.531 ± 0.001
2018 May 05.906	7.916	AAVSO EHEA	V		8.544 ± 0.010
2018 May 06.044	8.054	AAVSO LDJ	V		8.624 ± 0.010
2018 May 06.780	8.790	AAVSO PMAK	V		8.625 ± 0.070
2018 May 06.794	8.804	AAVSO TRT	V		8.715 ± 0.002
2018 May 06.816	8.826	AAVSO VOL	V		8.749 ± 0.035
2018 May 06.873	8.883	AAVSO EHEA	V		8.717 ± 0.010
2018 May 06.890	8.900	AAVSO MIW	V		9.033 ± 0.021
2018 May 07.169	9.179	AAVSO STYA	V		8.806 ± 0.001
2018 May 07.197	9.207	AAVSO RRIB	V		8.760 ± 0.004
2018 May 07.197	9.207	AAVSO RBRB	V		8.760 ± 0.004
2018 May 07.803	9.813	AAVSO VMAG	V		8.901 ± 0.020
2018 May 07.805	9.815	AAVSO TRT	V		8.963 ± 0.002
2018 May 07.819	9.829	AAVSO VOL	V		8.948 ± 0.027
2018 May 07.878	9.888	AAVSO EHEA	V		8.818 ± 0.030
2018 May 07.892	9.902	AAVSO MIW	V		8.927 ± 0.036
2018 May 08.044	10.054	AAVSO SHS	V		8.694 ± 0.133
2018 May 08.056	10.066	AAVSO LDJ	V		8.872 ± 0.005
2018 May 08.068	10.078	AAVSO FRL	V		8.651 ± 0.065
2018 May 08.789	10.799	AAVSO TRT	V		9.105 ± 0.002
2018 May 08.820	10.830	AAVSO VOL	V		9.170 ± 0.050
2018 May 08.881	10.891	AAVSO EHEA	V		9.118 ± 0.030
2018 May 08.889	10.899	AAVSO MIW	V		9.134 ± 0.018
2018 May 09.048	11.058	AAVSO SFRA	V		8.937 ± 0.074
2018 May 09.051	11.061	AAVSO SHS	V		8.930 ± 0.172
2018 May 09.795	11.805	AAVSO PMAK	V		9.042 ± 0.070
2018 May 09.879	11.889	AAVSO EHEA	V		9.110 ± 0.025
2018 May 10.177	12.187	AAVSO RBRB	V		9.342 ± 0.002
2018 May 10.178	12.188	AAVSO STYA	V		9.351 ± 0.003

Continued on next page

Table A.3 – continued from previous page

Date (UT)	Δ t / days	Telescope & Instrument	Filter	Exp. time /s	Photometry /mag
2018 May 10.787	12.797	AAVSO PMAK	V		9.339 ± 0.060
2018 May 10.885	12.895	AAVSO AFSA	V		9.349 ± 0.009
2018 May 10.885	12.895	AAVSO AFSA	V		9.374 ± 0.009
2018 May 11.819	13.829	AAVSO TRT	V		9.714 ± 0.005
2018 May 12.039	14.049	AAVSO SHS	V		9.651 ± 0.055
2018 May 12.170	14.180	AAVSO SSTA	V		9.824 ± 0.003
2018 May 12.798	14.808	AAVSO TRT	V		9.898 ± 0.003
2018 May 12.804	14.814	AAVSO VMAG	V		9.872 ± 0.020
2018 May 12.847	14.857	AAVSO ETOA	V		9.848 ± 0.004
2018 May 12.849	14.859	AAVSO ETOA	V		9.895 ± 0.009
2018 May 12.851	14.861	AAVSO ETOA	V		9.889 ± 0.014
2018 May 12.853	14.863	AAVSO ETOA	V		9.886 ± 0.017
2018 May 12.854	14.864	AAVSO ETOA	V		9.916 ± 0.005
2018 May 12.859	14.869	AAVSO AFSA	V		9.797 ± 0.009
2018 May 12.860	14.870	AAVSO AFSA	V		9.876 ± 0.009
2018 May 12.860	14.870	AAVSO AFSA	V		9.818 ± 0.009
2018 May 13.193	15.203	AAVSO RBRB	V		10.025 ± 0.004
2018 May 13.194	15.204	AAVSO LRCA	V		10.030 ± 0.017
2018 May 13.197	15.207	AAVSO STYA	V		10.097 ± 0.002
2018 May 13.800	15.810	AAVSO TRT	V		10.144 ± 0.003
2018 May 13.824	15.834	AAVSO MMAO	V		10.145 ± 0.022
2018 May 14.042	16.052	AAVSO LDJ	V		10.163 ± 0.005
2018 May 14.188	16.198	AAVSO STYA	V		10.257 ± 0.012
2018 May 14.204	16.214	AAVSO RBRB	V		10.241 ± 0.004
2018 May 14.828	16.838	AAVSO MMAO	V		10.286 ± 0.024
2018 May 14.865	16.875	AAVSO AFSA	V		10.277 ± 0.011
2018 May 14.865	16.875	AAVSO AFSA	V		10.277 ± 0.011
2018 May 14.865	16.875	AAVSO AFSA	V		10.255 ± 0.011
2018 May 14.865	16.875	AAVSO AFSA	V		10.255 ± 0.011
2018 May 14.865	16.875	AAVSO AFSA	V		10.298 ± 0.011

Continued on next page

Table A.3 – continued from previous page

Date (UT)	Δ t / days	Telescope & Instrument	Filter	Exp. time /s	Photometry /mag
2018 May 14.865	16.875	AAVSO AFSA	V		10.298 ± 0.011
2018 May 14.890	16.900	AAVSO EHEA	V		10.364 ± 0.035
2018 May 15.042	17.052	AAVSO SHS	V		10.153 ± 0.123
2018 May 15.043	17.053	AAVSO LDJ	V		10.396 ± 0.005
2018 May 15.838	17.848	AAVSO MMAO	V		10.492 ± 0.028
2018 May 16.220	18.230	AAVSO RBRB	V		10.562 ± 0.006
2018 May 16.826	18.836	AAVSO MMAO	V		10.666 ± 0.032
2018 May 18.830	20.840	AAVSO MMAO	V		11.030 ± 0.040
2018 May 18.838	20.848	AAVSO NRNA	V		11.081 ± 0.012
2018 May 19.046	21.056	AAVSO LDJ	V		11.142 ± 0.009
2018 May 19.088	21.098	AAVSO SHS	V		10.975 ± 0.170
2018 May 19.201	21.211	AAVSO RBRB	V		11.126 ± 0.005
2018 May 20.846	22.856	AAVSO NRNA	V		11.198 ± 0.032
2018 May 21.197	23.207	AAVSO RBRB	V		11.214 ± 0.012
2018 May 22.857	24.867	AAVSO NRNA	V		11.647 ± 0.017
2018 May 31.870	33.880	AAVSO AFSA	V		11.827 ± 0.034
2018 May 31.870	33.880	AAVSO AFSA	V		12.011 ± 0.037
2018 May 31.870	33.880	AAVSO AFSA	V		11.713 ± 0.031
2018 Jun 12.373	45.383	AAVSO MRV	V		12.377 ± 0.174
2018 Jun 14.377	47.387	AAVSO MRV	V		12.445 ± 0.213
2018 Jun 26.361	59.371	AAVSO MRV	V		12.966 ± 0.160
2018 Jun 26.370	59.380	AAVSO MRV	V		13.006 ± 0.190
2018 Jun 30.368	63.378	AAVSO MRV	V		13.204 ± 0.084
2018 Jul 07.357	70.367	AAVSO MRV	V		13.271 ± 0.052
2018 Jul 08.202	71.212	AAVSO SHS	V		13.354 ± 0.164
2018 Jul 09.360	72.370	AAVSO MRV	V		13.507 ± 0.058
2018 Jul 14.352	77.362	AAVSO MRV	V		13.593 ± 0.116
2018 Jul 14.477	77.487	AAVSO SGEA	V		13.640 ± 0.035
2018 Jul 16.497	79.507	AAVSO SGEA	V		13.819 ± 0.088
2018 Jul 17.472	80.482	AAVSO SGEA	V		13.850 ± 0.028
2018 Jul 17.500	80.510	AAVSO SGEA	V		13.765 ± 0.122

Continued on next page

Table A.3 – continued from previous page

Date (UT)	Δ t / days	Telescope & Instrument	Filter	Exp. time /s	Photometry /mag
2018 Jul 18.476	81.486	AAVSO SGEA	V		13.842 ± 0.058
2018 Jul 18.495	81.505	AAVSO SGEA	V		13.922 ± 0.040
2018 Jul 19.349	82.359	AAVSO CDJA	V		13.714 ± 0.012
2018 Jul 19.350	82.360	AAVSO CDJA	V		13.751 ± 0.011
2018 Jul 19.351	82.361	AAVSO CDJA	V		13.714 ± 0.011
2018 Jul 19.353	82.363	AAVSO MRV	V		13.849 ± 0.047
2018 Jul 21.191	84.201	LT IO:O	V	3×30	13.830 ± 0.010
2018 Jul 21.453	84.463	AAVSO SGEA	V		13.900 ± 0.030
2018 Jul 22.215	85.225	LT IO:O	V	3×30	13.874 ± 0.009
2018 Jul 23.192	86.202	LT IO:O	V	3×30	13.880 ± 0.009
2018 Jul 24.183	87.193	LT IO:O	V	3×30	13.903 ± 0.009
2018 Jul 25.180	88.190	LT IO:O	V	3×30	13.990 ± 0.010
2018 Jul 26.188	89.198	LT IO:O	V	3×30	14.020 ± 0.012
2018 Jul 27.180	90.190	LT IO:O	V	3×30	13.923 ± 0.011
2018 Jul 28.173	91.183	LT IO:O	V	3×30	14.034 ± 0.012
2018 Jul 29.172	92.182	LT IO:O	V	3×30	14.082 ± 0.018
2018 Jul 31.167	94.177	LT IO:O	V	3×30	14.141 ± 0.011
2018 Aug 01.181	95.191	LT IO:O	V	3×30	14.092 ± 0.010
2018 Aug 02.157	96.167	LT IO:O	V	3×30	14.023 ± 0.009
2018 Aug 02.342	96.352	AAVSO CDJA	V		14.075 ± 0.010
2018 Aug 02.343	96.353	AAVSO CDJA	V		14.059 ± 0.010
2018 Aug 02.344	96.354	AAVSO CDJA	V		14.057 ± 0.010
2018 Aug 02.486	96.496	AAVSO SGEA	V		14.148 ± 0.029
2018 Aug 03.155	97.165	LT IO:O	V	3×30	14.198 ± 0.011
2018 Aug 03.196	97.206	AAVSO MUY	V		14.200 ± 0.040
2018 Aug 03.484	97.494	AAVSO SGEA	V		14.314 ± 0.035
2018 Aug 04.150	98.160	AAVSO MRV	V		14.260 ± 0.037
2018 Aug 06.128	100.138	AAVSO SHS	V		14.340 ± 0.307
2018 Aug 06.146	100.156	LT IO:O	V	3×30	14.178 ± 0.011
2018 Aug 06.416	100.426	AAVSO DKS	V		14.261 ± 0.014
2018 Aug 06.493	100.503	AAVSO SGEA	V		14.251 ± 0.022

Continued on next page

Table A.3 – continued from previous page

Date (UT)	Δ t / days	Telescope & Instrument	Filter	Exp. time /s	Photometry /mag
2018 Aug 07.416	101.426	AAVSO DKS	V		14.349 ± 0.018
2018 Aug 08.162	102.172	LT IO:O	V	3×30	14.220 ± 0.009
2018 Aug 09.311	103.321	AAVSO BMSA	V		14.166 ± 0.011
2018 Aug 09.312	103.322	AAVSO BMSA	V		14.121 ± 0.010
2018 Aug 09.314	103.324	AAVSO BMSA	V		14.117 ± 0.010
2018 Aug 10.169	104.179	LT IO:O	V	3×30	14.287 ± 0.008
2018 Aug 10.480	104.490	AAVSO SGEA	V		14.320 ± 0.045
2018 Aug 13.171	107.181	LT IO:O	V	3×30	14.260 ± 0.020
2018 Aug 13.320	107.330	AAVSO MRV	V		14.512 ± 0.055
2018 Aug 13.325	107.335	AAVSO BMSA	V		14.398 ± 0.017
2018 Aug 13.326	107.336	AAVSO BMSA	V		14.403 ± 0.018
2018 Aug 13.327	107.337	AAVSO BMSA	V		14.453 ± 0.018
2018 Aug 13.472	107.482	AAVSO SGEA	V		14.425 ± 0.028
2018 Aug 14.419	108.429	AAVSO SGEA	V		14.336 ± 0.029
2018 Aug 14.519	108.529	AAVSO SGEA	V		14.509 ± 0.043
2018 Aug 15.447	109.457	AAVSO SGEA	V		14.377 ± 0.026
2018 Aug 15.510	109.520	AAVSO SGEA	V		14.349 ± 0.019
2018 Aug 16.120	110.130	LT IO:O	V	3×30	14.296 ± 0.011
2018 Aug 16.449	110.459	AAVSO SGEA	V		14.529 ± 0.027
2018 Aug 17.442	111.452	AAVSO SGEA	V		14.403 ± 0.025
2018 Aug 17.501	111.511	AAVSO SGEA	V		14.291 ± 0.015
2018 Aug 18.409	112.419	AAVSO SGEA	V		14.335 ± 0.026
2018 Aug 18.502	112.512	AAVSO SGEA	V		14.355 ± 0.016
2018 Aug 19.163	113.173	LT IO:O	V	3×30	14.327 ± 0.009
2018 Aug 19.447	113.457	AAVSO SGEA	V		14.383 ± 0.024
2018 Aug 19.481	113.491	AAVSO SGEA	V		14.346 ± 0.017
2018 Aug 20.188	114.198	AAVSO MRV	V		14.341 ± 0.037
2018 Aug 20.223	114.233	AAVSO MUY	V		14.400 ± 0.055
2018 Aug 20.417	114.427	AAVSO SGEA	V		14.333 ± 0.023
2018 Aug 20.486	114.496	AAVSO SGEA	V		14.341 ± 0.015
2018 Aug 21.430	115.440	AAVSO SGEA	V		14.331 ± 0.023

Continued on next page

Table A.3 – continued from previous page

Date (UT)	Δ t / days	Telescope & Instrument	Filter	Exp. time /s	Photometry /mag
2018 Aug 21.506	115.516	AAVSO SGEA	V		14.370 ± 0.026
2018 Aug 22.215	116.225	LT IO:O	V	3×30	14.243 ± 0.008
2018 Aug 22.440	116.450	AAVSO SGEA	V		14.390 ± 0.025
2018 Aug 22.521	116.531	AAVSO SGEA	V		14.309 ± 0.021
2018 Aug 23.472	117.482	AAVSO SGEA	V		14.417 ± 0.024
2018 Aug 23.508	117.518	AAVSO SGEA	V		14.352 ± 0.015
2018 Aug 25.095	119.105	LT IO:O	V	3×30	14.389 ± 0.009
2018 Aug 26.514	120.524	AAVSO SGEA	V		14.392 ± 0.030
2018 Aug 27.109	121.119	AAVSO MRV	V		14.334 ± 0.027
2018 Aug 27.515	121.525	AAVSO SGEA	V		14.407 ± 0.028
2018 Aug 28.105	122.115	LT IO:O	V	3×30	14.315 ± 0.010
2018 Aug 28.522	122.532	AAVSO SGEA	V		14.369 ± 0.029
2018 Aug 29.511	123.521	AAVSO SGEA	V		14.524 ± 0.030
2018 Aug 30.519	124.529	AAVSO SGEA	V		14.415 ± 0.037
2018 Aug 31.083	125.093	LT IO:O	V	3×30	14.282 ± 0.011
2018 Aug 31.515	125.525	AAVSO SGEA	V		14.410 ± 0.027
2018 Aug 31.529	125.539	AAVSO SGEA	V		14.442 ± 0.029
2018 Sep 01.525	126.535	AAVSO SGEA	V		14.433 ± 0.037
2018 Sep 02.516	127.526	AAVSO SGEA	V		14.588 ± 0.034
2018 Sep 02.519	127.529	AAVSO SGEA	V		14.514 ± 0.024
2018 Sep 03.071	128.081	LT IO:O	V	3×30	14.426 ± 0.010
2018 Sep 03.507	128.517	AAVSO SGEA	V		14.433 ± 0.028
2018 Sep 04.519	129.529	AAVSO SGEA	V		14.575 ± 0.028
2018 Sep 05.512	130.522	AAVSO SGEA	V		14.548 ± 0.027
2018 Sep 05.519	130.529	AAVSO SGEA	V		14.446 ± 0.018
2018 Sep 06.064	131.074	LT IO:O	V	3×30	14.431 ± 0.011
2018 Sep 06.502	131.512	AAVSO SGEA	V		14.486 ± 0.024
2018 Sep 06.510	131.520	AAVSO SGEA	V		14.446 ± 0.016
2018 Sep 07.496	132.506	AAVSO SGEA	V		14.606 ± 0.029
2018 Sep 08.509	133.519	AAVSO SGEA	V		14.628 ± 0.025
2018 Sep 08.524	133.534	AAVSO SGEA	V		14.650 ± 0.020

Continued on next page

Table A.3 – continued from previous page

Date (UT)	Δ t / days	Telescope & Instrument	Filter	Exp. time /s	Photometry /mag
2018 Sep 09.052	134.062	LT IO:O	V	3×30	14.534 ± 0.009
2018 Sep 09.530	134.540	AAVSO SGEA	V		14.561 ± 0.031
2018 Sep 09.533	134.543	AAVSO SGEA	V		14.458 ± 0.023
2018 Sep 10.074	135.084	AAVSO SHS	V		14.578 ± 0.126
2018 Sep 10.279	135.289	AAVSO VRG	V		14.487 ± 0.013
2018 Sep 10.280	135.290	AAVSO VRG	V		14.482 ± 0.015
2018 Sep 10.283	135.293	AAVSO VRG	V		14.489 ± 0.016
2018 Sep 10.285	135.295	AAVSO VRG	V		14.512 ± 0.017
2018 Sep 10.286	135.296	AAVSO VRG	V		14.516 ± 0.016
2018 Sep 10.290	135.300	AAVSO VRG	V		14.553 ± 0.017
2018 Sep 10.294	135.304	AAVSO VRG	V		14.577 ± 0.019
2018 Sep 10.297	135.307	AAVSO VRG	V		14.500 ± 0.017
2018 Sep 10.298	135.308	AAVSO VRG	V		14.555 ± 0.018
2018 Sep 10.302	135.312	AAVSO VRG	V		14.497 ± 0.020
2018 Sep 11.529	136.539	AAVSO SGEA	V		14.555 ± 0.030
2018 Sep 12.060	137.070	LT IO:O	V	3×30	14.572 ± 0.010
2018 Sep 13.203	138.213	AAVSO MDYA	V		14.633 ± 0.014
2018 Sep 13.204	138.214	AAVSO MDYA	V		14.630 ± 0.014
2018 Sep 13.205	138.215	AAVSO MDYA	V		14.651 ± 0.015
2018 Sep 13.526	138.536	AAVSO SGEA	V		14.593 ± 0.027
2018 Sep 13.529	138.539	AAVSO SGEA	V		14.450 ± 0.019
2018 Sep 14.039	139.049	AAVSO SHS	V		14.496 ± 0.092
2018 Sep 14.538	139.548	AAVSO SGEA	V		14.650 ± 0.047
2018 Sep 15.265	140.275	AAVSO MRV	V		14.703 ± 0.044
2018 Sep 16.540	141.550	AAVSO SGEA	V		14.511 ± 0.038
2018 Sep 18.084	143.094	LT IO:O	V	3×30	14.622 ± 0.009
2018 Sep 23.016	148.026	LT IO:O	V	3×30	14.676 ± 0.020
2018 Sep 26.012	151.022	LT IO:O	V	3×30	14.739 ± 0.011
2018 Sep 29.055	154.065	LT IO:O	V	3×30	14.663 ± 0.009
2018 Oct 02.010	157.020	LT IO:O	V	3×30	14.734 ± 0.009
2018 Oct 08.282	163.292	AAVSO SGEA	V		14.627 ± 0.048

Continued on next page

Table A.3 – continued from previous page

Date (UT)	Δ t / days	Telescope & Instrument	Filter	Exp. time /s	Photometry /mag
2018 Oct 28.559	183.569	AAVSO SGEA	V		15.004 ± 0.179
2018 Nov 01.109	187.119	LT IO:O	V	3×30	15.036 ± 0.009
2018 Nov 01.515	187.525	AAVSO SGEA	V		14.967 ± 0.054
2018 Nov 03.467	189.477	AAVSO SGEA	V		14.829 ± 0.038
2018 Nov 05.152	191.162	AAVSO MRV	V		14.942 ± 0.045
2018 Nov 07.565	193.575	AAVSO SGEA	V		14.926 ± 0.081
2018 Nov 08.042	194.052	AAVSO SHS	V		15.358 ± 0.157
2018 Nov 08.157	194.167	LT IO:O	V	3×30	15.071 ± 0.010
2018 Nov 16.115	202.125	LT IO:O	V	3×30	15.067 ± 0.008
2018 Nov 26.022	212.032	LT IO:O	V	3×30	15.049 ± 0.010
2018 Nov 26.316	212.326	AAVSO MRV	V		15.138 ± 0.026
2018 Dec 03.962	219.972	AAVSO ODEA	V		15.075 ± 0.116
2018 Dec 03.965	219.975	AAVSO ODEA	V		15.069 ± 0.132
2018 Dec 03.968	219.978	AAVSO ODEA	V		15.111 ± 0.136
2018 Dec 10.062	226.072	LT IO:O	V	3×30	15.076 ± 0.008
2018 Dec 15.961	231.971	LT IO:O	V	3×30	15.134 ± 0.011
2018 Dec 22.838	238.848	LT IO:O	V	3×30	15.148 ± 0.015
2018 Dec 28.892	244.902	LT IO:O	V	3×30	15.383 ± 0.023
2018 Dec 28.967	244.977	AAVSO MRV	V		15.199 ± 0.018
2019 Jan 04.918	251.928	LT IO:O	V	3×30	15.182 ± 0.009
2019 Jan 10.971	257.981	LT IO:O	V	3×30	15.170 ± 0.010
2019 Jan 11.073	258.083	AAVSO MRV	V		15.181 ± 0.018
2019 Jan 19.985	266.995	LT IO:O	V	3×30	15.133 ± 0.010
2019 Jan 25.901	272.911	LT IO:O	V	3×30	15.097 ± 0.009
2019 Jan 31.905	278.915	AAVSO MRV	V		14.981 ± 0.024
2019 Jan 31.937	278.947	LT IO:O	V	3×30	14.991 ± 0.008
2019 Feb 06.886	284.896	LT IO:O	V	3×30	15.140 ± 0.009
2019 Feb 12.872	290.882	LT IO:O	V	3×30	15.209 ± 0.009
2019 Feb 12.945	290.955	AAVSO MRV	V		15.236 ± 0.016
2019 Feb 19.897	297.907	LT IO:O	V	3×30	15.184 ± 0.040
2019 Feb 26.857	304.867	AAVSO RZD	V		15.032 ± 0.067

Continued on next page

Table A.3 – continued from previous page

Date (UT)	Δ t / days	Telescope & Instrument	Filter	Exp. time /s	Photometry /mag
2019 Feb 28.886	306.896	LT IO:O	V	3×30	15.289 ± 0.008
2019 Mar 04.964	310.974	AAVSO MRV	V		15.214 ± 0.020
2019 Mar 16.844	322.854	LT IO:O	V	3×30	15.245 ± 0.009
2019 Apr 08.857	345.867	LT IO:O	V	3×30	15.240 ± 0.009
2019 Apr 25.849	362.859	LT IO:O	V	3×30	15.261 ± 0.013
2019 Jul 19.213	447.223	LT IO:O	V	3×30	15.201 ± 0.010
2019 Aug 01.216	460.226	LT IO:O	V	3×30	15.238 ± 0.009
2019 Aug 19.123	478.133	LT IO:O	V	3×30	15.236 ± 0.010
2019 Sep 14.110	504.120	LT IO:O	V	3×60	15.182 ± 0.012
2019 Oct 14.974	534.984	LT IO:O	V	3×60	15.195 ± 0.012
2019 Nov 16.934	567.944	LT IO:O	V	3×60	14.877 ± 0.009
2019 Dec 09.902	590.912	LT IO:O	V	3×60	15.188 ± 0.012
2020 Aug 31.162	856.172	LT IO:O	V	3×120	15.383 ± 0.008
2021 Feb 02.858	1011.868	LT IO:O	V	3×180	15.027 ± 0.007
2018 Apr 30.807	2.817	AAVSO VMAG	r'		6.500 ± 0.020
2018 May 01.029	3.039	AAVSO KHAB	r'		6.743 ± 0.070
2018 May 01.029	3.039	AAVSO KHAB	r'		6.682 ± 0.070
2018 May 01.029	3.039	AAVSO KHAB	r'		6.837 ± 0.070
2018 May 01.029	3.039	AAVSO KHAB	r'		6.797 ± 0.070
2018 May 01.848	3.858	AAVSO NRNA	r'		7.265 ± 0.031
2018 May 01.848	3.858	AAVSO NRNA	r'		6.949 ± 0.009
2018 May 01.877	3.887	AAVSO BRIA	r'		7.959 ± 0.117
2018 May 01.880	3.890	AAVSO BRIA	r'		7.989 ± 0.121
2018 May 01.882	3.892	AAVSO BRIA	r'		7.926 ± 0.127
2018 May 01.884	3.894	AAVSO BRIA	r'		7.959 ± 0.114
2018 May 01.887	3.897	AAVSO BRIA	r'		8.041 ± 0.073
2018 May 01.889	3.899	AAVSO BRIA	r'		7.957 ± 0.119
2018 May 01.892	3.902	AAVSO BRIA	r'		7.939 ± 0.133
2018 May 01.894	3.904	AAVSO BRIA	r'		7.919 ± 0.155
2018 May 01.896	3.906	AAVSO BRIA	r'		8.013 ± 0.089
2018 May 01.899	3.909	AAVSO BRIA	r'		8.024 ± 0.070

Continued on next page

Table A.3 – continued from previous page

Date (UT)	Δ t / days	Telescope & Instrument	Filter	Exp. time /s	Photometry /mag
2018 May 01.901	3.911	AAVSO BRIA	r'		7.921 ± 0.099
2018 May 01.903	3.913	AAVSO BRIA	r'		8.034 ± 0.109
2018 May 01.905	3.915	AAVSO BRIA	r'		7.947 ± 0.057
2018 May 01.907	3.917	AAVSO BRIA	r'		7.959 ± 0.084
2018 May 01.910	3.920	AAVSO BRIA	r'		7.985 ± 0.063
2018 May 01.912	3.922	AAVSO BRIA	r'		7.875 ± 0.125
2018 May 01.916	3.926	AAVSO BRIA	r'		7.901 ± 0.154
2018 May 01.918	3.928	AAVSO BRIA	r'		7.901 ± 0.083
2018 May 02.782	4.792	AAVSO JPG	r'		7.584 ± 0.040
2018 May 02.846	4.856	AAVSO NRNA	r'		7.295 ± 0.004
2018 May 02.849	4.859	AAVSO NRNA	r'		7.564 ± 0.003
2018 May 03.849	5.859	AAVSO BRIA	r'		8.548 ± 0.078
2018 May 03.851	5.861	AAVSO BRIA	r'		8.495 ± 0.092
2018 May 03.854	5.864	AAVSO BRIA	r'		8.524 ± 0.038
2018 May 03.856	5.866	AAVSO BRIA	r'		8.485 ± 0.033
2018 May 03.858	5.868	AAVSO BRIA	r'		8.509 ± 0.058
2018 May 03.861	5.871	AAVSO BRIA	r'		8.457 ± 0.077
2018 May 03.863	5.873	AAVSO BRIA	r'		8.543 ± 0.069
2018 May 03.865	5.875	AAVSO BRIA	r'		8.463 ± 0.119
2018 May 03.868	5.878	AAVSO BRIA	r'		8.524 ± 0.043
2018 May 03.870	5.880	AAVSO BRIA	r'		8.486 ± 0.088
2018 May 03.873	5.883	AAVSO BRIA	r'		8.512 ± 0.097
2018 May 04.808	6.818	AAVSO VMAG	r'		7.756 ± 0.020
2018 May 04.820	6.830	AAVSO ETOA	r'		7.745 ± 0.002
2018 May 04.820	6.830	AAVSO ETOA	r'		7.765 ± 0.002
2018 May 04.821	6.831	AAVSO ETOA	r'		7.723 ± 0.011
2018 May 04.827	6.837	AAVSO ETOA	r'		7.767 ± 0.035
2018 May 04.828	6.838	AAVSO ETOA	r'		7.730 ± 0.027
2018 May 04.829	6.839	AAVSO ETOA	r'		7.756 ± 0.020
2018 May 04.830	6.840	AAVSO ETOA	r'		7.714 ± 0.009
2018 May 04.854	6.864	AAVSO AFSA	r'		7.995 ± 0.005

Continued on next page

Table A.3 – continued from previous page

Date (UT)	Δ t / days	Telescope & Instrument	Filter	Exp. time /s	Photometry /mag
2018 May 04.854	6.864	AAVSO AFSA	r'		7.989 ± 0.005
2018 May 04.854	6.864	AAVSO AFSA	r'		7.967 ± 0.005
2018 May 04.854	6.864	AAVSO AFSA	r'		7.965 ± 0.005
2018 May 05.215	7.225	AAVSO RBRB	r'		7.777 ± 0.002
2018 May 05.824	7.834	AAVSO NRNA	r'		7.861 ± 0.002
2018 May 05.828	7.838	AAVSO NRNA	r'		8.089 ± 0.002
2018 May 05.858	7.868	AAVSO BRIA	r'		8.710 ± 0.051
2018 May 05.860	7.870	AAVSO BRIA	r'		8.747 ± 0.049
2018 May 05.863	7.873	AAVSO BRIA	r'		8.775 ± 0.073
2018 May 05.863	7.873	AAVSO DPA	r'		7.662 ± 0.029
2018 May 05.865	7.875	AAVSO BRIA	r'		8.741 ± 0.065
2018 May 05.867	7.877	AAVSO BRIA	r'		8.698 ± 0.035
2018 May 05.869	7.879	AAVSO BRIA	r'		8.766 ± 0.029
2018 May 05.871	7.881	AAVSO AFSA	r'		7.945 ± 0.005
2018 May 05.871	7.881	AAVSO AFSA	r'		7.973 ± 0.006
2018 May 05.871	7.881	AAVSO AFSA	r'		7.906 ± 0.005
2018 May 05.871	7.881	AAVSO AFSA	r'		7.944 ± 0.005
2018 May 05.871	7.881	AAVSO BRIA	r'		8.679 ± 0.084
2018 May 05.873	7.883	AAVSO BRIA	r'		8.724 ± 0.048
2018 May 05.876	7.886	AAVSO BRIA	r'		8.739 ± 0.084
2018 May 05.878	7.888	AAVSO BRIA	r'		8.754 ± 0.035
2018 May 05.880	7.890	AAVSO BRIA	r'		8.746 ± 0.043
2018 May 05.882	7.892	AAVSO BRIA	r'		8.765 ± 0.061
2018 May 05.886	7.896	AAVSO BRIA	r'		8.679 ± 0.071
2018 May 05.888	7.898	AAVSO BRIA	r'		8.723 ± 0.093
2018 May 05.890	7.900	AAVSO BRIA	r'		8.744 ± 0.073
2018 May 05.892	7.902	AAVSO BRIA	r'		8.679 ± 0.028
2018 May 06.012	8.022	AAVSO KHAB	r'		7.858 ± 0.070
2018 May 06.849	8.859	AAVSO BRIA	r'		8.887 ± 0.074
2018 May 06.851	8.861	AAVSO BRIA	r'		8.879 ± 0.155
2018 May 06.853	8.863	AAVSO BRIA	r'		8.911 ± 0.052

Continued on next page

Table A.3 – continued from previous page

Date (UT)	Δ t / days	Telescope & Instrument	Filter	Exp. time /s	Photometry /mag
2018 May 06.855	8.865	AAVSO BRIA	r'		8.911 ± 0.048
2018 May 06.857	8.867	AAVSO BRIA	r'		8.865 ± 0.059
2018 May 06.859	8.869	AAVSO BRIA	r'		8.851 ± 0.073
2018 May 06.861	8.871	AAVSO BRIA	r'		8.845 ± 0.046
2018 May 06.864	8.874	AAVSO BRIA	r'		8.884 ± 0.077
2018 May 06.866	8.876	AAVSO BRIA	r'		8.887 ± 0.072
2018 May 06.868	8.878	AAVSO BRIA	r'		8.891 ± 0.031
2018 May 06.870	8.880	AAVSO BRIA	r'		8.877 ± 0.054
2018 May 06.872	8.882	AAVSO BRIA	r'		8.876 ± 0.056
2018 May 06.874	8.884	AAVSO BRIA	r'		8.841 ± 0.034
2018 May 06.876	8.886	AAVSO BRIA	r'		8.875 ± 0.062
2018 May 06.879	8.889	AAVSO BRIA	r'		8.890 ± 0.060
2018 May 06.881	8.891	AAVSO BRIA	r'		8.826 ± 0.087
2018 May 06.883	8.893	AAVSO BRIA	r'		8.884 ± 0.060
2018 May 06.886	8.896	AAVSO BRIA	r'		8.867 ± 0.042
2018 May 07.007	9.017	AAVSO KHAB	r'		8.122 ± 0.070
2018 May 07.188	9.198	AAVSO STYA	r'		7.887 ± 0.002
2018 May 07.221	9.231	AAVSO RRIB	r'		7.943 ± 0.003
2018 May 07.221	9.231	AAVSO RBRB	r'		7.962 ± 0.003
2018 May 07.803	9.813	AAVSO VMAG	r'		8.137 ± 0.020
2018 May 07.845	9.855	AAVSO BRIA	r'		9.019 ± 0.068
2018 May 07.847	9.857	AAVSO BRIA	r'		8.946 ± 0.032
2018 May 07.849	9.859	AAVSO BRIA	r'		8.981 ± 0.052
2018 May 07.851	9.861	AAVSO BRIA	r'		9.020 ± 0.079
2018 May 07.853	9.863	AAVSO DPA	r'		7.976 ± 0.043
2018 May 07.853	9.863	AAVSO BRIA	r'		9.011 ± 0.055
2018 May 07.855	9.865	AAVSO BRIA	r'		8.939 ± 0.023
2018 May 07.857	9.867	AAVSO BRIA	r'		8.991 ± 0.083
2018 May 07.859	9.869	AAVSO BRIA	r'		9.003 ± 0.077
2018 May 07.862	9.872	AAVSO BRIA	r'		8.993 ± 0.035
2018 May 07.864	9.874	AAVSO BRIA	r'		8.956 ± 0.071

Continued on next page

Table A.3 – continued from previous page

Date (UT)	Δ t / days	Telescope & Instrument	Filter	Exp. time /s	Photometry /mag
2018 May 08.849	10.859	AAVSO BRIA	r'		9.172 ± 0.107
2018 May 08.851	10.861	AAVSO BRIA	r'		9.133 ± 0.049
2018 May 08.853	10.863	AAVSO BRIA	r'		9.292 ± 0.120
2018 May 08.855	10.865	AAVSO BRIA	r'		9.314 ± 0.074
2018 May 08.862	10.872	AAVSO BRIA	r'		9.233 ± 0.069
2018 May 08.865	10.875	AAVSO BRIA	r'		9.262 ± 0.105
2018 May 08.868	10.878	AAVSO BRIA	r'		9.183 ± 0.067
2018 May 08.870	10.880	AAVSO BRIA	r'		9.194 ± 0.029
2018 May 09.858	11.868	AAVSO BRIA	r'		9.348 ± 0.154
2018 May 09.860	11.870	AAVSO BRIA	r'		9.172 ± 0.111
2018 May 09.862	11.872	AAVSO BRIA	r'		9.223 ± 0.135
2018 May 09.864	11.874	AAVSO BRIA	r'		9.204 ± 0.087
2018 May 09.866	11.876	AAVSO BRIA	r'		9.328 ± 0.135
2018 May 09.868	11.878	AAVSO BRIA	r'		9.245 ± 0.149
2018 May 10.190	12.200	AAVSO RBRB	r'		8.392 ± 0.004
2018 May 10.190	12.200	AAVSO STYA	r'		8.402 ± 0.004
2018 May 10.886	12.896	AAVSO AFSA	r'		8.790 ± 0.007
2018 May 10.887	12.897	AAVSO AFSA	r'		8.674 ± 0.007
2018 May 10.887	12.897	AAVSO AFSA	r'		8.645 ± 0.007
2018 May 12.184	14.194	AAVSO SSTA	r'		8.794 ± 0.009
2018 May 12.804	14.814	AAVSO VMAG	r'		8.950 ± 0.020
2018 May 12.847	14.857	AAVSO ETOA	r'		8.947 ± 0.014
2018 May 12.849	14.859	AAVSO ETOA	r'		8.907 ± 0.055
2018 May 12.851	14.861	AAVSO ETOA	r'		8.901 ± 0.055
2018 May 12.853	14.863	AAVSO ETOA	r'		8.878 ± 0.007
2018 May 12.855	14.865	AAVSO ETOA	r'		8.897 ± 0.035
2018 May 12.860	14.870	AAVSO AFSA	r'		9.030 ± 0.006
2018 May 12.860	14.870	AAVSO AFSA	r'		9.091 ± 0.006
2018 May 12.860	14.870	AAVSO AFSA	r'		9.025 ± 0.006
2018 May 12.865	14.875	AAVSO BRIA	r'		9.953 ± 0.216
2018 May 13.217	15.227	AAVSO LRCA	r'		9.012 ± 0.009

Continued on next page

Table A.3 – continued from previous page

Date (UT)	Δ t / days	Telescope & Instrument	Filter	Exp. time /s	Photometry /mag
2018 May 13.217	15.227	AAVSO LRCA	r'		8.809 ± 0.004
2018 May 13.218	15.228	AAVSO RBRB	r'		9.027 ± 0.003
2018 May 13.219	15.229	AAVSO STYA	r'		8.988 ± 0.002
2018 May 13.905	15.915	AAVSO BRIA	r'		10.099 ± 0.074
2018 May 13.907	15.917	AAVSO BRIA	r'		10.101 ± 0.150
2018 May 13.911	15.921	AAVSO BRIA	r'		10.135 ± 0.022
2018 May 13.913	15.923	AAVSO BRIA	r'		10.123 ± 0.108
2018 May 13.916	15.926	AAVSO BRIA	r'		10.083 ± 0.060
2018 May 13.918	15.928	AAVSO BRIA	r'		10.148 ± 0.087
2018 May 14.201	16.211	AAVSO STYA	r'		9.146 ± 0.002
2018 May 14.208	16.218	AAVSO RBRB	r'		8.992 ± 0.002
2018 May 14.857	16.867	AAVSO BRIA	r'		10.241 ± 0.059
2018 May 14.864	16.874	AAVSO AFSA	r'		9.480 ± 0.008
2018 May 14.864	16.874	AAVSO AFSA	r'		9.480 ± 0.008
2018 May 14.864	16.874	AAVSO AFSA	r'		9.367 ± 0.007
2018 May 14.864	16.874	AAVSO AFSA	r'		9.367 ± 0.007
2018 May 14.864	16.874	AAVSO AFSA	r'		9.384 ± 0.007
2018 May 14.864	16.874	AAVSO AFSA	r'		9.384 ± 0.007
2018 May 14.868	16.878	AAVSO BRIA	r'		10.273 ± 0.055
2018 May 18.840	20.850	AAVSO NRNA	r'		10.096 ± 0.006
2018 May 18.843	20.853	AAVSO NRNA	r'		10.336 ± 0.006
2018 May 19.206	21.216	AAVSO RBRB	r'		10.045 ± 0.007
2018 May 20.848	22.858	AAVSO NRNA	r'		10.389 ± 0.024
2018 May 20.877	22.887	AAVSO BRIA	r'		11.084 ± 0.138
2018 May 21.222	23.232	AAVSO RBRB	r'		10.264 ± 0.005
2018 May 22.855	24.865	AAVSO NRNA	r'		10.697 ± 0.007
2018 May 31.869	33.879	AAVSO AFSA	r'		11.266 ± 0.024
2018 May 31.870	33.880	AAVSO AFSA	r'		11.041 ± 0.022
2018 May 31.870	33.880	AAVSO AFSA	r'		11.201 ± 0.023
2018 Jul 14.370	77.380	AAVSO MRV	r'		13.154 ± 0.059
2018 Jul 14.477	77.487	AAVSO SGEA	r'		13.103 ± 0.052

Continued on next page

Table A.3 – continued from previous page

Date (UT)	Δ t / days	Telescope & Instrument	Filter	Exp. time /s	Photometry /mag
2018 Jul 16.497	79.507	AAVSO SGEA	r'		13.314 ± 0.076
2018 Jul 17.472	80.482	AAVSO SGEA	r'		13.446 ± 0.026
2018 Jul 18.477	81.487	AAVSO SGEA	r'		13.434 ± 0.030
2018 Jul 19.345	82.355	AAVSO CDJA	r'		13.335 ± 0.008
2018 Jul 19.346	82.356	AAVSO CDJA	r'		13.344 ± 0.008
2018 Jul 19.347	82.357	AAVSO CDJA	r'		13.315 ± 0.008
2018 Jul 19.363	82.373	AAVSO MRV	r'		13.460 ± 0.039
2018 Jul 21.194	84.204	LT IO:O	r'	3×30	13.525 ± 0.007
2018 Jul 21.454	84.464	AAVSO SGEA	r'		13.540 ± 0.024
2018 Jul 22.219	85.229	LT IO:O	r'	3×30	13.594 ± 0.007
2018 Jul 23.196	86.206	LT IO:O	r'	3×30	13.598 ± 0.006
2018 Jul 24.187	87.197	LT IO:O	r'	3×30	13.610 ± 0.007
2018 Jul 25.184	88.194	LT IO:O	r'	3×30	13.710 ± 0.007
2018 Jul 26.192	89.202	LT IO:O	r'	3×30	13.719 ± 0.010
2018 Jul 27.184	90.194	LT IO:O	r'	3×30	13.587 ± 0.009
2018 Jul 28.177	91.187	LT IO:O	r'	3×30	13.782 ± 0.008
2018 Jul 29.176	92.186	LT IO:O	r'	3×30	13.850 ± 0.011
2018 Jul 31.170	94.180	LT IO:O	r'	3×30	13.857 ± 0.007
2018 Aug 01.184	95.194	LT IO:O	r'	3×30	13.834 ± 0.008
2018 Aug 02.161	96.171	LT IO:O	r'	3×30	13.776 ± 0.007
2018 Aug 02.336	96.346	AAVSO CDJA	r'		13.751 ± 0.007
2018 Aug 02.337	96.347	AAVSO CDJA	r'		13.749 ± 0.007
2018 Aug 02.339	96.349	AAVSO CDJA	r'		13.731 ± 0.008
2018 Aug 02.487	96.497	AAVSO SGEA	r'		13.828 ± 0.028
2018 Aug 03.159	97.169	LT IO:O	r'	3×30	13.935 ± 0.007
2018 Aug 03.484	97.494	AAVSO SGEA	r'		13.886 ± 0.031
2018 Aug 04.149	98.159	AAVSO MRV	r'		13.977 ± 0.053
2018 Aug 06.150	100.160	LT IO:O	r'	3×30	13.934 ± 0.007
2018 Aug 06.494	100.504	AAVSO SGEA	r'		13.932 ± 0.023
2018 Aug 08.166	102.176	LT IO:O	r'	3×30	13.992 ± 0.007
2018 Aug 09.324	103.334	AAVSO BMSA	r'		13.908 ± 0.008

Continued on next page

Table A.3 – continued from previous page

Date (UT)	Δ t / days	Telescope & Instrument	Filter	Exp. time /s	Photometry /mag
2018 Aug 09.325	103.335	AAVSO BMSA	r'		13.896 ± 0.008
2018 Aug 09.326	103.336	AAVSO BMSA	r'		13.900 ± 0.008
2018 Aug 10.172	104.182	LT IO:O	r'	3×30	14.038 ± 0.005
2018 Aug 10.481	104.491	AAVSO SGEA	r'		13.965 ± 0.045
2018 Aug 13.174	107.184	LT IO:O	r'	3×30	14.130 ± 0.017
2018 Aug 13.317	107.327	AAVSO BMSA	r'		14.119 ± 0.010
2018 Aug 13.318	107.328	AAVSO BMSA	r'		14.135 ± 0.011
2018 Aug 13.319	107.329	AAVSO BMSA	r'		14.125 ± 0.010
2018 Aug 13.337	107.347	AAVSO MRV	r'		14.081 ± 0.055
2018 Aug 13.473	107.483	AAVSO SGEA	r'		14.037 ± 0.028
2018 Aug 14.420	108.430	AAVSO SGEA	r'		14.024 ± 0.029
2018 Aug 15.448	109.458	AAVSO SGEA	r'		14.095 ± 0.029
2018 Aug 16.124	110.134	LT IO:O	r'	3×30	14.094 ± 0.007
2018 Aug 16.450	110.460	AAVSO SGEA	r'		14.242 ± 0.027
2018 Aug 17.443	111.453	AAVSO SGEA	r'		14.017 ± 0.025
2018 Aug 18.410	112.420	AAVSO SGEA	r'		14.041 ± 0.027
2018 Aug 19.167	113.177	LT IO:O	r'	3×30	14.080 ± 0.007
2018 Aug 19.448	113.458	AAVSO SGEA	r'		14.057 ± 0.025
2018 Aug 20.187	114.197	AAVSO MRV	r'		14.091 ± 0.047
2018 Aug 20.418	114.428	AAVSO SGEA	r'		13.986 ± 0.024
2018 Aug 22.219	116.229	LT IO:O	r'	3×30	14.031 ± 0.006
2018 Aug 22.441	116.451	AAVSO SGEA	r'		13.994 ± 0.024
2018 Aug 23.472	117.482	AAVSO SGEA	r'		14.011 ± 0.023
2018 Aug 25.099	119.109	LT IO:O	r'	3×30	14.157 ± 0.007
2018 Aug 26.515	120.525	AAVSO SGEA	r'		14.033 ± 0.028
2018 Aug 27.107	121.117	AAVSO MRV	r'		14.123 ± 0.039
2018 Aug 27.516	121.526	AAVSO SGEA	r'		14.047 ± 0.028
2018 Aug 28.109	122.119	LT IO:O	r'	3×30	14.049 ± 0.009
2018 Aug 28.522	122.532	AAVSO SGEA	r'		14.034 ± 0.031
2018 Aug 29.512	123.522	AAVSO SGEA	r'		14.174 ± 0.030
2018 Aug 30.520	124.530	AAVSO SGEA	r'		14.035 ± 0.040

Continued on next page

Table A.3 – continued from previous page

Date (UT)	Δ t / days	Telescope & Instrument	Filter	Exp. time /s	Photometry /mag
2018 Aug 31.087	125.097	LT IO:O	r'	3×30	14.088 ± 0.009
2018 Aug 31.515	125.525	AAVSO SGEA	r'		13.953 ± 0.025
2018 Sep 02.517	127.527	AAVSO SGEA	r'		14.267 ± 0.034
2018 Sep 03.075	128.085	LT IO:O	r'	3×30	14.176 ± 0.007
2018 Sep 03.507	128.517	AAVSO SGEA	r'		14.077 ± 0.032
2018 Sep 04.520	129.530	AAVSO SGEA	r'		14.199 ± 0.029
2018 Sep 05.513	130.523	AAVSO SGEA	r'		14.132 ± 0.026
2018 Sep 06.067	131.077	LT IO:O	r'	3×30	14.180 ± 0.006
2018 Sep 06.503	131.513	AAVSO SGEA	r'		14.124 ± 0.026
2018 Sep 07.497	132.507	AAVSO SGEA	r'		14.212 ± 0.030
2018 Sep 08.510	133.520	AAVSO SGEA	r'		14.243 ± 0.026
2018 Sep 09.056	134.066	LT IO:O	r'	3×30	14.286 ± 0.007
2018 Sep 09.531	134.541	AAVSO SGEA	r'		14.160 ± 0.031
2018 Sep 11.530	136.540	AAVSO SGEA	r'		14.251 ± 0.035
2018 Sep 12.064	137.074	LT IO:O	r'	3×30	14.341 ± 0.007
2018 Sep 13.527	138.537	AAVSO SGEA	r'		14.213 ± 0.030
2018 Sep 15.291	140.301	AAVSO MRV	r'		14.417 ± 0.037
2018 Sep 16.540	141.550	AAVSO SGEA	r'		14.201 ± 0.048
2018 Sep 18.088	143.098	LT IO:O	r'	3×30	14.355 ± 0.006
2018 Sep 23.020	148.030	LT IO:O	r'	3×30	14.459 ± 0.012
2018 Sep 26.016	151.026	LT IO:O	r'	3×30	14.448 ± 0.007
2018 Sep 29.059	154.069	LT IO:O	r'	3×30	14.430 ± 0.007
2018 Oct 02.014	157.024	LT IO:O	r'	3×30	14.496 ± 0.007
2018 Nov 01.113	187.123	LT IO:O	r'	3×30	14.781 ± 0.006
2018 Nov 05.149	191.159	AAVSO MRV	r'		14.829 ± 0.037
2018 Nov 08.161	194.171	LT IO:O	r'	3×30	14.781 ± 0.006
2018 Nov 16.119	202.129	LT IO:O	r'	3×30	14.761 ± 0.007
2018 Nov 26.026	212.036	LT IO:O	r'	3×30	14.688 ± 0.008
2018 Dec 10.066	226.076	LT IO:O	r'	3×30	14.733 ± 0.006
2018 Dec 15.965	231.975	LT IO:O	r'	3×30	14.753 ± 0.006
2018 Dec 22.841	238.851	LT IO:O	r'	3×30	14.814 ± 0.012

Continued on next page

Table A.3 – continued from previous page

Date (UT)	Δ t / days	Telescope & Instrument	Filter	Exp. time /s	Photometry /mag
2018 Dec 28.896	244.906	LT IO:O	r'	3×30	14.886 ± 0.011
2018 Dec 28.965	244.975	AAVSO MRV	r'		14.826 ± 0.033
2019 Jan 04.921	251.931	LT IO:O	r'	3×30	14.881 ± 0.007
2019 Jan 10.975	257.985	LT IO:O	r'	3×30	14.840 ± 0.006
2019 Jan 11.071	258.081	AAVSO MRV	r'		14.791 ± 0.030
2019 Jan 19.989	266.999	LT IO:O	r'	3×30	14.820 ± 0.007
2019 Jan 25.904	272.914	LT IO:O	r'	3×30	14.749 ± 0.007
2019 Jan 31.903	278.913	AAVSO MRV	r'		14.629 ± 0.035
2019 Jan 31.940	278.950	LT IO:O	r'	3×30	14.629 ± 0.007
2019 Feb 06.890	284.900	LT IO:O	r'	3×30	14.808 ± 0.008
2019 Feb 12.876	290.886	LT IO:O	r'	3×30	14.869 ± 0.006
2019 Feb 12.943	290.953	AAVSO MRV	r'		14.811 ± 0.037
2019 Feb 19.901	297.911	LT IO:O	r'	3×30	14.890 ± 0.020
2019 Feb 28.890	306.900	LT IO:O	r'	3×30	14.925 ± 0.007
2019 Mar 04.962	310.972	AAVSO MRV	r'		14.812 ± 0.035
2019 Mar 16.848	322.858	LT IO:O	r'	3×30	14.849 ± 0.007
2019 Apr 08.861	345.871	LT IO:O	r'	3×30	14.892 ± 0.007
2019 Apr 25.853	362.863	LT IO:O	r'	3×30	14.878 ± 0.009
2019 Jul 19.217	447.227	LT IO:O	r'	3×30	14.823 ± 0.007
2019 Aug 01.220	460.230	LT IO:O	r'	3×30	14.856 ± 0.006
2019 Aug 19.127	478.137	LT IO:O	r'	3×30	14.843 ± 0.008
2019 Sep 14.116	504.126	LT IO:O	r'	3×60	14.799 ± 0.009
2019 Oct 14.980	534.990	LT IO:O	r'	3×60	14.770 ± 0.008
2019 Nov 16.940	567.950	LT IO:O	r'	3×60	14.438 ± 0.010
2019 Dec 09.908	590.918	LT IO:O	r'	3×60	14.760 ± 0.008
2020 Aug 31.172	856.182	LT IO:O	r'	3×120	14.968 ± 0.005
2021 Feb 02.872	1011.882	LT IO:O	r'	3×180	14.653 ± 0.005
2018 Apr 30.807	2.817	AAVSO VMAG	i'		5.730 ± 0.020
2018 May 01.148	3.158	AAVSO SSTA	i'		5.929 ± 0.002
2018 May 01.162	3.172	AAVSO STYA	i'		6.005 ± 0.001
2018 May 01.162	3.172	AAVSO RBRB	i'		6.016 ± 0.001

Continued on next page

Table A.3 – continued from previous page

Date (UT)	Δ t / days	Telescope & Instrument	Filter	Exp. time /s	Photometry /mag
2018 May 01.860	3.870	AAVSO NRNA	i'		6.795 ± 0.011
2018 May 02.845	4.855	AAVSO NRNA	i'		7.524 ± 0.012
2018 May 04.168	6.178	AAVSO RBRB	i'		7.217 ± 0.001
2018 May 04.808	6.818	AAVSO VMAG	i'		7.356 ± 0.020
2018 May 04.821	6.831	AAVSO ETOA	i'		7.349 ± 0.174
2018 May 04.821	6.831	AAVSO ETOA	i'		7.365 ± 0.096
2018 May 04.827	6.837	AAVSO ETOA	i'		7.414 ± 0.091
2018 May 04.828	6.838	AAVSO ETOA	i'		7.399 ± 0.143
2018 May 04.829	6.839	AAVSO ETOA	i'		7.408 ± 0.089
2018 May 04.830	6.840	AAVSO ETOA	i'		7.394 ± 0.095
2018 May 05.180	7.190	AAVSO RBRB	i'		7.418 ± 0.002
2018 May 05.199	7.209	AAVSO STYA	i'		7.329 ± 0.002
2018 May 05.829	7.839	AAVSO NRNA	i'		7.902 ± 0.003
2018 May 05.867	7.877	AAVSO DPA	i'		7.246 ± 0.027
2018 May 05.896	7.906	AAVSO MIW	i'		7.787 ± 0.026
2018 May 06.892	8.902	AAVSO MIW	i'		7.999 ± 0.015
2018 May 07.162	9.172	AAVSO STYA	i'		7.535 ± 0.004
2018 May 07.185	9.195	AAVSO RRIB	i'		7.617 ± 0.001
2018 May 07.185	9.195	AAVSO RBRB	i'		7.619 ± 0.001
2018 May 07.803	9.813	AAVSO VMAG	i'		7.777 ± 0.020
2018 May 07.855	9.865	AAVSO DPA	i'		7.558 ± 0.070
2018 May 07.897	9.907	AAVSO MIW	i'		7.875 ± 0.035
2018 May 10.172	12.182	AAVSO RBRB	i'		8.084 ± 0.005
2018 May 10.172	12.182	AAVSO STYA	i'		8.084 ± 0.004
2018 May 12.165	14.175	AAVSO SSTA	i'		8.516 ± 0.003
2018 May 12.804	14.814	AAVSO VMAG	i'		8.732 ± 0.020
2018 May 12.848	14.858	AAVSO ETOA	i'		8.645 ± 0.125
2018 May 12.849	14.859	AAVSO ETOA	i'		8.676 ± 0.025
2018 May 12.851	14.861	AAVSO ETOA	i'		8.688 ± 0.015
2018 May 12.853	14.863	AAVSO ETOA	i'		8.605 ± 0.027
2018 May 12.855	14.865	AAVSO ETOA	i'		8.705 ± 0.017

Continued on next page

Table A.3 – continued from previous page

Date (UT)	Δ t / days	Telescope & Instrument	Filter	Exp. time /s	Photometry /mag
2018 May 13.181	15.191	AAVSO RBRB	i'		8.820 ± 0.002
2018 May 13.181	15.191	AAVSO LRCA	i'		8.811 ± 0.003
2018 May 13.187	15.197	AAVSO STYA	i'		8.767 ± 0.001
2018 May 14.209	16.219	AAVSO RBRB	i'		9.038 ± 0.002
2018 May 14.211	16.221	AAVSO STYA	i'		8.995 ± 0.002
2018 May 16.230	18.240	AAVSO RBRB	i'		9.535 ± 0.007
2018 May 18.844	20.854	AAVSO NRNA	i'		10.439 ± 0.009
2018 May 19.222	21.232	AAVSO RBRB	i'		10.136 ± 0.005
2018 May 21.189	23.199	AAVSO RBRB	i'		10.262 ± 0.004
2018 Jun 30.374	63.384	AAVSO MRV	i'		12.471 ± 0.061
2018 Jul 07.369	70.379	AAVSO MRV	i'		12.531 ± 0.080
2018 Jul 09.365	72.375	AAVSO MRV	i'		12.711 ± 0.049
2018 Jul 14.365	77.375	AAVSO MRV	i'		12.895 ± 0.066
2018 Jul 14.478	77.488	AAVSO SGEA	i'		12.942 ± 0.058
2018 Jul 17.473	80.483	AAVSO SGEA	i'		13.168 ± 0.040
2018 Jul 18.478	81.488	AAVSO SGEA	i'		13.230 ± 0.052
2018 Jul 19.356	82.366	AAVSO CDJA	i'		12.989 ± 0.006
2018 Jul 19.357	82.367	AAVSO CDJA	i'		12.984 ± 0.006
2018 Jul 19.358	82.368	AAVSO CDJA	i'		12.989 ± 0.006
2018 Jul 19.359	82.369	AAVSO MRV	i'		13.140 ± 0.045
2018 Jul 21.196	84.206	LT IO:O	i'	3×30	13.316 ± 0.006
2018 Jul 21.455	84.465	AAVSO SGEA	i'		13.256 ± 0.033
2018 Jul 22.220	85.230	LT IO:O	i'	3×30	13.370 ± 0.006
2018 Jul 23.198	86.208	LT IO:O	i'	3×30	13.360 ± 0.006
2018 Jul 24.189	87.199	LT IO:O	i'	3×30	13.380 ± 0.006
2018 Jul 25.185	88.195	LT IO:O	i'	3×30	13.507 ± 0.007
2018 Jul 26.194	89.204	LT IO:O	i'	3×30	13.481 ± 0.009
2018 Jul 27.186	90.196	LT IO:O	i'	3×30	13.392 ± 0.009
2018 Jul 28.179	91.189	LT IO:O	i'	3×30	13.542 ± 0.006
2018 Jul 29.178	92.188	LT IO:O	i'	3×30	13.579 ± 0.008
2018 Jul 31.172	94.182	LT IO:O	i'	3×30	13.577 ± 0.008

Continued on next page

Table A.3 – continued from previous page

Date (UT)	Δ t / days	Telescope & Instrument	Filter	Exp. time /s	Photometry /mag
2018 Aug 01.186	95.196	LT IO:O	i'	3×30	13.543 ± 0.009
2018 Aug 02.163	96.173	LT IO:O	i'	3×30	13.503 ± 0.008
2018 Aug 02.350	96.360	AAVSO CDJA	i'		13.353 ± 0.005
2018 Aug 02.352	96.362	AAVSO CDJA	i'		13.362 ± 0.005
2018 Aug 02.353	96.363	AAVSO CDJA	i'		13.355 ± 0.005
2018 Aug 02.488	96.498	AAVSO SGEA	i'		13.510 ± 0.027
2018 Aug 03.161	97.171	LT IO:O	i'	3×30	13.675 ± 0.007
2018 Aug 03.485	97.495	AAVSO SGEA	i'		13.560 ± 0.039
2018 Aug 06.152	100.162	LT IO:O	i'	3×30	13.683 ± 0.007
2018 Aug 06.494	100.504	AAVSO SGEA	i'		13.609 ± 0.033
2018 Aug 08.168	102.178	LT IO:O	i'	3×30	13.718 ± 0.006
2018 Aug 09.328	103.338	AAVSO BMSA	i'		13.499 ± 0.005
2018 Aug 09.329	103.339	AAVSO BMSA	i'		13.523 ± 0.005
2018 Aug 09.330	103.340	AAVSO BMSA	i'		13.519 ± 0.005
2018 Aug 10.174	104.184	LT IO:O	i'	3×30	13.746 ± 0.007
2018 Aug 10.482	104.492	AAVSO SGEA	i'		13.563 ± 0.037
2018 Aug 13.177	107.187	LT IO:O	i'	3×30	13.764 ± 0.015
2018 Aug 13.330	107.340	AAVSO MRV	i'		13.811 ± 0.041
2018 Aug 13.336	107.346	AAVSO BMSA	i'		13.717 ± 0.005
2018 Aug 13.337	107.347	AAVSO BMSA	i'		13.722 ± 0.005
2018 Aug 13.338	107.348	AAVSO BMSA	i'		13.701 ± 0.005
2018 Aug 13.474	107.484	AAVSO SGEA	i'		13.752 ± 0.039
2018 Aug 14.420	108.430	AAVSO SGEA	i'		13.702 ± 0.042
2018 Aug 15.449	109.459	AAVSO SGEA	i'		13.636 ± 0.038
2018 Aug 16.126	110.136	LT IO:O	i'	3×30	13.799 ± 0.007
2018 Aug 16.451	110.461	AAVSO SGEA	i'		13.828 ± 0.041
2018 Aug 17.443	111.453	AAVSO SGEA	i'		13.793 ± 0.037
2018 Aug 18.411	112.421	AAVSO SGEA	i'		13.753 ± 0.039
2018 Aug 19.169	113.179	LT IO:O	i'	3×30	13.778 ± 0.007
2018 Aug 19.448	113.458	AAVSO SGEA	i'		13.676 ± 0.040
2018 Aug 20.418	114.428	AAVSO SGEA	i'		13.630 ± 0.034

Continued on next page

Table A.3 – continued from previous page

Date (UT)	Δ t / days	Telescope & Instrument	Filter	Exp. time /s	Photometry /mag
2018 Aug 21.433	115.443	AAVSO SGEA	i'		13.598 ± 0.042
2018 Aug 22.221	116.231	LT IO:O	i'	3 × 30	13.699 ± 0.006
2018 Aug 22.442	116.452	AAVSO SGEA	i'		13.671 ± 0.033
2018 Aug 23.473	117.483	AAVSO SGEA	i'		13.725 ± 0.035
2018 Aug 25.101	119.111	LT IO:O	i'	3 × 30	13.832 ± 0.006
2018 Aug 26.516	120.526	AAVSO SGEA	i'		13.680 ± 0.039
2018 Aug 27.516	121.526	AAVSO SGEA	i'		13.628 ± 0.037
2018 Aug 28.111	122.121	LT IO:O	i'	3 × 30	13.744 ± 0.009
2018 Aug 28.523	122.533	AAVSO SGEA	i'		13.726 ± 0.044
2018 Aug 29.513	123.523	AAVSO SGEA	i'		13.814 ± 0.043
2018 Aug 30.520	124.530	AAVSO SGEA	i'		13.611 ± 0.048
2018 Aug 31.088	125.098	LT IO:O	i'	3 × 30	13.776 ± 0.007
2018 Aug 31.516	125.526	AAVSO SGEA	i'		13.658 ± 0.036
2018 Sep 02.517	127.527	AAVSO SGEA	i'		13.776 ± 0.048
2018 Sep 03.077	128.087	LT IO:O	i'	3 × 30	13.815 ± 0.007
2018 Sep 03.508	128.518	AAVSO SGEA	i'		13.712 ± 0.043
2018 Sep 04.520	129.530	AAVSO SGEA	i'		13.783 ± 0.038
2018 Sep 05.513	130.523	AAVSO SGEA	i'		13.785 ± 0.039
2018 Sep 06.069	131.079	LT IO:O	i'	3 × 30	13.863 ± 0.006
2018 Sep 06.504	131.514	AAVSO SGEA	i'		13.746 ± 0.035
2018 Sep 07.497	132.507	AAVSO SGEA	i'		13.919 ± 0.046
2018 Sep 08.510	133.520	AAVSO SGEA	i'		13.892 ± 0.037
2018 Sep 09.058	134.068	LT IO:O	i'	3 × 30	13.957 ± 0.006
2018 Sep 09.532	134.542	AAVSO SGEA	i'		13.802 ± 0.043
2018 Sep 11.531	136.541	AAVSO SGEA	i'		13.793 ± 0.045
2018 Sep 12.066	137.076	LT IO:O	i'	3 × 30	13.987 ± 0.008
2018 Sep 13.527	138.537	AAVSO SGEA	i'		13.803 ± 0.040
2018 Sep 14.539	139.549	AAVSO SGEA	i'		13.872 ± 0.064
2018 Sep 15.278	140.288	AAVSO MRV	i'		13.957 ± 0.045
2018 Sep 18.090	143.100	LT IO:O	i'	3 × 30	14.022 ± 0.006
2018 Sep 23.022	148.032	LT IO:O	i'	3 × 30	14.056 ± 0.010

Continued on next page

Table A.3 – continued from previous page

Date (UT)	Δ t / days	Telescope & Instrument	Filter	Exp. time /s	Photometry /mag
2018 Sep 26.017	151.027	LT IO:O	i'	3×30	14.099 ± 0.008
2018 Sep 29.061	154.071	LT IO:O	i'	3×30	14.093 ± 0.006
2018 Oct 02.016	157.026	LT IO:O	i'	3×30	14.151 ± 0.006
2018 Nov 01.115	187.125	LT IO:O	i'	3×30	14.371 ± 0.006
2018 Nov 08.163	194.173	LT IO:O	i'	3×30	14.364 ± 0.006
2018 Nov 16.121	202.131	LT IO:O	i'	3×30	14.340 ± 0.006
2018 Nov 26.027	212.037	LT IO:O	i'	3×30	14.270 ± 0.007
2018 Nov 26.318	212.328	AAVSO MRV	i'		14.247 ± 0.042
2018 Dec 10.068	226.078	LT IO:O	i'	3×30	14.313 ± 0.005
2018 Dec 15.967	231.977	LT IO:O	i'	3×30	14.336 ± 0.009
2018 Dec 22.843	238.853	LT IO:O	i'	3×30	14.427 ± 0.009
2018 Dec 28.897	244.907	LT IO:O	i'	3×30	14.396 ± 0.010
2019 Jan 04.923	251.933	LT IO:O	i'	3×30	14.423 ± 0.005
2019 Jan 10.976	257.986	LT IO:O	i'	3×30	14.404 ± 0.006
2019 Jan 19.991	267.001	LT IO:O	i'	3×30	14.365 ± 0.007
2019 Jan 25.906	272.916	LT IO:O	i'	3×30	14.320 ± 0.006
2019 Jan 31.942	278.952	LT IO:O	i'	3×30	14.168 ± 0.006
2019 Feb 06.892	284.902	LT IO:O	i'	3×30	14.370 ± 0.007
2019 Feb 12.878	290.888	LT IO:O	i'	3×30	14.431 ± 0.007
2019 Feb 19.903	297.913	LT IO:O	i'	3×30	14.433 ± 0.012
2019 Feb 28.892	306.902	LT IO:O	i'	3×30	14.480 ± 0.007
2019 Mar 16.850	322.860	LT IO:O	i'	3×30	14.402 ± 0.006
2019 Apr 08.863	345.873	LT IO:O	i'	3×30	14.456 ± 0.007
2019 Apr 25.855	362.865	LT IO:O	i'	3×30	14.372 ± 0.007
2019 Jul 19.219	447.229	LT IO:O	i'	3×30	14.367 ± 0.008
2019 Aug 01.222	460.232	LT IO:O	i'	3×30	14.379 ± 0.006
2019 Aug 19.129	478.139	LT IO:O	i'	3×30	14.344 ± 0.008
2019 Sep 14.119	504.129	LT IO:O	i'	3×60	14.354 ± 0.009
2019 Oct 14.983	534.993	LT IO:O	i'	3×60	14.280 ± 0.007
2019 Nov 16.943	567.953	LT IO:O	i'	3×60	14.048 ± 0.006
2019 Nov 17.199	568.209	LCO	i'	1×180	13.892 ± 0.031

Continued on next page

Table A.3 – continued from previous page

Date (UT)	Δ t / days	Telescope & Instrument	Filter	Exp. time /s	Photometry /mag
2019 Nov 17.201	568.211	LCO	i'	1×180	13.838 ± 0.025
2019 Nov 17.203	568.213	LCO	i'	1×180	13.900 ± 0.026
2019 Nov 17.206	568.216	LCO	i'	1×180	14.082 ± 0.021
2019 Nov 17.208	568.218	LCO	i'	1×180	14.124 ± 0.018
2019 Nov 17.211	568.221	LCO	i'	1×180	14.050 ± 0.022
2019 Nov 17.213	568.223	LCO	i'	1×180	14.171 ± 0.015
2019 Nov 17.215	568.225	LCO	i'	1×180	14.149 ± 0.015
2019 Nov 17.218	568.228	LCO	i'	1×180	14.139 ± 0.013
2019 Nov 17.220	568.230	LCO	i'	1×180	14.200 ± 0.009
2019 Nov 17.223	568.233	LCO	i'	1×180	14.191 ± 0.008
2019 Nov 17.225	568.235	LCO	i'	1×180	14.197 ± 0.008
2019 Nov 17.228	568.238	LCO	i'	1×300	13.131 ± 0.052
2019 Nov 17.231	568.241	LCO	i'	1×300	13.034 ± 0.049
2019 Nov 17.235	568.245	LCO	i'	1×300	13.149 ± 0.045
2019 Nov 18.287	569.297	LCO	i'	1×180	14.135 ± 0.006
2019 Nov 18.289	569.299	LCO	i'	1×180	14.137 ± 0.005
2019 Nov 18.291	569.301	LCO	i'	1×180	14.144 ± 0.005
2019 Nov 18.292	569.302	LCO	i'	1×180	14.140 ± 0.006
2019 Nov 18.294	569.304	LCO	i'	1×180	14.159 ± 0.006
2019 Nov 18.297	569.307	LCO	i'	1×180	14.148 ± 0.007
2019 Nov 18.320	569.330	LCO	i'	1×180	14.073 ± 0.007
2019 Nov 18.322	569.332	LCO	i'	1×180	14.092 ± 0.007
2019 Nov 18.325	569.335	LCO	i'	1×180	14.071 ± 0.007
2019 Nov 18.356	569.366	LCO	i'	1×180	14.057 ± 0.008
2019 Nov 18.358	569.368	LCO	i'	1×180	14.065 ± 0.008
2019 Nov 18.361	569.371	LCO	i'	1×180	14.062 ± 0.008
2019 Nov 18.456	569.466	LCO	i'	1×180	14.151 ± 0.008
2019 Nov 18.458	569.468	LCO	i'	1×180	14.148 ± 0.007
2019 Nov 18.461	569.471	LCO	i'	1×180	14.114 ± 0.007
2019 Nov 18.490	569.500	LCO	i'	1×180	14.110 ± 0.007
2019 Nov 18.493	569.503	LCO	i'	1×180	14.093 ± 0.008

Continued on next page

Table A.3 – continued from previous page

Date (UT)	Δ t / days	Telescope & Instrument	Filter	Exp. time /s	Photometry /mag
2019 Nov 18.495	569.505	LCO	i'	1×180	14.113 ± 0.009
2019 Nov 19.168	570.178	LCO	i'	1×180	14.069 ± 0.006
2019 Nov 19.171	570.181	LCO	i'	1×180	14.078 ± 0.005
2019 Nov 19.173	570.183	LCO	i'	1×180	14.094 ± 0.007
2019 Nov 19.188	570.198	LCO	i'	1×180	14.154 ± 0.011
2019 Nov 19.191	570.201	LCO	i'	1×180	14.140 ± 0.009
2019 Nov 19.193	570.203	LCO	i'	1×143	14.128 ± 0.008
2019 Nov 19.237	570.247	LCO	i'	1×180	14.072 ± 0.007
2019 Nov 19.239	570.249	LCO	i'	1×180	14.113 ± 0.007
2019 Nov 19.241	570.251	LCO	i'	1×180	14.132 ± 0.006
2019 Nov 19.278	570.288	LCO	i'	1×180	14.132 ± 0.008
2019 Nov 19.280	570.290	LCO	i'	1×180	14.131 ± 0.007
2019 Nov 19.283	570.293	LCO	i'	1×180	14.131 ± 0.010
2019 Nov 19.320	570.330	LCO	i'	1×180	14.081 ± 0.007
2019 Nov 19.322	570.332	LCO	i'	1×180	14.119 ± 0.006
2019 Nov 19.325	570.335	LCO	i'	1×180	14.128 ± 0.006
2019 Nov 19.355	570.365	LCO	i'	1×180	14.131 ± 0.008
2019 Nov 19.357	570.367	LCO	i'	1×180	14.113 ± 0.007
2019 Nov 19.359	570.369	LCO	i'	1×180	14.077 ± 0.006
2019 Nov 19.396	570.406	LCO	i'	1×180	14.202 ± 0.007
2019 Nov 19.398	570.408	LCO	i'	1×180	14.167 ± 0.008
2019 Nov 19.401	570.411	LCO	i'	1×180	14.153 ± 0.007
2019 Nov 19.406	570.416	LCO	i'	1×180	14.142 ± 0.008
2019 Nov 19.409	570.419	LCO	i'	1×180	14.117 ± 0.008
2019 Nov 19.411	570.421	LCO	i'	1×180	14.119 ± 0.007
2019 Nov 19.438	570.448	LCO	i'	1×180	14.097 ± 0.010
2019 Nov 19.440	570.450	LCO	i'	1×180	14.091 ± 0.011
2019 Nov 19.443	570.453	LCO	i'	1×180	14.075 ± 0.012
2019 Nov 19.459	570.469	LCO	i'	1×180	14.090 ± 0.009
2019 Nov 19.461	570.471	LCO	i'	1×180	14.091 ± 0.009
2019 Nov 19.463	570.473	LCO	i'	1×180	14.098 ± 0.007

Continued on next page

Table A.3 – continued from previous page

Date (UT)	Δ t / days	Telescope & Instrument	Filter	Exp. time /s	Photometry /mag
2019 Nov 21.141	572.151	LCO	i'	1×180	14.219 ± 0.008
2019 Nov 21.144	572.154	LCO	i'	1×180	14.177 ± 0.009
2019 Nov 21.146	572.156	LCO	i'	1×180	14.194 ± 0.007
2019 Nov 21.157	572.167	LCO	i'	1×180	14.194 ± 0.008
2019 Nov 21.159	572.169	LCO	i'	1×180	14.223 ± 0.007
2019 Nov 21.161	572.171	LCO	i'	1×180	14.197 ± 0.007
2019 Nov 21.194	572.204	LCO	i'	1×180	14.262 ± 0.007
2019 Nov 21.196	572.206	LCO	i'	1×180	14.267 ± 0.007
2019 Nov 21.199	572.209	LCO	i'	1×180	14.249 ± 0.007
2019 Nov 21.295	572.305	LCO	i'	1×180	14.192 ± 0.006
2019 Nov 21.298	572.308	LCO	i'	1×180	14.185 ± 0.008
2019 Nov 21.300	572.310	LCO	i'	1×180	14.182 ± 0.007
2019 Nov 21.323	572.333	LCO	i'	1×180	14.265 ± 0.006
2019 Nov 21.326	572.336	LCO	i'	1×180	14.280 ± 0.006
2019 Nov 21.328	572.338	LCO	i'	1×180	14.290 ± 0.006
2019 Nov 21.354	572.364	LCO	i'	1×180	14.258 ± 0.006
2019 Nov 21.357	572.367	LCO	i'	1×180	14.125 ± 0.048
2019 Nov 21.359	572.369	LCO	i'	1×180	14.251 ± 0.006
2019 Nov 21.369	572.379	LCO	i'	1×180	14.256 ± 0.008
2019 Nov 21.371	572.381	LCO	i'	1×180	14.281 ± 0.006
2019 Nov 21.373	572.383	LCO	i'	1×180	14.269 ± 0.007
2019 Nov 21.396	572.406	LCO	i'	1×180	14.268 ± 0.007
2019 Nov 21.398	572.408	LCO	i'	1×180	14.271 ± 0.007
2019 Nov 21.401	572.411	LCO	i'	1×180	14.234 ± 0.007
2019 Nov 21.440	572.450	LCO	i'	1×180	14.220 ± 0.006
2019 Nov 21.443	572.453	LCO	i'	1×180	14.214 ± 0.007
2019 Nov 21.445	572.455	LCO	i'	1×180	14.206 ± 0.007
2019 Nov 21.462	572.472	LCO	i'	1×180	14.204 ± 0.007
2019 Nov 21.464	572.474	LCO	i'	1×180	14.192 ± 0.007
2019 Nov 21.467	572.477	LCO	i'	1×180	14.211 ± 0.007
2019 Nov 22.217	573.227	LCO	i'	1×180	14.137 ± 0.007

Continued on next page

Table A.3 – continued from previous page

Date (UT)	Δ t / days	Telescope & Instrument	Filter	Exp. time /s	Photometry /mag
2019 Nov 22.219	573.229	LCO	i'	1×180	14.136 ± 0.007
2019 Nov 22.222	573.232	LCO	i'	1×180	14.132 ± 0.007
2019 Nov 23.137	574.147	LCO	i'	1×180	14.039 ± 0.007
2019 Nov 23.139	574.149	LCO	i'	1×180	14.034 ± 0.007
2019 Nov 23.141	574.151	LCO	i'	1×180	14.032 ± 0.008
2019 Nov 23.142	574.152	LCO	i'	1×180	14.030 ± 0.007
2019 Nov 23.145	574.155	LCO	i'	1×180	14.043 ± 0.007
2019 Nov 23.147	574.157	LCO	i'	1×180	14.069 ± 0.008
2019 Nov 23.182	574.192	LCO	i'	1×180	14.069 ± 0.006
2019 Nov 23.185	574.195	LCO	i'	1×180	14.038 ± 0.007
2019 Nov 23.187	574.197	LCO	i'	1×180	14.053 ± 0.006
2019 Nov 23.191	574.201	LCO	i'	1×180	14.067 ± 0.007
2019 Nov 23.193	574.203	LCO	i'	1×180	14.070 ± 0.007
2019 Nov 23.196	574.206	LCO	i'	1×180	14.084 ± 0.006
2019 Nov 23.271	574.281	LCO	i'	1×180	14.094 ± 0.006
2019 Nov 23.274	574.284	LCO	i'	1×180	14.114 ± 0.007
2019 Nov 23.276	574.286	LCO	i'	1×180	14.101 ± 0.006
2019 Nov 23.280	574.290	LCO	i'	1×180	14.047 ± 0.007
2019 Nov 23.282	574.292	LCO	i'	1×180	14.075 ± 0.006
2019 Nov 23.285	574.295	LCO	i'	1×180	14.085 ± 0.007
2019 Nov 23.295	574.305	LCO	i'	1×180	14.062 ± 0.006
2019 Nov 23.298	574.308	LCO	i'	1×180	14.070 ± 0.007
2019 Nov 23.300	574.310	LCO	i'	1×180	14.047 ± 0.007
2019 Nov 23.359	574.369	LCO	i'	1×180	14.021 ± 0.007
2019 Nov 23.361	574.371	LCO	i'	1×180	14.042 ± 0.006
2019 Nov 23.363	574.373	LCO	i'	1×180	14.084 ± 0.007
2019 Nov 23.447	574.457	LCO	i'	1×180	14.137 ± 0.006
2019 Nov 23.449	574.459	LCO	i'	1×180	14.146 ± 0.007
2019 Nov 23.451	574.461	LCO	i'	1×180	14.173 ± 0.007
2019 Nov 23.466	574.476	LCO	i'	1×180	14.116 ± 0.008
2019 Nov 23.468	574.478	LCO	i'	1×180	14.078 ± 0.006

Continued on next page

Table A.3 – continued from previous page

Date (UT)	Δ t / days	Telescope & Instrument	Filter	Exp. time /s	Photometry /mag
2019 Nov 23.470	574.480	LCO	i'	1×180	14.106 ± 0.008
2019 Nov 23.897	574.907	LT IO:O	i'	1×120	14.356 ± 0.006
2019 Nov 23.899	574.909	LT IO:O	i'	1×120	14.297 ± 0.006
2019 Nov 23.901	574.911	LT IO:O	i'	1×120	14.528 ± 0.006
2019 Nov 23.951	574.961	LT IO:O	i'	1×120	14.257 ± 0.005
2019 Nov 23.953	574.963	LT IO:O	i'	1×120	14.269 ± 0.007
2019 Nov 23.954	574.964	LT IO:O	i'	1×120	14.318 ± 0.005
2019 Nov 24.011	575.021	LT IO:O	i'	1×120	14.503 ± 0.005
2019 Nov 24.013	575.023	LT IO:O	i'	1×120	14.679 ± 0.005
2019 Nov 24.014	575.024	LT IO:O	i'	1×120	14.680 ± 0.006
2019 Nov 24.108	575.118	LT IO:O	i'	1×120	14.350 ± 0.006
2019 Nov 24.110	575.120	LT IO:O	i'	1×120	14.439 ± 0.006
2019 Nov 24.112	575.122	LT IO:O	i'	1×120	14.534 ± 0.006
2019 Nov 24.159	575.169	LT IO:O	i'	1×120	14.297 ± 0.006
2019 Nov 24.160	575.170	LT IO:O	i'	1×120	14.346 ± 0.005
2019 Nov 24.162	575.172	LT IO:O	i'	1×120	14.328 ± 0.006
2019 Nov 24.211	575.221	LT IO:O	i'	1×120	14.435 ± 0.006
2019 Nov 24.213	575.223	LT IO:O	i'	1×120	14.549 ± 0.006
2019 Nov 24.215	575.225	LT IO:O	i'	1×120	14.445 ± 0.006
2019 Nov 24.261	575.271	LT IO:O	i'	1×120	14.380 ± 0.005
2019 Nov 24.262	575.272	LT IO:O	i'	1×120	14.295 ± 0.006
2019 Nov 24.264	575.274	LT IO:O	i'	1×120	14.292 ± 0.006
2019 Nov 24.882	575.892	LT IO:O	i'	1×120	14.130 ± 0.019
2019 Nov 24.884	575.894	LT IO:O	i'	1×120	14.126 ± 0.021
2019 Nov 24.885	575.895	LT IO:O	i'	1×120	14.359 ± 0.163
2019 Nov 25.020	576.030	LT IO:O	i'	1×120	14.125 ± 0.007
2019 Nov 25.021	576.031	LT IO:O	i'	1×120	14.094 ± 0.006
2019 Nov 25.023	576.033	LT IO:O	i'	1×120	14.089 ± 0.007
2019 Nov 25.069	576.079	LT IO:O	i'	1×120	14.044 ± 0.006
2019 Nov 25.071	576.081	LT IO:O	i'	1×120	14.057 ± 0.007
2019 Nov 25.072	576.082	LT IO:O	i'	1×120	14.046 ± 0.006

Continued on next page

Table A.3 – continued from previous page

Date (UT)	Δ t / days	Telescope & Instrument	Filter	Exp. time /s	Photometry /mag
2019 Nov 25.118	576.128	LT IO:O	i'	1×120	14.146 ± 0.006
2019 Nov 25.120	576.130	LT IO:O	i'	1×120	14.144 ± 0.005
2019 Nov 25.122	576.132	LT IO:O	i'	1×120	14.143 ± 0.005
2019 Nov 25.170	576.180	LT IO:O	i'	1×120	14.275 ± 0.005
2019 Nov 25.172	576.182	LT IO:O	i'	1×120	14.146 ± 0.005
2019 Nov 25.174	576.184	LT IO:O	i'	1×120	14.098 ± 0.005
2019 Nov 25.234	576.244	LT IO:O	i'	1×120	14.051 ± 0.006
2019 Nov 25.236	576.246	LT IO:O	i'	1×120	14.093 ± 0.006
2019 Nov 25.237	576.247	LT IO:O	i'	1×120	14.076 ± 0.006
2019 Nov 25.886	576.896	LT IO:O	i'	1×120	14.093 ± 0.007
2019 Nov 25.888	576.898	LT IO:O	i'	1×120	14.145 ± 0.007
2019 Nov 25.890	576.900	LT IO:O	i'	1×120	14.140 ± 0.006
2019 Nov 25.946	576.956	LT IO:O	i'	1×120	14.515 ± 0.005
2019 Nov 25.947	576.957	LT IO:O	i'	1×120	14.362 ± 0.005
2019 Nov 25.949	576.959	LT IO:O	i'	1×120	14.382 ± 0.005
2019 Nov 25.996	577.006	LT IO:O	i'	1×120	14.546 ± 0.005
2019 Nov 25.997	577.007	LT IO:O	i'	1×120	14.535 ± 0.006
2019 Nov 25.999	577.009	LT IO:O	i'	1×120	14.595 ± 0.006
2019 Nov 26.048	577.058	LT IO:O	i'	1×120	14.208 ± 0.006
2019 Nov 26.049	577.059	LT IO:O	i'	1×120	14.436 ± 0.006
2019 Nov 26.051	577.061	LT IO:O	i'	1×120	14.303 ± 0.006
2019 Nov 26.099	577.109	LT IO:O	i'	1×120	14.325 ± 0.006
2019 Nov 26.101	577.111	LT IO:O	i'	1×120	14.233 ± 0.006
2019 Nov 26.102	577.112	LT IO:O	i'	1×120	14.253 ± 0.005
2019 Nov 26.150	577.160	LT IO:O	i'	1×120	14.376 ± 0.006
2019 Nov 26.151	577.161	LT IO:O	i'	1×120	14.320 ± 0.006
2019 Nov 26.153	577.163	LT IO:O	i'	1×120	14.496 ± 0.006
2019 Nov 26.200	577.210	LT IO:O	i'	1×120	14.391 ± 0.006
2019 Nov 26.201	577.211	LT IO:O	i'	1×120	14.332 ± 0.006
2019 Nov 26.203	577.213	LT IO:O	i'	1×120	14.368 ± 0.005
2019 Nov 26.253	577.263	LT IO:O	i'	1×120	14.214 ± 0.006

Continued on next page

Table A.3 – continued from previous page

Date (UT)	Δ t / days	Telescope & Instrument	Filter	Exp. time /s	Photometry /mag
2019 Nov 26.255	577.265	LT IO:O	i'	1×120	14.226 ± 0.006
2019 Nov 26.257	577.267	LT IO:O	i'	1×120	14.230 ± 0.006
2019 Nov 26.911	577.921	LT IO:O	i'	1×120	14.596 ± 0.006
2019 Nov 26.912	577.922	LT IO:O	i'	1×120	14.588 ± 0.006
2019 Nov 26.914	577.924	LT IO:O	i'	1×120	14.595 ± 0.005
2019 Nov 26.971	577.981	LT IO:O	i'	1×120	14.350 ± 0.005
2019 Nov 26.973	577.983	LT IO:O	i'	1×120	14.328 ± 0.005
2019 Nov 26.974	577.984	LT IO:O	i'	1×120	14.333 ± 0.005
2019 Nov 27.021	578.031	LT IO:O	i'	1×120	14.516 ± 0.007
2019 Nov 27.023	578.033	LT IO:O	i'	1×120	14.535 ± 0.006
2019 Nov 27.025	578.035	LT IO:O	i'	1×120	14.503 ± 0.006
2019 Nov 27.084	578.094	LT IO:O	i'	1×120	14.558 ± 0.005
2019 Nov 27.086	578.096	LT IO:O	i'	1×120	14.578 ± 0.005
2019 Nov 27.087	578.097	LT IO:O	i'	1×120	14.453 ± 0.005
2019 Nov 27.134	578.144	LT IO:O	i'	1×120	14.495 ± 0.005
2019 Nov 27.135	578.145	LT IO:O	i'	1×120	14.565 ± 0.005
2019 Nov 27.137	578.147	LT IO:O	i'	1×120	14.521 ± 0.005
2019 Nov 27.183	578.193	LT IO:O	i'	1×120	14.494 ± 0.005
2019 Nov 27.185	578.195	LT IO:O	i'	1×120	14.552 ± 0.005
2019 Nov 27.186	578.196	LT IO:O	i'	1×120	14.463 ± 0.005
2019 Nov 27.944	578.954	LT IO:O	i'	1×120	14.157 ± 0.014
2019 Nov 27.945	578.955	LT IO:O	i'	1×120	14.123 ± 0.014
2019 Nov 27.947	578.957	LT IO:O	i'	1×120	14.351 ± 0.039
2019 Nov 27.979	578.989	LT IO:O	i'	1×120	14.168 ± 0.006
2019 Nov 27.980	578.990	LT IO:O	i'	1×120	14.161 ± 0.012
2019 Nov 27.982	578.992	LT IO:O	i'	1×120	14.168 ± 0.007
2019 Nov 28.012	579.022	LT IO:O	i'	1×120	14.225 ± 0.007
2019 Nov 28.013	579.023	LT IO:O	i'	1×120	14.223 ± 0.007
2019 Nov 28.015	579.025	LT IO:O	i'	1×120	14.203 ± 0.009
2019 Nov 28.042	579.052	LT IO:O	i'	1×120	14.208 ± 0.006
2019 Nov 28.043	579.053	LT IO:O	i'	1×120	14.207 ± 0.005

Continued on next page

Table A.3 – continued from previous page

Date (UT)	Δ t / days	Telescope & Instrument	Filter	Exp. time /s	Photometry /mag
2019 Nov 28.045	579.055	LT IO:O	i'	1×120	14.213 ± 0.006
2019 Nov 28.071	579.081	LT IO:O	i'	1×120	14.194 ± 0.006
2019 Nov 28.073	579.083	LT IO:O	i'	1×120	14.208 ± 0.006
2019 Nov 28.074	579.084	LT IO:O	i'	1×120	14.228 ± 0.005
2019 Nov 28.098	579.108	LT IO:O	i'	1×120	14.229 ± 0.005
2019 Nov 28.099	579.109	LT IO:O	i'	1×120	14.182 ± 0.005
2019 Nov 28.101	579.111	LT IO:O	i'	1×120	14.195 ± 0.006
2019 Nov 28.914	579.924	LT IO:O	i'	1×120	14.199 ± 0.006
2019 Nov 28.916	579.926	LT IO:O	i'	1×120	14.196 ± 0.006
2019 Nov 28.917	579.927	LT IO:O	i'	1×120	14.507 ± 0.005
2019 Nov 28.951	579.961	LT IO:O	i'	1×120	14.266 ± 0.005
2019 Nov 28.953	579.963	LT IO:O	i'	1×120	14.280 ± 0.005
2019 Nov 28.954	579.964	LT IO:O	i'	1×120	14.245 ± 0.005
2019 Nov 28.993	580.003	LT IO:O	i'	1×120	14.194 ± 0.006
2019 Nov 28.994	580.004	LT IO:O	i'	1×120	14.171 ± 0.006
2019 Nov 28.996	580.006	LT IO:O	i'	1×120	14.153 ± 0.007
2019 Nov 29.022	580.032	LT IO:O	i'	1×120	14.165 ± 0.007
2019 Nov 29.024	580.034	LT IO:O	i'	1×120	14.172 ± 0.007
2019 Nov 29.026	580.036	LT IO:O	i'	1×120	14.172 ± 0.006
2019 Nov 29.052	580.062	LT IO:O	i'	1×120	14.201 ± 0.005
2019 Nov 29.054	580.064	LT IO:O	i'	1×120	14.206 ± 0.006
2019 Nov 29.056	580.066	LT IO:O	i'	1×120	14.214 ± 0.005
2019 Nov 29.082	580.092	LT IO:O	i'	1×120	14.203 ± 0.006
2019 Nov 29.083	580.093	LT IO:O	i'	1×120	14.196 ± 0.006
2019 Nov 29.085	580.095	LT IO:O	i'	1×120	14.198 ± 0.006
2019 Nov 29.938	580.948	LT IO:O	i'	1×120	14.225 ± 0.005
2019 Nov 29.939	580.949	LT IO:O	i'	1×120	14.203 ± 0.006
2019 Nov 29.941	580.951	LT IO:O	i'	1×120	14.216 ± 0.006
2019 Nov 29.943	580.953	LT IO:O	i'	1×120	14.225 ± 0.006
2019 Nov 29.944	580.954	LT IO:O	i'	1×120	14.243 ± 0.006
2019 Nov 29.946	580.956	LT IO:O	i'	1×120	14.252 ± 0.006

Continued on next page

Table A.3 – continued from previous page

Date (UT)	Δ t / days	Telescope & Instrument	Filter	Exp. time /s	Photometry /mag
2019 Nov 29.947	580.957	LT IO:O	i'	1×120	14.244 ± 0.006
2019 Nov 29.949	580.959	LT IO:O	i'	1×120	14.255 ± 0.006
2019 Nov 29.951	580.961	LT IO:O	i'	1×120	14.265 ± 0.005
2019 Nov 29.952	580.962	LT IO:O	i'	1×120	14.255 ± 0.006
2019 Nov 29.954	580.964	LT IO:O	i'	1×120	14.255 ± 0.005
2019 Nov 29.956	580.966	LT IO:O	i'	1×120	14.259 ± 0.006
2019 Nov 29.957	580.967	LT IO:O	i'	1×120	14.252 ± 0.006
2019 Nov 29.959	580.969	LT IO:O	i'	1×120	14.258 ± 0.006
2019 Nov 29.960	580.970	LT IO:O	i'	1×120	14.238 ± 0.006
2019 Nov 29.962	580.972	LT IO:O	i'	1×120	14.234 ± 0.006
2019 Nov 29.964	580.974	LT IO:O	i'	1×120	14.198 ± 0.006
2019 Nov 29.965	580.975	LT IO:O	i'	1×120	14.190 ± 0.006
2019 Nov 29.967	580.977	LT IO:O	i'	1×120	14.183 ± 0.006
2019 Nov 29.968	580.978	LT IO:O	i'	1×120	14.171 ± 0.006
2019 Nov 30.009	581.019	LT IO:O	i'	1×120	14.190 ± 0.007
2019 Nov 30.011	581.021	LT IO:O	i'	1×120	14.208 ± 0.006
2019 Nov 30.013	581.023	LT IO:O	i'	1×120	14.207 ± 0.007
2019 Nov 30.014	581.024	LT IO:O	i'	1×120	14.205 ± 0.006
2019 Nov 30.016	581.026	LT IO:O	i'	1×120	14.210 ± 0.007
2019 Nov 30.017	581.027	LT IO:O	i'	1×120	14.205 ± 0.006
2019 Nov 30.019	581.029	LT IO:O	i'	1×120	14.201 ± 0.007
2019 Nov 30.021	581.031	LT IO:O	i'	1×120	14.207 ± 0.006
2019 Nov 30.022	581.032	LT IO:O	i'	1×120	14.196 ± 0.006
2019 Nov 30.024	581.034	LT IO:O	i'	1×120	14.204 ± 0.006
2019 Nov 30.026	581.036	LT IO:O	i'	1×120	14.195 ± 0.006
2019 Nov 30.027	581.037	LT IO:O	i'	1×120	14.179 ± 0.006
2019 Nov 30.029	581.039	LT IO:O	i'	1×120	14.191 ± 0.006
2019 Nov 30.030	581.040	LT IO:O	i'	1×120	14.214 ± 0.006
2019 Nov 30.032	581.042	LT IO:O	i'	1×120	14.244 ± 0.006
2019 Nov 30.034	581.044	LT IO:O	i'	1×120	14.227 ± 0.005
2019 Nov 30.035	581.045	LT IO:O	i'	1×120	14.237 ± 0.006

Continued on next page

Table A.3 – continued from previous page

Date (UT)	Δ t / days	Telescope & Instrument	Filter	Exp. time /s	Photometry /mag
2019 Nov 30.037	581.047	LT IO:O	i'	1×120	14.249 ± 0.006
2019 Nov 30.038	581.048	LT IO:O	i'	1×120	14.284 ± 0.005
2019 Nov 30.040	581.050	LT IO:O	i'	1×120	14.296 ± 0.005
2019 Nov 30.076	581.086	LT IO:O	i'	1×120	14.334 ± 0.006
2019 Nov 30.077	581.087	LT IO:O	i'	1×120	14.391 ± 0.005
2019 Nov 30.079	581.089	LT IO:O	i'	1×120	14.288 ± 0.006
2019 Nov 30.080	581.090	LT IO:O	i'	1×120	14.310 ± 0.006
2019 Nov 30.082	581.092	LT IO:O	i'	1×120	14.388 ± 0.005
2019 Nov 30.084	581.094	LT IO:O	i'	1×120	14.388 ± 0.005
2019 Nov 30.085	581.095	LT IO:O	i'	1×120	14.377 ± 0.005
2019 Nov 30.087	581.097	LT IO:O	i'	1×120	14.355 ± 0.005
2019 Nov 30.088	581.098	LT IO:O	i'	1×120	14.393 ± 0.006
2019 Nov 30.090	581.100	LT IO:O	i'	1×120	14.432 ± 0.006
2019 Nov 30.092	581.102	LT IO:O	i'	1×120	14.495 ± 0.006
2019 Nov 30.093	581.103	LT IO:O	i'	1×120	14.556 ± 0.006
2019 Nov 30.095	581.105	LT IO:O	i'	1×120	14.411 ± 0.005
2019 Nov 30.096	581.106	LT IO:O	i'	1×120	14.349 ± 0.005
2019 Nov 30.098	581.108	LT IO:O	i'	1×120	14.372 ± 0.005
2019 Nov 30.100	581.110	LT IO:O	i'	1×120	14.607 ± 0.006
2019 Nov 30.101	581.111	LT IO:O	i'	1×120	14.531 ± 0.006
2019 Nov 30.103	581.113	LT IO:O	i'	1×120	14.445 ± 0.005
2019 Nov 30.104	581.114	LT IO:O	i'	1×120	14.345 ± 0.005
2019 Nov 30.106	581.116	LT IO:O	i'	1×120	14.311 ± 0.005
2019 Nov 30.132	581.142	LT IO:O	i'	1×120	14.345 ± 0.005
2019 Nov 30.133	581.143	LT IO:O	i'	1×120	14.501 ± 0.005
2019 Nov 30.135	581.145	LT IO:O	i'	1×120	14.425 ± 0.006
2019 Nov 30.137	581.147	LT IO:O	i'	1×120	14.507 ± 0.005
2019 Nov 30.138	581.148	LT IO:O	i'	1×120	14.515 ± 0.005
2019 Nov 30.140	581.150	LT IO:O	i'	1×120	14.360 ± 0.006
2019 Nov 30.142	581.152	LT IO:O	i'	1×120	14.508 ± 0.006
2019 Nov 30.143	581.153	LT IO:O	i'	1×120	14.397 ± 0.005

Continued on next page

Table A.3 – continued from previous page

Date (UT)	Δ t / days	Telescope & Instrument	Filter	Exp. time /s	Photometry /mag
2019 Nov 30.145	581.155	LT IO:O	i'	1×120	14.500 ± 0.006
2019 Nov 30.146	581.156	LT IO:O	i'	1×120	14.496 ± 0.006
2019 Nov 30.148	581.158	LT IO:O	i'	1×120	14.516 ± 0.006
2019 Nov 30.150	581.160	LT IO:O	i'	1×120	14.527 ± 0.005
2019 Nov 30.151	581.161	LT IO:O	i'	1×120	14.550 ± 0.005
2019 Nov 30.153	581.163	LT IO:O	i'	1×120	14.602 ± 0.005
2019 Nov 30.154	581.164	LT IO:O	i'	1×120	14.547 ± 0.005
2019 Nov 30.156	581.166	LT IO:O	i'	1×120	14.591 ± 0.006
2019 Nov 30.158	581.168	LT IO:O	i'	1×120	14.525 ± 0.006
2019 Nov 30.159	581.169	LT IO:O	i'	1×120	14.598 ± 0.006
2019 Nov 30.161	581.171	LT IO:O	i'	1×120	14.706 ± 0.006
2019 Nov 30.162	581.172	LT IO:O	i'	1×120	14.574 ± 0.005
2019 Dec 01.941	582.951	LT IO:O	i'	1×120	14.441 ± 0.006
2019 Dec 01.943	582.953	LT IO:O	i'	1×120	14.527 ± 0.005
2019 Dec 01.945	582.955	LT IO:O	i'	1×120	14.520 ± 0.006
2019 Dec 01.946	582.956	LT IO:O	i'	1×120	14.574 ± 0.006
2019 Dec 01.948	582.958	LT IO:O	i'	1×120	14.609 ± 0.005
2019 Dec 01.950	582.960	LT IO:O	i'	1×120	14.595 ± 0.006
2019 Dec 01.951	582.961	LT IO:O	i'	1×120	14.657 ± 0.006
2019 Dec 01.953	582.963	LT IO:O	i'	1×120	14.792 ± 0.005
2019 Dec 01.954	582.964	LT IO:O	i'	1×120	14.666 ± 0.006
2019 Dec 01.956	582.966	LT IO:O	i'	1×120	14.542 ± 0.005
2019 Dec 01.958	582.968	LT IO:O	i'	1×120	14.602 ± 0.005
2019 Dec 01.959	582.969	LT IO:O	i'	1×120	14.535 ± 0.006
2019 Dec 01.961	582.971	LT IO:O	i'	1×120	14.573 ± 0.006
2019 Dec 01.962	582.972	LT IO:O	i'	1×120	14.583 ± 0.005
2019 Dec 01.964	582.974	LT IO:O	i'	1×120	14.546 ± 0.006
2019 Dec 01.966	582.976	LT IO:O	i'	1×120	14.588 ± 0.006
2019 Dec 01.967	582.977	LT IO:O	i'	1×120	14.595 ± 0.006
2019 Dec 01.969	582.979	LT IO:O	i'	1×120	14.504 ± 0.005
2019 Dec 01.970	582.980	LT IO:O	i'	1×120	14.642 ± 0.006

Continued on next page

Table A.3 – continued from previous page

Date (UT)	Δ t / days	Telescope & Instrument	Filter	Exp. time /s	Photometry /mag
2019 Dec 01.972	582.982	LT IO:O	i'	1×120	14.479 ± 0.006
2019 Dec 01.999	583.010	LT IO:O	i'	1×120	14.446 ± 0.006
2019 Dec 02.001	583.011	LT IO:O	i'	1×120	14.591 ± 0.006
2019 Dec 02.003	583.013	LT IO:O	i'	1×120	14.509 ± 0.006
2019 Dec 02.005	583.015	LT IO:O	i'	1×120	14.625 ± 0.006
2019 Dec 02.006	583.016	LT IO:O	i'	1×120	14.551 ± 0.006
2019 Dec 02.008	583.018	LT IO:O	i'	1×120	14.643 ± 0.006
2019 Dec 02.009	583.019	LT IO:O	i'	1×120	14.530 ± 0.006
2019 Dec 02.011	583.021	LT IO:O	i'	1×120	14.622 ± 0.006
2019 Dec 02.013	583.023	LT IO:O	i'	1×120	14.474 ± 0.005
2019 Dec 02.014	583.024	LT IO:O	i'	1×120	14.640 ± 0.006
2019 Dec 02.016	583.026	LT IO:O	i'	1×120	14.585 ± 0.006
2019 Dec 02.017	583.027	LT IO:O	i'	1×120	14.560 ± 0.006
2019 Dec 02.019	583.029	LT IO:O	i'	1×120	14.568 ± 0.006
2019 Dec 02.021	583.031	LT IO:O	i'	1×120	14.613 ± 0.006
2019 Dec 02.022	583.032	LT IO:O	i'	1×120	14.609 ± 0.006
2019 Dec 02.024	583.034	LT IO:O	i'	1×120	14.591 ± 0.006
2019 Dec 02.025	583.035	LT IO:O	i'	1×120	14.456 ± 0.006
2019 Dec 02.027	583.037	LT IO:O	i'	1×120	14.734 ± 0.006
2019 Dec 02.029	583.039	LT IO:O	i'	1×120	14.539 ± 0.006
2019 Dec 02.030	583.040	LT IO:O	i'	1×120	14.569 ± 0.006
2019 Dec 02.058	583.068	LT IO:O	i'	1×120	14.496 ± 0.006
2019 Dec 02.060	583.070	LT IO:O	i'	1×120	14.444 ± 0.006
2019 Dec 02.061	583.071	LT IO:O	i'	1×120	14.532 ± 0.006
2019 Dec 02.063	583.073	LT IO:O	i'	1×120	14.552 ± 0.005
2019 Dec 02.064	583.074	LT IO:O	i'	1×120	14.502 ± 0.005
2019 Dec 02.066	583.076	LT IO:O	i'	1×120	14.525 ± 0.005
2019 Dec 02.068	583.078	LT IO:O	i'	1×120	14.529 ± 0.005
2019 Dec 02.069	583.079	LT IO:O	i'	1×120	14.552 ± 0.005
2019 Dec 02.071	583.081	LT IO:O	i'	1×120	14.436 ± 0.005
2019 Dec 02.073	583.083	LT IO:O	i'	1×120	14.521 ± 0.005

Continued on next page

Table A.3 – continued from previous page

Date (UT)	Δ t / days	Telescope & Instrument	Filter	Exp. time /s	Photometry /mag
2019 Dec 02.074	583.084	LT IO:O	i'	1×120	14.596 ± 0.005
2019 Dec 02.076	583.086	LT IO:O	i'	1×120	14.558 ± 0.006
2019 Dec 02.077	583.087	LT IO:O	i'	1×120	14.381 ± 0.005
2019 Dec 02.079	583.089	LT IO:O	i'	1×120	14.592 ± 0.006
2019 Dec 02.081	583.091	LT IO:O	i'	1×120	14.585 ± 0.006
2019 Dec 02.082	583.092	LT IO:O	i'	1×120	14.542 ± 0.005
2019 Dec 02.084	583.094	LT IO:O	i'	1×120	14.414 ± 0.006
2019 Dec 02.085	583.095	LT IO:O	i'	1×120	14.520 ± 0.006
2019 Dec 02.087	583.097	LT IO:O	i'	1×120	14.429 ± 0.006
2019 Dec 02.089	583.099	LT IO:O	i'	1×120	14.373 ± 0.005
2019 Dec 02.114	583.124	LT IO:O	i'	1×120	14.517 ± 0.006
2019 Dec 02.116	583.126	LT IO:O	i'	1×120	14.504 ± 0.006
2019 Dec 02.117	583.127	LT IO:O	i'	1×120	14.576 ± 0.006
2019 Dec 02.119	583.129	LT IO:O	i'	1×120	14.467 ± 0.007
2019 Dec 02.121	583.131	LT IO:O	i'	1×120	14.589 ± 0.006
2019 Dec 02.122	583.132	LT IO:O	i'	1×120	14.586 ± 0.006
2019 Dec 02.124	583.134	LT IO:O	i'	1×120	14.470 ± 0.005
2019 Dec 02.125	583.135	LT IO:O	i'	1×120	14.539 ± 0.005
2019 Dec 02.127	583.137	LT IO:O	i'	1×120	14.516 ± 0.006
2019 Dec 02.129	583.139	LT IO:O	i'	1×120	14.686 ± 0.007
2019 Dec 02.130	583.140	LT IO:O	i'	1×120	14.601 ± 0.006
2019 Dec 02.132	583.142	LT IO:O	i'	1×120	14.628 ± 0.006
2019 Dec 02.133	583.143	LT IO:O	i'	1×120	14.530 ± 0.006
2019 Dec 02.135	583.145	LT IO:O	i'	1×120	14.669 ± 0.006
2019 Dec 02.137	583.147	LT IO:O	i'	1×120	14.736 ± 0.005
2019 Dec 02.138	583.148	LT IO:O	i'	1×120	14.667 ± 0.006
2019 Dec 02.140	583.150	LT IO:O	i'	1×120	14.671 ± 0.006
2019 Dec 02.142	583.152	LT IO:O	i'	1×120	14.625 ± 0.006
2019 Dec 02.143	583.153	LT IO:O	i'	1×120	14.666 ± 0.006
2019 Dec 02.145	583.155	LT IO:O	i'	1×120	14.582 ± 0.005
2019 Dec 02.196	583.206	LT IO:O	i'	1×120	14.439 ± 0.005

Continued on next page

Table A.3 – continued from previous page

Date (UT)	Δ t / days	Telescope & Instrument	Filter	Exp. time /s	Photometry /mag
2019 Dec 02.197	583.207	LT IO:O	i'	1×120	14.531 ± 0.005
2019 Dec 02.199	583.209	LT IO:O	i'	1×120	14.446 ± 0.006
2019 Dec 02.201	583.211	LT IO:O	i'	1×120	14.527 ± 0.005
2019 Dec 02.202	583.212	LT IO:O	i'	1×120	14.425 ± 0.006
2019 Dec 02.204	583.214	LT IO:O	i'	1×120	14.128 ± 0.008
2019 Dec 02.205	583.215	LT IO:O	i'	1×120	14.126 ± 0.010
2019 Dec 02.207	583.217	LT IO:O	i'	1×120	14.156 ± 0.010
2019 Dec 02.209	583.219	LT IO:O	i'	1×120	14.106 ± 0.010
2019 Dec 02.210	583.220	LT IO:O	i'	1×120	14.091 ± 0.008
2019 Dec 02.212	583.222	LT IO:O	i'	1×120	14.141 ± 0.011
2019 Dec 02.214	583.224	LT IO:O	i'	1×120	14.173 ± 0.009
2019 Dec 02.215	583.225	LT IO:O	i'	1×120	14.152 ± 0.011
2019 Dec 02.217	583.227	LT IO:O	i'	1×120	14.160 ± 0.009
2019 Dec 02.218	583.228	LT IO:O	i'	1×120	14.170 ± 0.010
2019 Dec 02.220	583.230	LT IO:O	i'	1×120	14.209 ± 0.011
2019 Dec 02.222	583.232	LT IO:O	i'	1×120	14.175 ± 0.010
2019 Dec 02.223	583.233	LT IO:O	i'	1×120	14.198 ± 0.010
2019 Dec 02.225	583.235	LT IO:O	i'	1×120	14.187 ± 0.010
2019 Dec 02.226	583.236	LT IO:O	i'	1×120	14.179 ± 0.011
2019 Dec 09.911	590.921	LT IO:O	i'	1×60	14.338 ± 0.007
2019 Dec 09.912	590.922	LT IO:O	i'	1×60	14.331 ± 0.007
2019 Dec 09.913	590.923	LT IO:O	i'	1×60	14.322 ± 0.005
2020 Aug 31.177	856.187	LT IO:O	i'	3×120	14.509 ± 0.006
2021 Feb 02.879	1011.889	LT IO:O	i'	3×180	14.329 ± 0.006
2018 Jul 21.198	84.208	LT IO:O	z'	3×30	13.075 ± 0.008
2018 Jul 22.222	85.232	LT IO:O	z'	3×30	13.087 ± 0.008
2018 Jul 23.199	86.209	LT IO:O	z'	3×30	13.097 ± 0.007
2018 Jul 24.191	87.201	LT IO:O	z'	3×30	13.121 ± 0.006
2018 Jul 25.187	88.197	LT IO:O	z'	3×30	13.224 ± 0.006
2018 Jul 26.196	89.206	LT IO:O	z'	3×30	13.200 ± 0.010
2018 Jul 27.187	90.197	LT IO:O	z'	3×30	13.136 ± 0.011

Continued on next page

Table A.3 – continued from previous page

Date (UT)	Δ t / days	Telescope & Instrument	Filter	Exp. time /s	Photometry /mag
2018 Jul 28.181	91.191	LT IO:O	z'	3×30	13.283 ± 0.007
2018 Jul 29.180	92.190	LT IO:O	z'	3×30	13.300 ± 0.010
2018 Jul 31.174	94.184	LT IO:O	z'	3×30	13.317 ± 0.007
2018 Aug 01.188	95.198	LT IO:O	z'	3×30	13.338 ± 0.009
2018 Aug 02.164	96.174	LT IO:O	z'	3×30	13.253 ± 0.007
2018 Aug 03.163	97.173	LT IO:O	z'	3×30	13.406 ± 0.007
2018 Aug 06.154	100.164	LT IO:O	z'	3×30	13.410 ± 0.009
2018 Aug 08.170	102.180	LT IO:O	z'	3×30	13.449 ± 0.007
2018 Aug 10.176	104.186	LT IO:O	z'	3×30	13.467 ± 0.006
2018 Aug 13.178	107.188	LT IO:O	z'	3×30	13.563 ± 0.014
2018 Aug 16.128	110.138	LT IO:O	z'	3×30	13.510 ± 0.007
2018 Aug 19.171	113.181	LT IO:O	z'	3×30	13.482 ± 0.008
2018 Aug 22.223	116.233	LT IO:O	z'	3×30	13.424 ± 0.007
2018 Aug 25.103	119.113	LT IO:O	z'	3×30	13.537 ± 0.006
2018 Aug 28.113	122.123	LT IO:O	z'	3×30	13.460 ± 0.008
2018 Aug 31.090	125.100	LT IO:O	z'	3×30	13.495 ± 0.007
2018 Sep 03.079	128.089	LT IO:O	z'	3×30	13.534 ± 0.007
2018 Sep 06.071	131.081	LT IO:O	z'	3×30	13.574 ± 0.008
2018 Sep 09.060	134.070	LT IO:O	z'	3×30	13.677 ± 0.007
2018 Sep 12.068	137.078	LT IO:O	z'	3×30	13.701 ± 0.008
2018 Sep 18.091	143.101	LT IO:O	z'	3×30	13.720 ± 0.006
2018 Sep 23.023	148.033	LT IO:O	z'	3×30	13.742 ± 0.012
2018 Sep 26.019	151.029	LT IO:O	z'	3×30	13.785 ± 0.008
2018 Sep 29.062	154.072	LT IO:O	z'	3×30	13.786 ± 0.007
2018 Oct 02.018	157.028	LT IO:O	z'	3×30	13.874 ± 0.006
2018 Nov 01.117	187.126	LT IO:O	z'	3×30	14.032 ± 0.007
2018 Nov 08.165	194.175	LT IO:O	z'	3×30	14.009 ± 0.007
2018 Nov 16.123	202.133	LT IO:O	z'	3×30	14.015 ± 0.007
2018 Nov 26.029	212.039	LT IO:O	z'	3×30	13.965 ± 0.007
2018 Dec 10.070	226.080	LT IO:O	z'	3×30	14.004 ± 0.007
2018 Dec 15.969	231.979	LT IO:O	z'	3×30	14.009 ± 0.008

Continued on next page

Table A.3 – continued from previous page

Date (UT)	Δ t / days	Telescope & Instrument	Filter	Exp. time /s	Photometry /mag
2018 Dec 22.845	238.855	LT IO:O	z'	3×30	14.108 ± 0.011
2018 Dec 28.899	244.909	LT IO:O	z'	3×30	14.123 ± 0.010
2019 Jan 04.925	251.935	LT IO:O	z'	3×30	14.106 ± 0.006
2019 Jan 10.978	257.988	LT IO:O	z'	3×30	14.107 ± 0.007
2019 Jan 19.993	267.003	LT IO:O	z'	3×30	14.015 ± 0.007
2019 Jan 25.908	272.918	LT IO:O	z'	3×30	14.000 ± 0.006
2019 Jan 31.944	278.954	LT IO:O	z'	3×30	13.812 ± 0.007
2019 Feb 06.894	284.904	LT IO:O	z'	3×30	14.043 ± 0.009
2019 Feb 12.880	290.890	LT IO:O	z'	3×30	14.095 ± 0.007
2019 Feb 19.904	297.914	LT IO:O	z'	3×30	14.138 ± 0.013
2019 Feb 28.894	306.904	LT IO:O	z'	3×30	14.127 ± 0.006
2019 Mar 16.852	322.862	LT IO:O	z'	3×30	14.073 ± 0.007
2019 Apr 08.864	345.874	LT IO:O	z'	3×30	14.111 ± 0.007
2019 Apr 25.857	362.867	LT IO:O	z'	3×30	14.117 ± 0.008
2019 Jul 19.220	447.230	LT IO:O	z'	3×30	14.038 ± 0.007
2019 Aug 01.224	460.234	LT IO:O	z'	3×30	14.043 ± 0.006
2019 Aug 19.131	478.141	LT IO:O	z'	3×30	14.014 ± 0.007
2019 Sep 14.122	504.132	LT IO:O	z'	3×60	14.163 ± 0.013
2019 Oct 14.986	534.996	LT IO:O	z'	3×60	13.959 ± 0.008
2019 Nov 16.946	567.956	LT IO:O	z'	3×60	13.783 ± 0.007
2019 Dec 09.914	590.924	LT IO:O	z'	3×60	13.991 ± 0.007
2020 Aug 31.182	856.192	LT IO:O	z'	3×120	14.165 ± 0.006
2021 Feb 02.907	1011.917	LT IO:O	z'	3×180	14.053 ± 0.006
2018 Jul 20.155	83.165	Swift UVOT	uvw1	252	16.708 ± 0.056
2018 Jul 26.804	89.814	Swift UVOT	uvw1	325	16.812 ± 0.054
2018 Jul 27.170	90.180	Swift UVOT	uvw1	523	16.934 ± 0.052
2018 Jul 27.934	90.944	Swift UVOT	uvw1	325	17.062 ± 0.056
2018 Aug 03.207	97.217	Swift UVOT	uvw1	632	17.257 ± 0.053
2018 Aug 18.651	112.661	Swift UVOT	uvw1	382	17.476 ± 0.058
2018 Aug 19.773	113.783	Swift UVOT	uvw1	195	17.522 ± 0.067
2018 Aug 24.335	118.345	Swift UVOT	uvw1	581	17.531 ± 0.055

Continued on next page

Table A.3 – continued from previous page

Date (UT)	Δ t / days	Telescope & Instrument	Filter	Exp. time /s	Photometry /mag
2018 Aug 31.436	125.446	Swift UVOT	uvw1	669	17.609 ± 0.054
2018 Sep 08.004	133.014	Swift UVOT	uvw1	480	17.878 ± 0.060
2018 Sep 14.052	139.062	Swift UVOT	uvw1	591	17.937 ± 0.058
2018 Sep 21.091	146.101	Swift UVOT	uvw1	595	18.053 ± 0.059
2018 Sep 28.297	153.307	Swift UVOT	uvw1	862	17.996 ± 0.055
2018 Oct 12.743	167.753	Swift UVOT	uvw1	702	18.242 ± 0.059
2018 Oct 26.618	181.628	Swift UVOT	uvw1	686	18.262 ± 0.060
2018 Nov 09.801	195.811	Swift UVOT	uvw1	360	18.399 ± 0.063
2018 Nov 23.120	209.130	Swift UVOT	uvw1	701	18.365 ± 0.060
2018 Dec 07.587	223.597	Swift UVOT	uvw1	256	18.417 ± 0.080
2018 Dec 11.436	227.446	Swift UVOT	uvw1	428	18.440 ± 0.069
2018 Dec 21.095	237.105	Swift UVOT	uvw1	852	18.280 ± 0.057
2019 Jan 04.516	251.526	Swift UVOT	uvw1	502	18.529 ± 0.068
2019 Jan 18.095	265.105	Swift UVOT	uvw1	607	18.261 ± 0.061
2019 Feb 02.431	280.441	Swift UVOT	uvw1	644	18.620 ± 0.065
2019 Feb 07.473	285.483	Swift UVOT	uvw1	622	18.373 ± 0.062
2019 Feb 15.350	293.360	Swift UVOT	uvw1	374	18.654 ± 0.076
2019 Feb 21.187	299.197	Swift UVOT	uvw1	89	18.422 ± 0.121
2019 Mar 07.635	313.645	Swift UVOT	uvw1	607	18.412 ± 0.063
2019 Mar 21.045	327.055	Swift UVOT	uvw1	473	18.202 ± 0.064
2019 Apr 04.198	341.208	Swift UVOT	uvw1	757	18.607 ± 0.063
2019 Apr 18.782	355.792	Swift UVOT	uvw1	689	18.396 ± 0.061
2019 Apr 24.657	361.667	Swift UVOT	uvw1	740	18.512 ± 0.062
2019 Jul 21.133	449.143	Swift UVOT	uvw1	354	18.371 ± 0.073
2019 Aug 18.757	477.767	Swift UVOT	uvw1	581	18.285 ± 0.063
2019 Sep 16.768	506.778	Swift UVOT	uvw1	625	18.439 ± 0.064
2019 Oct 14.722	534.732	Swift UVOT	uvw1	283	18.470 ± 0.079
2019 Nov 14.446	565.456	Swift UVOT	uvw1	592	18.214 ± 0.061
2019 Dec 09.235	590.245	Swift UVOT	uvw1	510	18.158 ± 0.062
2020 Jan 12.730	624.740	Swift UVOT	uvw1	319	18.267 ± 0.072
2020 Feb 12.130	655.140	Swift UVOT	uvw1	288	18.451 ± 0.079

Continued on next page

Table A.3 – continued from previous page

Date (UT)	Δ t / days	Telescope & Instrument	Filter	Exp. time /s	Photometry /mag
2020 Mar 12.123	684.133	Swift UVOT	uvw1	317	18.258 ± 0.072
2020 Apr 12.358	715.368	Swift UVOT	uvw1	292	18.053 ± 0.070
2020 Aug 24.436	849.446	Swift UVOT	uvw1	331	18.405 ± 0.074
2018 Jul 20.152	83.162	Swift UVOT	uvm2	252	18.676 ± 0.102
2018 Jul 27.167	90.177	Swift UVOT	uvm2	609	18.820 ± 0.079
2018 Jul 27.918	90.928	Swift UVOT	uvm2	323	19.037 ± 0.105
2018 Aug 03.207	97.217	Swift UVOT	uvm2	616	19.276 ± 0.091
2018 Aug 18.649	112.659	Swift UVOT	uvm2	377	19.229 ± 0.107
2018 Aug 19.771	113.781	Swift UVOT	uvm2	156	19.383 ± 0.166
2018 Aug 24.331	118.341	Swift UVOT	uvm2	657	19.365 ± 0.091
2018 Aug 31.432	125.442	Swift UVOT	uvm2	644	19.338 ± 0.091
2018 Sep 08.003	133.013	Swift UVOT	uvm2	538	19.729 ± 0.113
2018 Sep 14.048	139.058	Swift UVOT	uvm2	551	19.664 ± 0.110
2018 Sep 21.087	146.097	Swift UVOT	uvm2	648	19.947 ± 0.115
2018 Sep 28.294	153.304	Swift UVOT	uvm2	868	19.999 ± 0.105
2018 Oct 12.739	167.749	Swift UVOT	uvm2	618	20.045 ± 0.121
2018 Oct 26.614	181.624	Swift UVOT	uvm2	627	20.170 ± 0.127
2018 Nov 09.798	195.808	Swift UVOT	uvm2	341	20.184 ± 0.127
2018 Nov 23.116	209.126	Swift UVOT	uvm2	625	20.082 ± 0.122
2018 Dec 07.586	223.596	Swift UVOT	uvm2	238	20.218 ± 0.201
2018 Dec 11.434	227.444	Swift UVOT	uvm2	278	19.961 ± 0.166
2018 Dec 21.092	237.102	Swift UVOT	uvm2	733	20.102 ± 0.116
2019 Jan 04.514	251.524	Swift UVOT	uvm2	466	20.452 ± 0.165
2019 Jan 18.092	265.102	Swift UVOT	uvm2	642	20.045 ± 0.120
2019 Feb 02.429	280.439	Swift UVOT	uvm2	691	20.616 ± 0.150
2019 Feb 07.472	285.482	Swift UVOT	uvm2	647	20.245 ± 0.130
2019 Feb 15.346	293.356	Swift UVOT	uvm2	378	20.214 ± 0.163
2019 Feb 21.186	299.196	Swift UVOT	uvm2	108	20.082 ± 0.277
2019 Mar 07.632	313.642	Swift UVOT	uvm2	613	20.468 ± 0.151
2019 Mar 21.042	327.052	Swift UVOT	uvm2	434	20.320 ± 0.163
2019 Apr 04.194	341.204	Swift UVOT	uvm2	761	20.402 ± 0.132

Continued on next page

Table A.3 – continued from previous page

Date (UT)	Δ t / days	Telescope & Instrument	Filter	Exp. time /s	Photometry /mag
2019 Apr 18.780	355.790	Swift UVOT	uvm2	533	20.287 ± 0.146
2019 Apr 24.654	361.664	Swift UVOT	uvm2	615	20.145 ± 0.129
2019 Jul 21.263	449.273	Swift UVOT	uvm2	474	20.247 ± 0.154
2019 Aug 18.755	477.765	Swift UVOT	uvm2	548	19.987 ± 0.128
2019 Sep 16.765	506.775	Swift UVOT	uvm2	465	20.229 ± 0.138
2019 Oct 14.749	534.759	Swift UVOT	uvm2	451	20.462 ± 0.174
2019 Nov 14.442	565.452	Swift UVOT	uvm2	567	19.904 ± 0.118
2019 Dec 09.229	590.239	Swift UVOT	uvm2	475	19.845 ± 0.125
2020 Jan 12.728	624.738	Swift UVOT	uvm2	319	19.911 ± 0.152
2020 Feb 12.128	655.138	Swift UVOT	uvm2	288	20.067 ± 0.173
2020 Mar 12.121	684.131	Swift UVOT	uvm2	317	20.293 ± 0.186
2020 Apr 12.356	715.366	Swift UVOT	uvm2	292	19.751 ± 0.150
2020 Aug 24.434	849.444	Swift UVOT	uvm2	331	20.176 ± 0.170
2018 Jul 20.146	83.156	Swift UVOT	uvw2	252	17.863 ± 0.079
2018 Jul 26.787	89.797	Swift UVOT	uvw2	572	18.063 ± 0.072
2018 Jul 27.164	90.174	Swift UVOT	uvw2	609	18.239 ± 0.073
2018 Aug 03.204	97.214	Swift UVOT	uvw2	616	18.484 ± 0.075
2018 Aug 10.606	104.616	Swift UVOT	uvw2	48	18.802 ± 0.189
2018 Aug 18.617	112.627	Swift UVOT	uvw2	581	18.679 ± 0.078
2018 Aug 19.769	113.779	Swift UVOT	uvw2	159	18.948 ± 0.121
2018 Aug 24.327	118.337	Swift UVOT	uvw2	657	18.736 ± 0.077
2018 Aug 31.428	125.438	Swift UVOT	uvw2	644	18.825 ± 0.079
2018 Sep 08.002	133.012	Swift UVOT	uvw2	538	19.085 ± 0.087
2018 Sep 14.045	139.055	Swift UVOT	uvw2	551	19.118 ± 0.087
2018 Sep 21.084	146.094	Swift UVOT	uvw2	648	19.165 ± 0.084
2018 Sep 28.291	153.301	Swift UVOT	uvw2	868	19.232 ± 0.080
2018 Oct 12.735	167.745	Swift UVOT	uvw2	616	19.323 ± 0.088
2018 Oct 26.610	181.620	Swift UVOT	uvw2	627	19.470 ± 0.091
2018 Nov 09.796	195.806	Swift UVOT	uvw2	341	19.508 ± 0.092
2018 Nov 23.112	209.122	Swift UVOT	uvw2	625	19.597 ± 0.095
2018 Dec 07.584	223.594	Swift UVOT	uvw2	238	19.643 ± 0.134

Continued on next page

Table A.3 – continued from previous page

Date (UT)	Δ t / days	Telescope & Instrument	Filter	Exp. time /s	Photometry /mag
2018 Dec 11.432	227.442	Swift UVOT	uvw2	278	19.488 ± 0.120
2018 Dec 21.089	237.099	Swift UVOT	uvw2	733	19.466 ± 0.088
2019 Jan 04.489	251.499	Swift UVOT	uvw2	547	19.561 ± 0.097
2019 Jan 18.088	265.098	Swift UVOT	uvw2	642	19.360 ± 0.089
2019 Feb 02.427	280.437	Swift UVOT	uvw2	691	19.870 ± 0.101
2019 Feb 07.470	285.480	Swift UVOT	uvw2	647	19.672 ± 0.097
2019 Feb 15.341	293.351	Swift UVOT	uvw2	378	19.832 ± 0.122
2019 Feb 21.184	299.194	Swift UVOT	uvw2	108	19.891 ± 0.214
2019 Mar 07.628	313.638	Swift UVOT	uvw2	613	19.965 ± 0.111
2019 Mar 21.039	327.049	Swift UVOT	uvw2	434	19.509 ± 0.104
2019 Apr 04.189	341.199	Swift UVOT	uvw2	761	19.784 ± 0.096
2019 Apr 18.778	355.788	Swift UVOT	uvw2	533	19.563 ± 0.100
2019 Apr 24.651	361.661	Swift UVOT	uvw2	616	19.651 ± 0.098
2019 Jul 21.262	449.272	Swift UVOT	uvw2	491	19.705 ± 0.109
2019 Aug 18.753	477.763	Swift UVOT	uvw2	548	19.455 ± 0.096
2019 Sep 16.761	506.771	Swift UVOT	uvw2	465	19.589 ± 0.098
2019 Oct 14.747	534.757	Swift UVOT	uvw2	634	19.683 ± 0.097
2019 Nov 14.439	565.449	Swift UVOT	uvw2	567	19.256 ± 0.089
2019 Dec 09.223	590.233	Swift UVOT	uvw2	475	19.285 ± 0.094
2020 Jan 12.724	624.734	Swift UVOT	uvw2	319	19.342 ± 0.108
2020 Feb 12.124	655.134	Swift UVOT	uvw2	288	19.601 ± 0.125
2020 Mar 12.117	684.127	Swift UVOT	uvw2	317	19.293 ± 0.107
2020 Apr 12.353	715.363	Swift UVOT	uvw2	292	19.188 ± 0.108
2020 Aug 24.430	849.440	Swift UVOT	uvw2	331	19.722 ± 0.122

Table A.4: AAVSO observers, including their country and astronomical society (if available). Appears as Table A4 in Murphy-Glaysher et al. (2022) ['V392 Persei: A γ-ray bright nova eruption from a known dwarf nova', Murphy-Glaysher et al., Mon. Not. R. Astron. Soc., 514, 6183, 2022 DOI `https://doi.org/10.1093/mnras/stac1577`].

Observer code	Name	Country	Society
AAVSO AFSA	Soldán Alfaro, Francisco	ES	AAVSO
AAVSO ATE	Arranz, Teofilo	ES	AAVSO
AAVSO BDG	Boyd, David	GB	BAA-VSS
AAVSO BMSA	Bundas, Matthew	US	AAVSO
AAVSO BRIA	Biernikowicz, Richard	PL	AAVSO
AAVSO CDJA	Coulter, Daniel	US	AAVSO
AAVSO DKS	Dvorak, Shawn	US	AAVSO
AAVSO DPA	Diepvens, Alfons	BE	VVS
AAVSO EHEA	Eggenstein, Heinz-Bernd	DE	AAVSO
AAVSO ETOA	Eenmae, Tonis	EE	AAVSO
AAVSO FRL	Fournier, Ronald	US	AAVSO
AAVSO GJED	Gout, Jean-Francois	US	AAVSO
AAVSO JDAD	Janzen, Daryl	CA	
AAVSO JPG	Jordanov, Penko	BG	AAVSO
AAVSO KHAB	Kiiskinen, Harri	FI	URSA
AAVSO LDJ	Lane, David	CA	RASC
AAVSO LRCA	Larochelle, Riley	CA	AAVSO
AAVSO MDYA	Mankel, Dylan	US	AAVSO
AAVSO MIW	Miller, Ian	GB	BAA-VSS
AAVSO MMAO	Morales Aimar, Mario	ES	AAVSO
AAVSO MRV	Modic, Robert	US	AAVSO
AAVSO MUY	Muyllaert, Eddy	BE	
AAVSO NRNA	Naves, Ramon	ES	AAVSO
AAVSO OAR	Oksanen, Arto	FI	URSA
AAVSO ODEA	O'Keeffe, Derek	IE	AAVSO
AAVSO PMAK	Pyatnytskyy, Maksym	UA	AAVSO
AAVSO RBRB	Rodgers, Brennan	CA	
AAVSO RRIB	Rast, Rina	CA	RASC
AAVSO RZD	Rodriguez Perez, Diego	ES	AFOEV

Continued on next page

Table A.4 – continued from previous page

Observer code	Name	Country	Society
AAVSO SDM	Schwendeman, Erik	US	AAVSO
AAVSO SFRA	Schorr, Frank	US	AAVSO
AAVSO SGEA	Stone, Geoffrey	US	AAVSO
AAVSO SHS	Sharpe, Steven	CA	AAVSO
AAVSO SSTA	Shadick, Stanley	CA	RASC
AAVSO STYA	Sove, Tylor	CA	
AAVSO TRT	Tordai, Tamás	HU	MCSE
AAVSO VMAG	Vrastak, Martin	SK	AAVSO
AAVSO VOL	Vollmann, Wolfgang	AT	AAVSO
AAVSO VRG	Venne, Roger	CA	AAVSO
AAVSO WKL	Wenzel, Klaus	DE	BAV

Table A.5: V392 Per light curve parameters, under the assumption that each can be modelled by up to six broken power laws of form $f \propto t^{\alpha}$, where $t_{\rm i}$ and $t_{\rm f}$ denote the initial and final extent of each power law, respectively, and D is the duration of each power law's dominance. Appears as Table A5 in Murphy-Glaysher et al. (2022) ['V392 Persei: A γ-ray bright nova eruption from a known dwarf nova', Murphy-Glaysher et al., Mon. Not. R. Astron. Soc., 514, 6183, 2022 DOI `https://doi.org/10.1093/mnras/stac1577`].

uvw2	α	$t_{\rm i}$ [d]	$t_{\rm f}$ [d]	D [d]	uvm2	α	$t_{\rm i}$ [d]	$t_{\rm f}$ [d]	D [d]
5	-1.66 ± 0.14	70.0	186.4	116.4	5	-1.64 ± 0.11	70.0	181.0	111.0
6	0	186.4	849.4	663.1	6	0	181.0	849.4	668.4
uvw1	α	$t_{\rm i}$ [d]	$t_{\rm f}$ [d]	D [d]	u' fit	α	$t_{\rm i}$ [d]	$t_{\rm f}$ [d]	D [d]
4	...	-	...	-	4	-1.93 ± 0.42	70.0	103.5	33.5
5	-1.82 ± 0.09	70.0	182.2	112.2	5	-1.60 ± 0.10	103.5	195.9	92.3
6	0	182.2	849.4	667.2	6	-0.01 ± 0.09	195.9	1011.9	816.0
B	α	$t_{\rm i}$ [d]	$t_{\rm f}$ [d]	D [d]	V	α	$t_{\rm i}$ [d]	$t_{\rm f}$ [d]	D [d]
1	-1.75 ± 0.04	0.0	5.6	5.6	1	-1.76 ± 0.07	0.0	5.3	5.3
2	-0.15 ± 0.18	5.6	9.0	3.3	2	-0.45 ± 0.09	5.3	10.2	4.9
3	-2.18 ± 0.08	9.0	58.2	49.2	3	-2.72 ± 0.05	10.2	14.6	4.4
4	-2.42 ± 0.53	70.0	95.3	25.3	4	-2.08 ± 0.04	14.6	98.5	84.0
5	-1.22 ± 0.07	95.3	218.4	123.2	5	-1.07 ± 0.05	98.5	220.4	121.8
6	-0.11 ± 0.10	218.4	1011.9	793.5	6	-0.12 ± 0.05	220.4	1011.9	791.5
r'	α	$t_{\rm i}$ [d]	$t_{\rm f}$ [d]	D [d]	i'	α	$t_{\rm i}$ [d]	$t_{\rm f}$ [d]	D [d]
1	-1.78 ± 0.80	0.0	5.1	5.1	1	-3.22 ± 0.37	0.0	3.9	3.9
2	-0.52 ± 0.18	5.1	11.2	6.1	2	-1.05 ± 0.27	3.9	12.7	8.8
3	-2.86 ± 0.12	11.2	24.9	13.7	3	-3.78 ± 0.18	12.7	23.2	10.5
4	-2.37 ± 0.05	33.9	100.1	66.2	4	-2.52 ± 0.20	63.4	96.5	33.1
5	-0.94 ± 0.09	100.1	232.5	132.4	5	-0.83 ± 0.10	96.5	232.6	136.1
6	-0.06 ± 0.04	232.5	1011.9	779.4	6	-0.017 ± 0.04	232.6	1011.9	779.3
z'	α	$t_{\rm i}$ [d]	$t_{\rm f}$ [d]	D [d]					
4	-1.92 ± 0.27	70.0	96.0	26.0					
5	-0.86 ± 0.06	96.0	200.5	104.5					
6	-0.06 ± 0.08	200.5	1011.9	811.5					

Table A.6: P Cygni velocities of Balmer line profiles from early time spectra of V392 Per. Appears as Table A6 in Murphy-Glaysher et al. (2022) ['V392 Persei: A γ-ray bright nova eruption from a known dwarf nova', Murphy-Glaysher et al., Mon. Not. R. Astron. Soc., 514, 6183, 2022 DOI `https://doi.org/10.1093/mnras/stac1577`].

Time / days	Hα Slow / km s^{-1}	Hα Fast / km s^{-1}	Hβ Slow / km s^{-1}	Hβ Fast / km s^{-1}	Hγ Slow / km s^{-1}	Hγ Fast / km s^{-1}
1.91	-2994 ± 23	-4960 ± 23	-3209 ± 31	-5061 ± 31	-3180 ± 35	-4873 ± 35
2.13	-3070 ± 32	-5053 ± 32	-3602 ± 43	-5459 ± 43	-3583 ± 48	-5035 ± 48
2.88	-3748 ± 23	-5485 ± 23	-3796 ± 31	-5153 ± 31	-3802 ± 35	-5046 ± 35
2.90	-3840 ± 23	-5600 ± 23	-3641 ± 31	-5153 ± 31	-3664 ± 35	-5046 ± 35
3.85	...	-4068 ± 23	...	-5153 ± 31	...	-5046 ± 35
3.87	...	-4092 ± 26	...	-3861 ± 36	...	-3716 ± 40
4.16	...	-3829 ± 40	...	-3781 ± 54	...	-3249 ± 61
4.80	...	...	...	-3905 ± 11	...	...
4.82	...	-4007 ± 8	...	...	...	...
4.87	-3958 ± 73	...	-3593 ± 49	-3988 ± 49	-3216 ± 55	-3659 ± 55
4.88	...	-4274 ± 23	...	-4073 ± 31	-3664 ± 35	-4320 ± 35
5.16	...	-4031 ± 42	...	-3770 ± 57	...	-3749 ± 64
5.86	...	-4137 ± 23	...	-3765 ± 31	...	-3698 ± 35
5.87	-4049 ± 73	...	-3232 ± 49	-3677 ± 49	-3452 ± 55	-3673 ± 55
5.90	...	-4137 ± 23	...	-3580 ± 31	...	-3456 ± 35
5.94	...	-3991 ± 43	...	-3520 ± 58	...	-3485 ± 65
6.13	-3937 ± 32	...	-3307 ± 43	-3782 ± 43	-3321 ± 48	-3757 ± 48
6.86	...	-3954 ± 23	...	-3641 ± 31	...	-3767 ± 35
6.87	-3931 ± 27	...	-3366 ± 22	-3820 ± 22	-3410 ± 24	-3724 ± 24
6.90	...	-4023 ± 23	...	-3580 ± 31	...	-3491 ± 35
6.96	...	-4017 ± 22	...	-3763 ± 30	...	-3570 ± 34
7.13	-3904 ± 32	...	-3356 ± 43	-3831 ± 43	-3346 ± 48	-3782 ± 48
7.84	-3815 ± 2	-3981 ± 2	-3441 ± 3	-3823 ± 3	...	...
7.88	...	-3986 ± 26	...	-3576 ± 36	...	-3317 ± 40
7.87	...	-3931 ± 23	...	-3580 ± 31	...	-3698 ± 35
8.13	...	...	-3352 ± 43	-3785 ± 43	-3300 ± 48	...
8.14	...	...	...	-3642 ± 52	...	-3576 ± 58
8.85	...	-3975 ± 2	-3333 ± 3	-3468 ± 3	...	...

Continued on next page

Table A.6 – continued from previous page

Time / days	Hα Slow / km s^{-1}	Hα Fast / km s^{-1}	Hβ Slow / km s^{-1}	Hβ Fast / km s^{-1}	Hγ Slow / km s^{-1}	Hγ Fast / km s^{-1}
8.88	...	-4137 ± 23	...	-3518 ± 31	...	-3422 ± 35
8.90	...	-4320 ± 23	...	-3518 ± 31	-3387 ± 35	-3871 ± 35
9.13	...	-4099 ± 37	...	-3709 ± 50	...	-3668 ± 56
9.80	...	-4099 ± 37	...	...	...	...
9.83	...	...	...	-3369 ± 11	...	...
9.87	...	...	...	-3394 ± 31	...	...
9.88	...	-4160 ± 23	-3549 ± 31	-4012 ± 31	...	-3456 ± 35
9.93	...	-4161 ± 22	...	-3683 ± 30	...	-3453 ± 34
9.93	...	-4228 ± 23	...	-3394 ± 31	...	-3525 ± 35

Table A.7: Dereddened line fluxes for Hα, Hβ, [O III] 5007 Å and [O III] 4959 Å. Appears as Table A7 in Murphy-Glaysher et al. (2022) ['V392 Persei: A γ-ray bright nova eruption from a known dwarf nova', Murphy-Glaysher et al., Mon. Not. R. Astron. Soc., 514, 6183, 2022 DOI `https://doi.org/10.1093/mnras/stac1577`].

Time / days	Hα Flux / erg cm^{-2} s^{-1}	Hβ Flux / erg cm^{-2} s^{-1}	[O III] 5007 Å Flux / erg cm^{-2} s^{-1}	[O III] 4959 Å Flux / erg cm^{-2} s^{-1}
4.9	$(3.219 \pm 0.060) \times 10^{-7}$	$(1.815 \pm 0.018) \times 10^{-7}$	...	...
5.9	$(2.514 \pm 0.042) \times 10^{-7}$	$(1.119 \pm 0.018) \times 10^{-7}$	...	...
6.9	$(2.739 \pm 0.031) \times 10^{-7}$	$(1.026 \pm 0.014) \times 10^{-7}$	...	...
76.2	$(6.852 \pm 0.133) \times 10^{-10}$	...	...	...
77.2	$(6.811 \pm 0.118) \times 10^{-10}$	$(9.516 \pm 0.867) \times 10^{-11}$	$(9.448 \pm 0.257) \times 10^{-10}$	$(2.724 \pm 0.171) \times 10^{-10}$
82.2	$(5.179 \pm 0.105) \times 10^{-10}$	$(1.426 \pm 0.061) \times 10^{-10}$	$(1.359 \pm 0.022) \times 10^{-9}$	$(4.131 \pm 0.126) \times 10^{-10}$
84.2	$(4.645 \pm 0.122) \times 10^{-10}$	$(1.349 \pm 0.095) \times 10^{-10}$	$(1.336 \pm 0.034) \times 10^{-9}$	$(4.053 \pm 0.185) \times 10^{-10}$
87.2	$(4.175 \pm 0.093) \times 10^{-10}$	$(1.512 \pm 0.089) \times 10^{-10}$	$(1.968 \pm 0.026) \times 10^{-9}$	$(6.061 \pm 0.197) \times 10^{-10}$
89.2	$(4.012 \pm 0.086) \times 10^{-10}$	$(1.126 \pm 0.084) \times 10^{-10}$	$(1.226 \pm 0.028) \times 10^{-9}$	$(4.014 \pm 0.171) \times 10^{-10}$
101.2	$(3.351 \pm 0.076) \times 10^{-10}$	$(8.151 \pm 0.595) \times 10^{-11}$	$(1.000 \pm 0.018) \times 10^{-9}$	$(3.169 \pm 0.103) \times 10^{-10}$
112.1	$(2.088 \pm 0.041) \times 10^{-10}$	$(5.775 \pm 0.440) \times 10^{-11}$	$(7.511 \pm 0.126) \times 10^{-10}$	$(2.621 \pm 0.074) \times 10^{-10}$
143.2	$(1.519 \pm 0.030) \times 10^{-10}$	...	...	...
157.0	$(9.964 \pm 0.282) \times 10^{-11}$	$(1.918 \pm 0.295) \times 10^{-11}$	$(4.670 \pm 0.073) \times 10^{-10}$	$(1.655 \pm 0.046) \times 10^{-10}$
186.2	$(7.052 \pm 0.239) \times 10^{-11}$	$(1.402 \pm 0.290) \times 10^{-11}$	$(3.556 \pm 0.069) \times 10^{-10}$	$(1.211 \pm 0.042) \times 10^{-10}$
212.1	...	$(1.259 \pm 0.268) \times 10^{-11}$	$(2.523 \pm 0.061) \times 10^{-10}$	$(8.952 \pm 0.361) \times 10^{-11}$
226.1	$(4.899 \pm 0.181) \times 10^{-11}$	...	...	...

Continued on next page

Table A.7 – continued from previous page

Time / days	Hα Flux / erg cm^{-2} s^{-1}	Hβ Flux / erg cm^{-2} s^{-1}	[O III] 5007 Å Flux / erg cm^{-2} s^{-1}	[O III] 4959 Å Flux / erg cm^{-2} s^{-1}
252.0	$(3.158 \pm 0.222) \times 10^{-11}$	...	...	...
253.0	$(3.306 \pm 0.222) \times 10^{-11}$	$(7.745 \pm 1.507) \times 10^{-12}$	$(1.464 \pm 0.035) \times 10^{-10}$	$(5.066 \pm 0.204) \times 10^{-11}$
306.9	$(2.588 \pm 0.237) \times 10^{-11}$	$(7.583 \pm 1.455) \times 10^{-12}$	$(9.551 \pm 0.344) \times 10^{-11}$	$(3.862 \pm 0.222) \times 10^{-11}$
345.9	$(1.904 \pm 0.153) \times 10^{-11}$	$(4.157 \pm 1.110) \times 10^{-12}$	$(5.929 \pm 0.284) \times 10^{-11}$	$(2.541 \pm 0.203) \times 10^{-11}$
448.2	$(8.407 \pm 0.958) \times 10^{-12}$	...	...	...
478.2	$(7.274 \pm 0.947) \times 10^{-12}$	...	...	...
504.1	$(8.252 \pm 1.004) \times 10^{-12}$	...	...	...
535.0	$(6.146 \pm 0.861) \times 10^{-12}$	...	...	...
568.1	$(5.209 \pm 0.690) \times 10^{-12}$	...	...	...
591.0	$(4.961 \pm 0.570) \times 10^{-12}$	...	...	...
854.2	$(4.541 \pm 0.278) \times 10^{-12}$	...	...	...

Table A.8: Dereddened line fluxes for [O III] 4363 Å, He I 6678 Å, He I 7065 Å and He II 4686 Å. Appears as Table A8 in Murphy-Glaysher et al. (2022) ['V392 Persei: A γ-ray bright nova eruption from a known dwarf nova', Murphy-Glaysher et al., Mon. Not. R. Astron. Soc., 514, 6183, 2022 DOI `https://doi.org/10.1093/mnras/stac1577`].

Time / days	[O III] 4363 Å flux / erg cm^{-2} s^{-1}	He I 6678 Å flux / erg cm^{-2} s^{-1}	He I 7065 Å flux / erg cm^{-2} s^{-1}	He II 4686 Å flux / erg cm^{-2} s^{-1}
4.9	...	$(5.303 \pm 0.011) \times 10^{-9}$	$(3.735 \pm 0.038) \times 10^{-8}$	...
5.9	...	$(2.763 \pm 0.003) \times 10^{-9}$	$(2.754 \pm 0.032) \times 10^{-8}$	...
6.9	...	$(2.696 \pm 0.002) \times 10^{-9}$	$(2.107 \pm 0.021) \times 10^{-8}$	...
76.2	...	$(5.266 \pm 0.051) \times 10^{-12}$	$(1.989 \pm 0.061) \times 10^{-10}$	...
77.2	$(1.757 \pm 0.327) \times 10^{-10}$	$(4.664 \pm 0.012) \times 10^{-12}$	$(1.694 \pm 0.032) \times 10^{-10}$	...
82.2	$(3.897 \pm 0.216) \times 10^{-10}$	$(2.741 \pm 0.053) \times 10^{-12}$	$(8.373 \pm 0.364) \times 10^{-11}$	$(1.089 \pm 0.102) \times 10^{-10}$
84.2	$(4.595 \pm 0.289) \times 10^{-10}$	...	$(6.934 \pm 0.383) \times 10^{-11}$	$(9.858 \pm 1.208) \times 10^{-11}$
87.2	$(4.752 \pm 0.256) \times 10^{-10}$	$(2.436 \pm 0.010) \times 10^{-12}$	$(1.164 \pm 0.028) \times 10^{-10}$	...
89.2	$(3.101 \pm 0.281) \times 10^{-10}$	$(2.647 \pm 0.178) \times 10^{-12}$	$(5.933 \pm 0.411) \times 10^{-11}$	$(8.481 \pm 0.815) \times 10^{-11}$
101.2	$(2.540 \pm 0.198) \times 10^{-10}$	$(9.985 \pm 0.090) \times 10^{-13}$	$(5.602 \pm 0.326) \times 10^{-11}$	$(4.667 \pm 0.592) \times 10^{-11}$
112.1	$(1.388 \pm 0.104) \times 10^{-10}$	$(1673.492 \pm 0.001) \times 10^{-15}$	$(2.990 \pm 0.126) \times 10^{-11}$	$(4.503 \pm 0.430) \times 10^{-11}$
143.2	...	$(2.021 \pm 0.006) \times 10^{-12}$	$(6.177 \pm 0.180) \times 10^{-11}$	...
157.0	$(6.512 \pm 0.806) \times 10^{-11}$	$(15.503 \pm 0.004) \times 10^{-13}$	$(1.902 \pm 0.109) \times 10^{-11}$	$(2.391 \pm 0.155) \times 10^{-11}$
186.2	$(3.598 \pm 0.608) \times 10^{-11}$	$(1311.492 \pm 0.002) \times 10^{-15}$	$(1.026 \pm 0.067) \times 10^{-11}$	$(2.069 \pm 0.088) \times 10^{-11}$
212.1	$(2.464 \pm 0.607) \times 10^{-11}$	$(106.25 \pm 0.004) \times 10^{-14}$	$(1.096 \pm 0.141) \times 10^{-11}$	$(1.718 \pm 0.148) \times 10^{-11}$
226.1	...	$(1.318 \pm 0.004) \times 10^{-12}$	$(3.454 \pm 0.101) \times 10^{-11}$	...

Continued on next page

Table A.8 – continued from previous page

Time / days	[O III] 4363 Å flux / erg cm^{-2} s^{-1}	He I 6678 Å flux / erg cm^{-2} s^{-1}	He I 7065 Å flux / erg cm^{-2} s^{-1}	He II 4686 Å flux / erg cm^{-2} s^{-1}
252.0	...	$(1.166 \pm 0.011) \times 10^{-12}$	$(4.338 \pm 0.191) \times 10^{-11}$	...
253.0	$< 2.777 \times 10^{-11}$	$(92.876 \pm 0.005) \times 10^{-14}$	$(9.729 \pm 0.751) \times 10^{-12}$	$(1.357 \pm 0.053) \times 10^{-11}$
306.9	$< 3.037 \times 10^{-11}$	$(9.262 \pm 0.346) \times 10^{-13}$	$(8.284 \pm 0.782) \times 10^{-12}$	$(1.338 \pm 0.063) \times 10^{-11}$
345.9	$< 2.514 \times 10^{-11}$	$(1.070 \pm 0.003) \times 10^{-12}$	...	$(1.281 \pm 0.089) \times 10^{-11}$
448.2	...	$(1.080 \pm 0.001) \times 10^{-12}$	...	$(9.430 \pm 0.762) \times 10^{-12}$
478.2	...	$(9.950 \pm 0.063) \times 10^{-13}$	...	$(9.566 \pm 0.445) \times 10^{-12}$
504.1	...	$(1.219 \pm 0.013) \times 10^{-12}$	...	$(8.227 \pm 0.714) \times 10^{-12}$
535.0	...	$(8.822 \pm 0.053) \times 10^{-13}$	...	$(9.503 \pm 0.670) \times 10^{-12}$
568.1	...	$(8.295 \pm 0.050) \times 10^{-13}$	...	$(9.666 \pm 0.348) \times 10^{-12}$
591.0	...	$(1.270 \pm 0.048) \times 10^{-12}$	...	$(1.248 \pm 0.132) \times 10^{-11}$
854.2	...	...	...	$(9.493 \pm 0.407) \times 10^{-12}$

Bibliography

Abdo A. A., et al., 2010, Science, 329, 817

Acciari V. A., et al., 2022, Nature Astronomy, 6, 689

Ackermann M., et al., 2014, Science, 345, 554

Adamakis S., Eyres S. P. S., Sarkar A., Walsh R. W., 2011, Mon. Not. R. Astron. Soc., 414, 2195

Albert A., et al., 2022, arXiv e-prints, p. arXiv:2201.10644

Álvarez-Hernández A., et al., 2021, Mon. Not. R. Astron. Soc., 507, 5805

Anupama G. C., 2008, in Evans A., Bode M. F., O'Brien T. J., Darnley M. J., eds, Astronomical Society of the Pacific Conference Series Vol. 401, RS Ophiuchi (2006) and the Recurrent Nova Phenomenon. p. 31

Atwood W. B., et al., 2009, Astrophys. J., 697, 1071

Austin S. J., Wagner R. M., Starrfield S., Shore S. N., Sonneborn G., Bertram R., 1996, Astronom. J., 111, 869

Aydi E., et al., 2018a, Mon. Not. R. Astron. Soc., 474, 2679

Aydi E., et al., 2018b, Mon. Not. R. Astron. Soc., 480, 572

Aydi E., et al., 2020a, Nature Astronomy, 4, 776

Aydi E., et al., 2020b, Astrophys. J., 905, 62

Bailer-Jones C. A. L., Rybizki J., Fouesneau M., Demleitner M., Andrae R., 2021, Astronom. J., 161, 147

Balick B., Frank A., 2002, Ann. Rev. A&A, 40, 439

Banerjee D. P. K., Joshi V., Venkataraman V., Ashok N. M., Marion G. H., Hsiao E. Y., Raj A., 2014, Astrophys. J. L., 785, L11

Barnsley R. M., Smith R. J., Steele I. A., 2012, Astronomische Nachrichten, 333, 101

Barthelmy S. D., et al., 2005, Space Sci. Rev., 120, 143

Beardmore A. P., et al., 2012, A&A, 545, A116

Bianchini A., Sabbadin F., Favero G. C., Dalmeri I., 1986, A&A, 160, 367

Blanton M. R., Roweis S., 2007, Astronom. J., 133, 734

Bode M. F., 2010, Astronomische Nachrichten, 331, 160

Bode M. F., Evans A., 2008, Classical Novae. Cambridge University Press, Cambridge

Bode M. F., Kahn F. D., 1985, Mon. Not. R. Astron. Soc., 217, 205

Bode M. F., Darnley M. J., Shafter A. W., Page K. L., Smirnova O., Anupama G. C., Hilton T., 2009, Astrophys. J., 705, 1056

Bollimpalli D. A., Hameury J. M., Lasota J. P., 2018, Mon. Not. R. Astron. Soc., 481, 5422

Boumis P., Akras S., Xilouris E. M., Mavromatakis F., Kapakos E., Papamastorakis J., Goudis C. D., 2006, Mon. Not. R. Astron. Soc., 367, 1551

Brandt T. D., Tojeiro R., Aubourg É., Heavens A., Jimenez R., Strauss M. A., 2010, Astronom. J., 140, 804

Brown T. M., et al., 2013, PASP, 125, 1031

Burrows D. N., et al., 2005, Space Sci. Rev., 120, 165

Buson S., Jean P., Cheung C. C., 2019, ATel, 13114, 1

Campbell W. W., 1893, Astronomische Nachrichten, 133, 337

Chambers K. C., Pan-STARRS Team 2016, in American Astronomical Society Meeting Abstracts #227. p. 324.07

Chesneau O., et al., 2012, A&A, 545, A63

Cheung C. C., Jean P., Shore S. N., 2014, ATel, 5879, 1

Cheung C. C., et al., 2016, The Astrophysical Journal, 826, 142

Cheung C. C., Ciprini S., Johnson T. J., 2021, ATel, 14834, 1

Chochol D., Hric L., Urban Z., Komzik R., Grygar J., Papousek J., 1993, A&A, 277, 103

Chochol D., Grygar J., Pribulla T., Komzik R., Hric L., Elkin V., 1997, A&A, 318, 908

Chomiuk L., Metzger B. D., Shen K. J., 2021a, Ann. Rev. A&A, 59

Chomiuk L., et al., 2021b, Astrophys. J. S., 257, 49

Clark D. H., Parkinson J. H., Stephenson F. R., 1977, Quarterly Journal R.A.S., 18, 443

Clayton D. D., 1981, Astrophys. J. L., 244, L97

Clayton D. D., Hoyle F., 1974, Astrophys. J. L., 187, L101

Cohen J. G., 1985, Astrophys. J., 292, 90

Copperwheat C. M., et al., 2011, Mon. Not. R. Astron. Soc., 413, 3068

Darnley M. J., 2018a, The Astronomer's Telegram, 11846, 1

Darnley M. J., 2018b, The Astronomer's Telegram, 11872, 1

Darnley M. J., 2021, in The Golden Age of Cataclysmic Variables and Related Objects V. p. 44 (arXiv:1912.13209), doi:10.22323/1.368.0044

Darnley M. J., Henze M., 2020, Advances in Space Research, 66, 1147

Darnley M. J., Starrfield S., 2018, Research Notes of the American Astronomical Society, 2, 24

Darnley M. J., Ribeiro V. A. R. M., Bode M. F., Hounsell R. A., Williams R. P., 2012, Astrophys. J., 746, 61

Darnley M. J., et al., 2016, Astrophys. J., 833, 149

Darnley M. J., et al., 2017, Astrophys. J., 849, 96

Darnley M. J., Copperwheat C. M., Harvey E. J., Healy M. W., 2018a, The Astronomer's Telegram, 11601

Darnley M. J., Page K. L., Beardmore A. P., Henze M., Starrfield S., 2018b, The Astronomer's Telegram, 11905, 1

Darnley M. J., et al., 2019, Nature, 565, 460

Della Valle M., Izzo L., 2020, Astron. Astrophys. Rev., 28, 3

Dominguez I., Hoflich P., Straniero O., 2001, The Astrophysical Journal, 557, 279

Downes R. A., Duerbeck H. W., 2000, Astronom. J., 120, 2007

Downes R. A., Shara M. M., 1993, PASP, 105, 127

Evans P. A., et al., 2009, Mon. Not. R. Astron. Soc., 397, 1177

Evans A., Gehrz R. D., Woodward C. E., Helton L. A., 2014, Mon. Not. R. Astron. Soc., 444, 1683

Evans A., Gehrz R. D., Woodward C. E., Sarre P. J., van Loon J. T., Helton L. A., Starrfield S., Eyres S. P. S., 2016, Mon. Not. R. Astron. Soc., 457, 2871

Eyres S. P. S., et al., 2018, Mon. Not. R. Astron. Soc., 481, 4931

Ferland G. J., Shields G. A., 1978, Astrophys. J., 226, 172

Ferland G. J., Korista K. T., Verner D. A., Ferguson J. W., Kingdon J. B., Verner E. M., 1998, PASP, 110, 761

Ferland G. J., et al., 2013, Revista Mexicana de Astronomía y Astrofísica, 49, 137

Ferland G. J., et al., 2017, Revista Mexicana de Astronomía y Astrofísica, 53, 385

Fiedler R. L., Jones T. W., 1980, Astrophys. J., 239, 253

Franckowiak A., Jean P., Wood M., Cheung C. C., Buson S., 2018, A&A, 609, A120

Frank A., Chen Z., Reichardt T., De Marco O., Blackman E., Nordhaus J., 2018, Galaxies, 6, 113

GLAST Facility Science Team Gehrels N., Michelson P., 1999, Astroparticle Physics, 11, 277

Gaia Collaboration 2018, VizieR Online Data Catalog, p. I/345

Gaia Collaboration et al., 2016, A&A, 595, A1

Gaia Collaboration et al., 2021, A&A, 649, A1

Gallagher J. S. I., Code A. D., 1974, Astrophys. J., 189, 303

Gehrels N., et al., 2004, Astrophys. J., 611, 1005

Gehrz R. D., Truran J. W., Williams R. E., Starrfield S., 1998, PASP, 110, 3

Gehrz R. D., et al., 2018, Astrophys. J., 858, 78

Gill C. D., O'Brien T. J., 1998, Mon. Not. R. Astron. Soc., 300, 221

Ginzburg S., Quataert E., 2021, Mon. Not. R. Astron. Soc., 507, 475

Godon P., Sion E. M., Balman Ş., Blair W. P., 2017, Astrophys. J., 846, 52

Gordon A. C., Aydi E., Page K. L., Li K.-L., Chomiuk L., Sokolovsky K. V., Mukai K., Seitz J., 2021, Astrophys. J., 910, 134

Green G. M., Schlafly E., Zucker C., Speagle J. S., Finkbeiner D., 2019, Astrophys. J., 887, 93

Güver T., Özel F., 2009, Mon. Not. R. Astron. Soc., 400, 2050

H. E. S. S. Collaboration et al., 2022, Science, 376, 77

Hachisu I., Kato M., 2006, Astrophys. J. S., 167, 59

Harvey E., Redman M. P., Boumis P., Akras S., 2016, A&A, 595, A64

Harvey E. J., Redman M. P., Darnley M. J., Williams S. C., Berdyugin A., Piirola V. E., Fitzgerald K. P., O'Connor E. G. P., 2018, A&A, 611, A3

Harvey E. J., et al., 2020, Mon. Not. R. Astron. Soc., 499, 2959

Henze M., et al., 2011, A&A, 533, A52

Henze M., et al., 2014, A&A, 563, A2

Henze M., et al., 2018, Astrophys. J., 857, 68

Hernanz M., 2014, in Woudt P. A., Ribeiro V. A. R. M., eds, Astronomical Society of the Pacific Conference Series Vol. 490, Stellar Novae: Past and Future Decades. p. 319 (arXiv:1305.0769)

Hill J. M., et al., 2008, in Stepp L. M., Gilmozzi R., eds, Society of Photo-Optical Instrumentation Engineers (SPIE) Conference Series Vol. 7012, Ground-based and Airborne Telescopes II. p. 701203, doi:10.1117/12.790065

Hillebrandt W., Niemeyer J. C., 2000, Ann. Rev. A&A, 38, 191

Hillman Y., Prialnik D., Kovetz A., Shara M. M., 2016, Astrophys. J., 819, 168

Honeycutt R. K., Robertson J. W., Kafka S., 2011, Astronom. J., 141, 121

Hubble E. P., 1929, Astrophys. J., 69, 103

Hutchings J. B., 1972, Mon. Not. R. Astron. Soc., 158, 177

Izzo L., et al., 2015, Astrophys. J. L., 808, L14

Joiner D. A., 1999, PhD thesis, Rensselaer Polytechnic Institute, New York

Jose J., 2016, Stellar Explosions: Hydrodynamics and Nucleosynthesis. CRC Press, Boca Raton, doi:10.1201/b19165

Kafka S., 2021, Observations from the AAVSO International Database, `https://www.aavso.org`

Kasliwal M. M., Cenko S. B., Kulkarni S. R., Ofek E. O., Quimby R., Rau A., 2011, Astrophys. J., 735, 94

Kasliwal M. M., et al., 2017, Astrophys. J., 839, 88

Kato T., Kojiguchi N., 2021, arXiv e-prints, p. arXiv:2107.07055

Kato M., Saio H., Hachisu I., Nomoto K., 2014, Astrophys. J., 793, 136

Kato M., Saio H., Hachisu I., 2015, Astrophys. J., 808, 52

König O., et al., 2022, Nature, 605, 248

Konyves-Toth R., Csak B., Pal A., Vinko J., 2018, The Astronomer's Telegram, 11594

Kraft R. P., 1964, Astrophys. J., 139, 457

Laycock S., Tang S., Grindlay J., Los E., Simcoe R., Mink D., 2010, Astronom. J., 140, 1062

Leung S.-C., Siegert T., 2022, Mon. Not. R. Astron. Soc.,

Li Q., 1988, in High Energy Astrophysics. p. 2

Li K.-L., 2021, ATel, 14705, 1

Li K.-L., et al., 2017, Nature Astronomy, 1, 697

Li K.-L., Mukai K., Nelson T., Chomiuk L., 2018a, ATel, 11201, 1

Li K.-L., Chomiuk L., Strader J., 2018b, The Astronomer's Telegram, 11590, 1

Li K.-L., Hambsch F.-J., Munari U., Metzger B. D., Chomiuk L., Frigo A., Strader J., 2020a, Astrophys. J., 905, 114

Li K.-L., Kong A., Aydi E., Sokolovsky K., Chomiuk L., Kawash A., Strader J., 2020b, ATel, 13868, 1

Linford J. D., et al., 2018, The Astronomer's Telegram, 11647, 1

Lipkin Y. M., Leibowitz E. M., 2008, Mon. Not. R. Astron. Soc., 387, 289

Livio M., Shankar A., Burkert A., Truran J. W., 1990, Astrophys. J., 356, 250

Lloyd H. M., O'Brien T. J., Bode M. F., 1997, Mon. Not. R. Astron. Soc., 284, 137

Luridiana V., Morisset C., Shaw R. A., 2015, A&A, 573, A42

Martin P., Dubus G., Jean P., Tatischeff V., Dosne C., 2018, A&A, 612, A38

Martini P., et al., 2011, PASP, 123, 187

Mason E., Shore S. N., De Gennaro Aquino I., Izzo L., Page K., Schwarz G. J., 2018, Astrophys. J., 853, 27

Mclaughlin D. B., 1945, PASP, 57, 69

Meegan C., et al., 2009, Astrophys. J., 702, 791

Metzger B. D., Finzell T., Vurm I., Hascoët R., Beloborodov A. M., Chomiuk L., 2015, Mon. Not. R. Astron. Soc., 450, 2739

Meyer F., Meyer-Hofmeister E., 1981, A&A, 104, L10

Miszalski B., et al., 2016, Mon. Not. R. Astron. Soc., 456, 633

Molaro P., et al., 2022, Mon. Not. R. Astron. Soc., 509, 3258

Mondal A., Das R., Shaw G., Mondal S., 2019, Mon. Not. R. Astron. Soc., 483, 4884

Morisset C., Pequignot D., 1996, A&A, 312, 135

Morisset C., et al., 2016, A&A, 594, A37

Morisset C., Luridiana V., García-Rojas J., Gómez-Llanos V., Bautista M., Mendoza Claudio 2020, Atoms, 8, 66

Mróz P., et al., 2016, Nature, 537, 649

Mugrauer M., Gilbert H., Hoffmann S., 2018, The Astronomer's Telegram, 11617, 1

Mukai K., 2017, PASP, 129, 062001

Munari U., Ochner P., 2018, The Astronomer's Telegram, 11926, 1

Munari U., Ribeiro V. A. R. M., Bode M. F., Saguner T., 2011, Mon. Not. R. Astron. Soc., 410, 525

Munari U., Moretti S., Maitan A., 2020a, A&A, 639, L10

Munari U., Moretti S., Maitan A., 2020b, ATel, 13381, 1

Murphy-Glaysher F. J., et al., 2022, Mon. Not. R. Astron. Soc., 514, 6183

Nelson T., et al., 2019, Astrophys. J., 872, 86

Ness J. U., Schwarz G., Starrfield S., Osborne J. P., Page K. L., Beardmore A. P., Wagner R. M., Woodward C. E., 2008, Astronom. J., 135, 1328

Ness J. U., et al., 2012, Astrophys. J., 745, 43

Ness J. U., et al., 2013, A&A, 559, A50

Ögelman H., Beuermann K., Krautter J., 1984, Astrophys. J. L., 287, L31

Oke J. B., 1990, Astronom. J., 99, 1621

Osaki Y., 1974, PASJ, 26, 429

Osaki Y., 1996, PASP, 108, 39

Osborne J. P., 2015, Journal of High Energy Astrophysics, 7, 117

Osborne J. P., et al., 2011, Astrophys. J., 727, 124

Osterbrock D. E., Ferland G. J., 2006, Astrophysics of gaseous nebulae and active galactic nuclei. University Science Books, California

Osterbrock D. E., Tran H. D., Veilleux S., 1992, Astrophys. J., 389, 305

Page K. L., et al., 2010, Mon. Not. R. Astron. Soc., 401, 121

Page K. L., Osborne J. P., Wagner R. M., Beardmore A. P., Shore S. N., Starrfield S., Woodward C. E., 2013, Astrophys. J. L., 768, L26

Page K. L., et al., 2015, Mon. Not. R. Astron. Soc., 454, 3108

Page K. L., Beardmore A. P., Osborne J. P., 2020, Advances in Space Research, 66, 1169

Page K. L., et al., 2022, Mon. Not. R. Astron. Soc., 514, 1557

Pagnotta A., Schaefer B. E., 2014, Astrophys. J., 788, 164

Pavana M., Anche R. M., Anupama G. C., Ramaprakash A. N., Selvakumar G., 2019, A&A, 622, A126

Pavana M., Raj A., Bohlsen T., Anupama G. C., Gupta R., Selvakumar G., 2020, Mon. Not. R. Astron. Soc., 495, 2075

Payne-Gaposchkin C. H., 1957, The Galactic Novae. Dover Publication, New York

Payne-Gaposchkin C., 1964, The galactic novae. Dover Publication, New York

Piascik A. S., Steele I. A., Bates S. D., Mottram C. J., Smith R. J., Barnsley R. M., Bolton B., 2014, in Ramsay S. K., McLean I. S., Takami H., eds, Society of Photo-Optical Instrumentation Engineers (SPIE) Conference Series Vol. 9147, Ground-based and Airborne Instrumentation for Astronomy V. p. 91478H, doi:10.1117/12.2055117

Pogge R. W., et al., 2010, in McLean I. S., Ramsay S. K., Takami H., eds, Society of Photo-Optical Instrumentation Engineers (SPIE) Conference Series Vol. 7735, Ground-based and Airborne Instrumentation for Astronomy III. p. 77350A, doi:10.1117/12.857215

Porter J. M., O'Brien T. J., Bode M. F., 1998, Mon. Not. R. Astron. Soc., 296, 943

Rafanelli P., Rosino L., Radovich M., 1995, A&A, 294, 488

Ribeiro V. A. R. M., 2011, PhD thesis, Liverpool John Moores University, UK

Ribeiro V. A. R. M., et al., 2009, Astrophys. J., 703, 1955

Ribeiro V. A. R. M., Munari U., Valisa P., 2013, Astrophys. J., 768, 49

Roming P. W. A., et al., 2005, Space Sci. Rev., 120, 95

Rosino L., Iijima T., 1987, in Bode M. F., ed., RS Ophiuchi (1985) and the Recurrent Nova Phenomenon. VNU Science Press, Utrecht, p. 27

Rosino L., Iijima T., Benetti S., D'Ambrosio V., di Paolantonio A., Kolotilov E. A., 1992, A&A, 257, 603

Sahman D. I., Dhillon V. S., Knigge C., Marsh T. R., 2015, Mon. Not. R. Astron. Soc., 451, 2863

Saizar P., Pachoulakis I., Shore S. N., Starrfield S., Williams R. E., Rothschild E., Sonneborn G., 1996, Mon. Not. R. Astron. Soc., 279, 280

Santamaría E., Guerrero M. A., Ramos-Larios G., Toalá J. A., Sabin L., Rubio G., Quino-Mendoza J. A., 2020, Astrophys. J., 892, 60

Santamaría E., Guerrero M. A., Zavala S., Ramos-Larios G., Toalá J. A., Sabin L., 2022, Mon. Not. R. Astron. Soc., 512, 2003

Schaefer B. E., 2010, Astrophys. J. S., 187, 275

Schaefer B. E., 2013, The Observatory, 133, 227

Schaefer B. E., 2018, Mon. Not. R. Astron. Soc., 481, 3033

Schaefer B. E., 2021, Research Notes of the American Astronomical Society, 5, 150

Schmidt R. E., 2020, Journal of the American Association of Variable Star Observers, 48, 53

Schmidtobreick L., Shara M., Tappert C., Bayo A., Ederoclite A., 2015, Mon. Not. R. Astron. Soc., 449, 2215

Schwarz G. J., et al., 2011, Astrophys. J. S., 197, 31

Science Software Branch at STScI 2012, PyRAF: Python alternative for IRAF (ascl:1207.011)

Selvelli P., Gilmozzi R., 2019, A&A, 622, A186

Shara M. M., Moffat A. F. J., Webbink R. F., 1985, Astrophys. J., 294, 271

Shara M. M., Zurek D. R., Williams R. E., Prialnik D., Gilmozzi R., Moffat A. F. J., 1997, Astronom. J., 114, 258

Shara M. M., et al., 2007, Nature, 446, 159

Shara M. M., Yaron O., Prialnik D., Kovetz A., Zurek D., 2010, Astrophys. J., 725, 831

Shara M. M., Mizusawa T., Wehinger P., Zurek D., Martin C. D., Neill J. D., Forster K., Seibert M., 2012, Astrophys. J., 758, 121

Shara M. M., et al., 2016, Astrophys. J. S., 227, 1

Shara M. M., et al., 2017a, Nature, 548, 558

Shara M. M., et al., 2017b, Astrophys. J., 839, 109

Shore S. N., 2013, A&A, 559, L7

Shrestha M., Steele I. A., Piascik A. S., Jermak H., Smith R. J., Copperwheat C. M., 2020, Mon. Not. R. Astron. Soc., 494, 4676

Siegert T., et al., 2018, A&A, 615, A107

Siegert T., Ghosh S., Mathur K., Spraggon E., Yeddanapudi A., 2021, A&A, 650, A187

Skrutskie M. F., et al., 2006, Astronom. J., 131, 1163

Slavin A. J., O'Brien T. J., Dunlop J. S., 1995, Mon. Not. R. Astron. Soc., 276, 353

Smak J., 1983, Astrophys. J., 272, 234

Smith R., Steele I., 2017, Liverpool Telescope Technical Note 1: Telescope and IO:O Throughput, doi:10.6084/m9.figshare.4659421.v1, http://researchonline.ljmu.ac.uk/id/eprint/5699/

Smith R. K., Brickhouse N. S., Liedahl D. A., Raymond J. C., 2001, Astrophys. J. L., 556, L91

Sokolovsky K. V., et al., 2022, Mon. Not. R. Astron. Soc., 514, 2239

Stanek K. Z., et al., 2018, ATel, 11454, 1

Starrfield S., 1989, in Classical Novae. pp 39–60

Starrfield S., Sparks W. M., Truran J. W., 1976, in Eggleton P., Mitton S., Whelan J., eds, IAU Symposium Vol. 73, Structure and Evolution of Close Binary Systems. p. 155

Starrfield S., Iliadis C., Hix W. R., 2016, PASP, 128, 051001

Steele I. A., et al., 2004, in Oschmann Jacobus M. J., ed., Society of Photo-Optical Instrumentation Engineers (SPIE) Conference Series Vol. 5489, Ground-based Telescopes. pp 679–692, doi:10.1117/12.551456

Steffen W., Koning N., Wenger S., Morisset C., Magnor M., 2011, IEEE Transactions on Visualization and Computer Graphics, 17, 454

Stone R. P. S., 1977, Astrophys. J., 218, 767

Stoyanov K. A., Tomov T., Stateva I., Georgiev S., 2020, Bulgarian Astronomical Journal, 32, 63

Strope R. J., Schaefer B. E., Henden A. A., 2010, Astronom. J., 140, 34

Tajitsu A., Sadakane K., Naito H., Arai A., Aoki W., 2015, Nature, 518, 381

Takeda L., Diaz M., Campbell R., Lyke J., 2018, Mon. Not. R. Astron. Soc., 473, 355

Takei D., Drake J. J., Yamaguchi H., Slane P., Uchiyama Y., Katsuda S., 2015, Astrophys. J., 801, 92

Teyssier F., 2019, Contributions of the Astronomical Observatory Skalnate Pleso, 49, 217

Tody D., 1986, in Crawford D. L., ed., Society of Photo-Optical Instrumentation Engineers (SPIE) Conference Series Vol. 627, Instrumentation in astronomy VI. p. 733, doi:10.1117/12.968154

Tomov T., Stateva I., Georgiev S., Konstantinova-Antova R., Stoyanov K., 2018, ATel, 11605, 1

Tonry J. L., et al., 2012, The Astrophysical Journal, 750, 99

Toraskar J., Mac Low M.-M., Shara M. M., Zurek D. R., 2013, Astrophys. J., 768, 48

Vanlandingham K. M., Starrfield S., Wagner R. M., Shore S. N., Sonneborn G., 1996, Mon. Not. R. Astron. Soc., 282, 563

Vogt F. P. A., Dopita M. A., Kewley L. J., Sutherland R. S., Scharwächter J., Basurah H. M., Ali A., Amer M. A., 2014, Astrophys. J., 793, 127

Vurm I., Metzger B. D., 2018, Astrophys. J., 852, 62

Wagner R. M., Terndrup D., Darnley M. J., Starrfield S., Woodward C. E., Henze M., 2018, The Astronomer's Telegram, 11588

Walker M. F., 1954, PASP, 66, 230

Warner B., 1995, Cambridge Astrophysics Series, 28

Warner B., 2008, Properties of novae: an overview, 2 edn. Cambridge University Press, p. 16–33, doi:10.1017/CBO9780511536168.004

Warner B., Woudt P. A., 2003, arXiv e-prints, pp astro–ph/0310244

Webbink R. F., 1984, Astrophys. J., 277, 355

Whelan J., Iben Icko J., 1973, Astrophys. J., 186, 1007

Worters H. L., Eyres S. P. S., Bromage G. E., Osborne J. P., 2007, Mon. Not. R. Astron. Soc., 379, 1557

Woudt P. A., Ribeiro V. A. R. M., 2014, in Stellar Novae: Past and Future Decades.

Yaron O., Prialnik D., Shara M. M., Kovetz A., 2005, Astrophys. J., 623, 398

Zemko P., Orio M., Luna G. J. M., Mukai K., Evans P. A., Bianchini A., 2017, Mon. Not. R. Astron. Soc., 469, 476

Zwitter T., Munari U., 1994, A&A Supp., 107, 503

de Vaucouleurs G., 1978, Astrophys. J., 223, 351

della Valle M., Livio M., 1995, Astrophys. J., 452, 704

van Loon J. T., Marshall J. R., Cohen M., Matsuura M., Wood P. R., Yamamura I., Zijlstra A. A., 2006, A&A, 447, 971